Climate Model Simulations of Winter Northern Hemisphere Atmospheric Blocking: Statistical Assessment, Dynamical Perspective, Regional Impacts and Future Change

By

Jessica Vial

Thesis
Submitted to the University of East Anglia
for the degree of
Doctor of Philosophy

Supervisors: Dr Timothy Osborn, Dr Clare Goodess and Prof. Ian Renfrew

Climatic Research Unit
School of Environmental Sciences
March 2012

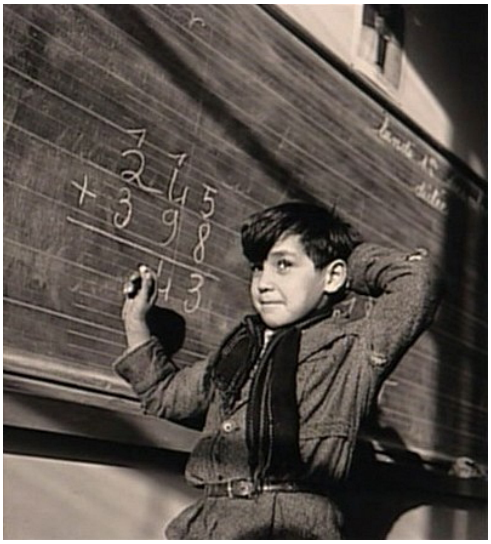

Robert Doisneau

La vie devient une chose délicieuse aussitôt qu'on décide de ne plus la prendre au sérieux.

Henry Millon de Montherlant

Abstract

Characterized by its persistence and quasi-stationary features, atmospheric blocking is often responsible for extreme weather events, which in turn can have enormous impacts on human life, economy and environment. Despite considerable effort made in the comprehension and numerical simulation of this phenomenon, some dynamical aspects of blocking are still not well understood and its poor representation in climate models is a long-standing problem, which has important implications for climate change projections. The basis for this thesis lies in improving understanding of mid-latitude winter-time atmospheric blocking over the two preferred regions of blocking development of the Northern Hemisphere (the Euro-Atlantic and North Pacific sectors), through a multi-faceted study, which includes research on phenomena such as stratospheric sudden warmings and extreme temperature and precipitation events.

First, the ability of six European coupled Atmosphere-Ocean General Circulation Models to simulate atmospheric blocking is evaluated, considering various sources of errors and uncertainties. Although model performance can be affected by the choice of the blocking detection method, errors in representing the frequency, duration and geographical location of blocks are mostly inherent to the models. These errors are primarily linked with the time-mean atmospheric circulation bias (too strong average westerlies and zonality of the flow) and, to a lesser extent, with the high-frequency activity of the transient eddies in the areas affected by blocking. The blocking responses to errors in the low-frequency variability are substantial, but differ according to the region and model considered.

The second aspect of this thesis investigates potential dynamical mechanisms linking blocking lifetime and variability with stratospheric sudden warmings in the IPSL-LMDZ fifth-generation multi-century climate model simulation. The results show a robust connection between the occurrence of stratospheric sudden warmings and blocking in both the Euro-Atlantic and Pacific regions, up to 40 days before and after the onset date of the warmings. The results are explained through the evolution of the large- and small-scale planetary wave disturbances during the weakening and breakdown of the stratospheric polar vortex.

Finally, the influence of European blocking on extreme weather precipitation and temperature events over Europe is examined from the observation/re-analysis dataset and in the present-day and future climates of the IPSL-LMDZ4 variable-grid Atmosphere-only General Circulation Model. The observations reveal that warm and wet extreme weather conditions are four times more frequent (cold and dry five times less frequent) over northern Europe, while over central and southern Europe cold and dry extremes are twice as frequent (warm and wet five times less frequent) during European blocking than during average conditions. The model is able to reproduce these overall relationships reasonable well, except that it overestimates the blocking impact by up to twice the observed values. In the future climate, blocking episodes bring less extreme conditions over northern Europe, while over central Europe blocking-driven weather events are projected to shift toward warmer and wetter extremes. The robustness of the relationships between blocking and extreme events to changes in horizontal model resolution in the core of the blocking region (where the wind is the weakest) implies that the mechanisms responsible for the occurrence of extremes under the action of the blocking high are weakly sensitive to the horizontal resolution of the IPSL-LMDZ4 model.

Acknowledgements

This research project would not have been possible without the assistance and support of many people. The first people I would like to thank are my supervisors, Tim Osborn and Clare Goodess, who strongly encouraged and supported me during the slow and circuitous process of my PhD application. Thanks to Tim and Clare for their guidance and support throughout the period of my PhD, all the while expressing their complete confidence in my abilities and giving me the total control of my work. Thanks to Tim and Clare for having a supportive and understandable attitude in the difficult times. I acknowledge Professor Ian Renfrew, who is also part of my supervisory team, for making suggestions and raising critical points during the committee meetings.

I thank our IT manager, Mike Salmon, who is brilliant and always available (despite having a thousand other things to do) to ensure a smooth running of our computing facilities.

I would like to thank the School of Environmental Sciences for financially supporting the project, conference and conferences-orientated travel expenses and a 2-month extension to my PhD studentship funding.

I am very grateful to Laurent Li, who offered me a 4-month project hosted at the Laboratoire de Météorologie Dynamique (LMD) in Paris, which also contributed to the realisation of the thesis. Thanks to Laurent for his work guidance, financial support toward my living expenses in Paris and for giving me the opportunity to collaborate and have helpful discussions with other researchers within the LMD, François Lott and Francis Codron, and meet important people for the continuation of my career as a researcher, Sandrine Bony and Jean-Louis Dufresne. I would like to thank the secretary of the LMD, Martine Maherou, for her support in all administrive tasks and kindness.

A big thanks to ...
The fantastic people and now friends I met throughout this period for making my time more meaningful and fun,
My old friends and familly in France, for their continuous support of any kind,
And especially to Nicolas, for being my best confident, my love, my source of happiness and energy, and for being supportive no matter what.

Finally, I would like to acknowledge my examiners, Adam Scaife and Adrian Matthews, for their interest in my work and for initiating rewarding discussions during the Viva examination.

Contents

List of tables

List of figures

CHAPTER 1

Introduction

The Earth's planetary atmospheric circulation is governed to a large extent by the uneven distribution of radiative heating between low and high latitudes, with meridional circulations transporting energy from regions in surplus (i.e., tropics) to regions in deficit (i.e., poles) (Lockwood, 2005). The rising motion near the equator and sinking motion in the extratropics, within the so-called *Hadley cell*, transports energy from the equator to the subtropics (at $\sim 30^{\circ}$). In the mid-latitudes, however, energy is transported via synoptic-scale transient cyclones and anticyclones within the prevailing westerly flow (at the higher altitudes this is known as the *jet-stream*). The preferred areas of action for these incipient and maturing weather systems are in midlatitude regions of strong surface baroclinicity (i.e., off the eastern coasts of continental air masses in winter), within meridionally and zonally restricted areas, called *storm tracks* (Brayshaw *et al.*, 2008). Occasionally the prevailing westerly current is blocked and the storm tracks are deflected by the presence of large-scale high pressure systems referred to as *atmospheric blocking*.

1.1 Atmospheric blocking: a general description

The main observational features of atmospheric blocking, being widely established in the literature are (i) their quasi-stationarity, with eventually a slight westward retrogression (Kushnir, 1987; Carlson, 1991), (ii) a relatively long life-time (i.e., typically longer than the synoptic-scale weather systems), from one to several weeks (Rex, 1950a; Dole and Gordon, 1983; Lupo and Smith, 1995a; Tyrlis and Hoskins, 2008), and (iii) a predilection for the Euro-Atlantic and Pacifc regions in the Northern Hemisphere cold season (Elliot and Smith, 1949; Dole and Gordon, 1983; Tibaldi and Molteni, 1990; Wiedenmann and Lupo, 2002; Pelly and Hoskins, 2003).

Figure 1.1 illustrates two snapshots of Northern Hemisphere winter blocking events. The first case is a blocking event that occurred over the Euro-Atlantic region in February 1986 (Fig. 1.1, left), which consists of a meridional high-low dipole structure at upper tropospheric levels, formed by a large intrusion of subtropical air masses into the mid-latitudes over northwest Europe (Hoskins and Sardeshmukh, 1987). This event is an example of what is called *dipole* or *'Rex' block* (named after the study by Rex, 1950b), being frequently observed in the Euro-Atlantic region. The second event occurred over the northeast Pacific in late December 1978 and early January 1979 (Fig. 1.1, right; see also Hansen and Chen, 1982). It is characterized by an upper flow situation reminiscent of the capital letter 'Ω', with an anticyclone in its centre associated with low-pressure systems upstream and downstream of it. This type of blocking pattern, a so-called Ω-*block*, is also frequently observed, but especially in the Pacific region.

Occasionally, blocking episodes can persist for several days with the subtropical air mass being cut-off and isolated from the subtropics, as is the case for the Pacific event shown in Figure 1.1 (right).

Atmospheric blocking is barotropic in nature, with a surface anticyclone, called the *blocking high*, underneath these upper level features (Rex, 1950a; Green, 1977). This is illustrated in Figure 1.1 by the quasi-superposition of the high geopotential values at 1000 hPa (dashed white contours) and at 500 hPa (color shading).

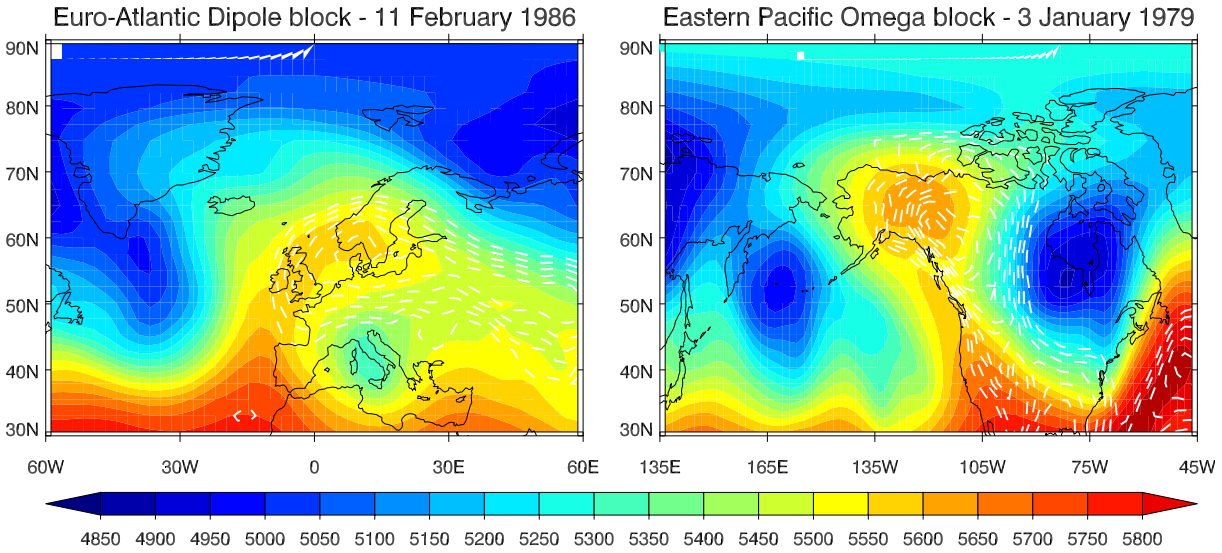

Figure 1.1: Snapshots of blocking episodes showing a Dipole block over the Euro-Atlantic sector on the 11 February 1986 (left) and an Omega block over the eastern Pacific sector on the 3 January 1979 (right). Color shading represents the geopotential height (in meters) at 500 hPa, white dashed contours are the geopotential at 1000 hPa (above 200 m, with 20-m interval). Data are from the ERA-40 reanalysis.

Atmospheric blocking is subject to large seasonal variability, and different regions exhibit different annual cycles in blocking activity. Earlier studies of blocking climatology have shown that blocking occurs predominantly in the cold season in both the Northern and Southern Hemisphere, with less frequent, less persistent and weaker blocking patterns in the Southern Hemisphere when compared to blocking in the Northern Hemisphere (Wiedenmann and Lupo, 2002). The geographic variation of blocking is affected by the land-sea distribution, the topography and other factors disturbing the zonality of the flow (Shakina and Ivanova, 2010). Additionally, it was found that cold season (i.e., winter/spring) blocking episodes in both hemispheres are stronger and more persistent than their warm season counterparts (Lupo and Smith, 1995a; Wiedenmann and Lupo, 2002).

The cold season Northern Hemisphere blocking is the focus of the thesis, because it occurs more often, lasts longer and is more intense than its summer or Southern Hemisphere counterpart.

1.2 Relevance, aims and outline of the research

Atmospheric blocking is recognized as a phenomenon of great dynamical interest and of capital relevance to operational forecasting and climate model simulations. The following relevant aspects related to atmospheric blocking are considered hereinafter.

- Large-scale atmospheric blocking can affect surface weather conditions (e.g., temperature, precipitation, solar insolation) as well as the character of an entire season. The persistence and quasi-stationary features seem to be the key characteristics of blocking that determine the magnitude of its impacts, since it is often responsible for extreme weather events, which in turn can greatly affect the economy, society and the environment. Examples of such episodes are the cold spell that hit Europe in February 1986 (Hoskins and Sardeshmukh, 1987), or the extremely dry and hot weather over western Europe in July 1976 (Green, 1977) or in August 2003 (Black *et al.*, 2004; Beniston, 2004), the latter causing a severe increase in fatalities (Trigo *et al.*, 2005). Fortunately, only a small proportion of blocking events have such extreme consequences. Nevertheless, the broad temporal spectrum and the adverse impacts of blocking on society calls for a better understanding of this phenomenon, and of its influence on the spatial and temporal variability of surface weather conditions.

- Since the acknowledgement of the importance of blocking, several theories explaining different features of blocking have been developed (see Chapter 2), and its predictability using either numerical weather forecasting or climate models has been addressed (Tibaldi and Molteni, 1990; D'Andrea *et al.*, 1998), when it was recognized that an increased predictability could be anticipated during long-lasting blocking situations (Tibaldi and Molteni, 1990).
  Despite the considerable progress made in that area, some aspects of blocking are still not well understood. In particular, there is still a lack of understanding of the dynamics concerning blocking onset, caused by models' failure to predict the regime change from zonal to blocked flow (Shakina and Ivanova, 2010), and its maintenance over prolonged periods. As a result, the model simulation of blocking is still a difficult and challenging task for climate studies. On a climatological level, a systematic underestimation of blocking frequency, particularly for long-lasting episodes, is a long-standing and common deficiency to all models considered (Tibaldi and Molteni, 1990; Tibaldi *et al.*, 1994; D'Andrea *et al.*, 1998; Vial and Osborn, 2011). In order to address this problem, improvements in numerical simulation are assessed in the use of ensembles of models (D'Andrea *et al.*, 1998; Scaife *et al.*, 2010; Vial and Osborn, 2011), and hypotheses are tested in sensitivity experiment studies (Ferranti *et al.*, 1994b; Brankovic and Molteni, 1997). In addition, further blocking studies with a focus on the dynamical mechanisms are crucial for a better representation of blocking, its predictability and its response to climate change.

- There is evidence that the stratosphere may play an important role in blocking variability. The mechanisms responsible for the combined occurrence of blocking and stratospheric sudden warming events is currently being investigated to further study and understand the processes involved in blocking life-time (Naujokat *et al.*, 2002; Martius *et al.*, 2009; Woollings *et al.*, 2010). However, the rarity of stratospheric sudden warmings and the ubiquity of blocking events make it difficult to establish strong and clear evidence of a statistical or dynamical link between both phenomena. This area of research therefore calls for further study to gain a better understanding of blocking.

- Finally, there is some indication that recent climate change is apparent in trends of blocking statistics (Wiedenmann and Lupo, 2002; Croci-Maspoli *et al.*, 2007b). The knowledge of possible long-term changes of blocking activity is therefore of particular interest for a climate change perspective, and yet only a few studies have investigated this question (Matsueda *et al.*, 2009; Sillmann and Croci-Maspoli, 2009, further discussed in Chapter 6).

The aspects related to atmospheric blocking emphasized above provide ample motivation for the further study of this phenomenon, contributing to a better understanding of atmospheric blocking through multi-faceted research into its representation in climate models, certain aspects of its dynamics, its regional impacts and potential for change.

The thesis is presented in seven chapters, including this Introduction, outlined as followed:

Chapter 2 - Literature review and theoretical background

This chapter presents a review of the principal concepts developed to date, which provide theoretical explanations regarding the general structure, geographical distribution, persistence, onset and decay of winter Northern Hemisphere blocking. Some aspects of the literature on atmospheric blocking are relevant only to one chapter of this thesis; in those cases, this literature is introduced and discussed at the start of the relevant chapter rather than in Chapter 2.

Chapter 3 - Blocking detection method

What is blocking? How is it defined? There is still not a consensus on a definition of blocking, which is viewed as either a reversal of the westerly flow (Tibaldi and Molteni, 1990), or a large anticyclonic anomaly (Dole and Gordon, 1983), or as a weather regime (Michelangeli *et al.*, 1995). While these techniques certainly identify the same events in many cases, there are clear differences in the resulting climatologies, which can affect the assessment of climate models when examining their performance at simulating blocking. This aspect is therefore equally important to consider in the study of blocking. The first section of this chapter presents a review of the main blocking detection methodologies employed up to date, followed by the description of the blocking index used in this present study and an assessment of its performance in identifying blocking episodes.

Chapter 4 - Assessment of model simulations of blocking

This part of the thesis investigates the behaviour of different coupled atmosphere-ocean climate models in simulating blocking activity for the winter Northern Hemisphere. This study constitutes an important contribution in assessing the performance of state-of-the-art climate models, as it comprehensively analyses the reasons why models generally underestimate blocking occurrence, differentiating between different sources of systematic errors.

The work presented in Chapters 3 and 4 has been published as Vial and Osborn (2011).

Chapter 5 - Relationships between blocking and stratospheric sudden warming

The aim of this chapter is to advance our understanding of dynamical processes that control blocking variability in relation with the low-frequency stratospheric variability, with a particular focus on stratospheric sudden warming events. Processes involved in the onset, growth and displacement of blocking are investigated by a detailed analysis of a multi-century climate model simulation. This study contributes to further the understanding of blocking, and could be used to improve its representation and its predictability in numerical models.

Chapter 6 - Blocking-related extreme weather events

In this chapter, the influence of blocking on extreme weather precipitation and temperature events

over Europe is examined in the present-day and a future projection of wintertime climate, to enable a better understanding of the mechanisms behind the occurrence of extremes. The sensitivity of the results to the horizontal resolution of the model is also considered. The study of the nature of extreme weather events is essential to gain an understanding of their possible occurrence and dimensions in present and future climate. The knowledge gained can provide valuable information to improve their predictability and eventually contribute to the development of adaptation and mitigation strategies, in order to reduce the damages caused to societies.

Chapter 7 - Summary and outlook

A summary of the results from the earlier chapters is presented and discussed, with a particular regard on future perspectives of research on this subject.

CHAPTER 2

Literature Review

This chapter covers the fundamental atmospheric blocking-related topics that are not studied in this thesis, but that are nevertheless important to be aware of for the understanding of this phenomenon. In addition, the key findings in each specific area of interest for this study will be reviewed in the introduction part of the following individual chapters.

2.1 Theories on blocking

Several theories that account for the general structure, geographical location, persistence, onset and decay of atmospheric blocking have been developed since the middle of the 20^{th} century. But it's only since the late 1970s, with the advent of large observational datasets and powerful computing capabilities, that progress has been made in providing a theoretical explanation of this phenomenon. This section reviews the principal concepts of these blocking theories up to date.

2.1.1 Blocking as linear Rossby wave resonance: a global theory

In global theories, the response in a localized region is determined by global-scale forcing. Linear wave theories view blocking as a global scale phenomenon, which results from the superposition of planetary-scale travelling and/or stationary waves in a blocking wave pattern.

There are two preferred locations for atmospheric blocking highs in the Northern Hemisphere, namely the north-east Atlantic and Pacific ocean basins, which have been observed to coincide with the climatological position of the planetary-scale stationary ridges. Amplification of these climatological ridges was therefore an appealing mechanism that might account for the initiation of blocking over these regions (Hoskins, 1987), and created the interest for understanding the physical processes that force those planetary waves. Since the pioneering work of Charney and Eliassen (1949), the results of numerous studies have demonstrated the importance of both thermal and orographic forcing of the mean flow.

Grose and Hoskins (1979) used a spherical barotropic model to study the steady, linear Rossby wave pattern on a 300mb zonal flow induced by simple mountains. They showed that when a jet impinges a mountain range, two Rossby wavetrains are produced to the north and south of the mountain, leading to a dipole blocking-like structure at 60-80° downstream when the waves are out of phase (Fig. 2.1).

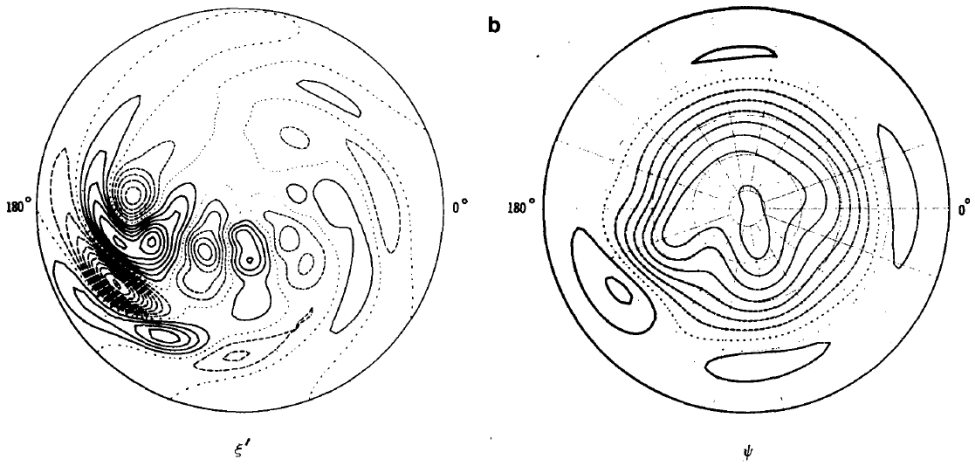

Figure 2.1: Schematic representation of the northern hemispheric flow response when a circular mountain, at 30°N and 180° in longitude, perturbs the zonal flow. The perturbation vorticity field ($\xi^{'}$) is on the left and the total streamfunction (ψ) on the right. Zero contours are dotted and negative contours dashed. The blocking-like structure is located at about 60° downstream from the mountain, where there is a ridge to the north (negative $\xi^{'}$ contours) and a trough to the south (positive $\xi^{'}$ contours) associated with the different phases of the two Rossby wavetrains. Figure taken from Grose and Hoskins (1979).

Tung and Lindzen (1979) showed that blocking could be explained by a linear Rossby wave resonance[1] initiated with both topography and land-sea differential heating forcing. Wave amplification occurs when free-travelling Rossby waves become stationary with respect to the Earth's surface, and can resonantly interact with the topography and differential heating forcing that are stationary. Hoskins and Karoly (1981) found similar results in a baroclinic model, and they also studied the atmospheric response to subtropical thermal forcing. In particular, they showed that subtropical sea surface temperature (SST) anomalies induce a poleward and eastward train of waves emanating from the source region, with longer wavelengths continuing poleward and eastward, while shorter wavelengths turn equatorward. Further downstream the long and short waves become out of phase, and result in a blocking-like pattern, as in the case of orographic forcing (Grose and Hoskins, 1979).

Since the work of Hoskins and Karoly (1981), further evidence of the importance of tropical and subtropical forcing for blocking has been given. Hoskins and Sardeshmukh (1987) presented a diagnostic study of the Northern Hemisphere winter of 1985-86. This winter was characterised by an abrupt change from mild weather conditions and zonal flow over the Atlantic during December and January, to an extremely cold February accompanied by a blocking pattern over the north Atlantic and northeast European region. They studied dynamical mechanisms that were thought to be important for this season, by examining basic diagnostic fields, and diagnosing the importance of different processes using a simplified vorticity equation. They showed that an unusual diabatic cooling and convergence aloft in the south American-Caribbean region would have initiated a dramatic blocking episode over the north Atlantic and northeast European region.

Later, Ferranti *et al.* (1994b) assessed the impact of tropical and extratropical SST anomalies on the winter large-scale atmospheric circulation in the Northern Hemisphere. They performed a series of ensemble integrations of the ECMWF numerical weather-prediction model forced with a climatological SST dataset with superimposed SST anomalies. It was found that with climatological SST the simulated blocking frequency was substantially lower in both the Atlantic and Pacific sectors compared to observed

[1]Resonance occurs when almost free Rossby waves are stationary with respect to the ground (Haines and Marshall, 1987)

blocking frequencies. However, a localized positive SST anomaly (+2 K) over Indonesia has a considerable impact on blocking frequency over the Atlantic and Pacific, in such a way as to reduce the model systematic errors in the tropics and the extratropics. They found a similar, although weaker, response for the Atlantic blocking to a localized negative anomaly (-2 K) over the Caribbean region, in agreement with the study of Hoskins and Sardeshmukh (1987). They also assessed the impact of El Niño/Southern Oscillation (ENSO)-like anomalies, and concluded that blocking frequencies were relatively unaffected by these SST anomalies. This latter result contradicts the finding of Renwick and Revell (1999) in their Southern Hemisphere study of atmospheric blocking. Using a 39-year record of 500 hPa geopotential height, SST and outgoing longwave radiation (OLR) reanalysis outputs, they found that the occurrence of blocking over the southeast Pacific (southern South America) is strongly modulated by ENSO during austral spring and summer. They used a linearized, barotropic vorticity equation model to demonstrate that the divergence associated with tropical OLR anomalies induce a propagation of a Rossby wavetrain into the midlatitudes, resulting in a blocking-like pattern over the southeast Pacific region. More recently, Hinton *et al.* (2009) performed sensitivity experiments with the atmospheric model HadGAM1, and found a marked increase in blocking frequency over the northeast Pacific region with a positive SST anomaly over Indonesia, as was the case in Ferranti *et al.* (1994b). Hinton *et al.* (2009) concluded that the lack of convection over this tropical region in the control simulation, contributed to the underestimation of northeast Pacific blocking frequency.

In this section, we discussed the usefulness of the linear wave theories to explain the existence of blocking through the use of simple mathematical models, dynamical diagnostics based on observational or analysed datasets and more complex and realistic atmospheric models. While blocking could partly be described by a linear Rossby wave response to a thermal and/or orographic forcing of the mean flow, such theories ignore the nonlinear behaviour of the atmosphere and in particular they don't explain the fact that blocking occurrences are often less persistent than SST anomalies, and especially than topographic features (Legras and Ghil, 1985). The extension of linear wave theories to include the nonlinearity arising from the interaction with the zonal flow or from wave-wave interaction will now be discussed in the next section.

2.1.2 Nonlinear wave theory & multiple flow equilibria

Egger (1978) proposed a mechanism for the buildup and the maintenance of blocking by nonlinear interaction of slowly moving free waves with orographically-forced standing waves. This theory was successfully tested numerically using a quasi-geostrophic inviscid flow confined to a channel under barotropic (with and without wave-mean flow interaction, the former giving more realistic blocking patterns) and baroclinic assumptions. They also performed an experiment with no orographic forcing that did not result in a blocking configuration, which clearly confirms the fact that in this model blocking is essentially due to wave-wave interactions.

Charney and DeVore (1979) used a simple highly spectrally truncated (6 waves were retained in the solution), nonlinear, one-layer barotropic channel model, perturbed with sinusoidal topography (form-drag instability) and a barotropic analogue of thermal driving (momentum driving for the mean zonal flow), to show that the interaction between orographically-forced zonal flow and wave perturbations could produce two stable equilibrium states, resembling blocked (closed to linear resonance) and zonal

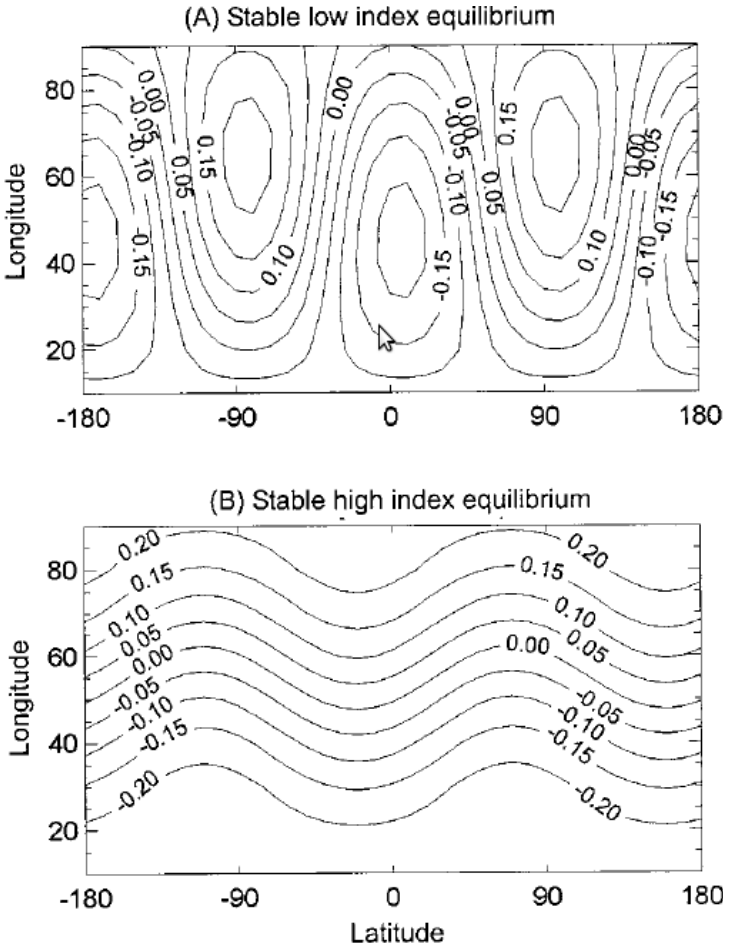

Figure 2.2: Streamfunction fields of the two stable equilibria for a wintertime type thermal forcing pattern of relatively warm ocean/cold land. The stable low index equilibrium (A) may be associated with a 'blocked' situation, while the stable high equilibrium index (B) is more related to a zonal circulation. Figure taken from Shabbar *et al.* (2001).

(farther from linear resonance) flow in the real atmosphere (Fig. 2.2). The existence of the two types of equilibrium was later confirmed by Charney and Straus (1980) in a two-layer baroclinic model forced with topography and thermal asymmetries of the lower boundary. It is suggested that the transition from zonal flow to blocking arises from orographic and baroclinic instabilities of the Hadley circulation (by eddy heat fluxes) with sufficiently strong thermal driving. Reinhold and Pierrehumbert (1985) extended the model of Charney and Straus (1980) by retaining an additional wave in the synoptic-scale that can interact with the externally-forced large-scale waves. They found that synoptic-scale waves were also of primary importance in maintaining and organising these large-scale flow regimes. The existence of this bimodal flow has also been found using more realistic situations with orographic and thermal forcing in a spherical model (Wiin-Nielsen, 1979; Kallen, 1981), and with a more realistic topography (Charney *et al.*, 1981; Malguzzi and Speranza, 1981). Charney *et al.* (1981) examined observed daily 500 hPa geopotential fields for 15 winters, and detected blocking episodes using a criterion based on geopotential height anomalies and minimum persistence thresholds. They found that 19 of the 34 observed events could be explained by their model, and 5 more might also be explained by altering the forcing and the geometry of the model. More specifically, they were able to reproduce equilibrium states with similar amplitudes as for observed blocking episodes, but the regional localization of blocking and the

transition between zonal and blocked flow could not be explained. They suggested that the inclusion of longitudinally-varying external forcing and dissipation could account for the former property. The mechanism of transition (onset or decay of a block) could occur by changes in external driving of the zonal flow (closer to or farther from resonance), such as synoptic-scale wave-mean flow interactions or time-varying heating, which were not included in their model.

Tung and Rosenthal (1985) reexamined the barotropic model of Charney *et al.* (1981) and showed that multiple equilibria of the large-scale flow no longer existed when full nonlinearity was retained (for higher order or less severely truncated models); instead, only one blocked regime was found. They argued that multiple equilibria could still exist in some nonlinear models, as in Legras and Ghil (1985) who used a less severely truncated model (25 modes), but the set of parameters adopted in previous studies, such as high enough mountains, low enough viscosity and strong enough thermal forcing, were found to be perhaps less realistic. Cehelsky and Tung (1987) found similar results for the 2-layer baroclinic models used in Charney and Straus (1980) and Reinhold and Pierrehumbert (1985), stating that these models did not allow proper energetic interactions between large-scale waves and synoptic-scale eddies. Reinhold (1989) attributed this inconsistency to the sensitivity of low-order weakly nonlinear models to the values of parameterized physical processes. Better-resolved baroclinic waves generate different energetics, which are not compatible with the unrealistic and simplified dissipative and forcing parameters that are required to produce a realistic flow in such less severely truncated models. More recently, Molteni (1996) contradicts the statement of Cehelsky and Tung (1987) that multiple states found in highly-truncated models are an artifact of excessive truncation and no longer exist when synoptic-scale waves can realistically interact with the larger-scale forced waves. By using a realistic set of dissipative parameters and orographic forcing as the only source of zonal asymmetry, he found two steady states with well-defined flow regimes in severely truncated hemispheric quasi-geostrophic models as well as at higher resolution.

The theories of multiple equilibria are appealing with regard to accounting for the observed variability of the atmosphere, i.e. alternation between strong zonal flow and weak waves and weak zonal flow and strong waves. However, the existence of multiple equilibrium states remains questionable under realistic atmospheric conditions, and there are still some controversies with regard to the statistical significance of such regime behaviour in observational studies (Nitsche *et al.*, 1994). On the other hand, the existence of quasi-stationary regimes have been found in GCMs. Haines and Hannachi (1995), Hannachi (1997) and Hannachi and O'Neill (2001) identified robust flow regimes over the north Pacific sector, resembling the positive and negative phases of the Pacific-North American (PNA) teleconnection pattern. Hannachi and O'Neill (2001) also analysed multiple weather regimes over the north Atlantic sector, but found only non-significant regime behaviour, corresponding to a weak ridge over the north Atlantic and over western Europe.

2.1.3 Local theories

Local theories consider blocking as a regional phenomenon, assuming that blocking in the Pacific and Atlantic sectors occur quasi-independently. The two examples of local theories that will be discussed in this section, are the *modon* and *soliton* theories.

2.1.3.1 Modons

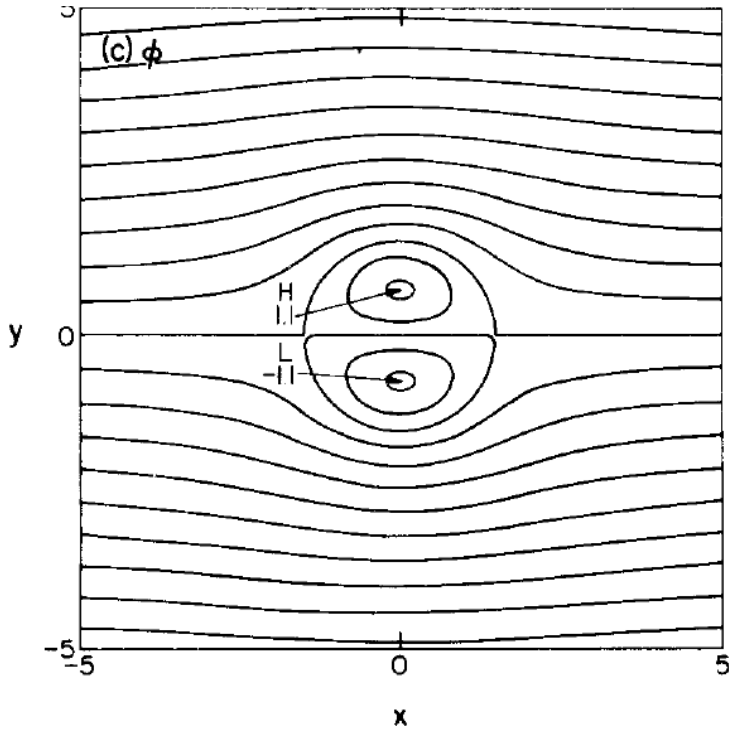

Figure 2.3: Total streamfunction field for a modon solution. Figure taken from McWilliams (1980). Please, refer to the article for more details on the solution's parameters.

The modon theory was exploited by McWilliams (1980) to study some properties related to blocking. He described an equivalent modon as a nonlinear, analytical solution to the inviscid, equivalent[2] quasi-geostrophic barotropic vorticity equation on a β-plane, which exhibits an isolated vortex pair structure (usually with a high pressure system to the north of a low) embedded in the westerlies, and which resembles some blocking events, particularly those occurring in the north Atlantic sector. An example of a modon solution is presented in Figure 2.3. McWilliams analysed a blocking event occurring over the eastern north Atlantic region in January 1963, and demonstrated that the modon solutions borne some resemblance to this blocking event in terms of spatial structures, persistence and intensity. McWilliams *et al.* (1981) performed numerical experiments to show that modons were resistant to small-scale perturbations and that dissipation occurred with larger-scale perturbations.

Although the modons have attractive properties characterising blocking, McWilliams (1980) raised some problems that needed to be addressed in order to validate this theoretical concept under more realistic conditions. Verkley (1984) claimed that the β-plane is an acceptable approximation for small-scale oceanic eddies, but that it is a poor approximation for describing large-scale atmospheric motions; Verkley demonstrated that this restriction was not necessary and that modons could also be constructed on a rotating sphere, therefore taking into account the spherical geometry of the Earth. Haines (1989) has shown that the equivalent modon solutions from a baroclinic two-layer quasi-geostrophic channel model can be excited under more realistic westerly zonal wind conditions that include vertical shear, and which can persist on comparable lifetimes with those of blocking. In their study, Haines and Marshall (1987)

[2] In an equivalent barotropic model, the variation of wind with height is vertically averaged, assuming that the thermal wind is in the same direction as the geostrophic wind. In a fully barotropic atmosphere, neither the speed nor the direction of the wind changes with height.

considered the initiation and maintenance of blocking against dissipation through their interaction with travelling synoptic-scale eddies. They adopted the equivalent barotropic modon as a model for blocking, to show that eddies embedded in a simulated storm track upstream of a blocking region, could excite and maintain a blocking event through nonlinear resonance, whereby the potential vorticity induced by the straining of the eddies propagating in a diffluent flow[3] is transferred into the blocking region.

2.1.3.2 Solitary waves

A baroclinic and weakly nonlinear counterpart of the modon solution, called soliton (or *solitary wave*), was discovered in the nineteenth century as a solution of certain nonlinear wave equations (e.g., the Korteweg and de Vries equation derived by Korteweg and Vries (1895)) (Marin, 2009), and extensively studied by Malguzzi and Malanotte-Rizzoli (1984), Malguzzi and Malanotte-Rizzoli (1985), Malanotte-Rizzoli and Malguzzi (1987) and Malanotte-Rizzoli and Hancock (1987) as a model for persistent blocking events. Malguzzi and Malanotte-Rizzoli (1984) and Malguzzi and Malanotte-Rizzoli (1985) adopted an inviscid, quasi-geostrophic, fully baroclinic potential vorticity equation as a model to explain the structure and persistence of blocking. The solution consists of a nonlinear, localized, stationary Rossby wave superimposed on a mean zonal wind with vertical and horizontal shear. As for the modon theory, the structure of a solitary wave is an equivalent barotropic vortex pair, with an anticyclone to the north of a cyclone. Malguzzi and Malanotte-Rizzoli (1985) performed a series of numerical experiments to investigate the persistence and robustness of the solution to superimposed perturbations (to simulate the real atmosphere) on a baroclinically unstable mean zonal wind; they found that the persistence of the solution was comparable with that of observed blocking events. Later, Malanotte-Rizzoli and Malguzzi (1987) studied the initiation and maintenance of a dipole structure. First, they demonstrated that the pre-existence of a large amplitude zonal wave (with sufficient energy) in an antisymmetric dipole mode (with the anticyclone north of the cyclone) was sufficient to initiate a soliton through nonlinear internal dynamics of the model. Second, they investigated the effect of synoptic-scale transient eddies on the maintenance of a dipole block, and their results were consistent with previous studies (Haines and Marshall, 1987), that eddies could maintain a block against dissipation and mean advection through potential vorticity forcing. Finally, Malanotte-Rizzoli and Hancock (1987) applied this theory to a series of 12 winter Atlantic blocking events; their "unambiguous and robust results" were in agreement with the observed cases.

The difference between the modon and soliton theory was explained in Haines and Marshall (1987). McWilliams (1980) included a restriction in his model that is vital for the existence of modons, according to which the mean westerly flow should be sufficiently large. This condition prevents the presence of stationary Rossby waves inside the vortex pairs, i.e. no coupling and energy transfer is permitted between the isolated dipole and the waves, such that modons cannot lose energy by exciting stationary Rossby waves in their lee. This would lead to the dissipation of the structure, which would then not persist on similar time-scales as blocking. In a modon solution, potential vorticity contours close off, trapping fluid parcels inside the solution, where nonlinear local resonance occurs. Under the modon theory, there is self-stabilisation of a vortex dipole in a westerly flow. In the weakly nonlinear soliton model however,

[3] A diffluent flow is referred to as a pattern of air flow in which the wind direction diverges from an axis oriented normal to the flow. The flow upstream of a blocking region is diffluent when the jet stream splits to separate into two branches and move northward or southward around the block.

the potential vorticity contours do not close off, fluid parcels are not trapped but act both to force and to dissipate the local structure. The soliton solution is a stationary Rossby wave superimposed on a mean zonal flow; the mechanism for sustaining solitary waves resembles the linear resonance described in section 2.1.1.

So far, a number of theories have been described to explain different aspects of blocking. Now a different mechanism is considered. A unified theory, namely the *instability theory*, that accounts for the onset of blocking, sudden stratospheric warming and cyclogenesis, has been proposed and extensively studied by Frederiksen and other contributors. In the next section, this theory will be reviewed with emphasis on the blocking phenomenon.

2.1.4 Instability theory

Frederiksen (1982) studied the instability characteristics of a three-dimensional Northern Hemisphere winter flow, using a two-layer spherical quasi-geostrophic model. Different properties of four fastest-growing perturbations, developing on the basic state, have been studied for three different static stability parameters corresponding to "most unstable", "less unstable" and "least unstable" flow. In the case of the most unstable flow, the fastest-growing perturbations propagate rapidly eastward, and have a monopole cyclogenesis structure with maximum amplitudes slightly downstream of the jet stream maxima, in the location of the Pacific and Atlantic storm tracks. As the static stability parameter increases, the perturbations have a large-scale, eastward slow-moving high-low dipole structure with maximum amplitudes slightly upstream of the regions in the Pacific and Atlantic oceans where mature blocking events occur. It is suggested in this study, that the slow-moving dipole perturbations in less unstable atmospheres correspond to the onset of blocking, while the rapid-moving monopole structures in the most unstable flow correspond to cyclogenesis.

Frederiksen (1983) extended his study to evaluate the relative contribution of barotropic and baroclinic instabilities[4] and the importance of nonlinear processes during the life cycle of a block. It is found that the onset of a slow-moving dipole block, which tilts westward with height, forms slightly upstream of the regions of mature blocks through the combined effect of barotropic and baroclinic instabilities. The dipole then slowly propagates downstream and amplifies through the effect of nonlinear transient processes, and at its mature phase becomes quasi-stationary and essentially equivalent barotropic.

In Frederiksen (1989) and Frederiksen and Bell (1990), the role of instabilities arising from topography was compared with barotropic instability for the formation of mature blocks. Both studies found that whether or not explicit topography is incorporated in either the barotropic or baroclinic model, barotropic instability remains the most dominant mechanism operating on the formation of mature dipole blocks, with the topographic form-drag instability mechanism of Charney and DeVore (1979) playing a minor role.

Frederiksen and Bell (1990) further emphasized on the role of a rapid cyclogenesis off the east coast of north America, which may have triggered the onset of a mature blocking event in the north Atlantic region a few days later. These results seem to support the combined baroclinic-barotropic mechanism for block formation described previously.

[4]Baroclinic instability arises from the existence of a meridional temperature gradient, and hence vertical shear of the mean flow, while barotropic instability results from horizontal wind shear.

The existence of a relationship between rapid or *explosive* cyclogenesis and blocking has been found in several other case studies as well as climatological studies, and will be discussed in more details in the next section along with the impact of high-frequency eddies upon blocking initiation and maintenance.

2.2 The role of transient eddies during the blocking life-cycle

The importance of synoptic-scale or larger-scale transient eddies for the initiation and maintenance of blocking has already been recognised in all the theories discussed in previous sections. This section will now focus on describing the main mechanisms involving such eddies during the life-cycle of blocking.

The *eddy straining mechanism*, which accounts for the building and maintenance of blocking events, was proposed by Shutts (1983). His study was motivated by the observation of Berggen *et al.* (1949) that synoptic-scale baroclinic eddies expand meridionally and compress zonally as they approach a blocking-like region (where the jet splits), to separate into two branches and move northward or southward around the block. The principle of Shutts' hypothesis is based on energy cascade and potential vorticity transfer within a deformation field, such as the splitting of the jet stream around a dipole block, as represented schematically in Figure 2.4.

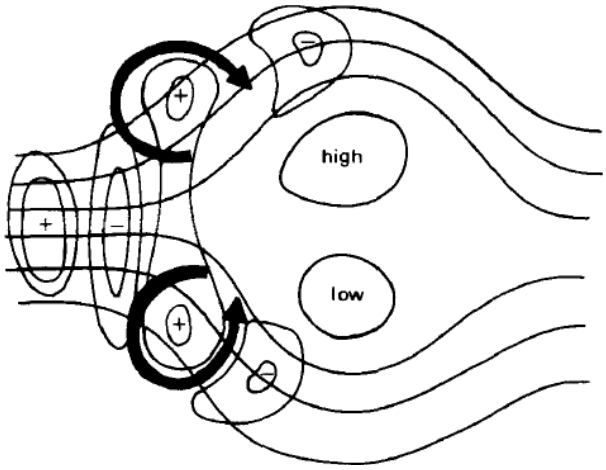

Figure 2.4: Schematic representation of the eddy straining mechanism, when eddies approach the splitting of the jet stream around a high-low dipole block. Black arrows represent the eddy vorticity forcing onto the large-scale structure. Reproduced from Shutts (1983).

In two-dimensional quasi-geostrophic flows, energy and enstrophy[5] conservation requires that energy should be transferred from smaller to larger-scales; this principle is called energy cascade. Following Shutts's hypothesis, barotropic eddies advected by the zonal flow and approaching a split jet stream suffer a strong deformation, which corresponds to an enhanced energy cascade from the eddies to the block flow. As a result, in the region of large eddy enstrophy, upstream of the blocking dipole, eddy vorticity flux is transferred to the blocked flow, which is then expected to induce anticyclonic forcing to the north and cyclonic forcing to the south of the dipole block (Fig. 2.4). The effect of this mechanism is to maintain the blocking structure against the advection of vorticity by the mean flow.

[5]Enstrophy is a measure of the kinetic energy of a fluid as a result of turbulence that corresponds to dissipation effects in the fluid.

Shutts (1983) performed a series of numerical experiments with linear and nonlinear barotropic vorticity equations on a β-plane to verify his hypothesis. In the linear experiments, eddy forcing was prescribed as a wavemaker upstream of a basic state representative of a split jet stream. The action of the eddies was to amplify and sustain the dipole structure. In the nonlinear experiments, Shutts demonstrated that a block could be initiated from a sufficiently weak and uniform westerly flow by the eddy straining mechanism alone, without external forcing such as orography. Anticyclonic eddy vorticity forcing appeared just upstream of the blocking high, rather than in phase with the dipole structure as suggested by Green (1977). This result is in agreement with the work of Austin (1980) and Illari (1984); in Austin (1980)'s model, the vorticity forcing was $\pi/2$ upstream of the blocking anticyclone.

A similar theory, called the *selective absorption mechanism* has been proposed recently by Yamazaki and Itoh (2009), by which the blocking high selectively absorbs the anticyclonic vorticity of the transient anticyclones, reinforcing its low potential vorticity, while synoptic cyclones will either travel south and downstream of an Omega-type block, or be attracted to the blocking low in a dipole-type block, which in either case will maintain the whole blocking structure. Those two theories essentially differ from each other because of the selection mechanism, and both have support from case studies and numerical experiments.

Arai and Mukougawa (2002) examined the effectiveness of the eddy straining mechanism using an identical model to that in Haines and Marshall (1987) except that the channel is twice as wide. They obtained two stationary solutions resembling the modon and zonal flow solutions that are used as basic states, on which synoptic-scale disturbances are generated by a wavemaker located upstream of the diffluence zone prescribed by each solution. Their study contradicts previous results in Austin (1980), Illari (1984) and Shutts (1983) that the eddy straining mechanism for the maintenance of blocked flow against dissipation is not always that effective; its effectiveness depends on the properties of synoptic-scale eddies and on the basic flow.

Another mechanism induced by the transient eddies moving north and south of the block, is the maintenance of the split jet structure by barotropic conversion of eddy kinetic energy into zonal kinetic energy at the location of the two branches, and by conversion of zonal kinetic energy into eddy kinetic energy inside the region of the split jet (Marques and Rao, 1999). Such conversion takes place because of convergence/divergence of the meridional transport of westerly momentum by the transient eddies ($\overline{u'v'}$).

However, while studying the life cycle of persistent anticyclonic anomalies under perpetual January conditions in a GCM, Higgins and Schubert (1994) found that the barotropic conversion of energy from both the high-frequency eddies and the mean flow occurred with the development of a height anomaly, while the contribution from the mean flow dominates for its maintenance. Blocking decay was predominantly associated with baroclinic processes within the low-frequency flow (e.g. thermal advection, latent heat release).

Lupo and Smith (1995b) found that the main mechanism responsible for blocking formation was the advection of synoptic-scale anticyclonic vorticity by the planetary-scale wind. Once established, the block was maintained by barotropic processes. Height falls through advection of planetary-scale cyclonic vorticity by the planetary-scale wind was the main mechanism responsible for block decay.

It appears from those studies (among many others) that both the mean flow and fast-moving transient eddies, as well as their interactions, play an important role in blocking formation and maintenance, while

blocks seem to decay through low-frequency processes.

The importance of the interaction between the mean zonal flow and high-frequency transient eddies was put forward by Hoskins *et al.* (1983) using the two-dimensional *E-vector*, defined as follows:

$$E = (-2M, -N) = \left(\overline{v'^2 - u'^2}, -\overline{u'v'}\right) \tag{2.1}$$

where the overbar signifies a time average and the prime a deviation from this average. u' and v' are the eastward and northward components of the eddy velocity respectively. u'^2 and v'^2 are measures of the zonal and meridional dimensions of the eddies respectively, so the tensor M provides information about the shape of the eddies. N is a measure of the poleward momentum flux by the eddies. Following Hoskins et al.'s demonstration, in a barotropic atmosphere and under the quasi-geostrophic approximation, the anisotropic part of the velocity correlation tensor provides information on the structure of the eddies and on the propagation of eddy activity. In this sense, a westerly E-vector indicates meridionally elongated eddies ($v'^2 > u'^2$) with a group velocity to the east relative to the mean flow.

In order to facilitate the interpretation of the mean-flow forcing by the high-frequency eddies, Hoskins *et al.* (1983) showed that the vorticity tendency created by the horizontal divergence of transient vorticity fluxes ($\nabla_H.\overline{v'\zeta'}$) could be well approximated by the meridional gradient of the horizontal divergence of the E-vector ($\frac{\partial}{\partial y}\nabla_H.E$), as follows:

$$\nabla_H.\overline{v'\zeta'} \simeq \frac{\partial}{\partial y}\nabla_H.E \tag{2.2}$$

where ζ is the absolute vorticity.

Convergence of the E-vector ($\nabla_H.E > 0$) indicates an anticyclonic (cyclonic) forcing to the north (south), and therefore an easterly acceleration of the time-mean flow by the eddies by barotropic processes. This case illustrates a blocking-like configuration. Following the same principle, a local zone of divergence of the E-vector ($\nabla_H.E < 0$) is characteristic of a cyclonic (anticyclonic) forcing to the north (south), and therefore a westerly acceleration of the mean flow, i.e. as in the regions of the maximum jet stream intensity and storm track activity.

Hoskins used the E-vector diagnostic to examine the feedback of the high-frequency transients onto the pattern of a blocking episode that occurred over the northeast Atlantic from the 26^{th} of November to the 7^{th} of December 1981. The vector field implies a convergence of the E-vectors, and therefore an easterly acceleration in the region of weak flow on the southern flank of the blocking anticyclone. The weak flow in the blocked region is therefore barotropically maintained by the action of the high-frequency transients.

Nakamura *et al.* (1997) studied the evolution of 30 strong blocking events over the north Pacific and Europe observed during 27 winter seasons, in order to isolate the role of high- and low-frequency dynamics in the formation of those blocking episodes. With the aid of composite analyses and numerical experiments, they examined the barotropic feedback of eddies on the mean flow due solely to the vorticity flux convergence associated with those eddies ($\nabla_H.\overline{v'\zeta'}$, as in Eq. 2.2). They found that feedback from the high-frequency eddies upon blocking formation accounts for more than 75% of the observed cases in the Pacific, but less than 45% for European blocks. They argued that the intrusion of low potential vorticity within a blocking region associated with low-frequency dynamics (in this case, a quasi-stationary Rossby wavetrain) was of primary importance in the formation of blocking events over Europe, while the

high-frequency eddy forcing was indispensable to blocking formation over the north Pacific. The work of Nakamura *et al.* (1997) suggests that the dynamics involved in the formation of blocking is different in the Atlantic/European and Pacific sectors.

As mentioned in section 2.1.4, several case studies and climatological studies have suggested that rapid or *explosive* cyclogenesis was an upstream precursor for blocking onset.

Since the first observational studies (e.g. Berggen *et al.* (1949) and Namias (1964)), which identified a possible relationship between atmospheric blocking and intense cyclogenesis upstream, considerable effort has been made in order to (1) understand the physical mechanisms in the blocking phenomenon, and (2) support the idea that explosive cyclogenesis could be used as a predictor for block onset. If this is true, substantial progress would be made toward numerical prediction of the onset of blocking episodes.

Hansen and Chen (1982) examined the temporal and geographical evolution of two blocking events for the winter 1978-79 over the north Atlantic and Pacific. They found that both the Atlantic and Pacific blocks developed downstream of intense cyclogenesis events. In the Atlantic, the block was initiated through nonlinear forcing of barotropic ultralong waves by intense baroclinic synoptic-scale waves, while in the Pacific a baroclinic amplification of planetary-scale waves was the main mechanism for the onset of the blocking event. However, Hansen and Chen (1982) emphasized that whether a block forms depends on the phase of the planetary-scale waves with respect to the baroclinic disturbances.

Two winter explosive surface cyclogenesis events were later examined in Colucci (1985). One event was associated with a downstream anticyclonic vortex (blocking high) at 500 mb over the Atlantic ocean, while in the other case, an upstream cyclonic vortex (cut-off low) over eastern North America was observed. With the aid of a quasi-geostrophic model, Colucci suggested that both upper level events resulted from synoptic- and planetary-scale interactions through energy and vorticity transfers from upper level synoptic-scale perturbations (associated with the surface cyclone) to the planetary waves, and that the type of response depends on the phase between the synoptic- and planetary-scale waves. Later, Colucci (1987) studied three case studies of synoptic-scale surface cyclone events associated with different atmospheric circulation changes at 500 mb. Two events lead to either a cyclonic or anticyclonic blocking downstream, as in Colucci (1985), through advection of 'large and spatially and temporally persistent' potential vorticity anomalies. During the third surface cyclone event, the planetary wave amplitude declined; no blocking (anticyclonic or cyclonic) pattern was observed. In this third case, advection of potential vorticity took place but the forcing did not persist in space and time. These results suggest that not only the phase of the synoptic-scale perturbations with respect to the planetary-scale wave was important, but also the amplitude of the existing planetary wave, in order for a blocking system to be established.

Colucci and Alberta (1996) conducted a climatological analysis to quantitatively examine the relationship between explosive cyclogenesis and the onset of blocking over the Northern Hemisphere during seven winter seasons. It was found that while each block onset, either in the Atlantic or Pacific, was preceded by an upstream surface cyclone, the latter was explosive for only 50% of the blocking episodes. The low statistical significance of these results suggests that explosive cyclogenesis might not be a sufficient predictor for block onset. However, the most common precursor of block onset was characterised, in 76% of the cases, by anomalously strong planetary-scale southerly winds over the antecedent cyclone (not necessarily explosive), and anomalously weak planetary-scale westerly winds near and prior to the

block onset. Colucci and Alberta (1996) hypothesized that block onset could occur through the interaction between synoptic-scale perturbations (whether associated with explosive surface cyclogenesis or not) and larger-scale flow if the existing planetary-scale waves have a sufficient amplitude to allow the mechanism to be triggered. The preconditioning of the planetary-scale flow (anomalously diffluent flow) upstream of, and prior to, a blocking episode over Europe that occurred in January 1985 was investigated by Colucci (2001). It was found that the advection of slowly-moving anticyclonic vorticity by high-frequency transients was the major forcing contributing to the preconditioning of the diffluent flow.

Another component of atmospheric variability that appears to be an important factor contributing to blocking variability, namely the teleconnection pattern, will be discussed in the next section.

2.3 Relationships between atmospheric teleconnection patterns and blocking

Temporal correlations between climate anomalies in one region and those in other widely separated regions are referred to as *atmospheric teleconnections* (Wallace and Gutzler, 1981). The relationships between teleconnection patterns and regional blocking parameters (frequency, persistence and geographical position) have been demonstrated in numerous studies, and will be reviewed in this section for the Northern Hemisphere. Understanding the statistical and physical connections between the teleconnection patterns and blocking is of interest for understanding the mechanisms underlying blocking variability, which still remains unclear in many aspects and therefore makes numerical modeling of blocking a difficult task.

2.3.1 Atlantic-Eurasian teleconnection patterns

The most prominent teleconnection pattern in the north Atlantic/Eurasian sector is the North Atlantic Oscillation (NAO) (Wallace and Gutzler, 1981). The NAO is associated with large changes in the strength and location of the north Atlantic jet, and appeared as the most influential pattern on north Atlantic blocking events. The positive phase of the NAO (NAO+) reflects negative geopotential height anomalies at high latitudes over Greenland and positive anomalies at lower latitudes spanning a large longitudinal sector from eastern north America to western Europe. This phase is therefore associated with a strong zonal flow from north America to the Atlantic basin, which starts to diverge just upstream of the European mainland. In the negative phase (NAO-), a different pattern is observed: the jet is weaker and splits in a region west of the Atlantic basin.

Shabbar *et al.* (2001), explored the relationship between wintertime NAO and north Atlantic blocking using 39 years (1958-1996) of daily 500 hPa geopotential height and monthly 1000 hPa temperature fields from the the National Centers for Environmental Prediction-National Center for Atmospheric Research (NCEP-NCAR) reanalysis dataset. They found 67% more winter blocked days, and blocking episodes nearly twice as long in the negative than in the positive phase of the NAO. They proposed a dynamical explanation relating the occurrence and persistence of blocking in the Atlantic sector with the state of the NAO, using a conceptual model based on the multiple flow equilibria theory of Charney and DeVore (1979). The dynamical connection is related to the zonally asymmetric thermal forcing induced by the land-sea thermal contrast, which in turn is modulated on an interannual timescale, by the phase

of the NAO. In the negative phase of the NAO, the distribution of the surface air temperature at mid and high latitudes of the north Atlantic basin is 'warm ocean/cold land', while it is the opposite in the positive phase. According to the model of Charney and DeVore (1979), the zonally asymmetric thermal forcing and topographic forcing are in phase when the 'warm ocean/cold land' pattern occurs; this configuration is favourable for more frequent and persistent blocks. Shabbar *et al.* (2001) therefore argued that the negative phase of the NAO provides the appropriate thermal forcing that creates an environment favourable for block formation, i.e, an amplified meridional wave-like flow.

A more recent statistically-based analysis performed by Barriopedro *et al.* (2006) confirms the relationship between north Atlantic blocks and the NAO: blocked days were between 55% and 60% more frequent in NAO- than in NAO+, the average persistence of blocking events were more than 11 days in NAO-, almost 30% longer than in NAO+ (8 days). The geographical characteristics of Atlantic blocks were also influenced by this pattern, with a significant northward displacement of nearly 5° and westward extension of about 10° in the negative phase. In addition, the dynamical connection proposed by Shabbar *et al.* (2001) was examined by compositing surface air temperature for both polarities of several teleconnection patterns, and was confirmed for the north Atlantic basin, and extended to the north Pacific when the 'east Pacific block-East Pacific pattern' linkage was considered. This strong and significant anti-correlation between NAO phases and Atlantic blocking is supported by other studies (Stein, 2000; Scherrer *et al.*, 2006; Croci-Maspoli *et al.*, 2007a).

Although the strongest influence of the NAO is on north Atlantic blocking, some studies showed evidence of enhanced blocking frequency in the European sector during the positive phase of the NAO, and which at first glance seem consistent with the synoptic situation of the NAO in its positive phase. Scherrer *et al.* (2006) used three two-dimensional blocking indices (one is an extension of the Tibaldi and Molteni (1990) blocking index, and the two others are based on vertically-averaged potential vorticity fields, see section 3.1 for more details), and all three indicators support this result. They also suggest that the occurrence of Atlantic blocking and the negative phase of the NAO are only significantly correlated at 60°N, while the positive NAO-European blocking correlation is significant at the more southern latitude of 50°N. Barriopedro *et al.* (2006) showed that the main influence on European blocking frequency and persistence was from the Scandinavian pattern (also referred as the Eurasian pattern), which according to Wallace and Gutzler (1981) shares centers of action with the Western Atlantic pattern in its positive phase, itself being closely related with the NAO+. Winter blocking in the European sector was 50% more frequent and 30% longer in the positive than in the negative phase, with an average northward and eastward displacement of 5° each.

2.3.2 Pacific teleconnection patterns

The Pacific-North American (PNA) pattern is the Pacific counterpart of the NAO pattern, contributing the most to the winter atmospheric variability in the Pacific and North American regions (Wallace and Gutzler, 1981). It is characterised by strong modulations in the strength and location of the west Pacific jet, and has its centers of action over western Canada and the southeastern United States. The positive phase (PNA+) is associated with an enhanced jet over the western Pacific that splits in the region of the western United States, while in the negative phase the jet suffers a westward retraction, weakens and splits in the region east of Japan. This pattern of variability mostly affects blocking occurring in the eastern part of the Pacific. Croci-Maspoli *et al.* (2007a) found a pronounced and significant enhancement

of winter blocking frequency (above 100% increase compared to climatological values) in the north Pacific Ocean during the negative phase, while almost no blocks in this region were found in the opposite phase. In addition, Croci-Maspoli *et al.* (2007a) noted a positive correlation between the PNA pattern and north Atlantic blocking, which according to Feldstein (2003) could be attributed to a Rossby wave propagation from the Pacific region during the positive phase of the PNA.

Barriopedro *et al.* (2006) found a relationship between the East Pacific pattern and east Pacific blocking: blocking events were almost 65% more frequent and 15% more spatially extended in the negative than in the positive phase. This difference was attributed to a pronounced northeastward extension of the Pacific jet with enhanced westerlies over western North America in the positive phase, and weaker westerlies over the north Pacific in the negative phase. As a result, blocks were more frequent over Alaska and Bering Strait in the negative phase of the PNA pattern. It is worth mentioning that according to Croci-Maspoli *et al.* (2007a) and Barriopedro *et al.* (2006), the East Pacific pattern affects east Pacific blocking at higher latitudes than the PNA pattern. In addition, Barriopedro *et al.* (2006) found that the West Pacific pattern was the primary teleconnection pattern affecting blocking variability in the west Pacific sector over the whole year, being particularly prominent during spring. Blocking frequencies in the negative phase were twice those in the positive phase, with an eastward shift of almost 10° over the east Asian continent. This change in blocking occurrence is attributed to the weak jet stream over Japan in the negative phase.

In Feldstein (2002) and Feldstein (2003) the dynamical processes that drive the PNA and NAO are investigated with the use of composites and projections of each of the terms in the streamfunction tendency equation. Their main results are summarised as follows. The NAO life-cycle is dominated by nonlinear processes. The NAO growth is driven by the high- and low-frequency transient eddy vorticity fluxes, and maintained by a positive feedback process between the NAO anomalies and the high-frequency transient eddy vorticity fluxes. The decay of the NAO occurred through the divergence term and the low-frequency eddy vorticity flux. Furthermore, it was found that the positive phase of the NAO was initiated by a wavetrain from the north Pacific, while NAO- appeared to develop in situ.

In contrast, it was found in Feldstein (2002), that linear processes played a crucial role in both the growth and decay of the PNA anomaly. The PNA anomaly develops by barotropic conversion from the climatological stationary eddies to the PNA anomaly, and the decay period is dominated by the divergence term.

There are some similarities between the NAO and PNA patterns: their decay stage is dominated by the divergence term (either through frictional processes via Ekman pumping or induced by upper-tropospheric vorticity advection), and the high-frequency transient eddies appear to have an important role in maintaining the anomaly. However, the principal difference between the two patterns was that NAO is dominated by nonlinear processes, whereas PNA is primarily linear. It could therefore be assumed that while Atlantic and Pacific blocking events bear some similarities, they might also be driven by different mechanisms (linear versus nonlinear) in the Atlantic and Pacific sectors, as suggested in several studies (e.g. Nakamura *et al.* (1997)).

2.3.3 El Niño Southern Oscillation

The El Niño Southern Oscillation (ENSO) cycle is the principal teleconnection pattern that seems to have a global-scale influence, and it has been observed to significantly affect winter blocking variability in all regions. ENSO is a coupled atmosphere-ocean interannual signal in the tropics, with a cycle of about 3 to 7 years. The warm phase, called El Niño (EL), involves warmer SST in the eastern tropical Pacific from east of the International Date Line to the west coast of south America, and is associated with a weakening of the zonal SST gradient in the tropical Pacific, which in turn affects directly the trade winds, the tropical circulation and precipitation, and indirectly the extratropical circulation. The cold phase, La Niña (LA), exhibits the opposite pattern (Trenberth *et al.*, 2007).

The literature provides evidence of a strong influence of ENSO on the PNA pattern, and perhaps a weak influence on the NAO. Pozo-Vazquez *et al.* (2001) found a statistically significant pattern resembling the positive phase of the NAO during strong LA events. Renwick and Wallace (1996) found that the PNA pattern tends to be in its positive phase during EL. Therefore, it could be expected (according to the previous sections) that Atlantic (Pacific) blocks occur less often during LA (EL).

Barriopedro *et al.* (2006) found that for the Atlantic, European, west Pacific and east Pacific sectors, blocking events were 14%, 15%, 16% and 52% stronger during LA, respectively. They also found that west and east Pacific blocks were 23% and 42% more spatially extended in the cold phase, respectively. Similar results were reported in other studies. Wiedenmann and Lupo (2002) found more frequent, more persistent and stronger blocks during LA than during EL or the neutral phase of ENSO, especially in the Pacific sector. They suggested that the increased blocking frequency in LA years were related to the increased cyclone activity over the midlatitude Northern Hemisphere. Consistent with their results, Renwick and Wallace (1996) found smaller 500 hPa variances during EL years, implying more zonal flow, enhanced westerlies and therefore less blocking over the north Pacific; the frequency of blocked days was approximately 40% lower relative to LA years. They claimed that the ENSO cycle affects both the mean and the variance of the geopotential height field over the north Pacific, which in turn influence the frequency distribution of the PNA index (more frequent PNA+ during EL) and of blocking over Alaska/Bering Strait (east Pacific blocks). Similar results were found in Chen and Van Den Dool (1997), in that blocked flow over the eastern north Pacific developed twice as much during LA than during EL periods. The mean field over the north Pacific was much more diffluent in LA than in EL, and the high-frequency transient eddies were more effective in maintaining blocked flow at high latitudes during LA, than at midlatitudes during EL. As a result more blocking events could develop and be maintained by transient eddies over the north Pacific during LA than EL years. Although, several studies have reported an increase in Pacific blocking occurrence during LA (Renwick and Wallace, 1996; Chen and Van Den Dool, 1997; Wiedenmann and Lupo, 2002), the differences between the two phases are not always significant. In Barriopedro *et al.* (2006), significant differences in blocking frequencies were found to be more related to a shift in the preferred location of block formation over the Pacific region, rather than a direct influence in the frequency of occurrence. They found that during the cold phase, more blocks occurred in the western and less blocks occurred in eastern part of the Pacific, without significant frequency change over the whole Pacific sector.

2.4 Blocking as Rossby wave-breaking

In addition to the studies mentioned previously, where blocking is mostly considered from the viewpoint of mid-tropospheric flow in the form of geopotential or streamfunction field, it has also been recognised that more dynamical information on blocking could be gained by analysing potential temperature on potential vorticity surfaces (and in particular potential temperature on the dynamical tropopause[6]) or potential vorticity on potential temperature surfaces (Pelly and Hoskins, 2003; Franzke *et al.*, 2004; Berrisford *et al.*, 2007; Woollings *et al.*, 2008; Franzke *et al.*, 2011).

Hoskins and Sardeshmukh (1987) stated that an essential ingredient to the formation of blocking, and in particular the Euro-Atlantic block that occurred in February 1986, was a large intrusion of subtropical air masses into the mid-latitude region (see also Figure 1.1, right panel). Large meridional elongation of potentially warm air which results in an irreversible mixing between high and low latitudes and a reversal of the normal negative meridional gradient of the potential temperature can be viewed as *"Rossby wave-breaking"* (e.g., Franzke *et al.* (2004)). Given the conservative properties of the potential temperature the only way for this wave-breaking (or blocking pattern) to decay is by the potentially warm air moving back to subtropics, by radiative cooling or by friction (Hoskins *et al.*, 1985, see also Section 3.1.1).

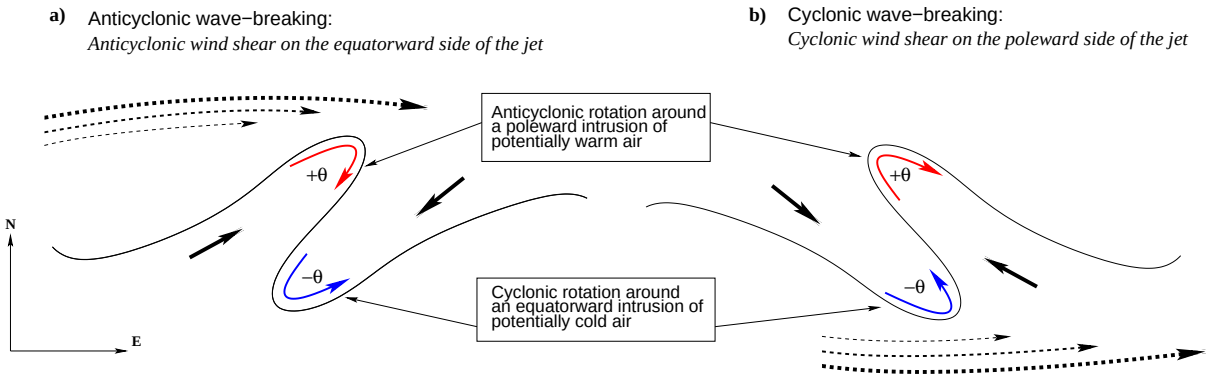

Figure 2.5: Schematic representation of the Northern Hemisphere (a) anticyclonic wave-breaking and (b) cyclonic wave-breaking. The contours indicate the potential temperature on the dynamical tropopause, the solid black arrows indicate the direction of the flow advection, the red (blue) arrows represent the anticyclonic (cyclonic) rotation in each of the potentially warm (cold) branch of the advected air and the dashed black arrows indicate the position and meridional shear of the jet stream relative to the wave-breaking.

The results presented in Franzke *et al.* (2004); Woollings *et al.* (2008); Franzke *et al.* (2011) and others indicate that not only blocking but also PNA and NAO-like anomalies can arise from cyclonic or anticyclonic wave-breaking (see Figure 2.5 for a schematic representation of Northern Hemisphere wave-breaking). The negative phase of the NAO, which is reminiscent of a blocking-like structure in the north Atlantic (see Section 2.3.1), involves cyclonic wave-breaking (along a southeast-northwest axis, Fig. 2.5b) on the poleward side of the climatological jet stream, while its positive phase, which has been linked with increased occurrence of European blocking events (Section 2.3.1), involves anticyclonic wave-breaking (along a southwest-northeast axis, Fig. 2.5a) at lower latitudes (Franzke *et al.*, 2004). These results are consistent with the work of Scherrer *et al.* (2006) showing that Atlantic blocks in the negative phase of the NAO occur at higher latitudes than European blocks during the positive

[6]The dynamical tropopause is defined as two potential-vorticity-unit (PVU) and 1 PVU = $10^{-6} m^2 s^{-1} K g^{-1}$

phase (see also Section 2.3.1). Similarly, the relationship between wave-breaking and the PNA indicates an anticyclonic wave-breaking in the subtropics prior the negative phase of the PNA (associated with a pronounced enhancement of blocking events in the northeast Pacific, see Section 2.3.2), while cyclonic wave-breaking on the poleward side of the jet excites the positive phase of the PNA (Martius *et al.*, 2007; Franzke *et al.*, 2011).

Several studies have also addressed the question of what factors influence the phase of the NAO/PNA patterns and therefore the type of wave-breaking (e.g., Woollings *et al.* (2008) and Franzke *et al.* (2011)). For instance, Franzke *et al.* (2011) found that the negative phase of the PNA is preceded by an enhanced convection over the tropical Indian ocean and a reduced convection over the western tropical Pacific region about 2 weeks before the maximum amplitude of the PNA anomalies. This tropical convection excites a small-amplitude negative PNA anomaly, which preconditions a background flow (i.e., a weakened and retracted subtropical jet, with a reduced cyclonic wind shear on its poleward side) favourable for an equatorward propagation of midlatitude synoptic-scale waves into the subtropics, which then undergo anticyclonic wave-breaking to further amplify the negative PNA. The positive PNA exhibits opposite features for the background flow (i.e., a strengthened and elongated subtropical jet, with enhanced cyclonic wind shear on its poleward side), which favours an eastward propagation of synoptic-scale waves into the midlatitude northeast Pacific where they undergo cyclonic wave-breaking.

This wave-breaking view of blocking provides another indication (from those already suggested in previous sections; Sections 2.2 and 2.3.2) that the onset of blocking events might be driven by different mechanisms according to their region of occurrence (cyclonic versus anticyclonic wave-breaking).

2.5 Summary

This chapter has presented some of the major theoretical concepts essential for understanding the dynamics of blocking life-time.

Overall, blocking theories could be classified in two categories, namely the *global* and *local* theories. Global theories consider blocking as a large-scale phenomenon resulting from the resonance of planetary-scale waves. The physical processes that force planetary-scale waves include topographic features, such as extended mountain ranges and land/sea thermal contrasts. While the linear Rossby wave resonance theory (Section 2.1.1) could partly explain the existence of blocking over the two preferred locations in the Northern Hemisphere (Atlantic and Pacific basins), nonlinearity arising from the wave-mean flow interaction or wave-wave interaction (Section 2.1.2) seems to be essential in order to account for the persistence of blocking. In contrast, local theories consider blocking as a regional phenomenon that is quasi-independent of the conditions prevailing away from the blocking region. The modon and soliton solutions are two examples of the local theories discussed in Section 2.1.3. They exhibit localized vortex pair structures (usually with a high pressure system to the north of a low), which are reminiscent of some observed blocking events, particularly those occurring in the north Atlantic sector.

Other theories that account for the initiation and maintenance of blocking episodes were also reviewed. The instability theory (Section 2.1.4) supports the combined baroclinic-barotropic instability mechanism for the formation of mature dipole blocks, while Section 2.2 also highlights the importance of synoptic-scale and larger-scale transient eddies for the initiation and maintenance of blocking episodes.

Finally, the mechanisms underlying blocking variability were discussed in terms of the statistical and dynamical relationships between the teleconnection patterns and regional blocking (Sections 2.3 and 2.4).

A literature review of other studies more specific to the purpose of this thesis is also presented in the introduction part of the following individual chapters.

CHAPTER 3

Atmosphere-ocean general circulation model simulations of atmospheric blocking. Part 1: description and assessment of the blocking detection method

3.1 Introduction: a review of blocking detection methods

Although theories on blocking are crucial to understand the dynamics of blocking life-time, and therefore make possible blocking simulation in numerical models, the method used to identify atmospheric blocking is equally important. There is a large variety of blocking indices in the literature, and it will be shown in the second part of this study (Chapter 4) how they can affect the assessment of climate models when examining their performance in simulating atmospheric blocking. The main objective of this first part is to present the blocking detection method employed in this study, and assess its performance in identifying blocking episodes.

A large variety of blocking detection methodologies have been employed since the mid-20^{th} century. The most recent classification reviewing the pioneering methods of each category was proposed by Barriopedro *et al.* (2010), and is presented in Figure 3.1. Although the identification of blocking events usually requires standard criteria, such as a minimum spatial extension and temporal persistence, the methods can vary in many aspects, with respect to their **degree of objectivity**, the **nature of the base field** on which the blocking index is applied, and the specific criteria employed by the blocking detection methodologies (i.e., the actual **blocking index**).

The degree of objectivity of the blocking index

Early studies, such as Rex (1950a) and Austin (1980), were highly subjective. Blocking events were visually detected from daily synoptic maps, following a set of arbitrary criteria based on features of observed blocking cases. The first well-accepted definition of blocking was given by Rex (1950a) as *a sharp transition from a zonal type flow to a splitting of the basic westerly current into two branches of appreciable mass, extending over at least 45° in longitude for a period of at least 10 days.* Latter, with the development of large observational datasets and powerful computer capabilities, studies started to design a variety of sophisticated and automated methods based on more objective criteria (these automated methods will be discussed later in more details). Nevertheless, all blocking detection methodologies have to adopt certain arbitrariness, particularly for defining the minimum spatial extension and temporal persistence thresholds, although the accuracy for theses parameters do not seem crucial (Barriopedro

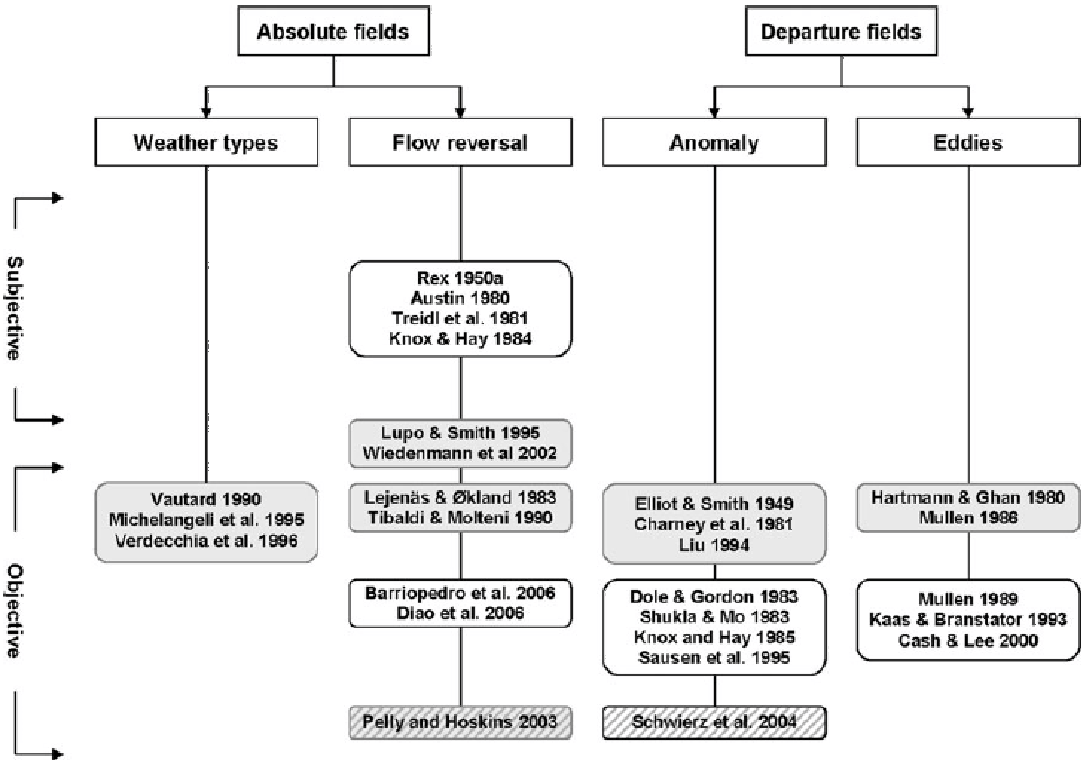

Figure 3.1: Classification of blocking detection methodologies as a function of their objectivity (left rows), the nature of the base field (header columns) and the specific criteria employed by the methodologies (sub-header columns). Shaded (not shaded) boxes are methods providing a 1-D (2-D) representation of the blocked flow. Dashed (not dashed) boxes are methods based on dynamical (standard isobaric) variables. Reproduced from Barriopedro *et al.* (2010).

et al., 2010), and therefore some subjectivity could be adopted in their definition.

The nature of the base field on which the blocking index is applied

The blocking detection methodologies can be applied on two different types of base field, namely the absolute field, or departure from a climatological (Dole and Gordon (1983); Liu (1994)), zonal (Kaas and Branstator, 1993) or regional (Mullen, 1989) mean. In both cases the geopotential height at mid-tropospheric levels, i.e. 500 hPa, is the most common variable used, although other standard isobaric variables, such as the meridional wind (Cash and Lee, 2000; Kaas and Branstator, 1993), or zonal wind components (Diao *et al.*, 2006; Scaife *et al.*, 2010), have also been adopted. More recently, some studies have employed dynamically-based approaches, including the 2-D representation of blocks defined using the potential temperature variable on a potential vorticity surface (Pelly and Hoskins, 2003), or the vertically averaged potential vorticity approach (Schwierz *et al.*, 2004; Scherrer *et al.*, 2006; Croci-Maspoli *et al.*, 2007a).

The specific criteria employed by the blocking index

The last, and not the least, aspect differentiating a blocking detection methodology from another, is the actual blocking index along with its associated criteria. The main blocking indices reported in the literature are based on: (1) meridional gradient reversal of the flow, (2) departures from a long-term climatological mean, or zonal or regional mean, and (4) atmospheric circulation patterns.

3.1.1 Flow reversal-based index

Since Rex's subjective definition (Rex, 1950a), there have been a large number of blocking detection methods based on the concept of *zonal index*, which measures the strength of the average westerly flow in the mid-latitudes. The first objective index was introduced by Lejenäs and Økland (1983), as the 500 hPa geopotential height difference between 40°N and 60°N ($Z_{40} - Z_{60}$), since in a typical Northern Hemisphere blocking situation the high-pressure cell was observed near 60°N and low-pressure cell near 40°N (Treidl *et al.*, 1981). The flow was then assumed to be blocked at a given longitude and time if the blocking index was negative, which implies from the geostrophic approximation, **an average geostrophic easterly flow in the blocked region**:

The scale analysis of the horizontal momentum equations shows that for mid-latitude synoptic-scale weather systems only the Coriolis force and pressure gradient force are retained and are therefore in approximate balance (Holton, 2004):

$$f u_g \simeq -g \left(\frac{\partial Z}{\partial y} \right)$$

where, u_g is the geostrophic zonal wind, f is the Coriolis parameter, g is the acceleration of gravity ($g = 9.81 m/s^2$) and Z is the geopotential height.

Integrating this relation between 40°N and 60°N yields:

$$\int_{40^\circ N}^{60^\circ N} u_g dy \simeq + \frac{g}{f} \left(Z_{40^\circ N} - Z_{60^\circ N} \right)$$

The zonal blocking index (i.e., a one-dimensional blocking index) is one of the most commonly used in the literature (e.g., Tibaldi and Molteni (1990), Tibaldi *et al.* (1997), D'Andrea *et al.* (1998), Barriopedro *et al.* (2006)). It has been extended so as to consider *large-scale blocking episodes*, requiring minimum spatial extension and temporal persistence thresholds, with more or less severe criteria, their exact values not being crucial in the blocking detection procedure (Barriopedro *et al.*, 2010). For instance, Lejenäs and Økland (1983) defined regions of blocked flow over at least 30° in longitude, while Tibaldi and Molteni (1990) relaxed this condition to 12° longitude. As for the minimum temporal persistence of a blocking episode, it ranges between 1 (Lejenäs and Økland, 1983) and 10 (Rex, 1950a) days .

Besides the adjustment of those criteria, which are also required for other types of blocking index, the zonal index has been modified with respect to more fundamental conditions, aiming at improving the blocking detection algorithm. For their assessment analysis of a forecast model to predict blocking, Tibaldi and Molteni (1990) used the same blocking index as in Lejenäs and Økland (1983), with an additional criterion requiring average westerlies on the poleward side of the high-pressure cell, so that large southward displacements of the westerly jet (with its northward low-pressure cell) are not included in the blocking catalogue. A two-dimensional expansion (longitude-latitude) of the Tibaldi and Molteni (1990) index was more recently proposed by Barriopedro *et al.* (2006), Scherrer *et al.* (2006) and others to improve the representation of the structures and dimensions of the blocks.

A dynamical approach of the flow reversal-based blocking index was proposed more recently by Pelly and Hoskins (2003). Their blocking index was defined under a potential vorticity (PV) framework in which the blocking anticyclone is associated with a reversal of the normal negative meridional gradient

of the potential temperature (θ) on a dynamical tropopause, defined as PV = 2 potential vorticity units (PVU, 1 PVU = $10^{-6} m^2 K s^{-1} kg^{-1}$):

$$\frac{2}{\Delta\phi}\int_{\phi_0}^{\phi_0+\Delta\phi/2}\theta d\theta - \frac{2}{\Delta\phi}\int_{\phi_0-\Delta\phi/2}^{\phi_0}\theta d\theta > 0$$

where ϕ_0 is the central latitude of the blocking structure (assuming a high-low dipole structure), and $\Delta\phi$ is the latitudinal scale of blocking.

This PV-θ (tropopause maps) framework offers a more detailed view of upper-level atmospheric features (ridges and troughs) compared to isobaric fields. More small scale features are identified by this index than with the Tibaldi and Molteni (1990)'s index, as the geopotential field is a smoother version of the equivalent PV field (i.e., PV is related to the geopotential by a Laplacian, which act as a smoothing operator, Pelly and Hoskins (2003)).

Dynamically speaking, as this framework assumes adiabatic and frictionless processes (which is a rather good approximation in the mid-latitudes), the only changes come from the horizontal advection of potential temperature on the PV surface by the natural flow. In that sense, cut-off blocking anticyclones are formed by advection of warm subtropical air northwards (Hoskins *et al.*, 1985). Advection of high potential temperature creates a potential temperature anomaly (relative to the surrounding region). This anomaly persists unless the warm air returns to the subtropical region, or is changed by diabatic processes. In the blocking anticyclone, the static stability is increased so convection is suppressed (opposite process occurs in the cyclone), therefore diabatic change will be essentially produced by radiational cooling, which has a time scale of approximately a week (Hoskins *et al.*, 1985).

In contrast with the blocking index defined by Lejenäs and Økland (1983) and Tibaldi and Molteni (1990), where the central blocking latitude is fixed and independent of the longitude, the Pelly and Hoskins (2003)'s methodology uses a longitudinal-dependent central latitude ϕ_0, taken as the latitude of the maximum climatological annual mean high-pass transient eddy kinetic energy at 300 hPa. This field is directly linked with circulations of cyclones and anticyclones of the mid-latitudes, and since blocking is associated with the interruption of transient weather systems, it is expected to be seen at those latitudes, and therefore this aspect was used to specify the central latitude of blocking (ϕ_0). $\Delta\phi$, being the typical latitudinal scale of blocking, is taken at 30° so as to be representative of the latitudinal width of the storm track.

Pelly and Hoskins (2003) compared their index with that of Tibaldi and Molteni (1990), and showed that some blocks identified by Tibaldi and Molteni (1990) were actually not blocks but pressure minima. This shortcoming has been noticed, and the geopotential-based zonal index has been modified in consequence by Barriopedro *et al.* (2006) by restricting the blocking definition with a third condition that ensures identification of high-pressure cells at the latitude of the blocking anticyclone. Another major difference between the Tibaldi and Molteni (1990) and Pelly and Hoskins (2003) blocking indices, is the identification of different blocking sectors in the Pacific, with a peak in the eastern Pacific at about 225° for the PV-θ index, and a peak in the western Pacific at about 170° for the Tibaldi and Molteni (1990) index. Pelly and Hoskins (2003) entirely attributed this discrepancy to the different blocking latitudes used in each calculation (compare the solid and dotted curves in Figure 3.2).

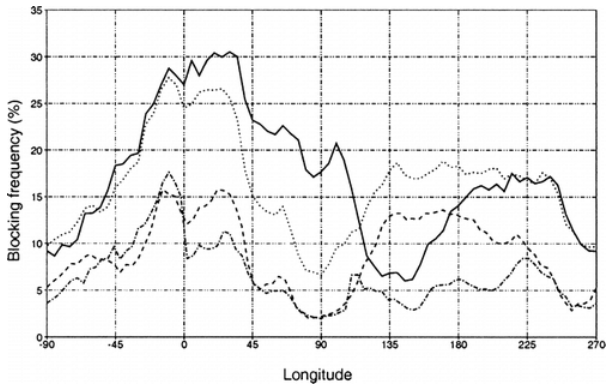

Figure 3.2: Comparison of the annual mean, instantaneous (in space and time) blocking frequency as a function of longitude between June 1996 and May 2001, calculated using the Pelly and Hoskins (2003)'s index (solid curve), the Tibaldi and Molteni (1990)'s index (dashed curve), the Pelly and Hoskins (2003)'s index with a constant blocking latitude (ϕ_0 = 50°N) (dotted curve), the Tibaldi and Molteni (1990)'s index with a variable blocking latitude (dot-dashed curve). Figure taken from Pelly and Hoskins (2003).

3.1.2 Departure field-based index

Temporal anomaly-based approach

Another blocking detection approach, which is also widely used in the literature, and which has also suffered a number of modifications through the years, identifies 2-dimensional blocking patterns as departures from the long-term climatological mean in the geopotential height field. Dole and Gordon (1983) first adopted this approach "objectively" by defining a blocking event as persistent positive 500 hPa geopotential height anomalies (departures from the mean wintertime seasonal cycle) exceeding a threshold value (150 m turned out to be a reasonable value). Other studies have chosen different anomaly thresholds, ranging from 100 m (Carrera *et al.*, 2004) to 300 m (Sausen *et al.*, 1995).

Unlike the Tibaldi and Molteni (1990)'s methodology, Dole and Gordon (1983)'s blocking index provides a straightforward way of blocking identification in a 2-D frame, with in addition the subjective criteria being reduced to a minimum (i.e., anomaly and minimum persistence thresholds). However, this type of index requires a long enough time series to derive a robust climatological mean field, used to compute the anomalies. The main limitation of Dole and Gordon (1983)'s approach however, which was reported by Liu (1994), concerns the latitudinal position of the height anomalies. Liu (1994)'s study, which compared the anomaly-based blocking index with Rex (1950a)'s subjective approach, revealed that a positive height anomaly does not necessarily imply a blocking high; it could instead represent a latitudinal shifts of the jet streams associated with a displacement of the subtropical and subpolar anticyclones, or an amplification of the latters, or anomalously weak troughs. A need to find an adequate position to search for positive anomalies is therefore stressed in this study; increasing the anomaly threshold, as in Sausen *et al.* (1995), could maybe partially alleviate these shortcomings, although with a too high threshold immature blocks could be missed.

The anomaly-based approach has also been developed using a dynamical potential vorticity variable (Schwierz *et al.*, 2004) to identify atmospheric blocking, whereby a block is identified as a persistent and quasi-isolated area of low PV ($<$ 1 PVU) or negative PV anomaly ($<$ -1.2 PVU), averaged from 500 hPa to 150 hPa. This method assumes that the block is in a barotropic atmosphere (i.e., no horizontal temperature gradient on isobaric surface, no fronts), which is a reasonable assumption.

Eddy field-based approach

Blocking patterns identified from eddy fields are regions bounded by southerly (northerly) winds upstream (downstream) (Kaas and Branstator, 1993; Cash and Lee, 2000), or geopotential height deviations from a regional zonal mean (Mullen, 1986; Hartmann and Ghan, 1980). The latter approach was criticized by Kaas and Branstator (1993), as they found that some identified blocks were in fact large-scale open ridges not blocking westerlies. The other drawbacks of Mullen's index are its limited 1-D representation of blocking episodes and the pre-definition of a large number of parameters (i.e., the latitudinal band where blocking are detected, blocking sectors used to compute the regional mean, the regional anomaly threshold and the minimum time persistence).

The meridional wind definition of Kaas and Branstator (1993) and Cash and Lee (2000) is less susceptible to the drawbacks of Mullen's approach, as (1) it does not require the pre-definition of blocking sectors or of a reference set of latitudes and (2) it provides an improved 2-D representation of the blocks. The number of blocks counted is however dependent on the choice of the meridional wind speed limits, the zonal extension of the bounded region and the minimum time persistence. Although not defining a reference latitudinal band reduces the degree of subjectivity of the method and the occurrence of missed blocks, it does not however alleviate the identification of patterns not considered as blocking (e.g., subtropical or subpolar anticyclones) as in the Dole and Gordon (1983)'s approach.

3.1.3 Blocking as weather patterns

The last type of blocking detection methodologies considers blocking as atmospheric circulation patterns derived from either weather regime classification (Vautard, 1990; Michelangeli *et al.*, 1995) or neural networks (Verdecchia *et al.*, 1996).

The Verdecchia *et al.* (1996)'s neural network approach for blocking detection consists in a set of interconnected neurons that receive daily input values of the 500 hPa geopotential height field and calculate output values using a set of characteristic coefficients. The output values of the whole network are then compared to a desired time sequence of "blocking-flags" whose values are 1 or 0 depending on whether or not a day is blocked. Such time sequence was derived by the Tibaldi and Molteni (1990) blocking index. The final output (i.e., blocking occurrence climatology) is obtained after a final step consisting in minimizing the difference between the computed and desired output by adjusting the characteristic coefficients of the network. An examination of the "synoptic" performance of the network output compared to the results derived from the Tibaldi and Molteni (1990) blocking index over the Euro-Atlantic sector revealed equivalent performances, the neural network approach being to some extent better than the Tibaldi and Molteni (1990) index. The former is able to identify blocking patterns which Tibaldi and Molteni (1990) index misses, while some patterns identified with Tibaldi and Molteni (1990) index and not by the neural network does not resemble typical blocking patterns, but rather reflect the signature of a quasi-stationary ridge over Greenland. Although this approach seems interesting in terms of its ability to identify blocking patterns with respect to the widely used Tibaldi and Molteni (1990) blocking index, it is a complex algorithm, involving a number of neurons that depends on the input sample size; as the data sample increases the algorithm complexity increases and its computational performances reduce.

The concept of weather regimes is the result of the observation that large-scale quasi-stationary persistent synoptic patterns occur in a recurrent way at one specific location, as for atmospheric blocking

(Michelangeli *et al.*, 1995). There is no universal definition for a weather regime; from one technique to another the resulting patterns differ significantly. Nevertheless, all the approaches adopted so far are based on one of the three properties that are *recurrence*, *persistence* and *quasi-stationarity* (Michelangeli *et al.*, 1995). In addition, the majority has one feature in common: the analysis is carried out on time series of a single variable (often geopotential height or streamfunction) expressed in a reduced dimensional representation of principal components (Straus, 2010). The concept of weather regimes is useful for theoretical and dynamical studies of a specific atmospheric pattern, such as blocking (e.g., for studying its onset and decay and the transition between zonal and blocked regimes, see Section 2.1.2). However, the classification of instantaneous weather maps into a finite number of atmospheric states is not straightforward and requires a certain number of assumptions, for instance in the specification of the number of clusters, or the number of principal components for the definition of the atmospheric states in a phase space (Michelangeli *et al.*, 1995).

3.1.4 Aim

This review clearly shows that there is no universally accepted methodology to detect atmospheric blocking. This large variety of blocking indices presumably arises from the fact that there is no universally accepted blocking definition neither. Although several blocking features are widely recognized now (i.e., blockage of the westerlies and storm tracks, large-scale, quasi-stationary and persistent features of a blocking episode, geographical location, annual and interannual variability), different blocking indices focus on different blocking characteristics, and this has led several authors to develop different techniques, often requiring a certain amount of subjectivity in the choice of criteria. Recent studies have emphasized that the choice of the reference latitude, used to define the location to search for blocking, is a crucial parameter in the blocking detection method (Liu, 1994; Pelly and Hoskins, 2003; Barriopedro et al, 2010), and constitute one major limitation in the applicability of blocking indices. Reference latitudes too far north or south of the jet streams may lead to "spurious" blocking detections, such as the blocking maximum in eastern Pacific, subtropical or subpolar anticyclones not blocking the westerlies, or even the detection of pressure minima.

In this present study, the blocking detection index combines the traditional approaches employed by Tibaldi and Molteni (1990) and Dole and Gordon (1983). This methodology is described and its performance in identifying "true" blocking patterns is assessed in order to show the importance of using a well located reference latitude.

3.2 Description of the ERA-40 dataset

The ERA-40 reanalysis dataset, provided by the European Centre for Medium-Range Weather Forecasts (ECMWF), is used in this study for the assessment of the blocking detection method and the verification of climate model simulations (in Chapter 4).

The reanalysis system, described by Uppala *et al.* (2005), used an updated version of the 3-dimensional variational (3D-Var) data assimilation system, which was operational between January 1996 and November 1997 at ECMWF, for the assimilation of surface, upper-air and satellite observation data, using a 6-hourly assimilation cycle. In addition, a forecasting model, based on a modified 23rd atmospheric model

version of the ECMWF's Integrated Forecast System (IFS), which was jointly developed by ECMWF and Meteo-France for operational use between June 2001 and January 2002, was used to produce the analyses every six hours at 00, 06, 12 and 18 UTC. The ERA-40 data was produced at a resolution of T159/L60 extending up to 0.1hPa. The products available on the ECMWF data server, and used in this study, had been interpolated to a 2.5° resolution.

The data analysed are daily fields of 500 hPa geopotential height, averaged from the 6-hourly data outputs spanning 42 years from September 1957 to August 1999. Only the winter months (December, January, February, DJF) are considered in this study.

3.3 Definition of the blocking criteria: BI and BI_{stlat}

The blocking detection methodology combines the traditional approaches employed by Tibaldi and Molteni (1990) and Dole and Gordon (1983), which identifies atmospheric blocking highs when easterlies are identified in the region of the mid-latitude jet streams and storm tracks, on the southward side of a region of anticyclonic circulation. The most commonly used reference latitude to search for easterly flow, is a fixed latitude at 60°N $\pm\Delta$, where Δ is usually taken as one or two grid latitudes (Tibaldi and Molteni, 1990; Tibaldi *et al.*, 1997; D'Andrea *et al.*, 1998). Because of their large-scale and stationary properties, atmospheric blocking are known to block the progression of the transient synoptic-scale cyclones and anticyclones. Therefore, Pelly and Hoskins (2003) suggested using the latitude of the maximum storm track intensity to search for the central latitude of a blocking structure. Scherrer *et al.* (2006) used all grid latitudes between 35°N and 70°N, which include the fixed reference latitudes of the Tibaldi and Molteni (1990) and the storm track latitudes of the Pelly and Hoskins (2003).

In this study, the same blocking index has been assessed with two different sets of latitudes. One index uses the latitude of the storm track (hereafter, BI_{stlat}), calculated for each longitude as the latitude with maximum temporal standard deviation of the 2-8 day band-pass filtered geopotential field at 500 hPa (using a finite impulse response filter based on Kaiser's window). The storm track latitude is climatology-dependent, so in order to take into account possible model biases (see Figure 4.4a), the latitude of the storm track is calculated for each reanalysis and model dataset used in this study. The other set of latitudes includes all grid latitudes between 45°N and 65°N (hereafter, BI). Note however, that subtropical (polar) anticyclones might be detected with the BI index if they are associated with a northward (southward) displacement of the jet stream sufficiently near or inside the zone of westerlies and transient eddies, such that the storm track can be deflected and the regional climate in the blocking region affected.

The blocking criteria used in this study are then defined as follows (see Fig. 3.3 for a schematic representation):

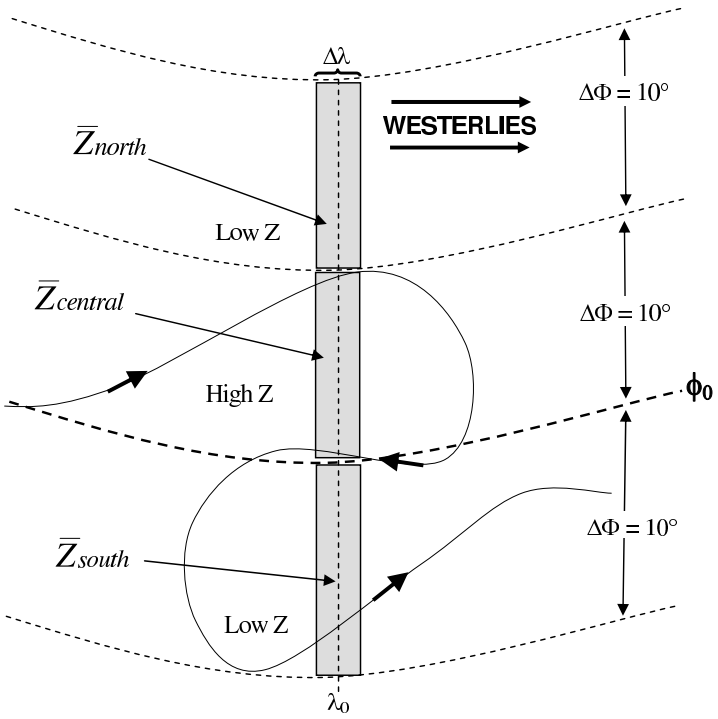

Figure 3.3: Schematic representation of a blocking candidate centered at the reference latitude ϕ_0 and longitude λ_0. Figure adapted from Fig. 2 in Pelly and Hoskins (2003).

$$\frac{1}{\Delta\phi}\left(\overline{Z}_{central} - \overline{Z}_{south}\right) > 0 \tag{3.1}$$

$$\frac{1}{\Delta\phi}\left(\overline{Z}_{north} - \overline{Z}_{central}\right) < -10m/^{\circ}lat \tag{3.2}$$

$$\overline{Z}'_{central} > 0.8 \times \sigma\left(\overline{Z}'_{central}\right) \tag{3.3}$$

Where,

$$\overline{Z}'_{central} = \overline{Z}_{central} - \mu\left(\overline{Z}_{central}\right)$$

$$\overline{Z}_{central} = \frac{1}{5}\sum_{j=\phi_0}^{\phi_0+\Delta\phi} Z(\lambda_0, j)$$

$$\overline{Z}_{south} = \frac{1}{5}\sum_{j=\phi_0-\Delta\phi}^{\phi_0} Z(\lambda_0, j)$$

$$\overline{Z}_{north} = \frac{1}{5}\sum_{j=\phi_0+\Delta\phi}^{\phi_0+2\Delta\phi} Z(\lambda_0, j)$$

The overbar signifies a latitudinal average over 5 grid latitudes, σ and μ symbolize the temporal standard deviation and mean, and the prime is a deviation from this time average. ϕ_0 is the reference

latitude of the blocking structure, taken as the storm track latitude, which is allowed to oscillate up to $\pm 7.5^{\circ}$ (BI_{stlat}), or as all grid latitudes between 45°N and 65°N in turn (BI). $\Delta\phi = 10^{\circ}$; other studies, such as Pelly and Hoskins (2003) and Barriopedro *et al.* (2010), have used 15°, although it was found that the exact value of this parameter is not crucial.

Although in this present study the models have been interpolated to 2.5° before computing the blocking index, the applicability of this methodology should not be restricted to this specific grid resolution. Therefore, a longitude λ is represented by a centered average of three grid longitudes (7.5°), in order to broaden the applicability of the blocking index by reducing the effect of resolution biases on coarser resolution climate models.

The criterion (3.3) requires an anomaly threshold at the location of the blocking high, chosen at $0.8 \times \sigma\left(Z'\right)$ (220 gpm on average for ERA-40). Other studies have adopted subjective values ranging between 100 gpm (Carrera *et al.*, 2004) to 300 gpm (Sausen *et al.*, 1995). However in this study, we choose to objectively derive this criterion from the specific analysed or simulated mean climate state, so as to take possible model biases into account (see Figure 4.4b). Following the same line of thoughts, Barriopedro *et al.* (2010) used an anomaly threshold computed as the one standard deviation level of the daily anomaly distribution. There is no crucial value for this parameter, the higher it is, the more mature and less frequent the blocks are, so to ensure statistically meaningful results a relatively low anomaly threshold should be used. However, a subjective sensitivity analysis performed using the full and anomaly geopotential height fields averaged for the life-cycle of large-scale blocking episodes (see Section 3.4 for more details), suggests that if the anomaly threshold is too low a large proportion of patterns identified by the blocking index are only small amplifications of the planetary ridges, which do not seem to deflect the basic current as a more intense block would do. Therefore, $0.8 \times \sigma\left(Z'\right)$ was found to be the more adequate value for this parameter.

The blocking index (Eq. 3.1 to 3.3) is computed at a given longitude, specific time and for any latitude ϕ_0, and an instantaneous (in space and time) blocking candidate is assigned to the reference latitude ϕ_0 where the zonal wind reversal (Eq. 3.1) is the greatest.

A *large-scale* blocking event is then defined when the index identifies instantaneous blocking at each grid longitude over at least 15°, within predefined blocking sectors, namely the Euro-Atlantic (EA, 90°W-90°E) and the Pacific (PAC, 90°E-270°E) sectors. To avoid edge problems in the attribution of a large-scale blocking event to a given sector, the central longitude of a large-scale blocking, defined here as the maximum height anomaly grid longitude (λ), is required to lie within that sector.

Finally, the definition of a large-scale blocking *episode* requires that a large-scale blocking candidate, having its center within a specified sector, persists for at least 5 days. However, one non-blocked day in a period of at least 4 blocked days is considered as blocked, and the entire period is then defined as a blocking episode.

Figure 3.4 shows the blocking frequency of all winter days belonging to large-scale blocking episodes for ERA-40, obtained with the index that uses only the storm track latitude (BI_{stlat}, grey curve), compared with the index that scans across all grid latitudes between 45°N and 65°N (BI, black curve). Both indices represent the two main blocking sectors in the Euro-Atlantic and Pacific sectors, with more frequent Atlantic than Pacific cases, which is in agreement with observational-based climatologies (e.g.

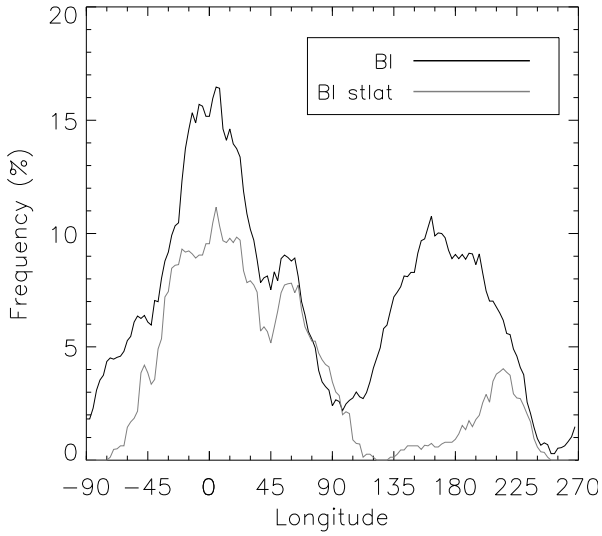

Figure 3.4: Frequency of all winter days that are part of large-scale blocking episodes as a function of longitude for the BI (black curve) and BI_{stlat} (grey curve) indices. Results for ERA-40 only are shown.

Rex, 1950b). However, the latter also emphasize that the Pacific blocking maximum is located over eastern regions between 210°E and 225°E, which is in line with the results obtained using the BI_{stlat} but not the BI index.

3.4 Assessment of the performance of the BI and BI_{stlat} blocking indices

The performance of each blocking index is now evaluated by a subjective assessment of the full and anomaly geopotential height fields averaged for the life-cycle of large-scale blocking episodes in three different sectors (Europe - EUR, 15°W-30°E, western Pacific - WPAC, 135°E-180°E and eastern Pacific - EPAC, 180°E-240°E), following a set of criteria based on well-known blocking features, as described in earlier synoptic-based blocking studies (Please, refer to Appendix A for all the Figures).

The following features must be identified to validate a blocking episode: (i) large-scale split of the westerly flow, leading to the deflection of the mid-latitude jet streams and/or storm tracks; (ii) large positive geopotential height anomaly on the northern branch. Other non-blocking structures, which satisfy the criteria of the blocking index above, are also identified and classified as *low-pressure*, when (i) and (ii) are characterised by large-scale southward deformation of the flow and negative geopotential height anomaly on the southern branch of the split current. Some structures, which do not satisfy the blocking or low-pressure patterns, are classified as *undefined* structures. They can be large extensions from blocking downstream or upstream of the regions considered, or small wave amplification of the climatological ridges. Some patterns can also show a mixture of both low-pressure and blocking high structures in the same geographical sector, and both can be identified by the indices, so whether the entire episode captured by the index is a blocking high, a low-pressure or a mixture of both is not clearly defined. Therefore, those patterns are also classified as undefined structures. The total number of events detected automatically using the blocking index described above, the number of blocking, low-pressure and undefined structures, identified in the composite analysis, are summarized in Table 3.1. It must be emphasized however, that this type of analysis is subjective to the author's eye, and that different conclusions might be drawn according to the reader's opinion.

The results of the composite analysis show that the number of blocking patterns detected using all grid latitudes is considerably higher than if the latitude of storm track alone is used. Although the number of misdetections is lower with the BI_{stlat} than with the BI index, it does miss out a large number of situations which would be considered to be blocked in the Euro-Atlantic and eastern Pacific regions but that an alternative index, based on the Tibaldi and Molteni (1990) approach such as the BI index, could not be devised that captured these events without also capturing a large number of non-blocked episodes (such as cut-off lows) in the western Pacific sector. As part of this region, the area north of Japan has a relative maximum activity of cut-off low systems, which can be seen in the average geopotential height field (Fig. B.1). So, if the reference latitude is located too far north (i.e., above 55°N - 60°N), those events will be counted in the blocking catalogue. On the other hand, the latitude of the storm track in this region is at about 45°N, so only events which centres have their latitude between 37.5°N and 52.5°N will be counted. This latitudinal band may miss a large number of blocking patterns, but it also excludes the majority of low pressure systems occurring in this area. Therefore, for consistency across all longitudes, the index with the storm-track reference latitude is being used in this study.

Table 3.1: Classification of the total count of patterns (bold numbers) identified in ERA-40 from the composite analysis in Figures A.1 to A.6, initially detected using the BI and BI_{stlat} indices. For reference, the labelling number of the composite maps are displayed in brackets (italic numbers) for the *low-pressure* and *undefined* categories (where the total count of events is the lowest); by deduction all the remaining composite maps are blocking structures).

BI	EUR (Fig. A.1)	WPAC (Fig. A.2)	EPAC (Fig. A.3)
Total events	**80**	**51**	**67**
Blocking	**75**	**25**	**61**
low-pressure	**1** *(5)*	**7** *(3, 10, 14, 16, 19, 20, 41)*	**0**
Undefined	**4** *(4, 19, 22, 78)*	**19** *(6, 7, 8, 11, 17, 23, 25, 26, 29, 32, 33, 36, 37, 39, 40, 45, 47, 50, 51)*	**6** *(23, 35, 36, 39, 55, 57)*
BI_{stlat}	(Fig. A.4)	(Fig. A.5)	(Fig. A.6)
Total events	**51**	**7**	**43**
Blocking	**47**	**2**	**41**
low-pressure	**3** *(3, 8, 47)*	**0**	**0**
Undefined	**1** *(29)*	**5** *(1, 2, 3, 4, 7)*	**2** *(17, 42)*

3.5 Concluding remarks

A blocking detection method, combining two traditional approaches employed by Tibaldi and Molteni (1990) and Dole and Gordon (1983), is described. Although not being a novel technique, as it shares some similarities with previous blocking indicators (Barriopedro *et al.*, 2006, 2010), this index accounts for essential well-accepted blocking features, as it ensures a reversal of the westerly flow on the southward side of an anticyclonic anomaly with a blockage of the westerlies and storm tracks. The blocking index is climatology-dependent but independent of the grid resolution, in order to take into account possible model biases and different grid resolutions, and therefore allows its applicability to different observation, reanalysis or model datasets. Regarding its performance in blocking detection, the derived blocking climatology shows a good agreement with observational-based climatology; the main blocking

sectors being in the Euro-Atlantic and eastern Pacific regions, with more frequent Atlantic blocks.

Finally, a subjective but comprehensive assessment of the blocking indicator regarding the dependence between the reference latitude used to search for blocking and its performance in identifying "true" blocking patterns, is performed. Following a set of criteria based on well-accepted blocking features, the results reveal that the identification of some blocks missed by the BI_{stlat} index is made at the expense of including too many patterns, captured with the BI index, that are not considered to be blocked.

It is concluded that the choice of the reference latitude used to search for blocking is a critical parameter regarding the detection performance of blocking indicators, and that a longitudinal-dependent reference blocking latitude, taken as the latitude of the maximum storm track intensity, provides a fairly good blocking climatology when compared with other types of indicators.

CHAPTER 4

Atmosphere-ocean general circulation model simulations of atmospheric blocking. Part 2: model assessment

4.1 Introduction

Several theories explaining different aspects of blocking including the mechanisms responsible for its onset, persistence and decay have been developed (refer to Chapter 2 for a review on blocking theories). This large number of theories indicates that mid-latitude blocking anticyclones are complex phenomena involving the interaction of several components of the atmospheric circulation at different scales and in different regions of the world. As a result, the model simulation of blocking is a difficult and challenging task for both operational forecast and climate studies.

Blocking highs have mostly been investigated in forecast models, as for example in Tibaldi and Molteni (1990) Anderson (1993), Ferranti *et al.* (1994b), Jung (2005) and Brankovic and Molteni (1997), and Atmosphere-only General Circulation Models (AGCMs) in Tibaldi *et al.* (1997), D'Andrea *et al.* (1998), Doblas-Reyes *et al.* (1998), Doblas-Reyes *et al.* (2002) and Matsueda *et al.* (2009). It is only recently that studies have started to deal with blocking in coupled climate models. Ringer *et al.* (2006) compared blocking frequency in the Northern Hemisphere in the atmosphere-only HadGAM1 and the coupled HadGEM1 climate models, and found that HadGAM1 has a tendency to produce more blocking events than HadGEM1, so consistent with the work done by Hinton *et al.* (2009) in the case of Pacific blocking, which suggests that the atmosphere-only model performs better than the equivalent coupled model. In their assessment of the AOGCM MPEH5/MPI-OM, Sillmann and Croci-Maspoli (2009) found that the frequency distribution and the location of atmospheric blocking occurring in the Euro-Atlantic sector were relatively well simulated.

4.1.1 Model simulations of atmospheric blocking: a review

As context for this work, the main conclusions drawn from relevant model studies will now be reviewed, emphasizing D'Andrea *et al.* (1998)'s intercomparison project in particular. A feature common to all AGCMs was to underestimate the frequency of large-scale blocking events. This model deficiency was also observed by Tibaldi and Molteni (1990) in the ECMWF operational medium-range forecast model, by Tibaldi *et al.* (1997) in their assessment of the ECHAM3 model at different horizontal resolutions, by Brankovic and Molteni (1997) in four different versions of the ECMWF NWP model, and by Doblas-Reyes *et al.* (2002) for the ARPEGE GCM with two different methods of blocking identification.

In D'Andrea *et al.* (1998)'s study, a few cases of blocking overestimation were found in the western Atlantic region, which was also prone to large decadal variability in the frequency of blocking.

D'Andrea *et al.* (1998) also noted that grid-point models with high resolution tend to perform better than grid-point models with lower resolution, while for spectral models the influence of resolution was less apparent on their performance. On the other hand, Tibaldi *et al.* (1997) found that increasing the horizontal resolution of ECHAM3 was sufficient to enhance the number of blocking events in the European-Atlantic sector, while in the Pacific higher resolution integrations using observed variations in sea surface temperature (SST) as boundary conditions simulated blocking frequency better than when climatological SST was used. As mentioned in D'Andrea *et al.* (1998), this fact suggests that blocking anticyclones in the European-Atlantic and Pacific regions might be the product of different processes. Ferranti *et al.* (1994a) investigated the impact of tropical diabatic heating anomalies on the mid-latitude circulation, and found that blocking occurring in the European-Atlantic and Pacific regions are both enhanced with a positive SST anomaly in the Indonesian region, while a cold anomaly in the tropical Caribbean sector results in an increase of Euro-Atlantic blocking only. The latter is consistent with Hoskins and Sardeshmukh (1987)'s findings in their diagnostic study of the 1986 winter blocking event.

Another feature common to all models in D'Andrea *et al.* (1998)'s work was an underestimation of blocking duration; none of the models were able to produce blocks as long as some that are observed. This feature was also observed by Tibaldi *et al.* (1997), especially for the lower resolution integration in the European-Atlantic sector.

In terms of blocking signatures (difference between the average field of blocked days and that of non-blocked days), which is a useful tool to evaluate the intensity, shape and location of blocking, some models tended to simulate blocking in the European-Atlantic sector with an apparent eastward shift, while in the Pacific, models showed more varied behaviour. The intensity of the simulated blocking varied across the models, however a few models simulated block intensity quite well (D'Andrea *et al.*, 1998). Apart from a slight westward displacement and a weaker low associated to the block, Tibaldi *et al.* (1997) noted that the main problems of the models are their inability to simulate localized signatures, and their tendency to overestimate the longitudinal extension of Pacific blocking.

4.1.2 Aim

The poor representation of atmospheric blocking in climate models is a long-standing problem, and despite considerable effort in model development, there is only a moderate improvement in blocking simulation. A comprehensive assessment of six coupled AOGCMs from the last generation of climate models is undertaken in order to evaluate their ability in simulating winter-time atmospheric blocking highs in the Northern Hemisphere. The use of an ensemble of climate models is useful to estimate the uncertainty due to model formulation, and in order to understand errors in blocking statistics due to model formulation, this study also assesses the systematic errors in the mean and variability that affect the applicability of this specific blocking index.

However, several other sources of uncertainty could also impact on the ability of the models to reproduce blocking, and in order to attest that model errors in blocking simulation are real, all the possible sources of uncertainty have to be explored. The following points are addressed in this study:

1. The robustness of the results from the reanalysis

2. The dependency between model errors and the blocking detection method

3. Internal model variability and changes in the external forcing

4.2 Datasets and models

Model acronym	Institution	Horizontal & vertical resolution Atmosphere & Ocean
CNRM-CM3 (CNCM3)	Centre National de Recherches Meteorologiques (CNRM), France	T42 (2.8° x 2.8°) L45 & 2° x 0.5°-2° L31
BCCR-BCM2 (BCM2)	Bjerknes Centre for Climate Research (BCCR), Norway	T42 (2.8° x 2.8°) L31 & 1.5° x 0.5°-1.5° L35
ECHAM5/MPI-OM (MPEH5)	Max Plank Institute for Meteorology (MPIM), Germany	T63 (1.9° x 1.9°) L31 & 1.5° x 1.5° L40
MA/ECHAM4 (EGMAM)	Institute for Meteorology, Freie Universitaet Berlin (FUB), Germany	T30 (3.8° x 3.8°) L39 & T42
IPSL-CM4 (IPCM4)	Institute Pierre Simon Laplace (IPSL), France	3.8° x 2.5° L19 & 2° x 2.5° L31
HadGEM1 (HADGEM)	Hadley Centre for Climate Prediction and Research/Met Office, United Kingdom	1.9° x 1.3° L38 & 1° x 0.3°-1° L40

Table 4.1: Summary of AOGCMs used.

The data analysed are daily fields of 500 hPa geopotential height, averaged from the 6-hourly data outputs spanning 42 years from September 1957 to August 1999, winter months (December, January, February, DJF) only are being considered in this analysis.

Data from the models was provided by the CERA database, run by the Model and Data group at the Max-Planck Institute for Meteorology, Hamburg, Germany. The models involved in this study are part of the ENSEMBLES (Ensembles-Based Predictions of Climate Changes and Their Impacts) European project, and contributed to the Intergovernmental Panel on Climate Change fourth assessment report (IPCC AR4). The ENSEMBLES project includes eight models; only the six models listed in Table 4.1 have been chosen because of data availability. The models are coupled Atmosphere-Ocean General Circulation Models (AOGCMs). The first run of the 20^{th} century (20C3M) simulation is used as a representation of the "present climate". ERA-40 reanalysis dataset was used for the verification of climate model simulations. The NCEP/NCAR reanalysis (Kalnay *et al.*, 1996) was also used to compare blocking climatology as it emerges from both reanalyses. All analyses have been done using model output regridded (using bilinear interpolation) to match the 2.5° resolution of the reanalyses.

The blocking index described in Chapter 3 (BI_{stlat}) is used to detect large-scale blocking episodes as diagnosed from ERA-40 and simulated by the models.

4.3 Statistical significance

A Monte Carlo statistical test is performed in order to verify whether the differences in blocking frequency and duration between ERA-40 and any other reanalysis or model output are or are not significant. A 95% confidence interval (shown by the grey area in the appropriate figures below) is constructed for ERA-40, by randomly removing one year from each of the performed 500 Monte Carlo simulations. Significantly different results from those of ERA-40 should lie beyond the confidence limits.

4.4 Intercomparison of reanalyses

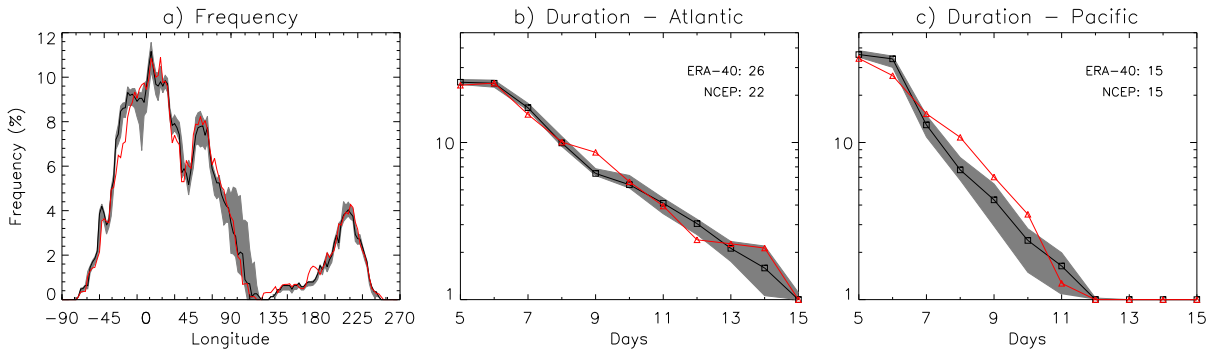

Figure 4.1: (a) Frequency of all winter days that are part of large-scale blocking episodes as a function of longitude, (b) blocking duration defined as the average frequency of winter large-scale blocking episodes (at least 5 days duration) as a function of duration (in days) for the Atlantic sector and (c) for the Pacific sector (right). ERA-40 (black) and the 95% confidence interval (grey area), NCEP/NCAR (red). Note that in panels b and c, the frequency of blocking episodes whose rarity is below 1% is not shown; instead the duration of the event is indicated by a marker at the base of the graph. And for ease of visualisation, the x-axis is cut at 15 days in the EA and PAC sectors; the maximum duration is indicated in each panel.

Blocking frequency and duration have first been analysed for the ERA-40 and NCEP/NCAR reanalyses, and results are presented in Figure 4.1. There are two main regions of blocking development: the Euro-Atlantic (EA, 90°W to 90°E) and the Pacific (PAC, 90°E to 90°W). There is possibly a third region of blocking development at the boundary between western Europe and Asia (at around 60°E, in the Siberian sector). This sector, presenting a sharper topography with the Ural Mountains, has been identified in other studies (Barriopedro et al, 2006; Doblas-Reyes et al, 2002; Pelly and Hoskins, 2003; Tibaldi and Molteni, 1990), but is mostly regarded as an extension of the EA blocking. Similar amplitudes of the blocking frequency are also found in Barriopedro *et al.* (2006).

The two reanalyses show almost identical frequency in both sectors (Fig. 4.1a). However, differences arise in blocking lifetime (Fig. 4.1b and c), especially in the Pacific sector. These differences might be related to an increased uncertainty in the reanalysis due to a smaller number of observations in this region compared to European-Atlantic sector. It could also be due to sampling errors, because of the smaller frequency of blocking events in the Pacific sector. But overall, ERA-40 and NCEP/NCAR reanalyses show similar blocking climatologies.

4.5 The impact of model internal variability on blocking

Uncertainties in blocking climatology due to model internal variability have been examined for CNCM3. Blocking frequency and duration have been computed for an ensemble of 3 runs (including anthropogenic forcing only), and are shown in Figure 4.2. For the blocking frequency diagnostic, all the three runs are very similar and the differences between them are very small compared to the difference with ERA-40. However, internal variability appears to affect more blocking duration, especially in the Pacific sector (Fig. 4.2c), which is consistent with a smaller number of cases in this region. The three sets of CNCM3 results span the ERA-40 frequencies for most durations (i.e., there is no systematic under or overestimation), even for the longest durations with one run producing longer blocking episodes than the longest diagnosed from ERA-40. However, in the Atlantic, the results are more uniform, and although the variability among simulations is also large, all runs produce more frequent short-lasting blocking events, and less frequent long-lasting episodes than ERA-40. In addition none of them are able to produce the longest blocks seen in the reanalysis. Therefore, overall the results show that uncertainties due to internal variability do not account significantly for the underestimation of blocking frequency and duration in the Atlantic sector, but that results should be considered with caution in the Pacific, at least for CNCM3. It must be emphasized, however, that the smaller the number of simulated blocking cases is, the larger the differences between the runs are, due to larger sampling errors. CNCM3 is the most affected by sampling errors as it is the model that underestimates the most blocking frequency in both the EA and PAC sectors (see Table 4.4 and Fig. 4.5).

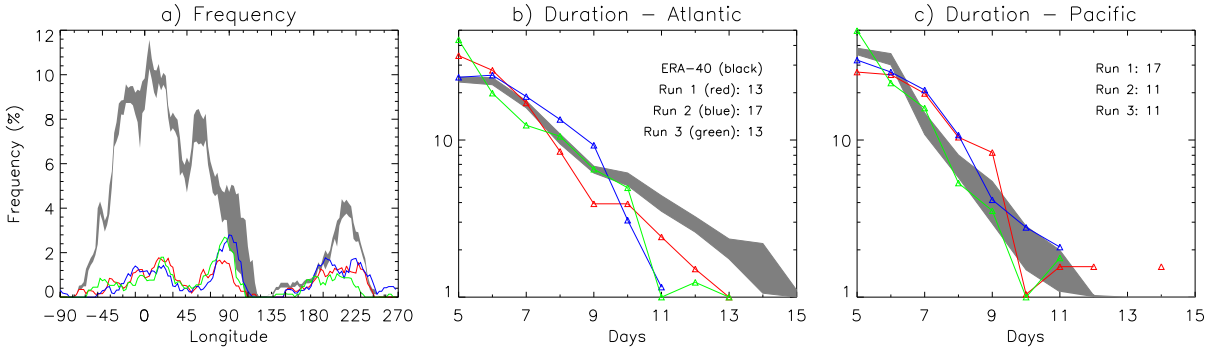

Figure 4.2: Same as figure 4.1 but for the 3 CNCM3 runs.

4.6 The impact of the sampling period on blocking

The estimation of blocking frequency over short time integrations can be significantly different according to the period considered because of long-term variability, driven by changing external forcing (Tibaldi *et al.*, 1997; D'Andrea *et al.*, 1998). Therefore, by using different periods of 42 years, the blocking responses to long-term variability have also been tested for HADGEM (Figure 4.3). The differences between the runs are relatively small in amplitude, suggesting that blocking frequency evaluated on such a time sample is not significantly sensitive to the long time-scale variability in the EA and PAC sectors. Note however that a different climatological mean-state resulting from transient climates might affect the latitude of the storm tracks, potentially causing changes in blocking distributions. For the duration diagnostic, the variability among simulations is more apparent in the Pacific than in the Atlantic,

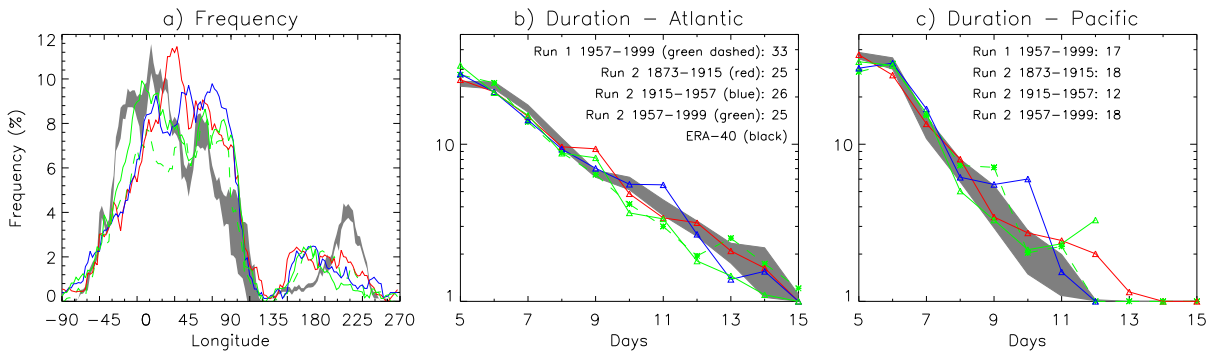

Figure 4.3: Same as figure 4.2 but for HADGEM runs. - HADGEM run 2 for 3 periods of 42 years from 1873 to 1999 - also shown for comparison, HADGEM run 1 from 1957 to 1999. Anthropogenic forcing only are included in those simulations.

similarly to CNCM3 (see the previous section). This variability increases as well with the duration of blocking episodes. There is no systematic under or overestimation of frequencies for most spells and for the maximum persistence of blocking episodes in the Pacific sector. In the Atlantic, all runs produce more frequent short-lasting blocking events (5 to 6-day duration) than ERA-40, and maximum duration is realistic for all three simulations of HADGEM run 2.

Overall, internal climate variability, either alone (evaluated by comparing different ensemble members, including or not natural forcing) or combined with externally-forced changes (different periods during 19^{th} and 20^{th} centuries), seems to have a relatively minor impact on blocking frequency compared with the magnitude of some of the apparent AOGCM errors (e.g. Figure 4.2). However, the large variability among simulations for the blocking duration, of similar or higher magnitudes than the errors in blocking duration in itself, arise when the number of simulated blocking cases is low (i.e. in the Pacific) and when considering the longest blocking episodes. This problem is likely to be due to sampling errors. D'Andrea *et al.* (1998) computed a least-squares fit of the frequency distribution of blocking duration for events lasting less than 20 days, in order to minimize this sampling problem. Having said that, the impact of internal variability and long-time variability is different according to the persistence of events and/or diagnostics considered. Consequently, it might not be possible to explain why blocking episodes seem to last longer or not in some models, and it would probably be more appropriate to focus on the frequency of shorter blocking persistence ranges (from 11 to 17 days, depending on the model; see Tables 4.2 and 4.3).

4.7 Model validation

4.7.1 Climatology-dependent blocking criteria

As described in Chapter 3, the criteria needed to detect blocking, namely the reference latitude and the anomaly threshold, are climatology-dependent (i.e., they are independently derived from the analysed and simulated climatologies). Being specific to each dataset, these parameters account for possible model biases, which can be examined in Figure 4.4. The reference latitudes (in Figure 4.4a) reveal similar analysed and simulated spatial variability, with higher latitudes in the Euro-Atlantic and east Pacific sectors, whereas in the Asian and western Pacific regions the storm track latitudes tend to be lower.

However, the models have a tendency to simulate the central latitude of blocking too far south in the Euro-Atlantic (up to 20° difference - e.g., MPEH5), while in the Pacific the storm track position suffers a northeastward shift, with errors reaching about 10° northward and 30° eastward over the Pacific (e.g., CNCM3). The maximum model biases being located over those respective blocking regions, it appears therefore essential to derive this parameter from each dataset. Note that the climatological position of the storm track is particularly well simulated by HADGEM.

Figure 4.4b shows the mean profile of geopotential height values being greater than the anomaly threshold, defined as $0.8 \times \sigma\left(Z'\right)$ (in Eq. 3.3) within the anticyclonic area (between ϕ_0 and $\phi_0 + 10°$ in Figure 3.3). Overall, there is a good agreement between the reanalysis and the models concerning the spatial variability, with a maximum over the Pacific, and secondary peak over the Atlantic. However, Pacific height values are sometimes strongly overestimated (e.g., CNCM3, MPEH5, IPCM4 and HADGEM) and the range of anomalies above the adopted threshold reflects a global underestimation over the Euro-Atlantic region (except for HADGEM which tends to perform well in this sector). Those results suggest that a model underestimation (overestimation) of the magnitude of blocking episodes could be expected over the Euro-Atlantic (Pacific) region.

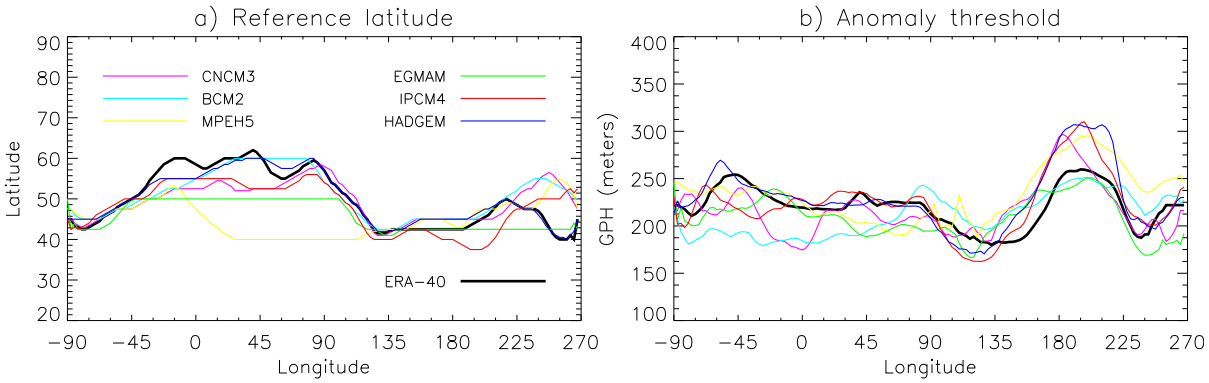

Figure 4.4: Blocking index parameters for ERA-40 (black) and the models (see legend). (a) Winter mean profile of the latitude of the maximum storm track intensity as a function of longitude. (b) Winter mean profile of geopotential height values being greater than the anomaly threshold ($0.8 \times \sigma\left(Z'\right)$, Eq. 3.3) within the anticyclonic area.

Now, we assess the ability of all six AOGCMs to simulate large-scale blocking episodes (i.e. spanning at least 15° longitude and persisting for at least 5 days) occurring in the Northern Hemisphere during the winter (DJF) season. For a general overview of the performance of each model to reproduce the atmospheric mean state and its variability, the 500 hPa mean state, stationary wave and high- and low-frequency variability have been computed from ERA-40 and the model outputs, and can be found within this Chapter (Section 4.8) and in the Appendix B).

4.7.2 Blocking frequency

The frequency of large-scale blocking episodes as diagnosed from ERA-40 and simulated by the models is shown in Figure 4.5. The Monte Carlo significance test (as shown by the grey area in each panel) is complementary to the earlier evaluation of the internal variability influence (compare the ensemble spread in Figure 4.2 with the model error in Figure 4.5d). All the models simulate two main sectors of blocking occurrence in the Euro-Atlantic and Pacific sectors, although the exact longitudinal position of each sector is not always well captured. In BCM2 and HADGEM the maximum in Pacific

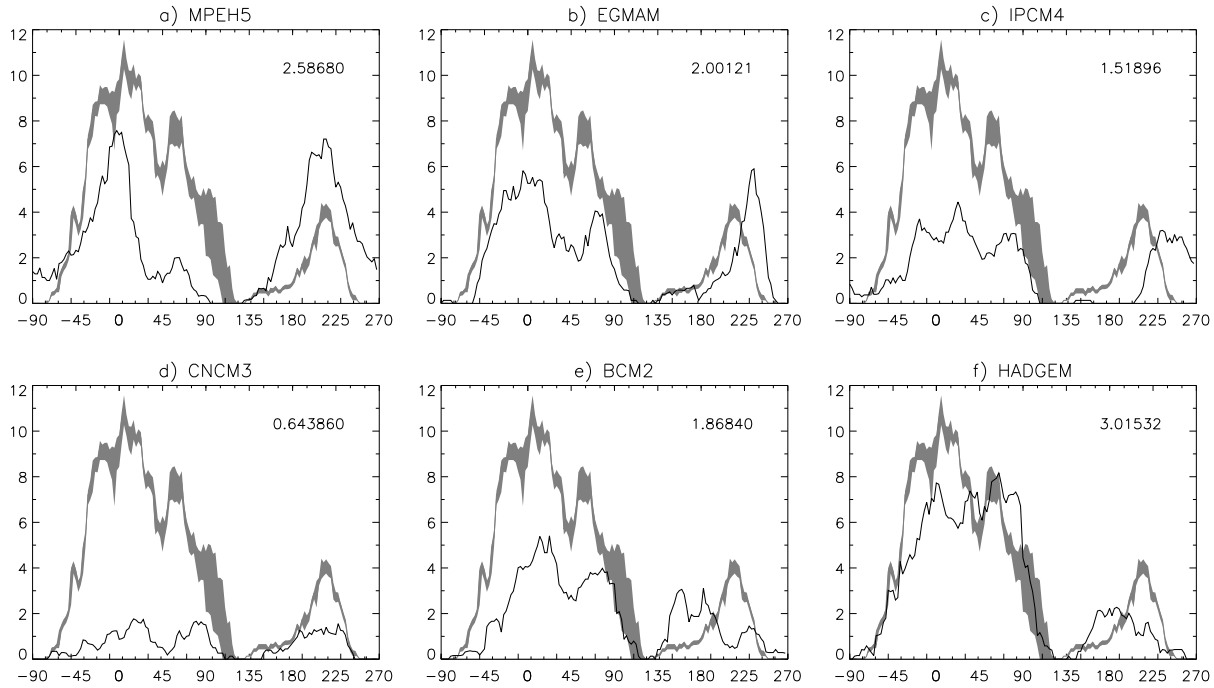

Figure 4.5: Frequency (in %) of winter large-scale blocking episodes (lasting at least 5 days) as a function of longitude. 95% confidence interval for ERA-40 (grey area), AOGCMs (black). The models' blocking frequency averaged over all longitudes is indicated in the upper left corner of each plot; the frequency for ERA-40 is 3.52%.

blocking frequency is shifted westward and centered at around 180°. This model deficiency is consistent with a less pronounced climatological trough between 135°E and 180°, as well as a pronounced ridge between 180° and 225°E, compared to the reanalysis (OR1 Fig. 1 and 5). On the other hand, simulated Pacific blocking is shifted eastward in IPCM4, because of a more pronounced trough and eastward extension of the Pacific jet stream. These features are also observed for EGMAM, although at a lesser extent.

A feature common to all models (except for MPEH5 and EGMAM in the Pacific) is a generalized underestimation of the large-scale blocking frequency, which is a well known problem that has been reported in several studies aiming at assessing climate models (D'Andrea et al, 1998; Doblas-Reyes et al, 1998; Matsueda et al, 2009; Mullen, 1989; Ringer et al, 2006; Sillmann and Croci-Maspoli, 2009; Tibaldi et al, 1997) and forecast models (Anderson, 1993; Brankovic and Molteni, 1997; Ferranti et al, 1994a;b; Jung, 2005; Tibaldi and Molteni, 1990). Here this problem is more prominent for the Atlantic than the Pacific sector, although it was found that Pacific blocking frequency is also clearly underestimated by the models when the BI index is used (at the exception of MPEH5, which performs relatively well when the BI index is used - see Figure 4.12). Such underestimation was suggested to be caused by several factors, such as too strong westerlies in the models, underestimation of transient wave activity, systematic errors in the tropical SST, model resolution and parametrization. In order to better understand model deficiencies, the role of errors in the time-mean atmospheric circulation and its variability on blocking simulations will be assessed in section 4.8.

4.7.3 Blocking duration

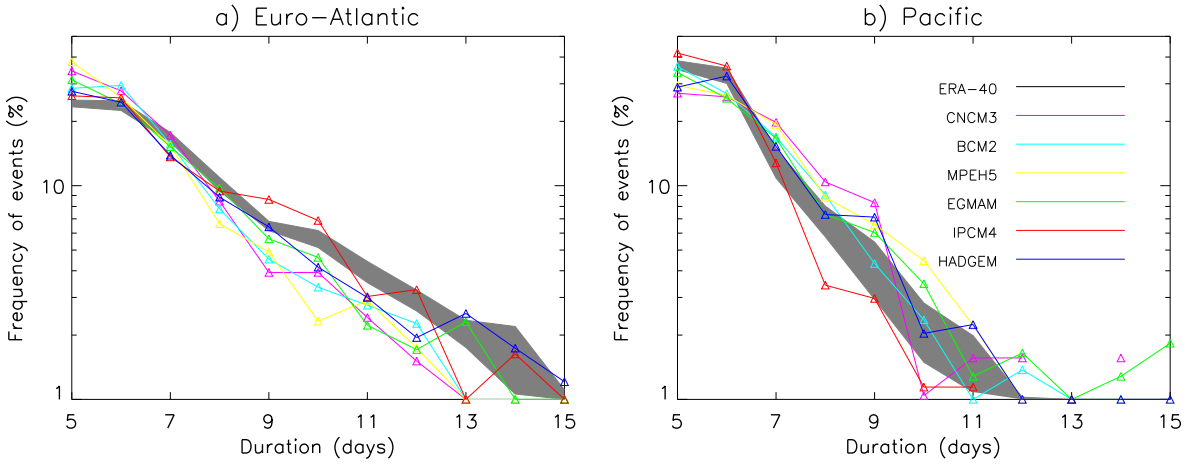

Figure 4.6: Frequency of winter large-scale blocking episodes (lasting at least 5 days) as a function of duration in days, for the Euro-Atlantic (left) and Pacific (right) sectors, for the 95% confidence interval for ERA-40 (grey area) and AOGCMs.

The winter large-scale blocking duration from ERA-40 and simulated by the models are shown in Figures 4.6a) and 4.6b) for EA and PAC sectors respectively, where the linearity of the results on the logarithmic scale used for the frequency axis suggests that the distributions of blocking lifetime follow an exponential decay. This result was verified in D'Andrea *et al.* (1998), and is also assessed for the AOGCMs used in this present study. The expected distribution for the models and ERA-40 is computed over different ranges of persistence from 10 days to the maximum blocking duration for ERA-40 and model simulations. The best exponential fit is then chosen at the range of persistence, such that the mean (μ) and the standard deviation (σ) of an exponential distribution of the form $Y(x) = \lambda e^{-\lambda x}$, truncated at 5 days of minimum duration for the case of blocking lifetime, satisfy the best the relation $\sigma = \mu - 5 = 1/\lambda$ (D'Andrea *et al.*, 1998). This relation can be derived by computing (using integrations by parts) the first and second moments of the exponential distribution $Y(x)$, to show that $E(X) = \mu = 1/\lambda$ and $E(X^2) = \sigma^2 = 1/\lambda^2$. Errors of the exponential fit as a function of the range of persistence are presented in Figure 4.7; the best exponential fit corresponds to the minimum error values.

As shown in Figure 4.8, all the models lie close to the straight line $\sigma = \mu - 5$, at similar ranges of persistence as ERA-40. It therefore indicates a good model representation of the exponential decay of blocking lifetime. The mean (μ) and the ranges of persistence of blocking episodes giving the best exponential fit (the smallest errors) are presented in Tables 4.2 and 4.3.

A common feature to all models that was reported for earlier generations (Tibaldi *et al.*, 1997; D'Andrea *et al.*, 1998) is the inability to reproduce the correct blocking duration for both EA and PAC regions. This problem of shorter simulated blocks seems to be alleviated in this present study, in the PAC sector. All models simulate blocking episodes at least as persistent on average as ERA-40, and are now able to produce longer blocks than in the reanalysis (see Table 4.3; except for IPCM4).

In the Atlantic sector, all models underestimate the average blocking lifetime, as well as the maximum duration for which the exponential distribution fits adequately the simulated distribution. The models tend to overestimate the frequency of very short-lived blocking events, and underestimate the frequency of longer-lasting episodes (Fig. 4.6a). It seems no longer to be the case in the Pacific, at least when the BI_{stlat} index is used, the frequency of short blocking episodes having a tendency to be

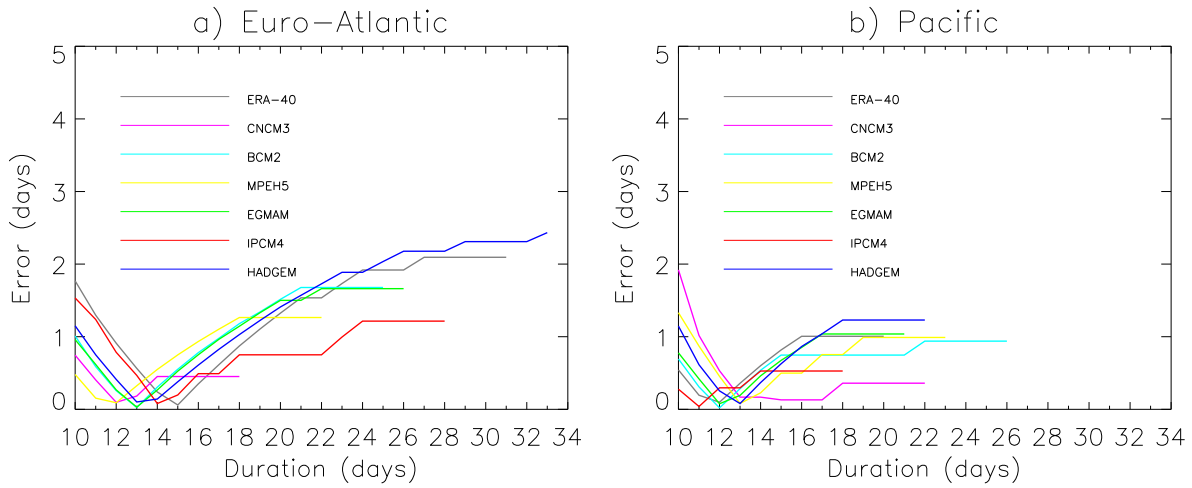

Figure 4.7: Errors (in days) of the exponential fits in the Euro-Atlantic (left) and Pacific (right) sectors for ERA-40 and AOGCMs, where the error is the difference (in absolute value) between the theoretical relation $\mu - \sigma = 5$, and the simulated relation. μ and σ for each simulation, plotted in Fig. 4.8, are taken at the maximum range of persistence where the error is minimum.

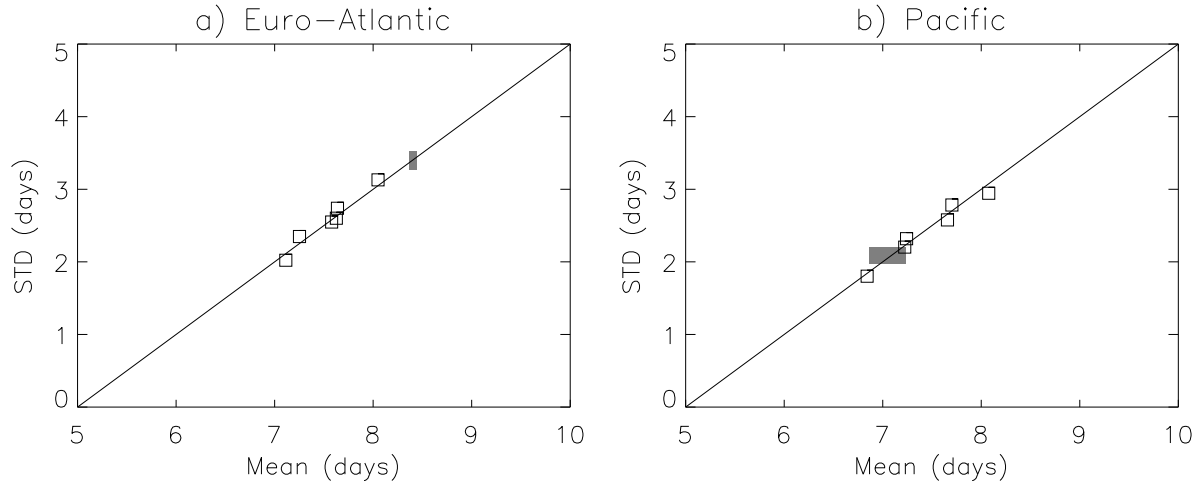

Figure 4.8: Scatter plot of the mean (μ) and standard deviation (σ) of the distributions of blocking lifetime (in days) for the Euro-Atlantic (left) and Pacific (right) sectors for ERA-40 (grey rectangle showing the 95% confidence limits from the Monte Carlo simulation) and AOGCMs (black squares). The straight line corresponds the relation between the mean and the standard deviation $\sigma = \mu - 5$ (see text).

underestimated, while no systematic under or overestimation is apparent for longer blocks. However, when blocking episodes are derived using the BI index, model errors are found to be different in PAC, where the frequency of short- (long-)lasting events have a similar tendency to be overestimated (underestimated) as in the EA sector.

Tibaldi *et al.* (1997) have noted that their lower resolution model reproduces more frequent short-lasting blocks, and less frequent long-lasting blocks than the analysis, which considering the straining mechanism theory by Shutts (1986), would be due to the lack of eddy activity. Their higher resolution model, on the other hand, was less affected by this problem, and could at least reproduce more longer blocks. They also emphasized that this problem was particularly prone to the Euro-Atlantic sector. In this assessment, underestimation of long-lasting blocking events and overestimation of short-lived blocks are also more prominent in the Atlantic than in the Pacific sector, but it is not clear whether this problem strictly relates to lower resolution models or not.

	Euro-Atlantic							
	μ				Max. range of persistence (max. duration)			
Models	Uncorrected	TM	TM+HFV	TM+STD	Uncorrected	TM	TM+HFV	TM+STD
ERA-40	8.4 (8.4,8.5)				5-15 (26)			
CNCM3	7.3	**8.4**$^+$	**8.4**	8.9$^-$	5-12 (13)	5-15 (28)	5-15 (21)	5-16 (32)
BCM2	7.6	7.6	7.6	8.0$^+$	5-13 (20)	5-13 (21)	5-13 (20)	5-14 (24)
MPEH5	7.1	7.6$^+$	7.6	7.7$^+$	5-12 (24)	5-13 (27)	5-13 (24)	5-13 (23)
EGMAM	7.6	8.0$^+$	8.0	8.0	5-13 (21)	5-14 (23)	5-14 (16)	5-14 (22)
IPCM4	8.0	9.2$^-$	9.2	9.1$^+$	5-14 (23)	5-17 (27)	5-17 (25)	5-17 (31)
HADGEM	7.6	8.0$^+$	8.0	**8.4**$^+$	5-13 (33)	5-14 (33)	5-14 (33)	5-15 (27)

Table 4.2: Mean (μ) and maximum range of persistence corresponding to the best exponential fit of the winter large-scale blocking episodes' lifetime in the Euro-Atlantic (ATL) sector. The lower and upper bounds of the 95% confidence interval from the Monte Carlo simulation is also indicated in brackets for ERA-40. Simulated mean values not significantly different from the analysed mean are in bold. The maximum duration of blocking episodes is indicated in brackets for ERA-40 and the models. Directions of the change toward ERA-40 results after corrections (computed with reference to the previous column) of the systematic errors (see in section 4.8) are also indicated. "+" = improvement, "−" = decline in model performance, no mark = no change.

	Pacific							
	μ				Max. range of persistence (max. duration)			
Models	Uncorrected	TM	TM+HFV	TM+STD	Uncorrected	TM	TM+HFV	TM+STD
ERA-40	7.2 (6.9,7.2)				5-12 (15)			
CNCM3	8.1	8.0$^+$	**7.2**$^+$	6.7$^-$	5-15 (17)	5-14 (17)	5-13 (12)	5-11 (13)
BCM2	**7.2**	7.6$^-$	**7.1**$^+$	6.8$^-$	5-12 (21)	5-13 (22)	5-12 (17)	5-11 (17)
MPEH5	7.7	7.6$^+$	7.6	6.8$^-$	5-13 (18)	5-13 (17)	5-13 (16)	5-11 (10)
EGMAM	**7.2**	6.8$^-$	**7.2**$^+$	6.8$^-$	5-12 (16)	5-11 (14)	5-12 (14)	5-11 (16)
IPCM4	6.8	8.0$^-$	6.8$^+$	**7.2**$^+$	5-11 (13)	5-14 (23)	5-11 (13)	5-12 (26)
HADGEM	7.7	8.0$^-$	8.0	8.0	5-13 (17)	5-14 (19)	5-14 (19)	5-14 (19)

Table 4.3: Same as Table 4.2 for the Pacific (PAC) sector.

4.7.4 Blocking signatures

Diagnosis of blocking signatures can provide information about the average shape, intensity and location of blocking events. They are obtained by subtracting the average field of all non-blocked days from the average field of all blocked days lasting at least 5 days. They have been computed for each sector separately and are presented in Figures 4.9 and 4.10 for the Atlantic and Pacific sectors, respectively. In addition, the average 500 hPa geopotential field during blocked days only (represented by the solid contours) can provide information about the average amplitude of the deflection of the basic flow. In the reanalysis, both the EA and PAC blocking show a clear dipole blocking structure in the 500 hPa geopotential heights, with the blocking anticyclone at high latitudes, and the associated blocking low on its equatorward side. The models mostly tend to perform well in reproducing these clear meridional dipole patterns. Tibaldi *et al.* (1997) found that the different versions of the ECHAM3 model were unable to produce localized signatures, and in particular wave propagation and/or larger extension of the blocking high and/or low could be identified.

In the Atlantic, the intensity and location of the signatures are relatively well simulated by the models, although CNCM3, BCM2 tend to underestimate the deflection of the flow during blocking episodes. It will be shown in section 4.8 that this deficiency is mainly related to the strong westerly bias in those models. Larger errors in the intensity and geographical location of the blocks emerge in the Pacific region. BCM2 and HADGEM shift blocking signature upstream (see also Fig. 4.5e, 4.5f). The opposite happens for EGMAM and IPCM4. A similar feature was also present in the frequency diagnostic (Fig. 4.5), and could be attributed to discrepancies in the climatological position and amplitude of the ridge and through in the Pacific region. CNCM3 and HADGEM tend to overestimate the intensity of the Pacific

blocking high, while BCM2 underestimates it. Note that the robustness of those results may depends on the number of blocked days (see Table 4.4). In the case of CNCM3 for example, the over-intensified signature in the Pacific sector might be biased by too few blocked days (159 days). Nevertheless, the amplitude of the geopotential anomaly at the location of the blocking high, when it satisfies Eq. 3.3 only (Fig. 4.4b), is consistent with the intensity of the signatures in Fig. 4.9 and 4.10.

	ERA-40	CNCM3	BCM2	MPEH5	EGMAM	IPCM4	HADGEM
EA	1331	261	676	1116	749	610	1144
PAC	397	159	366	850	285	239	340

Table 4.4: Number of blocked days belonging to blocking episodes for the Euro-Atlantic (EA) and Pacific (PAC) sectors independently.

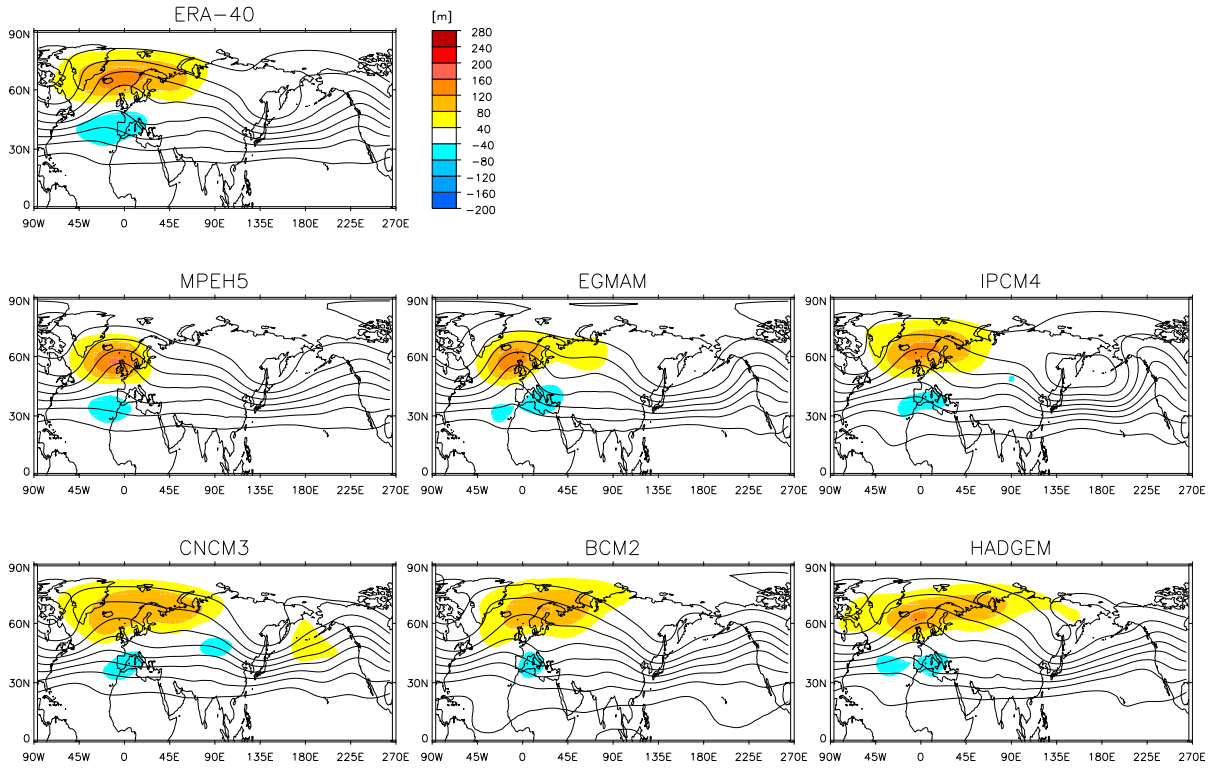

Figure 4.9: Blocking signature in the Atlantic of the 500 hPa geopotential field (color shading). Solid contours represent the average 500 hPa geopotential field during blocked days only. *At least 5-day blocking events*

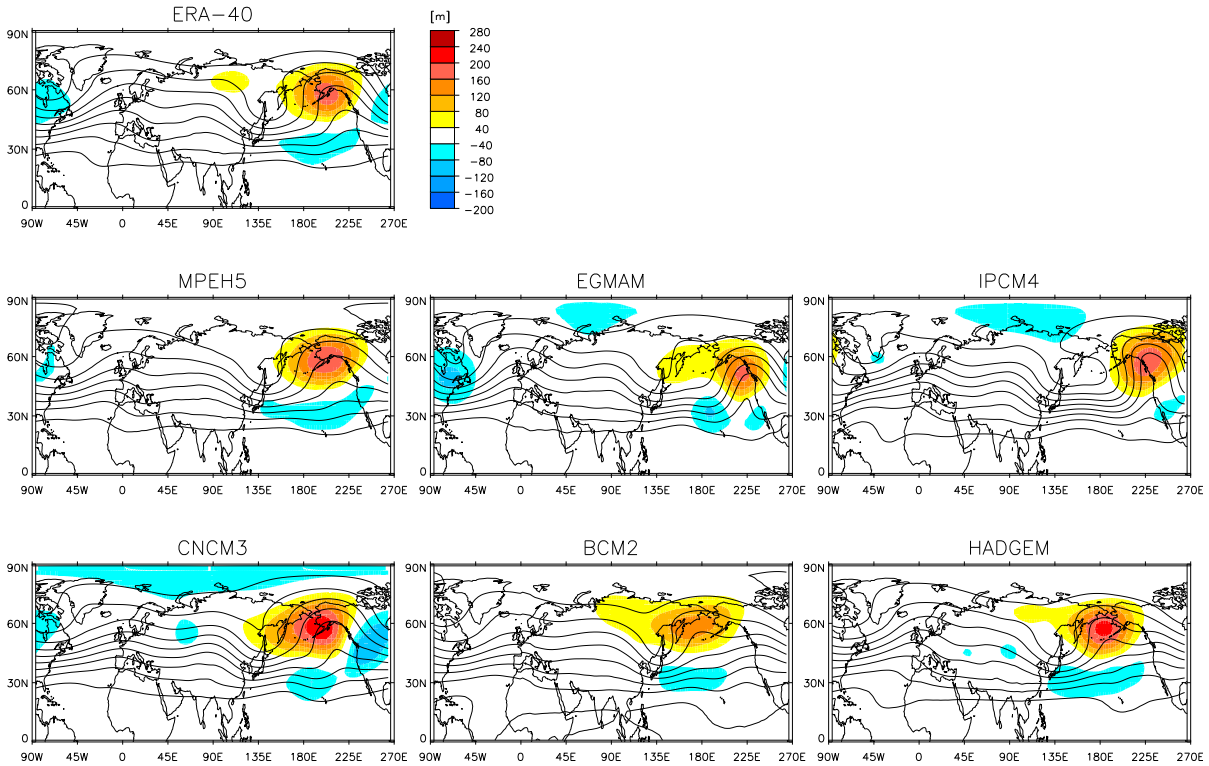

Figure 4.10: Same as figure 4.9 for the Pacific sector

4.7.5 Differences between the BI and BI_{stlat} blocking indices

An interesting feature when comparing the blocking frequency and duration obtained with both the BI_{stlat} and BI indices is an increased agreement of model errors in the EA sector but substantially different results in the PAC region. Whether the BI_{stlat} or BI index is used, the total frequency of EA blocking is underestimated, with a greater (lower) proportion of short- (long-) lasting events. In the PAC sector, the overall tendency of blocks underestimation using BI_{stlat} (Fig. 4.5 and Table 4.4) is enhanced when the BI index is used. In addition, the models are equally likely to overestimate or underestimate the frequency at different spell lengths with BI_{stlat}, while the prominent error emerging when BI is used instead is a shift toward shorter blocks (compare Figures 4.6b and 4.11b). However, model errors in the longitudinal position being identified with BI_{stlat} (i.e., eastward shift for EGMAM and IPCM4, and westward shift for BCM2 and HADGEM, in Figure 4.5) are no longer observed with the BI detection method (Fig. 4.12). Therefore, in the Pacific region, although model errors in blocking frequencies agree among the simulations and being somehow larger with the BI index, the geographical location of blocks is however better represented.

The results of this analysis suggest therefore that attention should be paid to significant errors or similarities in the diagnosis of blocking that can also arise from the choice of the blocking index or of the parameters needed employed by a specific methodology.

Model deficiencies in blocking simulations are not always straightforward to understand. For this purpose, systematic error in both the time-mean and time-variability of the atmospheric circulation are examined, and their relationship with errors in blocking simulations are evaluated in the next section.

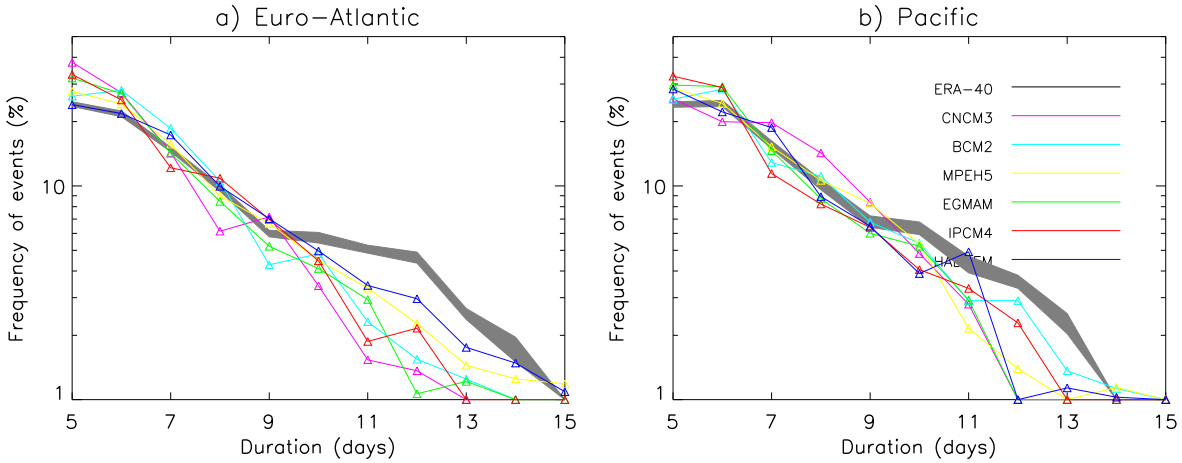

Figure 4.11: Same as Figure 4.6, but for blocking episodes detected using the *BI* index.

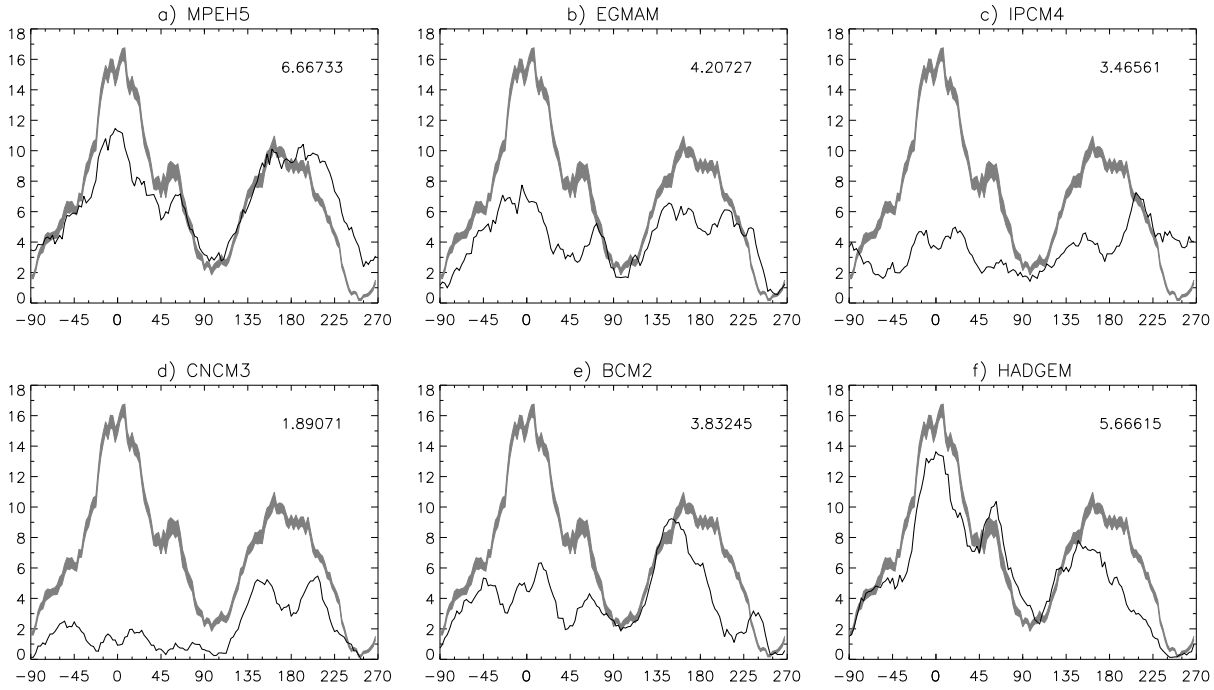

Figure 4.12: Same as Figure 4.5, but for blocking episodes detected using the *BI* index. The blocking frequency averaged over all longitudes for ERA-40 is 7.04%.

4.8 The impact of the time-mean and time-variability systematic errors on blocking

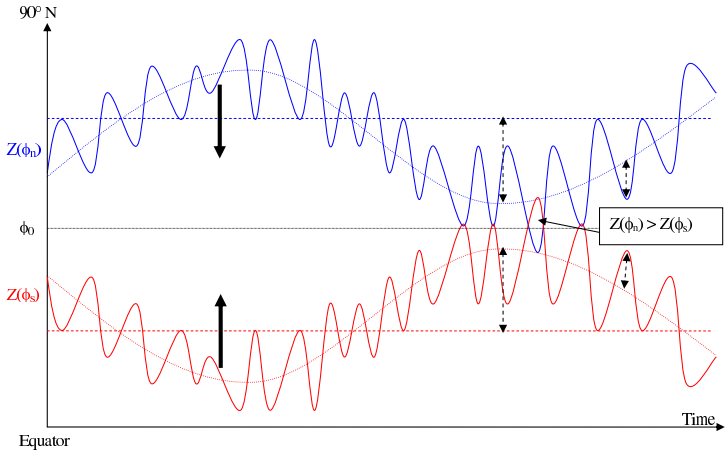

Figure 4.13: A schematic representation of the dependency between errors in the background flow and the GPH gradient reversal (Eq. 3.1) at ϕ_0. The variation of the GPH as a function of time at a latitude 10° south (ϕ_s) and north (ϕ_n) of ϕ_0 are represented in red and blue, respectively. The mean state, the low- and high-frequency variability are represented by the straight dashed, sinusoidal dotted and sinusoidal solid curves, respectively. The thick black arrows represent the time-mean bias correction, and the thin dashed arrows represent an increase or decrease in the amplitude of the low- and high-frequency variability. An occurrence of the GPH gradient reversal is indicated ($Z(\phi_n) > Z(\phi_s)$). A modification of any of the components of the flow affects the applicability of the blocking index.

The impact of the time-mean systematic error on blocking frequency has been analysed previously, as for example in the ARPEGE GCM (Doblas-Reyes *et al.*, 2002), in the ECHAM3 model (Tibaldi *et al.*, 1997), in two Hadley Centre AGCMs (HadAM3 and HadGAM1) (Scaife and Knight, 2008), and in a set of 18 AOGCMs used in the Intergovernmental Panel on Climate Change (IPCC) Fourth Assessment Report (AR4) (Scaife *et al.*, 2010). Those studies revealed that the frequency of blocking episodes increases substantially, although still underestimating the observed frequency, after correction of the time-mean state, which mainly corrected the too strong average zonal flow and the stationary wave pattern in the model climatology. Scaife *et al.* (2010) have also suggested that the time-mean bias, rather than errors in the variability of the model, is the main cause for the lack of simulated blocking episodes.

Doblas-Reyes *et al.* (2002) showed that blocking climatologies, as simulated by climate models, are dependent on the criterion employed to define blocking. For example, the use of the SKS index (identification of positive height anomalies) is preceded by the removal of the mean state and the annual cycle. Therefore, this method is sensitive to the model ability to simulate the variability, but not the mean. In this present study, the blocking index is based on geopotential height gradients, and is sensitive to both the mean and variability of the model. This is illustrated in Figure 4.13 for the geopotential height gradient reversal (Eq. 3.1) at the reference latitude (ϕ_0). The geopotential height gradient at ϕ_0 is reversed (Eq. 3.1) when the curves cross ($Z(\phi_n) > Z(\phi_s)$). Given that too strong westerlies are a common feature in most models, reducing the time-mean bias (thick black arrows) will often increase (decrease) the geopotential height at ϕ_n (ϕ_s), so the gradient will have more occasions to be reversed. Similarly, increasing or decreasing the amplitude of the low- and high-frequency variability (thin dashed arrows) will affect the occurrence of a positive gradient.

In order to assess systematic model errors that affect the applicability of the blocking index, blocking statistics have been re-computed for post-processed model output, in which the climatological mean

state and its variability have been corrected.

4.8.1 Impact of the time-mean model errors

Model errors in the mean state, which affect the stationary wave pattern and the meridional GPH gradient of each model, are removed by subtracting the time-mean systematic error from the daily geopotential field, as follows:

$$x'_M = x_M - (\mu_M - \mu_E) \tag{4.1}$$

where x_M and x'_M are the daily model and daily corrected model geopotential heights respectively, μ_M and μ_E are the time-average of the model and ERA-40 outputs, respectively. For reference, the time-mean systematic error $(\mu_M - \mu_E)$, is shown in Figure 4.14.

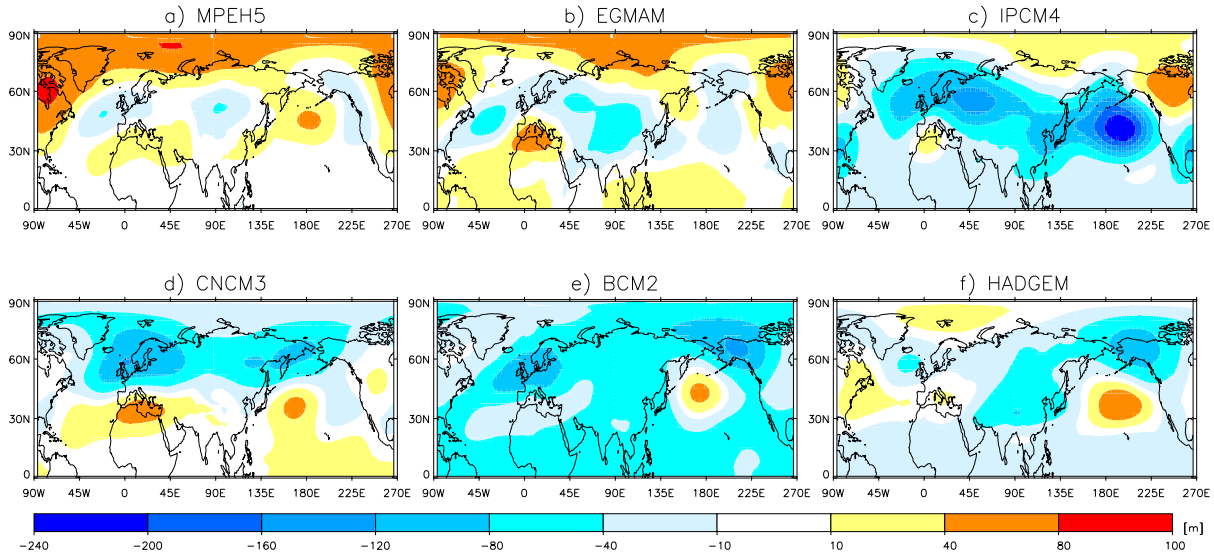

Figure 4.14: Systematic error $(\mu_M - \mu_E)$ of the time-average 500 hPa geopotential field.

Blocking frequency and duration diagnosed after removal of the time-mean bias are shown by the green curves in Figures 4.15 (for blocking frequency), Figures 4.16, 4.17 and in the second column of Tables 4.2 and 4.3 (for blocking duration). In all models blocking distribution is now improved (Fig. 4.15). Correction of the strong westerly bias and stationary wave pattern enhances blocking occurrence in the Atlantic, while in the Pacific BCM2, HADGEM and IPCM4 now simulate better blocking episodes over the right regions, although for BCM2 and HADGEM some events over western Pacific are still captured. All models tend to produce more persistent blocking events after correction of the time-mean systematic error in the Euro-Atlantic region (See Figure 4.16 and Table 4.2). The average blocking lifetime and maximum persistence increase in EA, and are now improved for all models; IPCM4 is the only model for which the correction is not beneficial in the EA sector. The frequency of short-lived blocking events decreases, and the frequency of long-lasting episodes increases (Fig. 4.16), such that the simulated blocking lifetime distributions in the EA sector are now substantially improved.

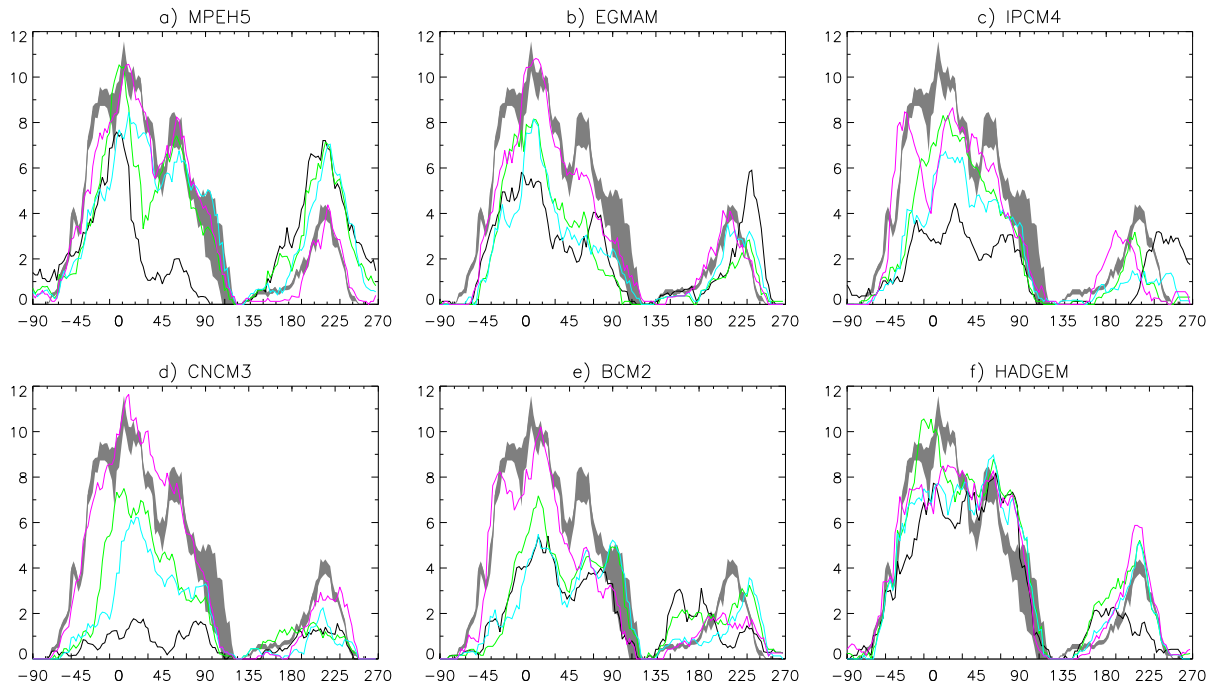

Figure 4.15: Frequency (in %) of winter large-scale blocking episodes as a function of longitude. 95% confidence interval for ERA-40 (grey area), uncorrected AOGCMs (black), time-mean corrected (green), time-mean and HFV correction (blue), time-mean and STD correction (magenta).

In the Pacific, however, the time-mean correction does not necessarily contribute to improve the blocking lifetime distribution; CNCM3 and MPEH5 are the only models for which the correction improves slightly the average persistence. It must be emphasized however, that because of the low number of Pacific blocks, the results are subject to sampling problems. Note the irregularities of the Pacific blocking lifetime distributions in Figures 4.6b and 4.17 for the models with the largest underestimation of blocked day frequency (CNCM3, IPCM4 in Table 4.4 and Figure 4.5).

Overall, those results suggest that the climatological time-mean state is important for the initiation and maintenance of blocking episodes in the EA region, and that a reduction of the time-mean systematic error in climate models would significantly improve blocking diagnostics in that sector. In addition, correction of the time-mean flow does also contribute to improve the frequency distributions in the Pacific sector, and particularly it enhances the number of blocking events in the right geographical sector (i.e. eastern Pacific), but it does not improve the average persistence and lifetime distribution of blocking episodes.

Blocking signatures have also been analysed after the corrections (Fig. 4.18 and 4.19). The time-mean corrected fields show more intense signatures and/or more pronounced deflection of the flow in the Atlantic for most models (except for MPEH5, Fig. 4.18). In the Pacific, correcting the time-mean geopotential field improves the geographical location of the blocking sectors for BCM2, HADGEM and IPCM4, which are now centered between 180° and 225°E (4.19). The intensity of the blocking anticyclone is modified for some models, leading to larger errors (IPCM4 and BCM2), while it is corrected for CNCM3. Therefore, time-mean circulation bias, such as too strong westerlies, underestimated or displaced stationary waves, can also induce errors in blocking intensity, longitudinal/latitudinal extension and geographic displacement of the whole structure and in the average deflection of the flow.

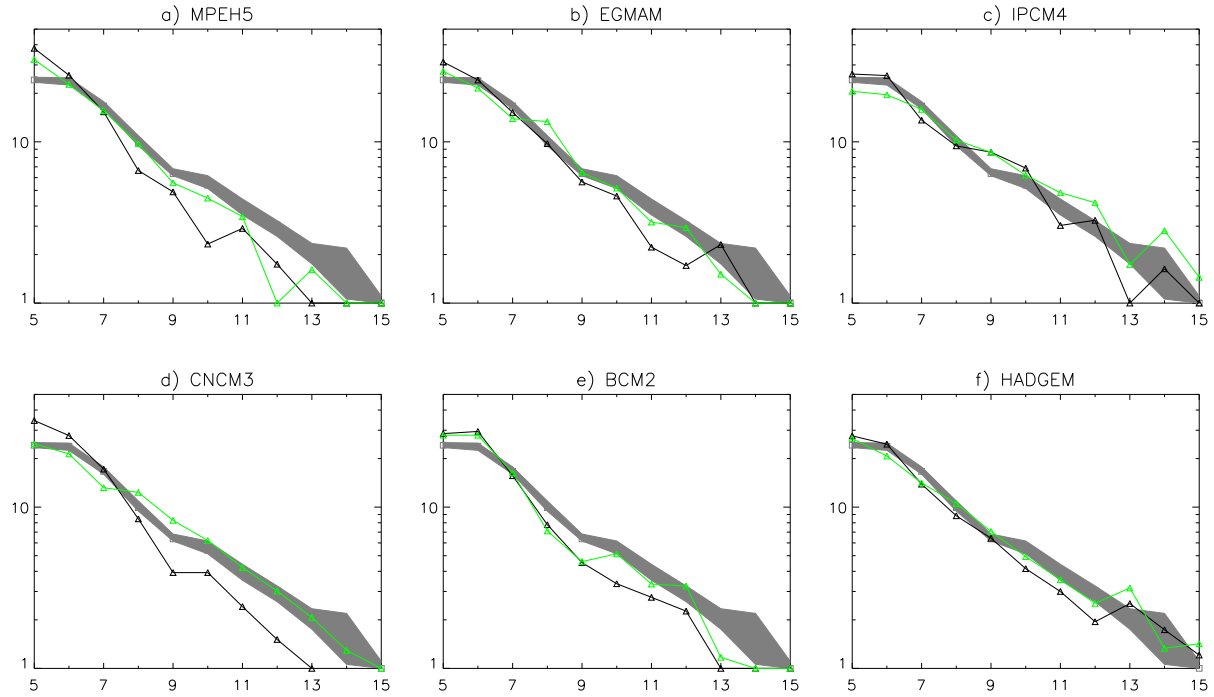

Figure 4.16: Frequency (in %) of winter large-scale blocking episodes (lasting at least 5 days) as a function of duration in days in the Atlantic sector. 95% confidence interval for ERA-40 (grey area), uncorrected AOGCMs (black). The green curve correspond to blocking frequencies after correction of the time-mean systematic error in each AOGCM (see in section 4.8).

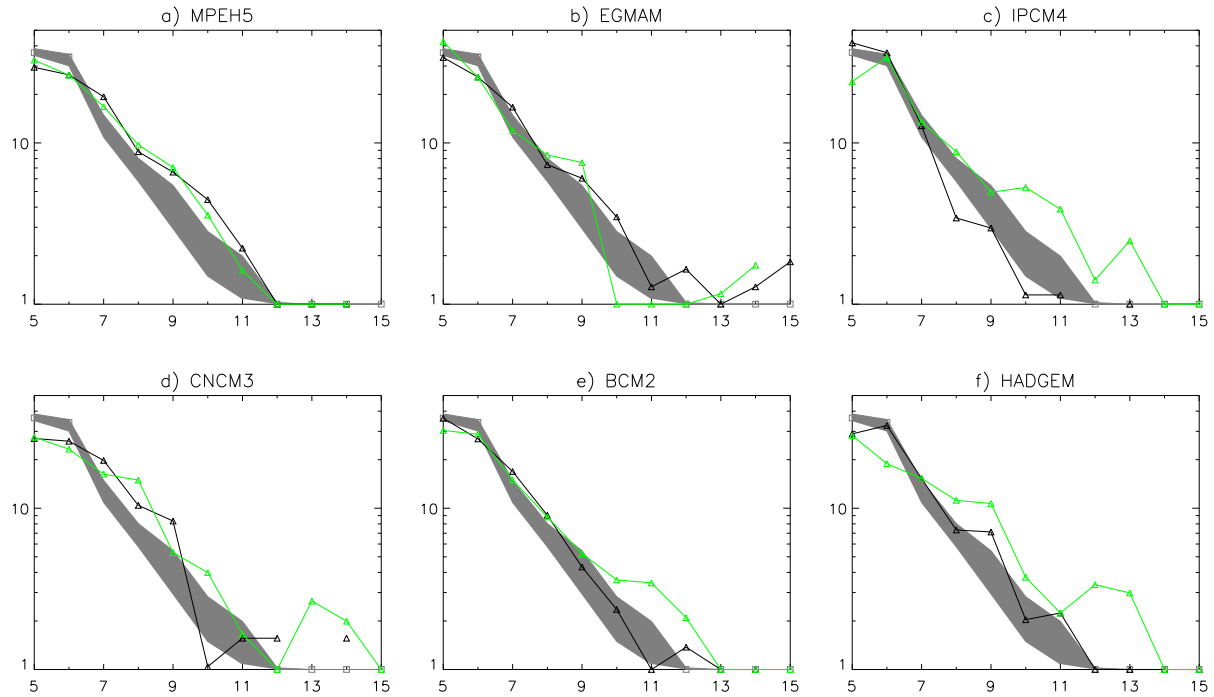

Figure 4.17: Same as Figure 4.16, but for the Pacific sector.

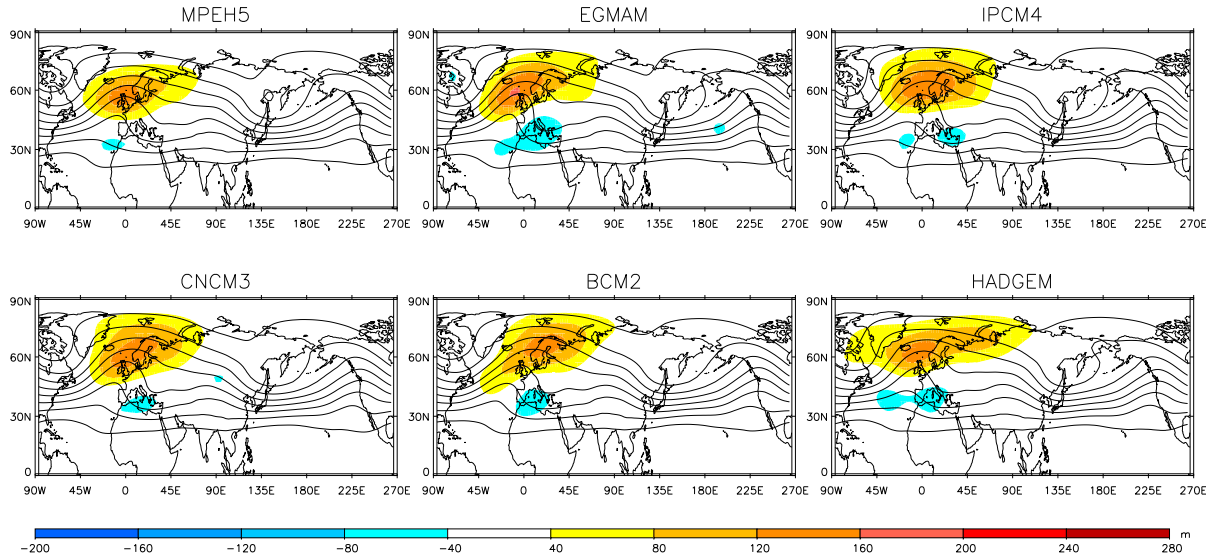

Figure 4.18: Blocking signature in the Atlantic of the 500 hPa geopotential field (color shading) after correction of the time-mean systematic error in each AOGCM. Solid contours represent the average 500 hPa geopotential field during blocked days only. *At least 5-day blocking events.*

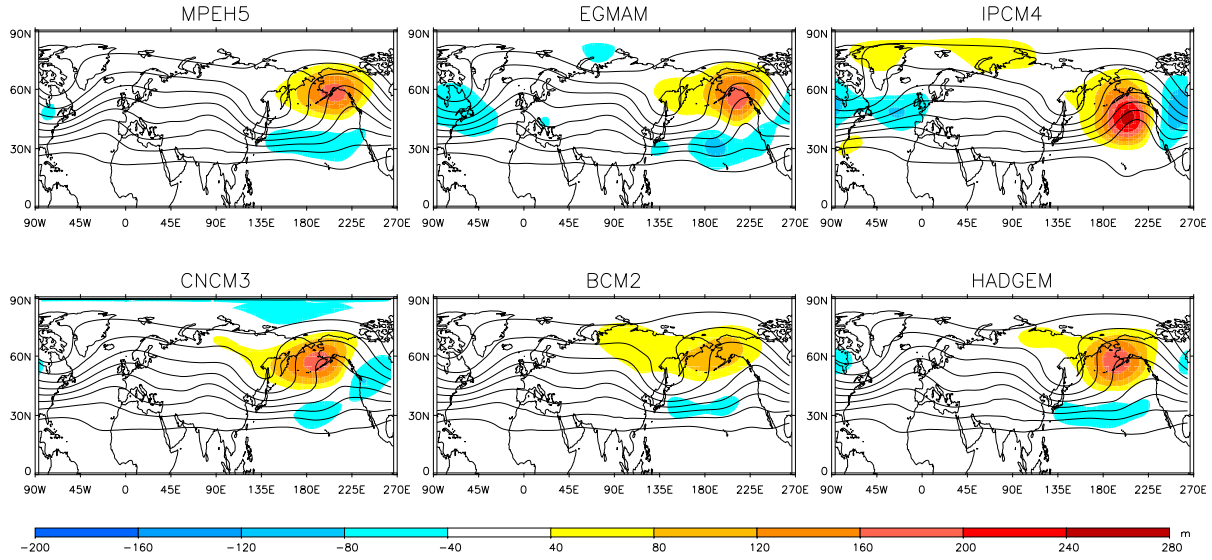

Figure 4.19: Same as Figure 4.18, but for the Pacific sector.

4.8.2 Impact of the time-variability model errors

To examine the impact of model errors in the amplitude of time-variability, two other analyses are considered. One consists of evaluating blocking statistics after "correction" of both the time-mean and standard deviation of the high-frequency (2-8 days) component of the variability (Figures 4.15, 4.20 and 4.21, blue line, and Tables 4.2 and 4.3, third column). In the second analysis, the time-mean and total time-variability (total standard deviation, STD) are corrected (Figures 4.15, 4.22 and 4.23, magenta line, and Tables 4.2 and 4.3, forth column). This "correction" consists of (1) increasing or decreasing the amplitude of the variability component (i.e., the daily geopotential height anomalies of the model $(x_M - \mu_M)$ are multiplied by the ratio ($\frac{\sigma_E}{\sigma_M}$, representative of the model errors in the low- or high-frequency variability), and (2) adding the time-average of ERA-40 output to the "corrected" model

anomalies to account for the time-mean correction. These two analyses will be useful to distinguish the impact of the HFV and LFV independently on blocking simulations. The calculation involved for this type of correction is as follow:

$$x'_M = \left[(x_M - \mu_M) \frac{\sigma_E}{\sigma_M} \right] + \mu_E \tag{4.2}$$

where x_M, x'_M, μ_M and μ_E are defined as in Eq. 4.1; σ_M and σ_E are the standard deviation of the model and ERA-40 outputs respectively. When the HFV is analysed, only the band-pass filtered (between 2 and 8 days, using a finite impulse response filter based on Kaiser's window) data are considered in this equation.

The performance of the models at representing the time-variability of the flow is presented in Figures 4.26 and 4.27, which show the ratio of the HFV and LFV, respectively. The main feature is an underestimation of the variability over the north Atlantic ocean and northern Europe, as well as in the north Pacific ocean, where the main storm tracks and LFV maxima are located (Fig. 4.24 and 4.25). In the Pacific region, MPEH5 overestimates both the HFV and LFV, while HADGEM overestimates the intensity of the storm track with a slight southward displacement. In the north Atlantic, however, HADGEM simulates relatively well the variability.

After HFV correction blocking frequency tends to decrease in regions and models with underestimated HFV (Fig. 4.15, green and blue lines), although the signal seems to be weak compared to the amplitude of the model errors (e.g. CNCM3 and BCM2, Fig. 4.26); the opposite occurs for overestimated HFV. In the EA sector, the change in total blocking frequency seems to affect all spell durations; the average persistence is unchanged as compared to the TM correction alone (the frequency distributions before and after the correction are more or less parallel on the semi-logarithmic plots - see Fig. 4.20), and the maximum duration is lower (Table 4.2). In the Pacific, however, the average persistence and maximum duration tend to be lower, with in addition, a tendency for an increased frequency of short-lived blocking episodes and less frequent long-lasting blocks (Fig. 4.21). In the case of EGMAM, the total frequency, average and maximum persistence increase; the results are in line with less short-lasting blocking episodes (5-day duration) and more long-lasting events (between 9- and 11-day duration), after correction of the overestimated amplitude of the HFV (Fig. 4.21b).

Underestimation of the LFV seems to be associated with lower blocking frequency in both sectors, and inversely (Fig. 4.15, compare the blue and magenta lines). In the Atlantic, the average and maximum blocking duration tend to be increased, and as compared to TM and TM+HFV corrections, results are now closer to ERA-40 (Table 4.2); there is a tendency for increased frequency of long-lasting blocking episodes, and decreased frequency of short-lived events (Fig. 4.22). In the Pacific, this correction tends to be associated with a decreased average persistence (Table 4.3) and frequency of long-lasting episodes (4.23, except for CNCM3 and IPCM4), whatever the change in the total frequency (Fig. 4.15) and the type of correction (increased or decreased LFV).

Correction of systematic error in the amplitude of the time-variability also impacts on blocking signatures and flow deflection (Fig. 4.28 to 4.31). The correction of the total time-variability tends to produce better results than the HFV correction only: the blocking events have a geographical position that is more comparable to those of ERA-40 events (e.g., CNCM3 and BCM2 in EA, BCM2 and IPCM4 in PAC), but substantial errors in the intensity of the blocking high also emerge after those corrections.

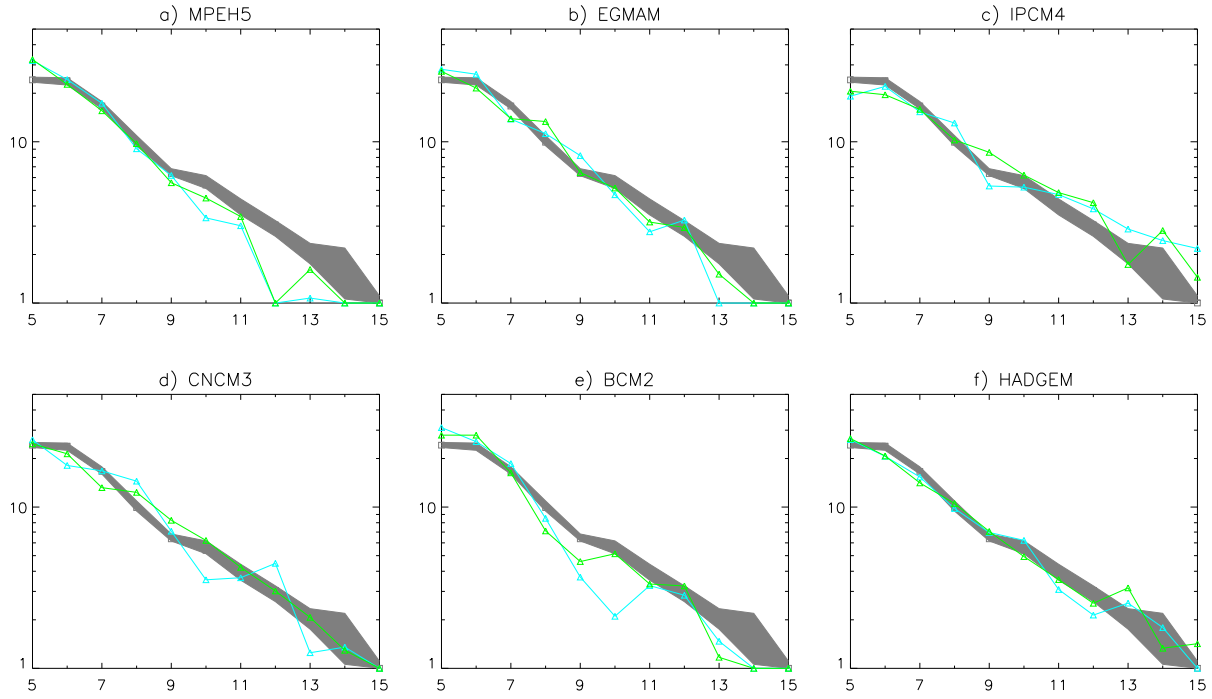

Figure 4.20: Same as Figure 4.16. 95% confidence interval for ERA-40 (grey area), time-mean correction (green), time-mean and HFV correction (cyan).

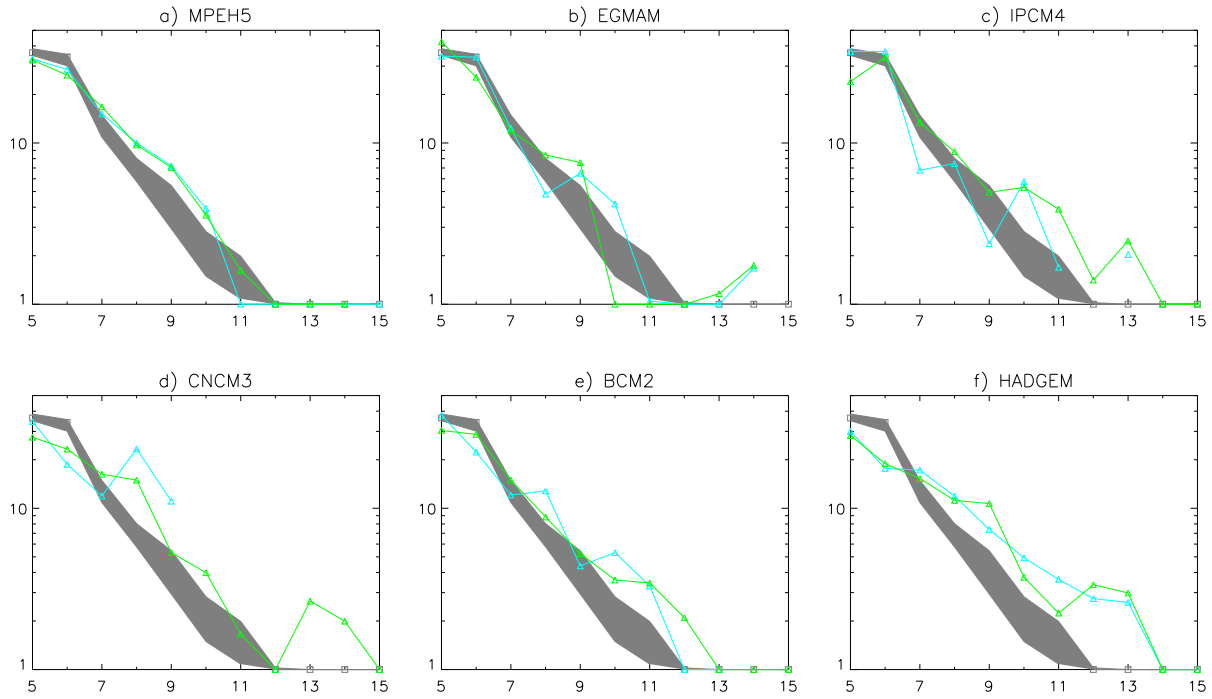

Figure 4.21: Same as Figure 4.20, but for the Pacific sector.

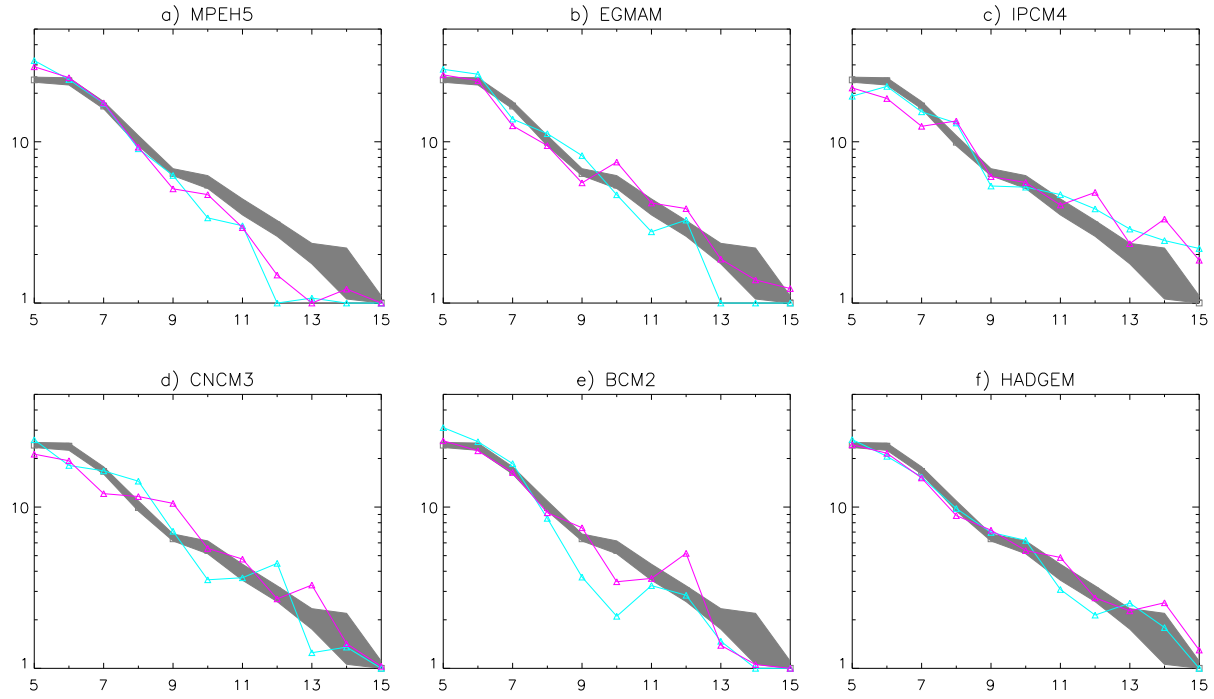

Figure 4.22: Same as Figure 4.16. 95% confidence interval for ERA-40 (grey area), time-mean and HFV correction (cyan), time-mean and STD correction (magenta).

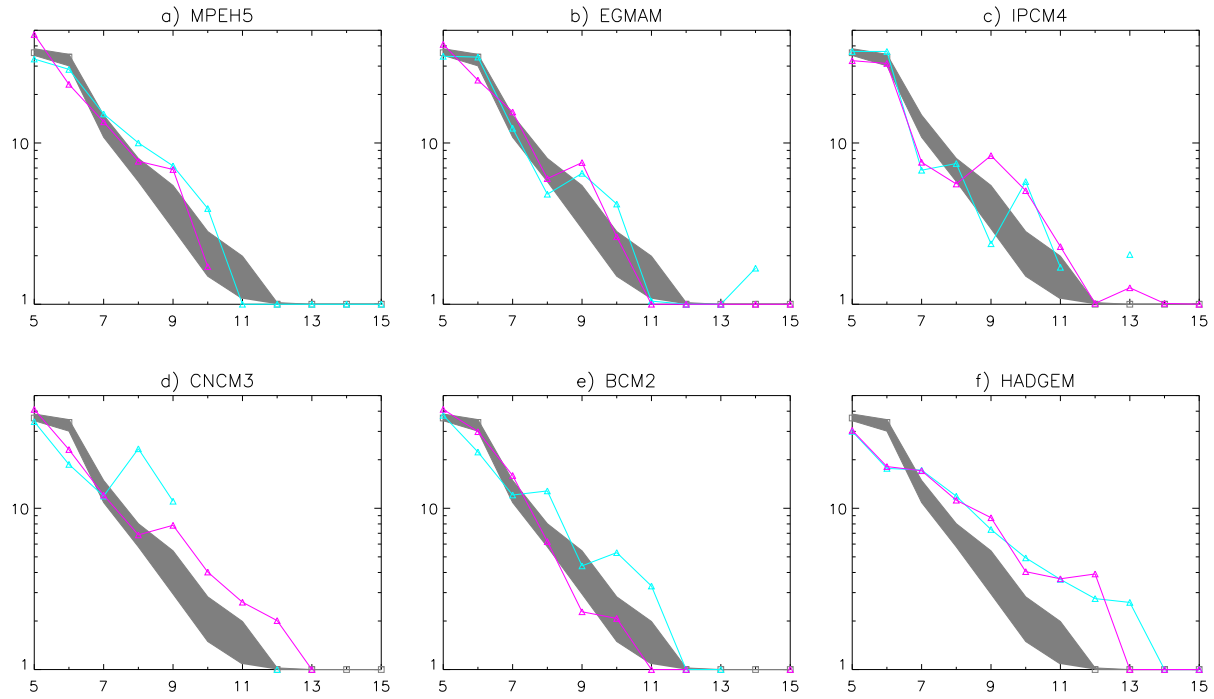

Figure 4.23: Same as Figure 4.22, but for the Pacific sector.

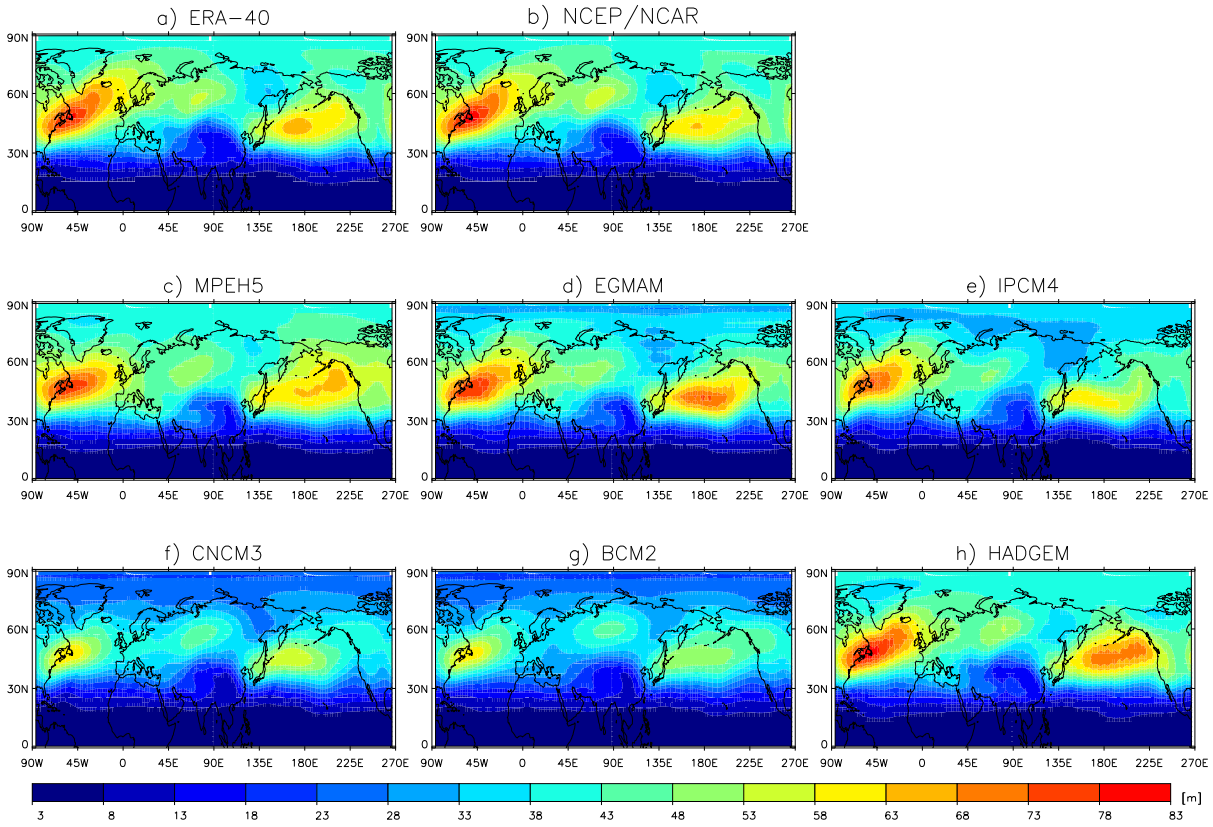

Figure 4.24: Storm track at 500 hPa - Standard deviation of the band-pass filtered (2-8 days) 500 hPa geopotential field.

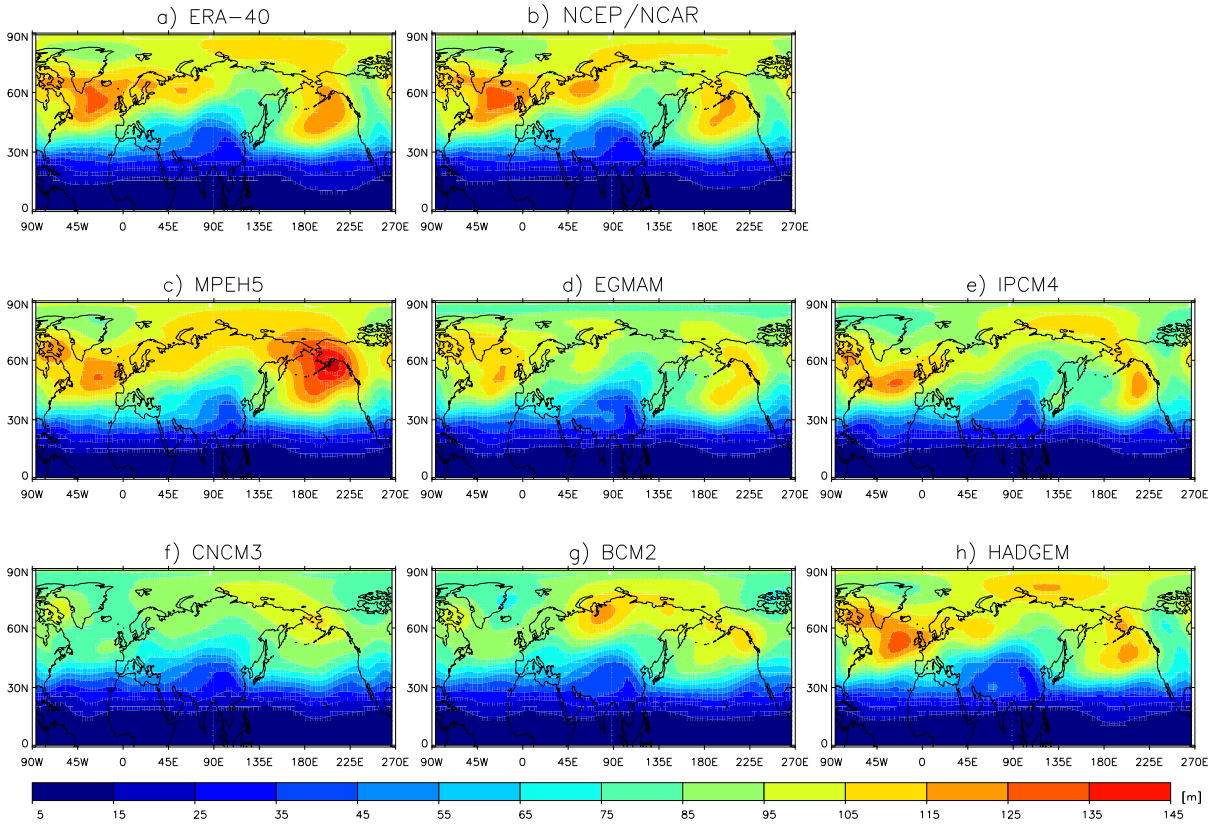

Figure 4.25: Low-frequency variability - Standard deviation of the low-pass filtered (above 8 days) 500 hPa geopotential field.

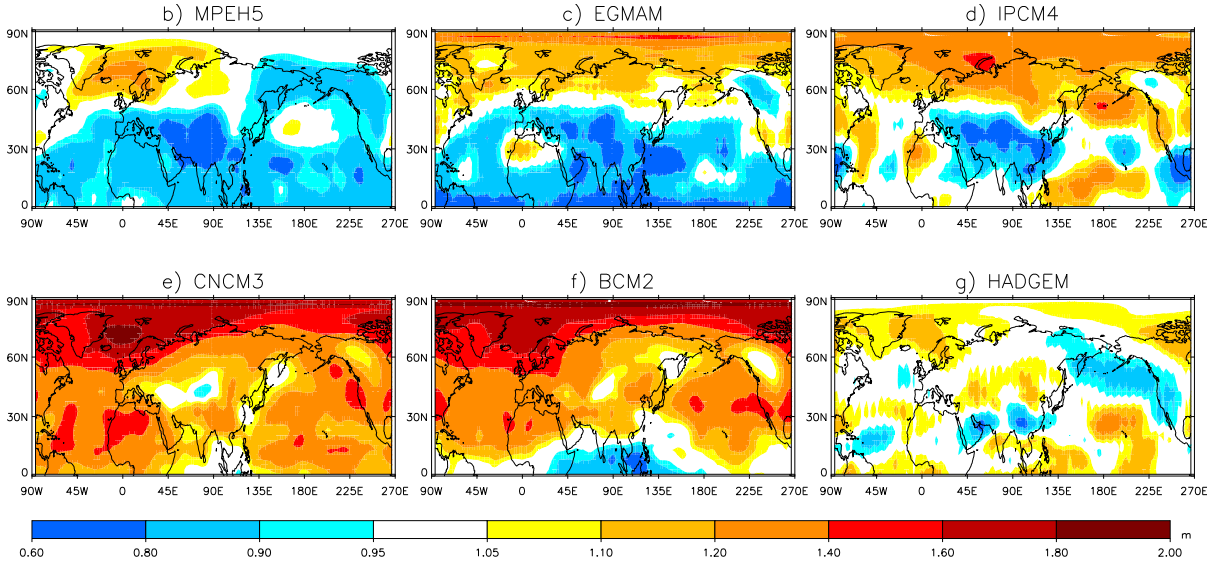

Figure 4.26: Ratio ($\frac{\sigma_E}{\sigma_M}$) of the high-frequency variability - Standard deviation of the band-pass filtered (2-8 days) 500 hPa geopotential field.

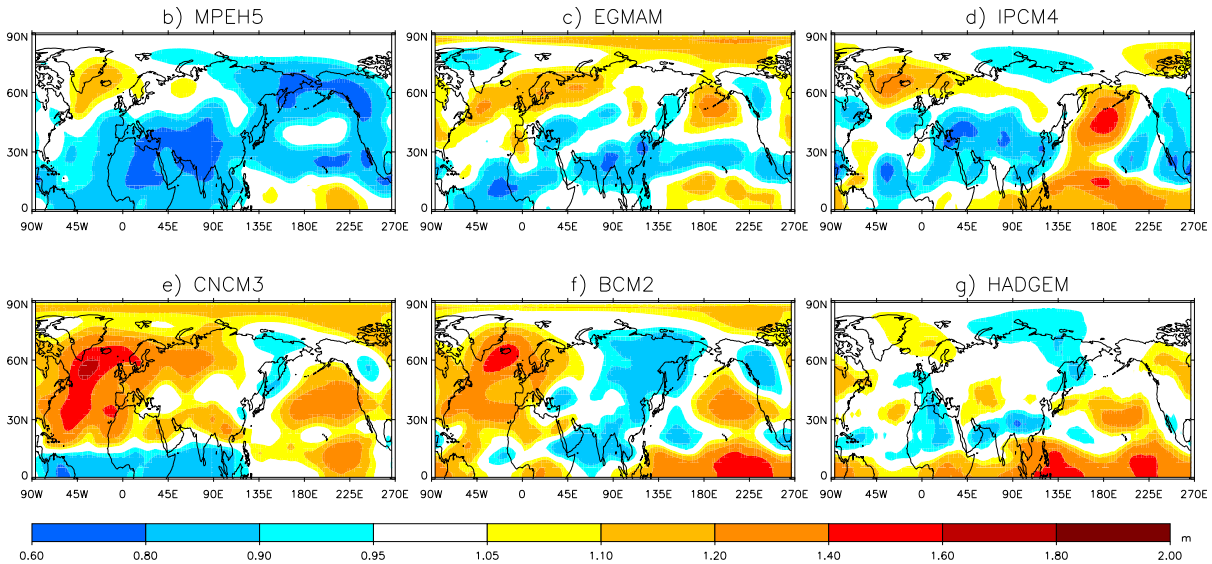

Figure 4.27: Ratio ($\frac{\sigma_E}{\sigma_M}$) of the low-frequency variability - Standard deviation of the low-pass filtered (above 8 days) 500 hPa geopotential field.

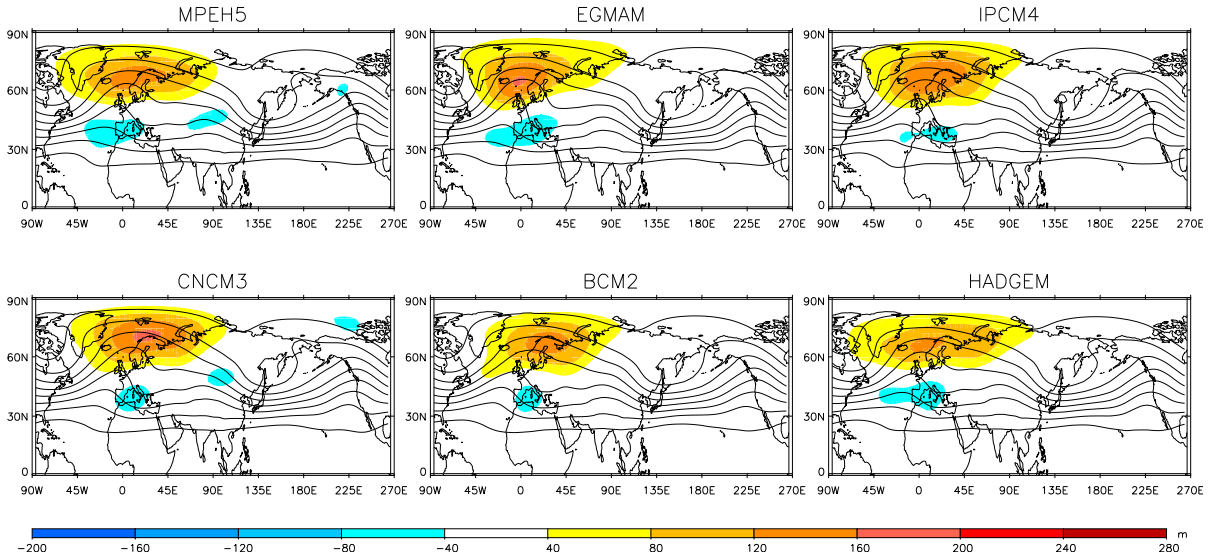

Figure 4.28: Same as Figure 4.18, but after correction of the time-mean and HFV systematic error.

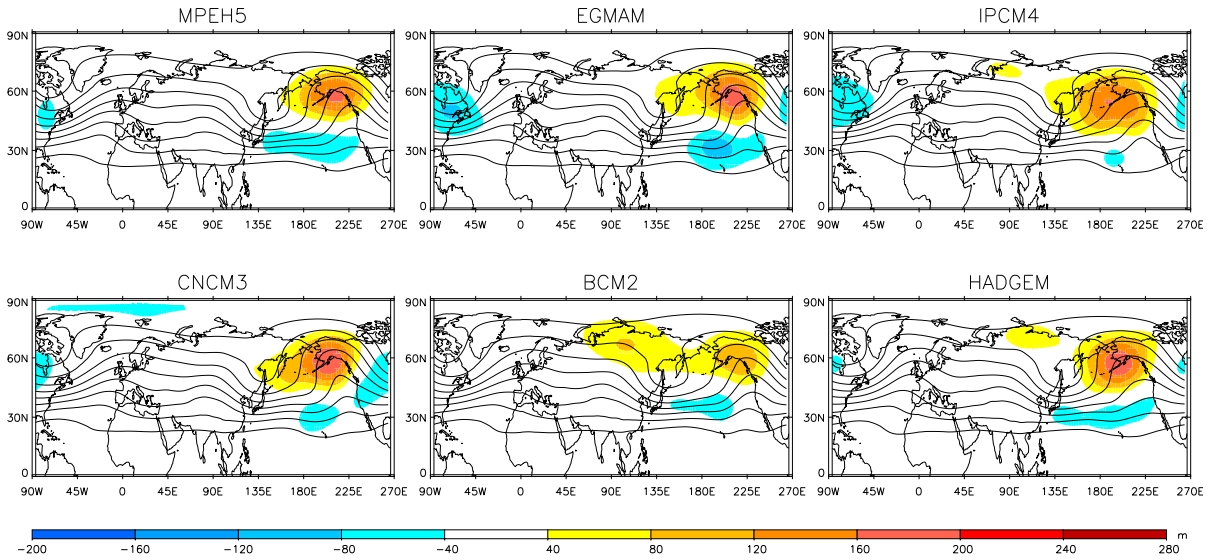

Figure 4.29: Same as Figure 4.28, but for the Pacific sector.

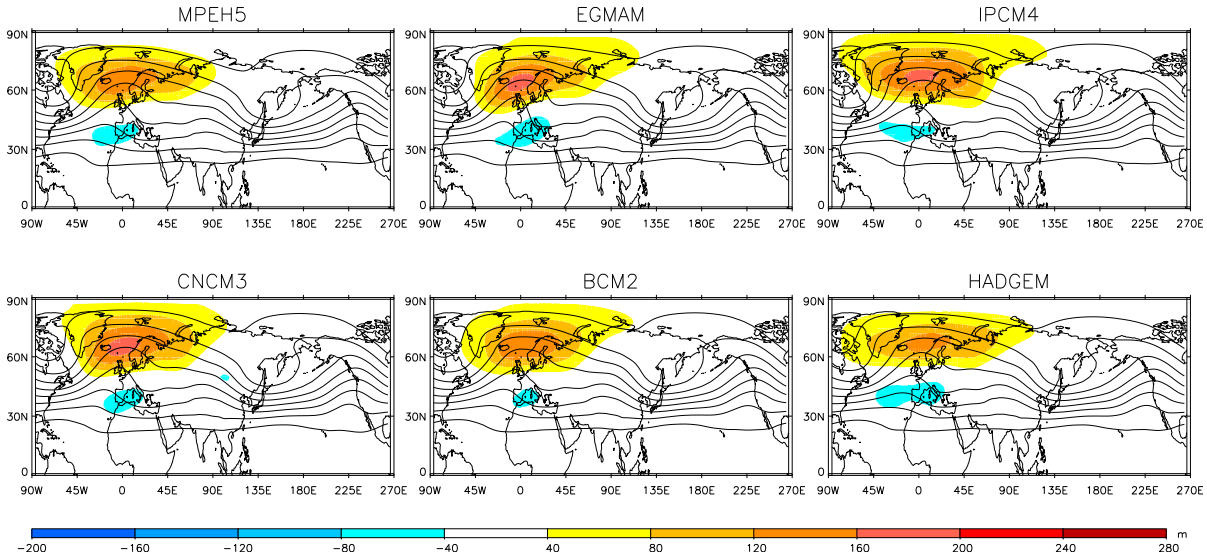

Figure 4.30: Same as Figure 4.18, but after correction of the time-mean and STD systematic error.

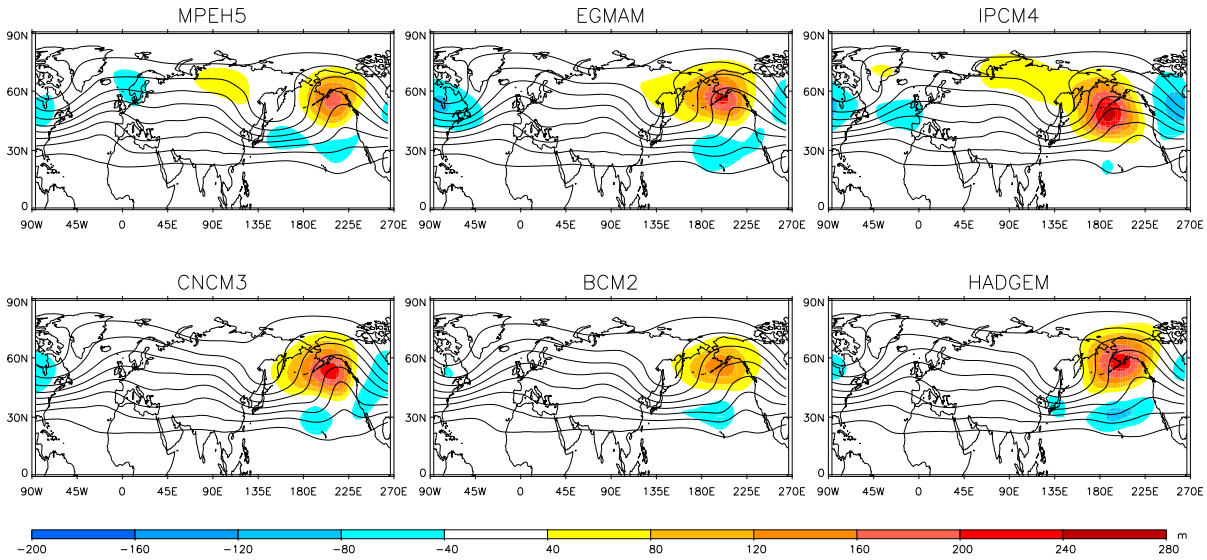

Figure 4.31: Same as Figure 4.30, but for the Pacific sector.

4.8.3 Summary and interpretation of results

	EA			PAC		
Models	TM	TM + HFV	TM + STD	TM	TM + HFV	TM + STD
CNCM3	211^{+}	-25^{-}	98^{+}	31^{+}	0.5^{+}	48^{+}
BCM2	3^{+}	-0.1^{-}	65^{+}	26^{-}	-5^{+}	-24^{-}
MPEH5	14^{+}	-11^{-}	14^{+}	-9^{+}	-3^{+}	-44^{+}
EGMAM	17^{+}	-13^{-}	43^{+}	-20^{-}	54^{+}	11^{+}
IPCM4	50^{+}	-18^{-}	32^{+}	-13^{-}	13^{+}	24^{-}
HADGEM	9^{+}	-4^{-}	4^{+}	43^{-}	-9^{+}	1^{-}

Table 4.5: Percentage change in the number of blocked days for the Euro-Atlantic and Pacific sectors after each correction (time-mean, TM; time-mean and HFV, TM + HFV; time-mean and STD, TM + STD). As in Tables 4.2 and 4.3, the directions of the change toward ERA-40 results after corrections (computed with reference to the previous column) of the systematic errors are indicated: "+" = improvement, "−" = decline in model performance, no mark = no change.

The percentage change in the number of blocked days for each sector independently after each correction is presented in Table 4.5. It provides an estimate of the importance of each type of model errors, as well as an indication of the direction of the change (improvement or decline in model performance) in the average number of blocked days for each sector. It shows that corrections of the time-mean and LFV amplitude both contribute the most toward an increase and an improvement in the number of EA blocking cases. In the Pacific, those corrections bring also the major changes, but do not always contribute to an improvement in the number of blocked days (similar results are found for the persistence diagnostic in Table 4.3). It is also interesting to note the type of systematic errors in each model that are linked with errors in blocking diagnostics. For some models, errors in the mean state only are important (e.g. HADGEM in the Pacific). For other models, corrections including the LFV bring the best match with ERA-40 (e.g. BCM2 in the Atlantic, MPEH5 in the Pacific). Most of the models, however, need corrections in both the mean state and the variability to produce realistic blocking statistics. It should be noted however that the main source of error for the Pacific sector is blocking mislocation (e.g. EGMAM, IPCM4, BCM2 and HADGEM in Fig. 4.15), and rating the results by looking only at the number of blocked of days in Table 4.5, might be reductive as this diagnostic does not take into account model errors due to blocking mislocation. For instance, Table 4.5 suggests that IPCM4 best performs after the HFV correction, while from Figure 4.15 TM correction is crucial for IPCM4 performance even more than what the HFV correction does. Therefore, both Table 4.5 and Figure 4.15 should be considered to rate model performance in terms of the number or frequency of blocked days, particularly in the Pacific sector.

The correction exercise reported here will only change the blocking statistics if the important systematic errors occur within the blocking area itself. Systematic errors from outside the blocking area could also influence the development or removal of blocks, but the corrections applied here cannot directly compensate for those errors. This is particularly relevant for errors in the high-frequency transient eddy activity, which can act from upstream to amplify and sustain a downstream blocking high (Austin, 1980; Shutts, 1983; Illari, 1984). For example, a positive bias in high-frequency synoptic activity could enhance blocking activity downstream (according to current understanding of the dynamical mechanisms linking eddies and blocking). As illustrated in Figure 4.13, if the HFV bias is located within the preferred area for blocking occurrence, the effect of the HFV correction would be weak compared to corrections

of the LFV bias and the time-mean bias, and a small or even null impact on the total blocking frequency might be expected. The HFV bias correction would, however, induce a change in the proportion of short and long-lasting blocks: greater eddy activity inside the blocking region will increase the frequency of short-lived blocks at the expense of long-lived blocks. This is supported by observing that transient eddy activity is reduced and/or displaced in the area affected by a blocking high. The effect of the various bias corrections is likely to depend, therefore, on the relative strengths and locations of the HFV, LFV and time-mean biases, and this could explain why corrections of the HFV bias tend to improve blocking activity in PAC (at least for the average persistence and maximum duration) but do not change (or even worsen) it in ATL.

It must also be emphasized that the STD correction involves the frequencies in which blocking operates (on intra-seasonal time-scales), and hence it might be expected to see large effects or even the largest improvements on blocking statistics after its correction. However, this correction also includes other time-scales (above the seasonal one), and therefore depending on where the largest model errors are (intra-seasonal or inter-seasonal time-scales), the effect of this correction might also be different, and would explain why more diverse results are obtained according to the model and region considered.

4.9 Concluding remarks

The ability of six AOGCMs to simulate winter atmospheric blocking in the Northern Hemisphere has been evaluated by comparison with the ERA-40 reanalysis. These six climate models all underestimate the total blocking frequency over the Northern Hemisphere to various degrees (except MPEH5 and EGMAM in the north Pacific). Analysis of multiple simulations and periods demonstrates that these errors are real and not the result of internal variability or changes in the external forcing.

All models underestimate the average persistence of blocking episodes in the Euro-Atlantic sector. However in the Pacific, the average blocking lifetime tends to be overestimated, and some models are even able to produce blocking episodes as long as those identified in the ERA-40 reanalyses.

In terms of blocking signatures, results are more satisfactory than reported in earlier studies (Tibaldi *et al.*, 1997; D'Andrea *et al.*, 1998), particularly in terms of their ability to simulate more localized signatures in both sectors. However, errors in the intensity and geographical location of blocking episodes still emerge in the Pacific region.

Another interesting feature drawn from this assessment is the difference in the ability of the models to simulate blocking in both regions, which seems to suggest that blocking highs result from different processes in each sector, as suggested in other studies (Tibaldi *et al.*, 1997; D'Andrea *et al.*, 1998). It must be emphasized however, that model performances in blocking simulations can also be affected by the choice of the blocking detection method and of the diagnostic. When using the BI_{stlat} index, the frequency and average lifetime of Pacific blocking episodes are not clearly underestimated by all the models, whereas it is no longer the case once the BI index is used.

The impact of models' systematic errors on blocking simulation has also been analysed. There is a primary need to reduce the time-mean atmospheric circulation bias to improve the representation of blocking in climate models. The time-mean systematic errors, which are mainly too strong average westerlies and zonality of the flow, as well as discrepancies in the stationary wave pattern, are mainly responsible for the underestimation of long-lasting blocking episodes, and a reduction of the maximum

event duration in the Euro-Atlantic region, as well as geographical displacements of the Pacific blocking sector. There seems to be a weak negative correlation between the amplitude of the HFV and the frequency of long-lasting blocking episodes, consistent with the observed deviation of the transient eddies' trajectory. The amplitude of the LFV is positively linked with the average blocking lifetime and frequency of long-lasting episodes in the Euro-Atlantic sector. In the Pacific, however, there is no systematic tendency: increased or decreased amplitude of the LFV tend to be linked with decreased average persistence and frequency of long-lasting blocking episodes. In addition, the correction of the time-mean and total standard deviation does not always contribute to improve blocking simulations in the Pacific.

Overall, depending on the model and region considered, errors in blocking diagnostics can be linked with the time-mean bias only, errors in the LFV only, or both. By splitting the total flow into its mean state and time-varying part, this assessment reveals if the simulated blocks are derived from a compensation of model errors or if blocking statistics are coherent with the background flow.

4.10 Further remarks

Three of the models evaluated in this study (EGMAM, CNCM3 and HADGEM) are improved versions of ECHAM, METEOFR and UKMO assessed in D'Andrea *et al.* (1998), in terms of parameterizations, dynamics and resolution. Furthermore, in this study the models are coupled atmosphere-ocean models, while in D'Andrea *et al.* (1998) atmosphere-only models with prescribed observed monthly mean SST were used. It has been demonstrated in a number of studies that the impact of SST is important for the development and maintenance of both Euro-Atlantic and Pacific blocking (e.g. Ferranti *et al.*, 1994b). Having said that, despite considerable differences between the two generations of models (about 10 years of model development), there is only a moderate improvement in blocking simulation - though different blocking indices, analysis periods and model coupling must be born in mind. Another consideration is the physics/dynamics resolution dependence. Boer *et al.* (1992) have mentioned that the impact of improving physical parameterizations is resolution dependent. Similar arguments hold concerning the improvement of the dynamics in the model. Ringer *et al.* (2006) explained that the representation of synoptic-scale eddies improves with increased resolution when climate models use a Semi-Lagrangian dynamical core. However, at lower horizontal resolutions (typical climate model resolution of 2.5° Williamson and Olson, 1998; Williamson *et al.*, 1998), Eulerian models represent transient activity better than the Semi-Lagrangian models. The AOGCMs used in this present study all use a Semi-Lagrangian scheme, except IPCM4 which uses a finite volume scheme, but it is not clear here whether or not higher resolution models represent synoptic-scale eddies better.

Ringer *et al.* (2006) found that the atmosphere-only model HadGAM1 has a tendency to reproduce more blocking events than the atmosphere-ocean HADGEM model, apparently a response to a cold bias in the equatorial Pacific ocean in the latter. Similar results were reported by Ferranti *et al.* (1994b), who found that Pacific blocking frequency was increased when a positive anomaly was superimposed on the climatological SST in the Indonesian region. So more realistic SST simulations (variability as well as mean state) in coupled climate models could enhance blocking development and maintenance. D'Andrea *et al.* (1998) noted that nine of their AGCMs, also analysed by Slingo *et al.* (1996), with low tropical variability were not able to simulate blocking well.

CNCM3, BCM2, IPCM4 and MPEH5 were also assessed in Scaife *et al.* (2010), using a zonal wind-based version of the Tibaldi and Molteni (1990) blocking index applied to all grid point between 50° and 70°N, and similar model errors in blocking frequency in both the Atlantic and Pacific sectors were also found. Therefore, even though model performance in simulating blocking is sensitive to the blocking detection method, the direction of model errors (under or overestimation) is generally insensitive.

CHAPTER 5

Relationship between sudden stratospheric warming and tropospheric blocking

5.1 Introduction

5.1.1 What is a sudden stratospheric warming?

Stratospheric sudden warmings (SSWs) are considered to be the most dramatic large-scale phenomena to occur in the extratropical stratosphere during the winter/spring seasons (Andrews *et al.*, 1987). Such events are characterized by temperature rises and weakening of the zonal-mean zonal flow in the stratosphere, which lead to major disruptions of the large-scale and persistent polar cyclone (polar vortex). Two types of warming events have been identified: the *vortex displacement* event when high potential vorticity over the pole is displaced equatorward and takes the form of "a comma shape" (Fig. 5.1a), and the *vortex splitting* event when the polar vortex splits into two distinct pieces (Fig. 5.1b) (Charlton and Polvani, 2007).

5.1.1.1 Dynamical perspective

A dynamical model of the SSW, pioneered by Matsuno (1971) and now widely referred to in the literature, is based on the idea that SSW is initiated via the interaction between the stratospheric polar zonal flow and amplified vertically propagating planetary waves (PWs), consisting primarily of zonal wavenumbers 1 and 2. Such amplification of the PWs is due to tropospheric disturbances, which can manifest as blocking events (Andrews *et al.*, 1987), or through the non-linear evolution of baroclinic eddies (Scinocca and Haines, 1998) or due to forcing at the surface (e.g., anomalous land/sea thermal contrasts, variation in snow cover). The stratosphere has to be in a specific state if a warming has to follow, such that PWs can propagate focusing toward the polar vortex instead of following their equatorward climatological path. The polar vortex is usually preconditioned when the zonal flow is displaced poleward and gets constricted about the pole (McIntyre, 1982; Andrews *et al.*, 1987).

Upward propagating PWs are associated with poleward heat transport. Divergence equatorward and convergence poleward of the maximum eddy heat flux result in a weakening of the equator-to-pole temperature gradient, and according to the thermal wind balance, the vertical wind shear must weaken as well. From the continuity of mass, this is achieved by poleward motion at low levels, turning eastward because of the Coriolis effect, and equatorward at high levels with a westward Coriolis deviation. As a result there is (1) an easterly acceleration in the high atmosphere, (2) an upper-atmospheric adiabatic

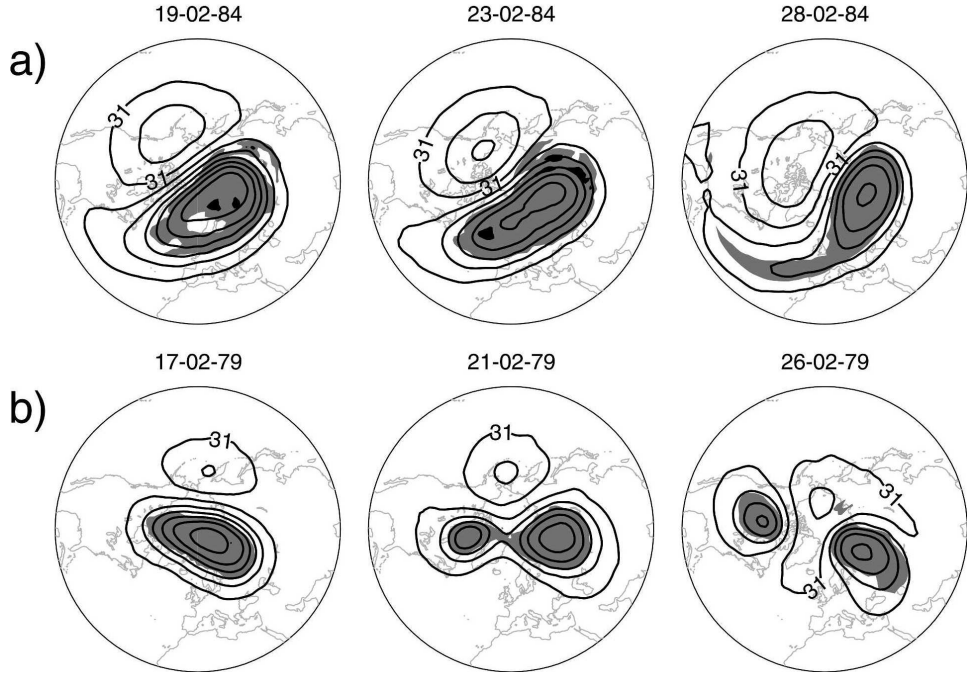

Figure 5.1: Two types of stratospheric warming events that occurred during two distinct boreal winter seasons. (a) A vortex displacement in February 1984, and (b) a vortex splitting in February 1979. Contours are geopotential height at 10 hPa (contour interval is 0.4 km), and shading shows high potential vorticity (> 4.0 x 10^{-6} K kg^{-1} m^2 s^{-1}). Reproduced from Charlton and Polvani (2007).

warming due to the descending motion associated with the "wave-induced meridional circulation", and causing the warming of the polar stratosphere, as the adiabatically compressed air is advected poleward.

5.1.2 Relationships between stratospheric sudden warming and tropospheric blocking: a review

There is evidence that there is a connection between SSW and blocking events; several cases studies have been described and longer datasets have been analysed for that purpose, but the literature doesn't yet provide strong and clear evidence of a statistical or dynamical link between both phenomena.

Labitzke (1965) investigated, by means of daily synoptic maps, the Northern Hemisphere tropospheric conditions before and after 11 pronounced stratospheric warming events that occurred in the winter seasons between 1957/58 and 1963/64. The SSW events were then divided into two categories with respect to their origin and direction of movement, namely the European and American SSWs. It was found that about 10 days after the onset of all of the European SSWs, blocking patterns formed and persisted from 1 to 3 weeks. However, those results are not entirely supported by the statistical study of Quiroz (1986), in the sense that blocking events led 17 of the 20 stratospheric warming episodes (85%) considered, by an average of 3.5 days, in contrast to the 10-day lag found in Labitzke (1965). Another example is the severe winter conditions experienced in the United States in 1963 and 1977, which are believed to be the results of large-scale blocking highs, during which a SSW and blocking events were simultaneously observed and preceded by amplifying stationary waves (Tung and Lindzen, 1979). Later, Naujokat *et al.* (2002) argued that the occurrence of free travelling Rossby waves interacting with

orographically and/or thermally forced stationary waves of zonal wavenumber 1 have led to three major warming events in December 1987, 1988 and 2001. In addition, they claimed that strong blocking episodes over the north Atlantic could have triggered these travelling waves before the warming initiated. This possible relationship was based on the fact that periods of blocking occurrence were almost coincident with the periods of travelling waves. So, whether the blocking caused the anomalous wave activity or vice versa does not seem to be so clear (Baldwin and Dunkerton, 1989).

More recently, Taguchi (2008) performed a statistical analysis, using a random bootstrap method, with 49 years of NCEP-NCAR reanalysis data from 1957/58 to 2005/2006, and considered two hypotheses that blocking events occur preferentially and last longer (1) in a pre-SSW period (blocking leads SSW by 10 days) or (2) in a post-SSW period (blocking follows SSW within a 60-day window). In contrast with previous studies, no significant association between SSW and blocking events were found. Contradictory results were then reported by Martius *et al.* (2009), who did find a significant link between SSW and blocking events: 25 of the 27 SSW events analysed in ERA-40 for the period 1957-2001 were preceded by blocking patterns within a time lag of 10 days. In addition, their study revealed a strong correlation between the type of stratospheric events and the geographical location of blocking. Vortex displacements were mostly associated with Atlantic blocks, while for vortex splitting events blocking in the Pacific or in both the Atlantic and Pacific simultaneously were observed. Woollings *et al.* (2010) examined the relationship between stratospheric variability and tropospheric blocking for the 44 boreal winter seasons from the reanalysis ERA-40 and a well-resolved stratosphere GCM from the Hadley centre (HadGAM). An empirical orthogonal function (EOF)-based approach was used to capture the stratospheric variability, rather than just stratospheric sudden warming events, in order to ensure more robust blocking-SSW links. It was found that the occurrence of blocking in different regions of the Northern Hemisphere, namely Europe, Greenland and west Pacific, modified the long stationary and/or transient tropospheric PWs (consistent with Naujokat *et al.* (2002)'s hypothesis), which led to upward propagation of these long wave anomalies into the stratosphere. Blocking influenced the stratosphere via PW activity, while the inverse influence, which appeared to show a stronger signal, was via the mean zonal flow and downward propagation of annular mode variations from the stratosphere to the troposphere.

Two main reasons could explain the difficulty in establishing a robust link between tropospheric blocking and stratospheric warming events. First, the rarity of SSWs (at most once a year, Andrews *et al.* (1987)), and the relatively short time-period of observational or analysed datasets (the first observation of SSW was made in 1952, Andrews *et al.* (1987)), result in small sample size of SSW catalogues for statistical analysis (between 25 and 40 SSWs can be identified in a typical 45-year reanalysis dataset depending on the definition used, see references above). The second reason is that tropospheric blocking occurs frequently at different locations within one year, so that at first glance most of SSWs appeared to be associated with blocking events (Taguchi, 2008), although it might not be statistically or physically meaningful. The related difficulty arising from ubiquitous blocking events is in establishing which blocking regions are linked with SSWs and at which time-lag (Woollings *et al.*, 2010).

5.1.3 Aim

In this study, the relationships between SSW and tropospheric blocking events is revisited with an attempt to alleviate these problems. A 1000-year model simulation is used to increase the sample size

of the SSW catalogue and provide more robust dynamical interpretations of the statistical stratosphere-blocking relationships. The precursor role of blocking on SSWs and the influence of SSWs on blocking are explored over a much larger sample size than previously used and over the different regions affected by blocking. Implications regarding the dependence between the annual cycle of blocking activity and the breaking of the stratospheric polar vortex are also considered. As a context for this study, when the stratospheric conditions change from sudden warming to a more climatological state, is there a change in tropospheric blocking variability?

5.2 Model simulation

The simulation used in this study is the 1000-year (nominally 1800-2799) Pre-industrial Control experiment of the LMDZ fifth-generation atmosphere-ocean coupled model, prepared for the Coupled Model Intercomparison Project Phase 5 (CMIP5). Its atmospheric component (LMDZ5) uses a horizontal resolution of 1.9° in latitude and 3.75° in longitude and 39 levels in the vertical (96x96L39)[1]. The model lid is at $\sim$ 50 km ($\sim$ 1.5 hPa, in the lower mesosphere), with 15 levels above 20 km ($\sim$ 50 hPa). The Pre-industrial Control experiment (hereafter, PiControl) imposes non-evolving and pre-industrial prescribed atmospheric concentrations of all well-mixed gases (including CO_2), and emissions or concentrations of natural aerosols (Taylor *et al.*, 2009). As there is no external forcing and no climate change signal, this experiment can be used to estimate the unforced internal variability of the coupled model, which mainly refers to the annual cycle and developing temporal and spatial scales variations due to different conditions within the period of integration. This simulation is therefore very useful to understand the climate dynamics in the model.

5.3 Methodology

5.3.1 Detection of stratospheric sudden warmings

The methodology for the detection of SSW events is adapted from Limpasuvan *et al.* (2004). The variability in the strength of the polar vortex is determined from the leading principal component (PC) associated with the first empirical orthogonal function (EOF) of the zonal-mean zonal wind anomalies[2] at 10 hPa.

When performing an EOF analysis, the data in the spatial domain have to be area weighted prior to calculation to account for the convergence of the meridians, which reduces the impact of high-latitude grid points. Here, the data are weighted by the square root of the cosine of latitude, as it is commonly used in the climate community (e.g. Limpasuvan *et al.* (2004)). The EOFs are then computed using the singular value decomposition (SVD) approach, described in section 2.6 of Press *et al.* (1992). This technique decomposes the original data matrix into a column orthogonal matrix of eigenvectors (the EOFs), and a diagonal matrix of singular values, which are the eigenvalues.

The only important characteristic of the EOFs is the spatial pattern of variance that they represent, the signs and units of the EOFs being totally arbitrary. As shown in Figure 5.2 (top), the leading EOF

[1] Model documentation and further reference are available at http://icmc.ipsl.fr

[2] All anomalies in this study are deviations from the daily climatological seasonal cycle calculated from the 1000-year simulation.

structure of the zonal-mean zonal wind anomalies at 10 hPa represents a dipole pattern with a reversal of sign at about 40°N. The sign and amplitude of the pattern as a function of time are then given by the PC associated with the corresponding EOF, and which is obtained by projecting the weighted data anomaly onto the leading EOF. The leading PC time series explains about 62% of the total variance in the 10 hPa zonal-mean zonal wind field (the percent variance being given by the squared eignevalue corresponding to the leading PC/EOF), and negative values correspond to weaker than normal westerlies poleward of 40°N.

The same EOF analysis was performed in Limpasuvan *et al.* (2004) at 10 hPa and 50 hPa, and it was found that the results were reasonably insensitive to the stratospheric level, although at 10 hPa the leading PC/EOF was not as clearly separated from the higher modes as was the case at 50 hPa.

The occurrence of a SSW event is determined from the amplitude of the PC time series, low-pass filtered with a 15-day boxcar average. The onset date of a SSW event is defined when the low-pass PC drops more than one standard deviation below its climatological mean ($-\sigma$), and the decay date is when the low-pass PC rises again above $-\sigma$. Here, $-\sigma \simeq 18.1\ m/s$. A SSW event (from onset to decay) must last at least 20 days, and two consecutive onset dates (within one year) must be separated by at least 120 days, to minimise the occurrence of overlapping periods preceding and following SSW events. Overall, 672 SSW events were detected based on the above criteria, which represents about 0.7 events per year (similar frequencies are found in the reanalyses - see for instance in Limpasuvan *et al.* (2004), Charlton and Polvani (2007), Taguchi (2008), Martius *et al.* (2009)). The onset dates associated with these events occur between mid October and end of April, with a maximum frequency in January (Fig. 5.2, bottom). Similar results were found in Lott *et al.* (2005) using a 20-year integration of the upward extended atmospheric-only LMDZ model. Only SSW events whose onset dates are between the 1^{st} of December to the 31^{st} of March are selected for this study, which reduces the number of SSW events to 480.

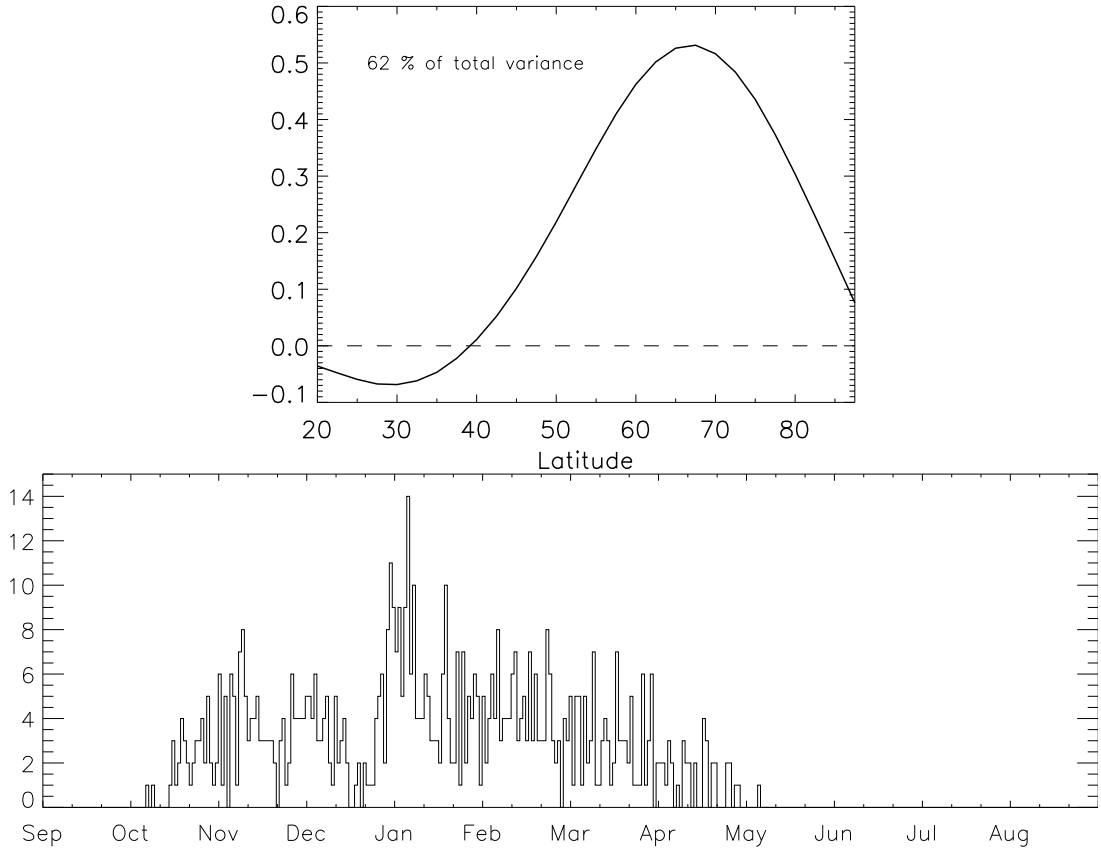

Figure 5.2: Top: The leading EOF structure of the zonal-mean zonal wind anomalies at 10 hPa. Bottom: Occurrence of the 672 SSW onset dates from 1 January 1800 to 31 December 2799, computed from the amplitude of the low-pass filtered PC time series.

5.3.2 Detection of tropospheric blocking

The blocking index BI_{stlat} has been calculated, following the methodology described in Chapter 3, at daily intervals during the extended winter (ONDJFMAM, October to May) season throughout the 1000 years of the PiControl simulation (1 October 1800 - 31 May 2799). The ONDJFMAM season is chosen because SSWs occurring in DJFM may be associated with tropospheric signals well before and after their onset dates. Here, the 2-month periods preceding and following the onset date of SSW events are inspected. The model output has been regridded (using bilinear interpolation) to 2.5° resolution, and the blocking index is calculated at each longitude and time step across the whole Northern Hemisphere. The central latitude of blocking is taken as the latitude of the maximum storm track intensity (corresponding to the mean storm track latitude calculated for the individual months from October to May - Fig. 5.3). Note the annual cycle in the position of the storm track latitude in Figure 5.3, with higher latitudes in the autumn/spring months and lower latitudes in winter months, especially in the European sector, whereas in the Asian and western Pacific regions the storm track latitude tends to be higher in winter than in other months. In order to account for this annual variation, the blocking index is calculated at all latitudes with $\pm 7.5°$ of the storm track latitude. At each specific longitude and time step, a local and instantaneous blocking candidate is assigned to the central blocking latitude where the zonal wind reversal (Eq. 3.1) is the greatest.

In order to account for the annual cycle in the amplitude of atmospheric variability, the anomaly

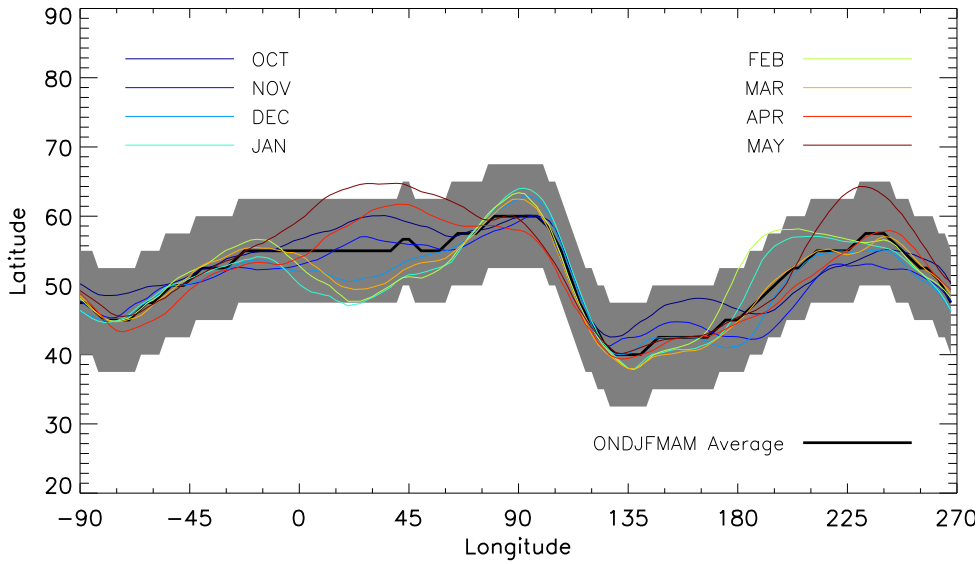

Figure 5.3: Monthly mean profiles of the latitude of the maximum storm track intensity as a function of longitude. The different colours of the curves correspond to the different months from October to May. The thick black curve corresponds to the ONDJFMAM mean profile, and is taken as the central blocking latitude. The blocking index is calculated at the central blocking latitude $\pm 7.5^{\circ}$ (grey shading).

threshold at the location of the blocking anticyclone ($0.8 \times \sigma\,(Z')$ in Eq. 3.3) is allowed to vary with the month of the year by calculating the standard deviation (σ) from the 3-month daily anomaly distribution centered in the given month. Finally, a large-scale blocking episode is defined when a local and instantaneous blocking candidate spans at least 15° longitude and persists for at least 5 days.

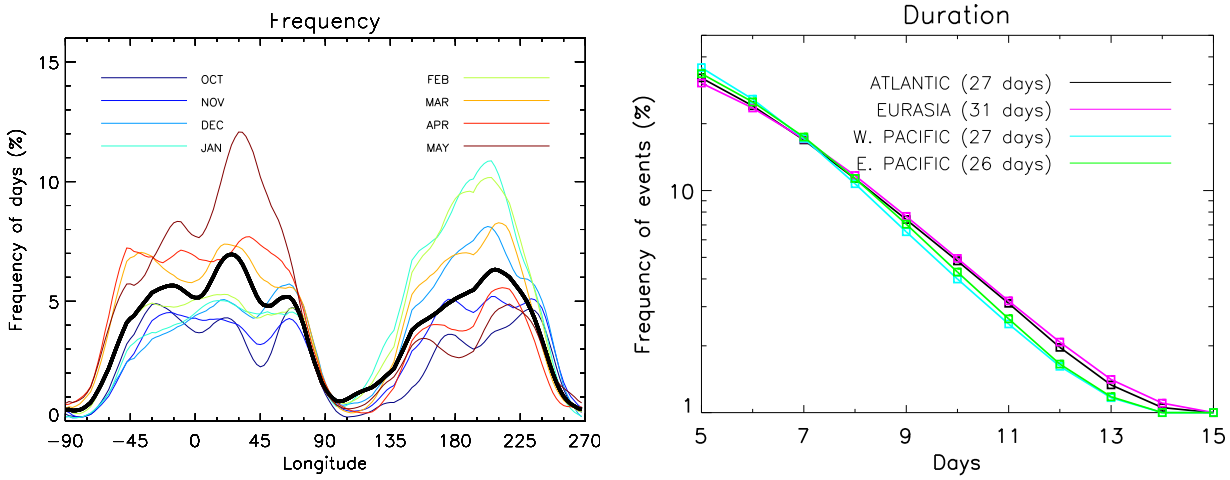

Figure 5.4: (left) Frequency of all days that are part of large-scale blocking episodes as a function of longitude, for the ONDJFMAM period (thick black line). Monthly mean frequencies are displayed by the different colours, as explained in the legend. (right) The average frequency of large-scale blocking episodes (at least 5 days duration) as a function of their duration (days) for the Atlantic, Eurasian, western and eastern Pacific sectors. The maximum episode duration in each sector is indicated in brackets.

For reference throughout this chapter, blocking frequency and duration have first been considered for the whole period of analysis during the ONDJFMAM season, and results are presented in Figure 5.4. The left panel illustrates the seasonal variability of Northern Hemisphere blocking frequency, with rising frequencies from a minimum in autumn to a sharp maximum in the late spring over the Euro-Atlantic

sector. In the Pacific region, there is a tendency for more frequent blocks in winter and early spring (December to March) than in the temperate months. These results are in agreement with the works of Rex (1950b) and D'Andrea *et al.* (1998), but differ to some extent from those presented in Pelly and Hoskins (2003), who found for instance a maximum blocking frequency in autumn over the Euro-Atlantic sector. It must be noticed that different blocking indices, analysis periods, types of datasets (i.e., reanalysis or model simulation), contribute to the differences between the results presented here and those from previous works. However, widely recognised blocking features identified in the literature arise from the overall shape of the blocking distribution, presented in Figure 5.4 (e.g., geographical location, longer-lasting Euro-Atlantic than Pacific blocks). Note that a substantial amount of blocking episodes are also identified in the western Pacific region (between 135°E and 195°E). According to the results presented in Chapter 4, an enhanced blocking activity in the western Pacific sector could be related to model systematic errors in the amplitude of the high-frequency variability (e.g., for BCM2 and HADGEM).

The dependence between the seasonal variability of blocking activity and SSWs will be analysed in Section 5.5 on the basis of different blocking features between periods preceding and following warming events. The procedure to quantify the occurrence and persistence of blocking over different SSW-related periods will be described in Sections 5.5.1 and 5.5.2. In the remaining discussions throughout this chapter, periods preceding and following the onset date of SSW events are referred to as PRE-SSW and POST-SSW periods, respectively.

5.4 Temporal evolution of stratospheric sudden warming events

In this section, the temporal evolution of various atmospheric fields, composited for the 480 SSW events, is described. The fields analysed are the zonal-mean zonal wind anomalies (Fig. 5.5), and the large-scale planetary waves in geopotential height (Fig. 5.6). All fields are averaged between 45°N and 75°N, as it is the latitudinal band of interest for blocking and other midlatitude tropospheric disturbances that are potentially linked with stratospheric variability. Other stratospheric-based studies carried analyses within that range (Polvani and Waugh, 2004; Taguchi, 2008), at single latitude circles between 60°N and 85°N (Limpasuvan *et al.*, 2004) or at all latitude circles averaged above 50°N (Limpasuvan *et al.*, 2004).

5.4.1 Zonal wind

The evolution of the anomalous zonal-mean zonal wind, composited for the 480 SSW events, is described. An average height profile of the zonal wind anomalies is calculated for each calendar day, spanning the 80-day PRE-SSW to the 80-day POST-SSW period, and is presented in Figure 5.5, where the time axis is shifted with respect to the onset dates of the SSWs. Due to the uneven temporal clustering of SSW events (Fig. 5.2, bottom), it is essential to remove the annual cycle of zonal wind before constructing this composite.

It exhibits a similar picture to that previously reported (Andrews *et al.*, 1987; Limpasuvan *et al.*, 2004), with a rapid weakening of the stratospheric zonal-mean zonal winds propagating down to the troposphere, where anomalous easterly winds then persist for up to two months. The rapid breakdown of the stratospheric zonal flow is preceded by anomalously strong westerlies, and is followed by the gradual

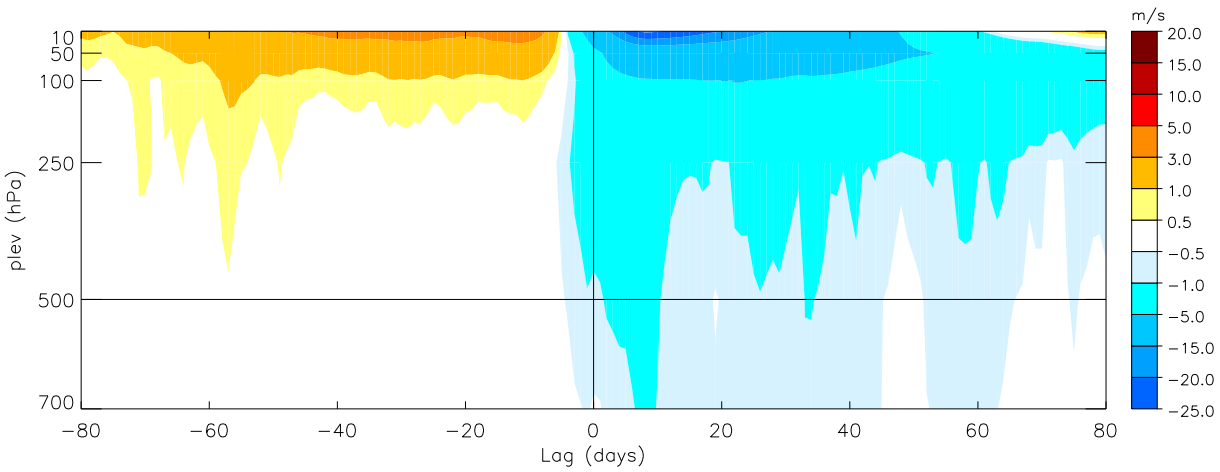

Figure 5.5: Temporal evolution of the zonal-mean zonal wind anomalies as a function of height (in pressure level), averaged between 45°N and 75°N. The horizontal (time) axis is shifted with respect to the onset date of each of the 480 SSW events (lag = 0 days), and then the wind anomalies are averaged across all 480 events (aligned so that SSW onset is always at lag = 0 days).

recovery of the stratospheric polar vortex. In that sense, the SSWs are embedded in a low-frequency variability cycle (e.g., the Polar Night Jet Oscillation (Kuroda and Kodera, 2001)), which assists in the preconditioning of the stratospheric zonal flow and the slow recovery of the polar vortex (Limpasuvan *et al.*, 2004). The preconditioning of the polar vortex being initiated either by a precursor planetary wave (McIntyre, 1982), or as a result of the low-frequency stratospheric vacillation cycle, in which zonal flow anomalies oscillate meridionally and vertically on a time-scale of several months (Holton and Mass, 1976).

The time-scale at which anomalous easterly winds propagate between the 10 hPa and 500 hPa atmospheric levels is about 5 days, so that at lag = 0 days easterly anomalies have reached the 500-hPa tropospheric level (the level at which blocking events are identified in this study). Recall from Section 5.3.1 that the onset date is defined when the low-pass PC drops at least one standard deviation below its climatological mean, so lower amplitude anomalies at 10 hPa should be observed a few days before (when the low-pass PC drops below 0).

It is well established from previous discussions throughout this thesis that weak mid-tropospheric westerly winds provide favourable conditions for the formation of blocking events. This is also supported by a large number of studies. For instance, Thompson and Wallace (2001) found more frequent blocking days over the Pacific and north Atlantic/Eurasian regions in the negative phase of the Northern Annular Mode (NAM), when high-latitude westerly winds are weaker than normal. Therefore it is reasonable to assume that the downward propagation of easterly wind anomalies seen in Figure 5.5 may have an impact on blocking activity. Following Thompson and Wallace (2001)'s results, blocking days are expected to be more frequent once SSW events initiate.

5.4.2 Planetary height waves

Next the evolution of the large-scale planetary height waves as a function of longitude and time at 10, 100 and 500 hPa is considered in Figure 5.6 to diagnose the existence of major wave disturbances through the atmosphere that could possibly be linked with blocking.

Fourier Analysis

The Fourier analysis of the geopotential height field $Z(\lambda, \phi, t)$ (hereafter, Z), performed in this study, is the decomposition of Z (averaged across the range of latitudes ϕ between 45°N and 75°N) into a sum of discrete harmonics (here, zonal wavenumbers), as:

$$Z = \overline{Z} + \sum_{n=1}^{N/2} Z_n cos\left(\frac{2\pi n\lambda}{N} - \lambda_n\right) \tag{5.1}$$

The overline represents the zonal mean at each time t, and each zonal wavenumber n is defined by its amplitude Z_n and phase λ_n at time t. The quantity $\frac{2\pi n}{N}$ is the angular frequency of the wave executing, n full cycles within the range (0, 2π) as the zonal index (longitude) varies from 0 to n (Wilks, 1995). Here, the original data is reconstructed by only retaining the individual wavenumbers $n = 1$ or $n = 2$ (denoted hereafter by PW 1 or PW 2, respectively), or the sum of $n = 1, 2, 3$ (denoted hereafter by PW 1..3). Note that PW 3 alone is not considered in order to show that its contribution in PW 1..3 is fairly minor compared to PW 1 and PW 2.

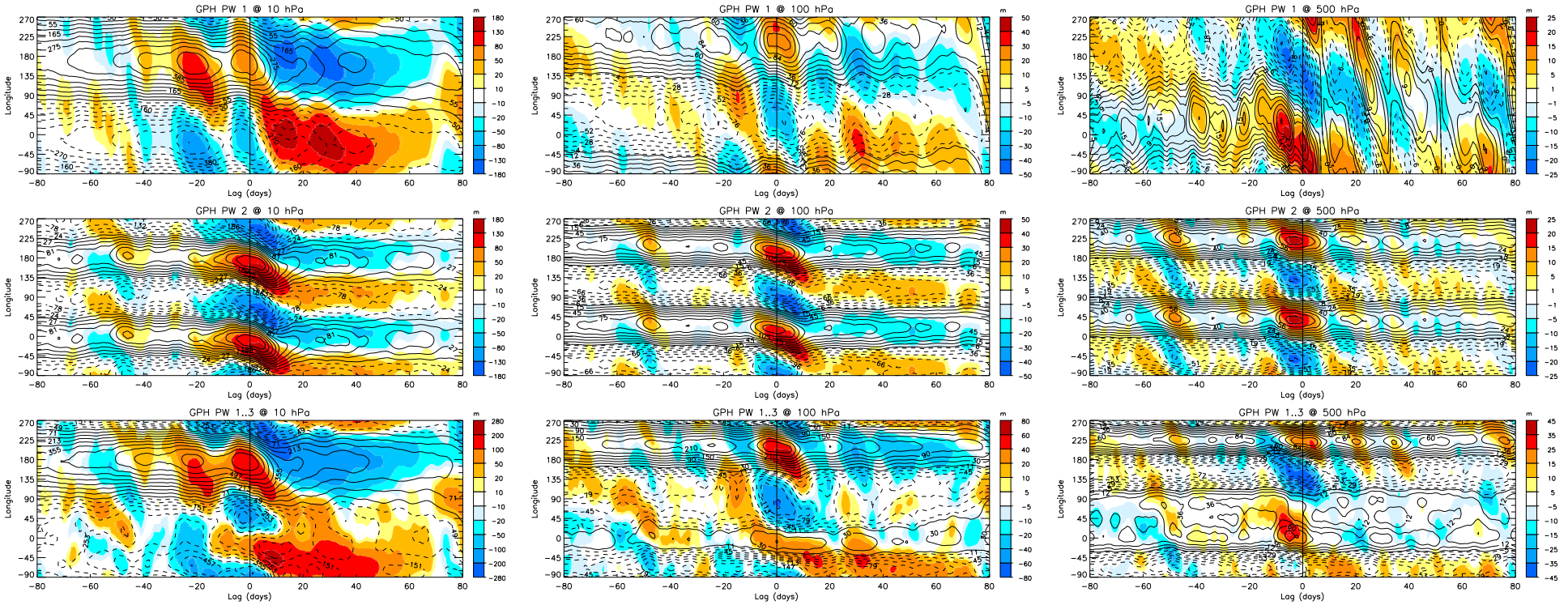

Figure 5.6: Temporal evolution of the planetary height waves PW 1, PW 2 and PW 1..3, at 10, 100 and 500 hPa as a function of longitude, averaged between 45°N and 75°N. The horizontal (time) axis is shifted with respect the the onset dates of the 480 SSW events (lag = 0 days). Labeled black contours represent the full field; positive (negative) values are solid (dashed). Shaded areas are anomalies from the annual cycle. The structure displayed for PW 1..3 compared with the individual PW 1 and PW 2, suggests that the contribution of PW 3 is fairly small.

General structure of the wave composites

The wave composites in Figure 5.6 exhibit the same structure previously reported in three cases studies (Naujokat *et al.*, 2002) and in the ERA-40 reanalysis dataset (Martius *et al.*, 2009), with PW 1 tilting westward with height by nearly 180° between 10 hPa and 500 hPa, and PW 2 exhibiting a more barotropic structure with a phase shift of approximately 45°. In their composite analysis, Martius *et al.* (2009) differentiated vortex displacement from vortex splitting SSW events, and they found that PW 2 tilts westward with height by approximately 90° for the displacement composite and 45° in the case of vortex splits. Another typical feature is the amplification of waves with height prior and during SSW events, which was found to be very strong for PWs 1 and 2 during splitting events, but nearly absent for PW 2 during displacement events (Martius *et al.*, 2009). Similar results were reported in Charlton and Polvani (2007), showing that strong wave activity preceded splitting events but not displacement events. Further results showed that for vortex splits the amplitude of PW 2 is larger up to 100 hPa, while PW 1 exceeds it above that height (Martius *et al.*, 2009). Figure 5.6 shows the same features observed during splitting events, with strong amplification for both PWs 1 and 2, PW 2 being larger below 100 hPa and lower above that level. It could therefore be assumed that the warming events considered in this study are mainly composed of vortex splits, with both PW 1 and 2 substantially contributing to the existence of these events. Of course, this assumption is only speculative, and it is beyond the scope of this thesis to differentiate displacement from splitting events.

Link between planetary scale waves and blocking

The importance of the geographical location of tropospheric blocking relative to planetary height waves was demonstrated in Martius *et al.* (2009), and is used in this present study to infer a possible link between both phenomena at 500 hPa.

The strongest wave amplification (refer to PW 1..3 in Figure 5.6) in the Pacific region seems to be colocated with the climatological Aleutian low (between 120°E and 195°E - see in Figure B.2) and Pacific ridge (between 195°E and 255°E, Fig. B.2) at that level. About 10 days before the warmings initiate, only PW 2 contributes to the amplification of the Pacific planetary ridge, where eastern Pacific blocks are usually observed. However, in the period following the warming, amplification of PW 1 seems to be the main contribution to the positive Pacific wave signal, PW 2 amplification being fairly short-lasting. Therefore, an increase in the occurrence of eastern Pacific blocks in association with PW 2 amplification a few days preceding the warming could be expected, while a more persistent impact in association with PW 1 would be observed in the period following the onset of SSWs.

Over the western Pacific sector, the contribution from PWs 1 and 2 is the same as over the east Pacific region, except that, with their inverted phase, they contribute to the strengthening of the Aleutian low (between 120°E and 195°E), and could therefore be associated with a decrease in the occurrence of western Pacific blocks.

In the Euro-Atlantic region (between 90°W and 90°E), the main signal in the global wave composite (PW 1..3) prior to the SSW onset date, seems to arise from the amplification of the planetary ridge over the Eurasian sector only (between 30°W and 90°E), with contributions from both PWs 1 and 2. However, once the warmings initiate PW 1 is the main source of wave disturbances over the Atlantic basin (between 90°W and 30°W), where (1) the amplitude of the negative height anomaly, presumably associated with the Icelandic low, decreases, and (2) the amplitude of the Eurasian planetary wave decreases

as well. In the period preceding the warming, amplification of both PWs 1 and 2 over the Eurasian region may be associated with an enhanced occurrence of blocked days over that sector. Whereas in the period following the warming, the PW 1 contribution to decrease the amplitude of the negative height signal over the Atlantic region, and also, but at a lesser extent, the amplitude of the positive signal over the Eurasian sector, might provide more (less) favourable conditions for blocking development over the Atlantic (Eurasian) regions.

5.4.3 Hypotheses

Overall, this analysis identifies a plausible link between SSW events and blocking activity, according to which:

1. **In the period preceding the warming**, an amplification of PW 2 over the eastern Pacific region could be associated with an increased occurrence of blocking days over that sector, about 10 days prior to the warmings. However, it could be assumed that the Eurasian region would be the most affected, since a stronger amplification of the Eurasian planetary ridge takes place about 20 days prior the warmings, due to the contribution of both PWs 1 and 2. The western Pacific sector could, however, exhibit a reduced blocking frequency, with the contribution from both PWs 1 and 2.

2. **In the period following the warming**, the amplification and westward travelling of PW 1 is the main contribution to the global wave disturbances. This might be associated with an increased occurrence of blocking events in the Atlantic, and at a lesser extent in the eastern Pacific sector, whereas a slight decrease in blocking activity might be observed in the Eurasian and western Pacific regions. However, the downward propagation of the zonal wind anomalies could also contribute to perturb the blocking activity, increasing the occurrence of blocking days in either or all sectors.

5.5 SSW-related tropospheric blocking climatology

The aim of this section is to study the frequency and temporal persistence of atmospheric blocking throughout the Northern Hemisphere, and to look for evidence that these blocking characteristics vary depending on the period when they occur with respect to the onset date of SSW events.

5.5.1 Frequency of blocking days

Here the anomalous frequency of blocking days as a function of time and longitude, composited for the 480 SSW events, is described. For this to be done, an average longitudinal profile of the anomalous frequency of blocking days is calculated for each calendar day (i.e., with the annual cycle removed), spanning the 60-day PRE-SSW to the 60-day POST-SSW period, and is shifted with respect the the onset date of each of the SSWs (at lag = 0 days). A Hovmöller representation of anomalous blocking frequency spanning all longitudes can be seen in Figure 5.7. For reference, a similar Hovmöller representation is also presented in Figure 5.8 for the annual cycle (top) and the full field (bottom) of blocking frequency.

Acknowledging the fact that the winter months (i.e., December, January, February) are centered around lag = 0 days (since SSWs mostly occur in January; see in Figure 5.2), and therefore that the autumn (spring) months correspond most often to periods closer to lag = -60 days (lag = +60 days), we

could make an analogy between the annual cycle in Figure 5.8 (top) and Figure 5.4 (left), by observing that Euro-Atlantic blocks are the most frequent in spring (approximately between lag = +40 days and lag = +60 days), and that the blocking frequency in the Pacific region is the highest during winter (approximately between lag = -40 days and lag = +30 days). When the full field in blocking frequency is considered (Fig. 5.8, bottom panel), it can be noticed that SSWs influence the frequency of blocking days in both the Euro-Atlantic and Pacific sectors and at different time lags. In order to quantitatively estimate the anomalies in blocking frequency due solely to the influence of SSW events (Fig. 5.7), it is essential to remove the annual cycle of blocking frequency. The results presented in Figure 5.7 are now described in more details.

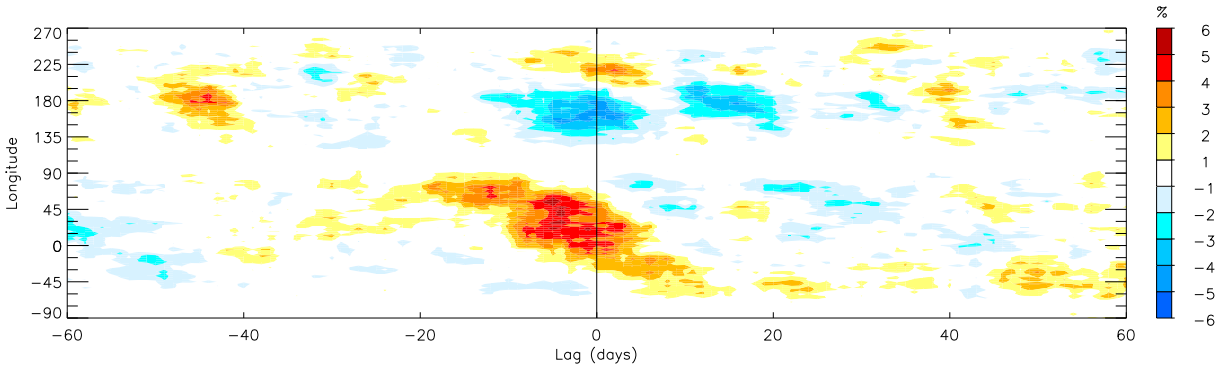

Figure 5.7: Temporal evolution of the anomalous frequency of all days within the extended winter season (OND-JFMAM) that are part of large-scale blocking episodes (at least 5-day duration) as a function of longitude. The horizontal (time) axis is shifted with respect to the onset dates of the SSW events (lag = 0 days). The anomalous blocking frequency is the deviation from the daily climatological seasonal cycle, composited for all 480 SSW events. Note that anomalies in blocking frequency beyond lag_{-60} and lag_{+60} days cannot be displayed, since the detection of blocking events from October to May only allows a 2-month window on either side of the SSW onset dates (i.e., from lag_{-60} to lag_{+60} days).

The eastern parts of the north Atlantic (45°W-0°) and Eurasia (0°-90°E), as well as north Pacific (135°E-255°E) basins emerge clearly as regions where the anomalies in blocking frequency acquires their highest values (Fig. 5.7). As it was previously shown in Section 5.3.2, these regions are where blocking events are the most abundant on the climatological timescale (see also Figures 5.4, left and 5.8).

An enhanced frequency of blocking days over the Euro-Atlantic sector is observed within the 40-day window period centered around the SSW onset dates (i.e., spanning approximately the 20-day PRE-SSW to the 20-day POST-SSW period). In general, the evolution of Euro-Atlantic blocks roughly coincides with periods of amplifying PW 1 and 2 (Fig. 5.6), which exhibit a slight wavenumber 1 amplification (up to 10 m) within the 40-to-10 day window preceding the warmings, and an abrupt and simultaneous increase (up to 25 m) in the amplitude of PWs 1 and 2 from 10 days before onset up to about 5 days after the onset date of the SSWs. Between lag_{+5} and lag_{+20}, PW 1 displaces over the Atlantic region, and PW 2 weakens, with a simultaneous longitudinal displacement of positive blocking frequency anomalies over the Atlantic basin, while the Eurasian region suffers a reduced frequency. The influence of PW amplification seems to persist beyond the 20-day POST-SSW period over the Atlantic region (although at a lesser extent), as positive anomalies in blocking frequency are observed up to lag_{+60}. These results support both hypotheses stated in Section 5.4.3, and provide further evidence that amplifying PWs may be associated with enhanced blocking activity over the Euro-Atlantic region before and after the onset of

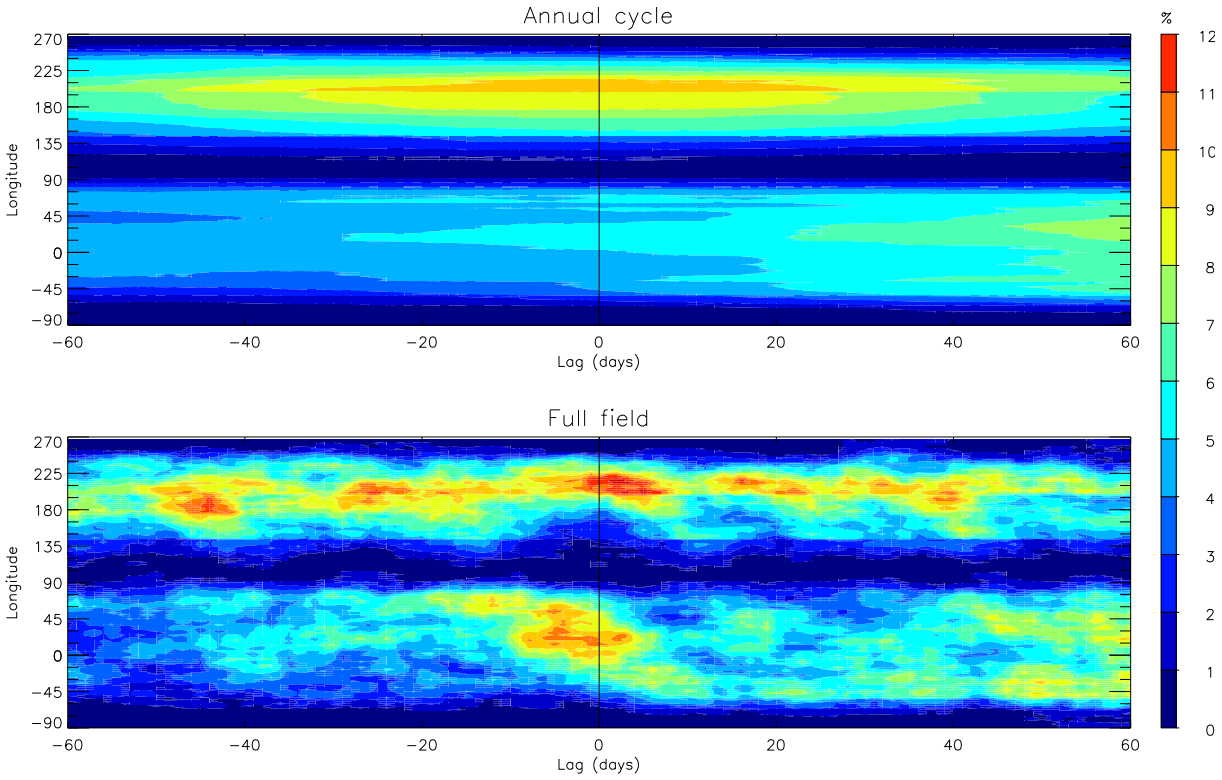

Figure 5.8: Same as Figure 5.7, but for the annual cycle (top) and the full field (bottom) of blocking frequency.

SSWs.

The tendency in the Pacific sector is a reduced frequency of blocking days over the western part of the region (135°E-195°E) spanning approximately the 15-day PRE-SSW to the 20-day POST-SSW period, and an enhanced frequency over eastern Pacific (195°E-255°E) within the 20-day window centered around the SSW onset dates. The evolution of blocking activity in this region coincides as well with periods of amplifying and decaying PW 1 and 2 (Fig. 5.6), with some resemblance to the structure of PW 2 amplification at about 45 days before onset, a strong decay in the amplitude of PW 1 between lag_{-20} and lag_{+20} over the whole Pacific region, and in PW 2 over the western part between lag_{-10} and lag_{+10}, while an amplification of PW 2 is observed over the east Pacific sector. As in the Euro-Atlantic region, these results support the existence of a link between blocking frequency and PW amplitudes over the Pacific region.

5.5.2 Seasonal variability

A further analysis is now performed in order to analyse the influence of SSWs on the seasonal cycle of blocking activity, seen in Figure 5.4 (left panel). For that purpose, the frequency and persistence of blocking are computed in four different pre-defined periods (as illustrated in Figure 5.9) during SSW years only: PRE-IN and POST-IN (denoting the 40-day periods preceding and following, respectively, the onset date of SSW events), and PRE-OUT and POST-OUT (being all the remaining days before and after the PRE-IN and POST-IN periods, respectively). More generally, the periods containing all days that precede or follow the onset date of SSW events are referred to as PRE-SSW and POST-SSW, respectively. This analysis must ensure that relatively large periods are defined in order to not exclude long-lasting blocking episodes (i.e., 40 days was judged to be the minimum with respect to the climatological

values - see Figure 5.4, right panel). Recall that 480 SSW events from 1 December to 31 March are selected for this study, so the number of days in each of the PRE-/POST-IN periods is $40 \times 480 = 19200$. The total number of days in PRE-/POST-OUT is 37462/40778.

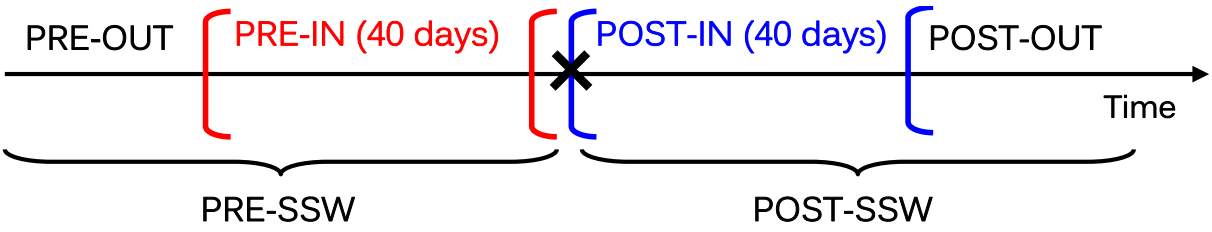

Figure 5.9: Schematic representation of the four pre-defined periods in which blocking events are regarded to occur: PRE-IN (time lag = -40 to -1 days, in red), POST-IN (time lag = 0 to +39 days, in blue), PRE-OUT (all days before lag_{-40}) and POST-OUT (all days after lag_{+39}) periods, with respect to the onset date of SSW events (black cross).

SSWs are most frequent in January (Fig. 5.2) and the 40-day periods preceding and following the onset date of SSW events that are regarded as the PRE-IN and POST-IN periods, respectively, are more likely to be analysed in December, January and February (DJF). Therefore, PRE-OUT (POST-OUT) would correspond most often to October and November (March, April and May), and the differences in blocking features between those periods (if significant), would be representative of the influence of SSWs on the seasonal cycle of blocking activity.

In order to quantify the influence of the annual cycle on the results, a Monte Carlo test is performed, whereby blocking frequencies are computed within each of the four pre-defined periods, with respect to the same SSW onset dates, but using 480 years randomly selected from the 520 years without any SSW events. The same analysis is performed 100 times, from which a 95% confidence interval is constructed (for each of the four pre-defined periods). If SSWs have any relationship with blocking variability then the "real results" will lie outside the confidence interval of the 100 random results drawn from years without SSWs.

Results are presented in Figures 5.10 and 5.11, where the solid (dashed) lines are the blocking frequency (Fig. 5.10) and duration (Fig. 5.11) in the "real" SSW-related PRE-/POST-IN (PRE-/POST-OUT) periods. The magenta (cyan) areas are the 95% confidence interval for the "random" SSW-related PRE-/POST-IN (PRE-/POST-OUT) periods.

Blocking frequency

Results presented in Figure 5.10 are consistent with those of Figure 5.7, with an enhanced frequency of blocking days over the Eurasian (Atlantic) in PRE-IN (POST-IN), and a tendency for a reduced frequency of western Pacific blocks in those two periods (compare the solid lines and magenta areas in the PRE- and POST-SSW panels). Note that, although the changes in blocking frequency between the "real" and "random" cases seem to be small, they are significant at the 95% confidence level. In addition, it is worth recalling that these results are drawn from a 1000-year simulation, so they are smoothed by the diversity of the tropospheric responses to stratospheric disturbances, and therefore are even more robust than if they were drawn from a smaller sample size dataset.

In the PRE-/POST-OUT periods, the frequency of blocking is not significantly affected by SSW events, as the "real" SSW-related blocking frequencies lie within the confidence intervals (compare the

dashed lines and the cyan areas). In the POST-OUT period, there are occasional longitudes in the Atlantic and central Pacific sectors where the SSW-related frequency is slightly (but significantly) different from the "random" POST-OUT period, suggesting that the influence of SSWs tends to persist longer than 40 days, as it is observed in Figure 5.7 and reported in other studies (e.g., Thompson *et al.* (2002)). Nevertheless, most of the significant SSW-related signal is within the PRE-/POST-IN periods (presumably spanning the 20-day PRE-SSW to the 20-day POST-SSW period according to Figure 5.7). Overall those results suggest that the seasonal cycle of blocking frequency is significantly related to stratospheric flow disturbances over the Euro-Atlantic and west Pacific regions, where wintertime blocking frequency is enhanced (reduced) in the former (latter) in years when SSW events occur. No significant relationship is found in autumn and spring.

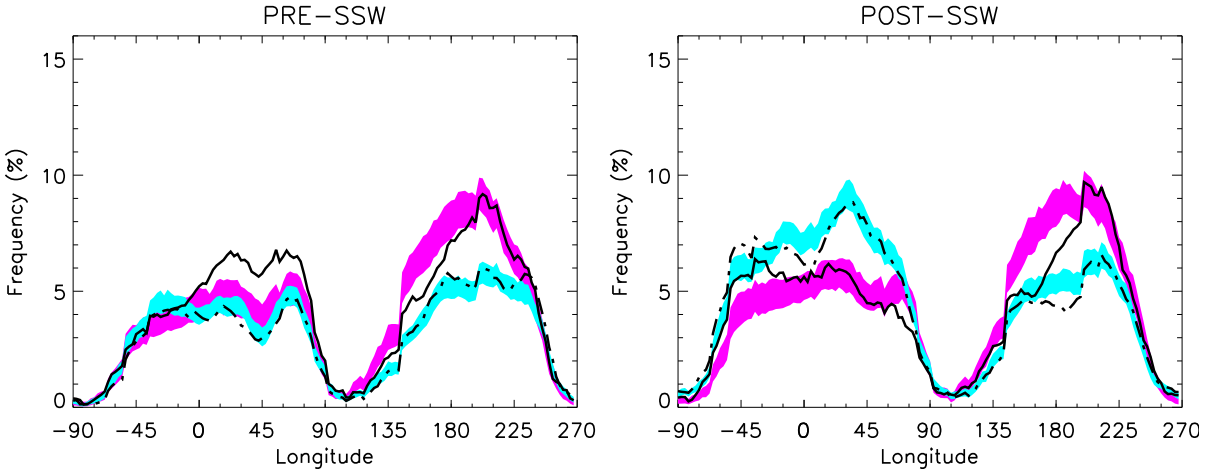

Figure 5.10: Frequency of all days that are part of large-scale blocking episodes, as a function of longitude. Frequencies in the periods preceding the warmings (PRE-SSW) are displayed in the left panels, and frequencies following the warmings (POST-SSW) are displayed in the right panels. The solid (dashed) black lines represent the "real" PRE-/POST-IN (PRE-/POST-OUT) period and the magenta (cyan) are represent the 95% confidence interval of the PRE-/POST-IN (PRE-/POST-OUT) periods.

Blocking duration

The frequency of large-scale blocking episodes as a function of their duration in the Atlantic, Eurasian and Pacific sectors are presented in Figure 5.11, during the "real" PRE-/POST-IN and PRE-/POST-OUT periods (solid and dashed lines, respectively), and "random" PRE-/POST-IN and PRE-/POST-OUT periods (magenta and cyan areas, respectively), obtained with the similar Monte Carlo approach as explained previously (i.e., using the timing of the SSW onset dates, but with data from random years without SSW events).

In the PRE-SSW period, the increase in the total frequency of blocking days over the Eurasian sector (Fig. 5.10, left panel), is associated with a significant shift in the distribution of blocking lifetime toward longer blocks (compare the solid line and magenta area in Figure 5.11, left panel, 2^{nd} row). This does not seem to be the case when the stratospheric signals propagate downward, increasing the frequency of blocking days in the POST-IN period over the Atlantic sector (Fig. 5.7 and 5.10, right panel), as the frequency of long-lasting blocking episodes (above 11-day duration) tends to decrease with respect to the POST-OUT period, although the results are not significant at the 95% level (Fig. 5.11, right panel, 1^{st} row). In the west Pacific sector, blocking tend to be less frequent in POST-IN (and at a lesser extent in PRE-IN) than in POST-OUT (and PRE-OUT) (Fig.5.10), and this decrease seems to be related to a shift

toward shorter blocks (with higher significance in the POST-SSW period in Figure 5.11, right panel, 3^{rd} row).

There are cases where the total frequency of blocked days is not significantly affected by the presence of SSW events, but the distribution of blocking lifetime is. In the Atlantic region, for instance, the frequency of PRE-OUT blocking episodes lasting between 7 and 13 days increases significantly (the dashed line lying outside the 95% confidence interval in Figure 5.11, left panel, 1^{st} row). Similarly over Eurasia, the distribution of POST-IN/OUT blocking episodes tends to be shifted toward shorter blocks (Fig. 5.11, right panel, 2^{nd} row), while no significant changes are found for the total frequency of blocking days (Fig. 5.10, right panel).

Overall it can be noticed that an increased (decreased) frequency of blocking days before the onset of SSWs seems to be associated with a shift in the distribution of blocking lifetime toward longer (shorter) blocks (i.e., for PRE-IN in Eurasia, west Pacific). However, when the frequency of days is not affected by SSWs, the frequency of long-lasting blocking episodes tend to be at the upper limit (or even above) the significance level (i.e., for PRE-IN/OUT in Atlantic, PRE-OUT in west Pacific - except in the eastern Pacific). This does not seem to be the case in the POST-SSW periods, as whether the frequency of blocking days is significantly affected by SSWs or not, there is a tendency for less frequent long-lasting blocking episodes in all regions (i.e., the frequencies of long-lasting blocking episodes lie at the lower limit or below the 95% confidence interval in Figure 5.11, right panels).

An attempt to explain this latter result is given by considering each contribution from large to smaller-scale waves within periods preceding and following the onset date of SSWs. For that purpose, the root mean squared (hereafter, RMS) PW anomalies, averaged over all longitudes, are computed for each calendar day, spanning the 60-day PRE-SSW to the 60-day POST-SSW period. Results are displayed in Figure 5.12 for PW 1 (top), PW 2 (middle) and the sum of PWs 3 to 6 (bottom). By taking the RMS of PW anomalies (as represented in Figure 5.6), the amplitude only (not the phase) of PW anomalies are being considered. In that way, the strength of the main wave disturbances related to the life cycle of SSWs are clearly quantifiable. The results in Figure 5.12 show that the first major change in wave amplitude for large- and small-scale disturbances is about 20 days before onset, with an average increase in the RMS PW anomalies of about 6 m for PW 1, 4 m for PW 2 and 3 m for PW 3+. Relatively high PW anomalies persist for about 40 days, up to lag = +20 days. This period is then followed by a progressive weakening of PW 1 anomalies, while a more abrupt decrease is observed for PW 2 anomalies, so that between lag = +20-25 days and lag = +60 days the average strength of the large-scale PW anomalies returns to similar values as in the period preceding the amplitude increase at lag = -20 days. However, the amplitude of smaller-scale disturbances remains large even after lag = +20 days (compared to the period preceding lag = -20 days). As a result, the contribution of small-scale disturbances to the global wave signal is higher in the POST-SSW (after lag = +20 days) than in the PRE-SSW (before lag = -20 days) period, as large-scale PW anomalies recover more rapidly to the breakdown of the stratospheric polar vortex.

It seems therefore plausible that in periods preceding the onset SSWs a larger contribution from large-scale than small-scale waves could enhance the frequency of long-lasting blocking episodes. However, in POST-SSW periods, a rapid weakening of large-scale planetary wave anomalies (i.e., PWs 1 and 2) and an increased wave contribution from smaller-scale disturbances (i.e., PW 3), could explain the enhanced frequency of short-lasting blocking episodes at the expense of long-lasting blocks.

The main conclusion drawn from this analysis is that, in the LMDZ climate model, the relationship between stratospheric flow disturbances and the seasonal cycle of blocking is different to some extent for the frequency and duration of blocking. Generally speaking, the occurrence of SSWs enhances (inhibits) the wintertime blocking frequency in the Euro-Atlantic (west Pacific) sector, while it has no influence in autumn and spring. However, the proportion of long-lasting blocking episodes tend to be higher before SSW events than after, with in particular, a significant shift in the distribution of blocking lifetime toward longer wintertime Eurasian blocks in PRE-IN and shorter wintertime west Pacific blocks in POST-IN.

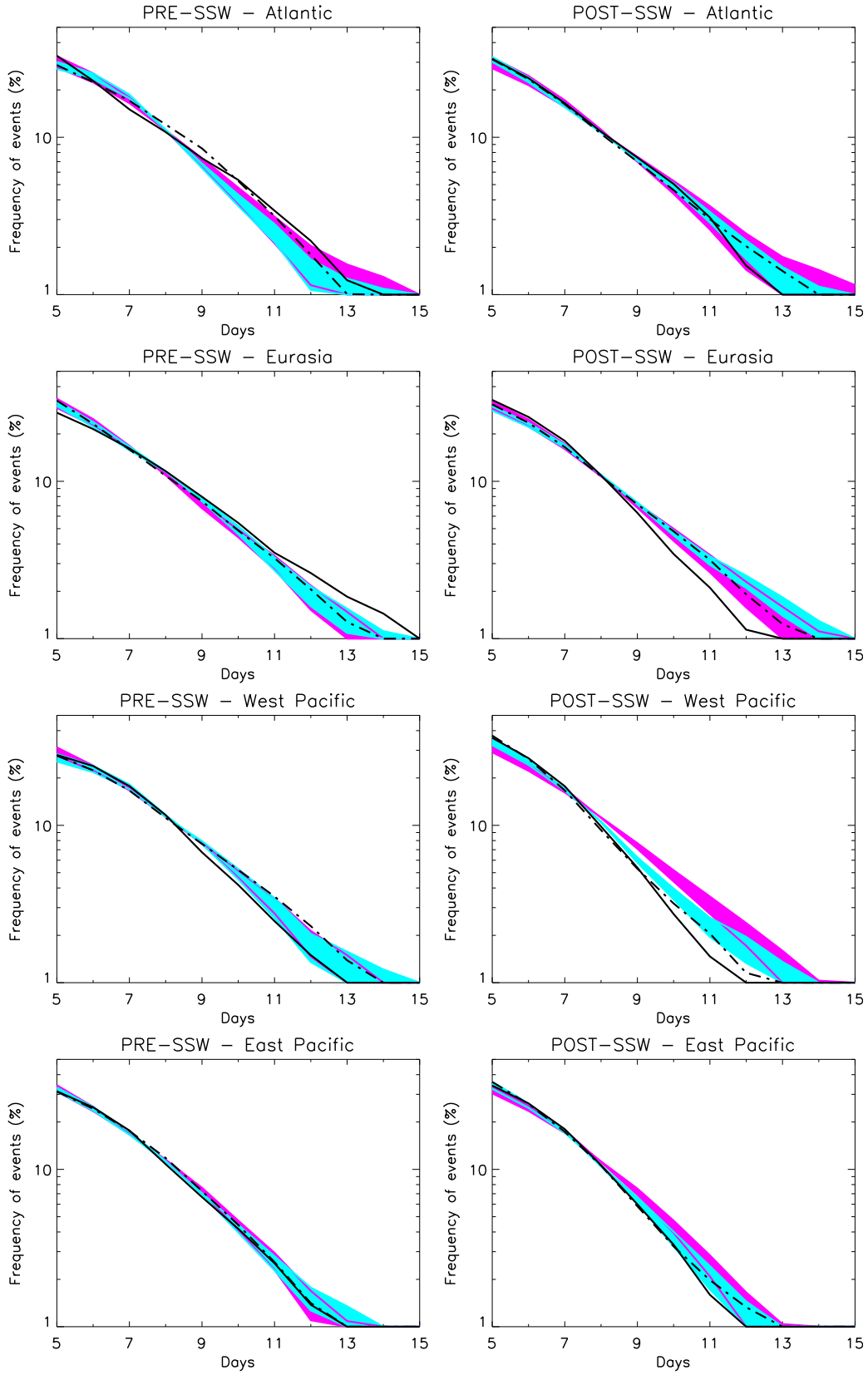

Figure 5.11: Blocking duration defined as the average frequency of large-scale blocking episodes as a function of duration (in days) for the Atlantic (75°W-0°, 1^{st} row), the Eurasian (0°-45°E, 2^{nd} row), the west Pacific (135°E-195°E, 3^{rd} row) and the east Pacific (195°E-255°E, 4^{th} row) sectors. Frequencies in the periods preceding the warmings (PRE-SSW) are displayed in the left panels, and the periods following the warmings (POST-SSW) are displayed in the right panels. The solid (dashed) black lines represent the "real" PRE-/POST-IN (PRE-/POST-OUT) period and the magenta (cyan) are represent the 95% confidence interval of the PRE-/POST-IN (PRE-/POST-OUT) periods.

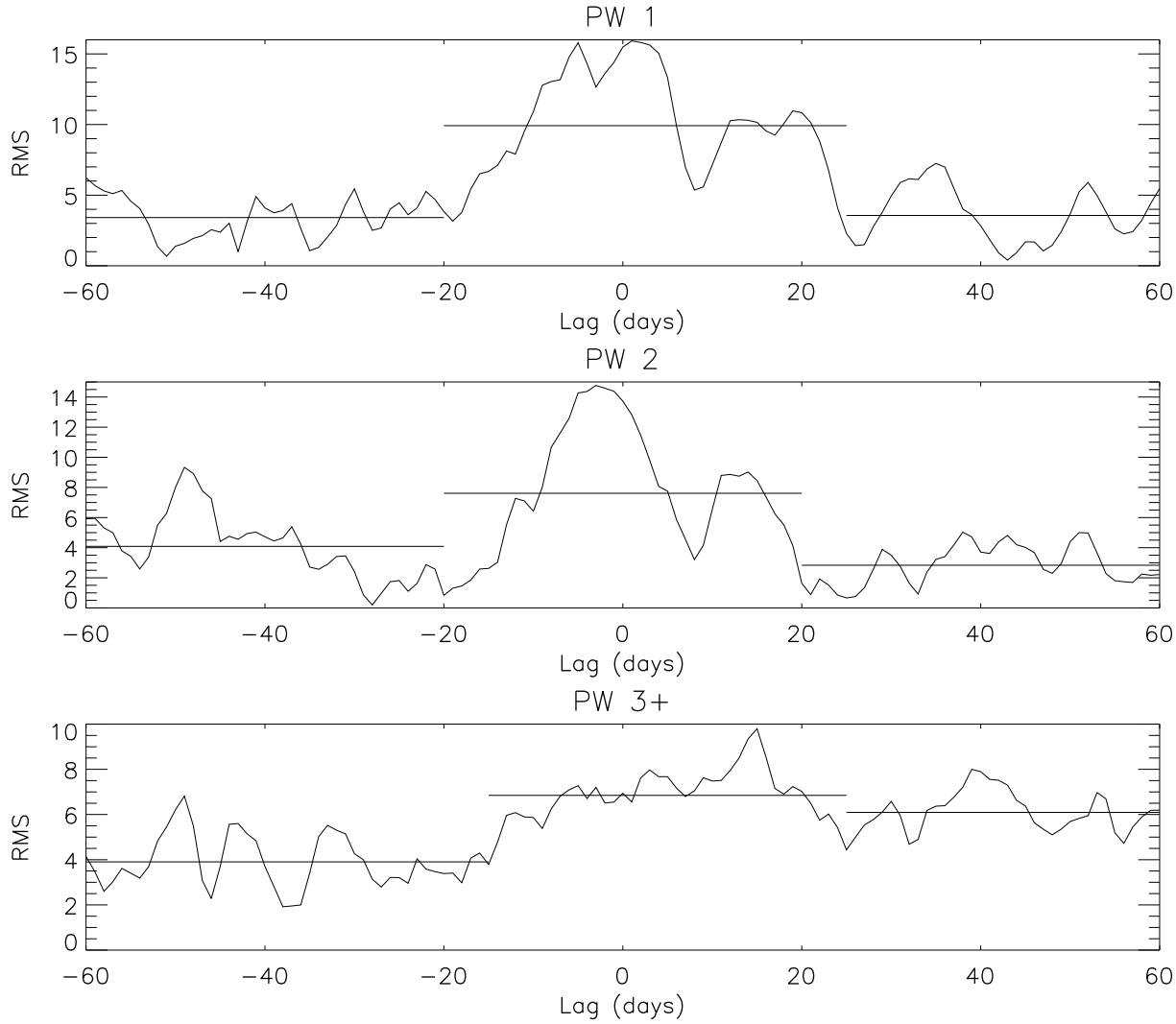

Figure 5.12: Root mean squared (RMS) PW anomalies averaged over all latitudes (between 45°N and 75°N) and all longitudes for each calendar day, spanning the 60-day PRE-SSW to the 60-day POST-SSW period for PW 1 (top), PW 2 (middle) and the sum of PWs 3 to 6 (bottom). The horizontal (time) axis is shifted with respect the the onset dates of the 480 SSW events (lag = 0 days). The horizontal lines represent the time averaged periods. $RMS_l = \frac{1}{N}\sum_{i=0}^{N}(pw_{i,l})^2$, where $pw_{i,l}$ represents the PW anomaly at a longitude i and lag l from lag = -60 days to lag = +60 days; units are in meters (m).

Synoptic description

Here the stratosphere-blocking link is examined in more details in order to synoptically describe how blocking may initiate, grow and displace in connection with planetary waves 1 and 2. For that purpose, 2-dimensional composite fields are constructed with respect to the onset date of SSW events (i.e., from lag_{-60} to lag_{+60} days). Figures 5.13 and 5.14 shows the 4-day average evolution of the 500 hPa daily height anomalies spanning the 60-day PRE-SSW to the 60-day POST-SSW period. This period is characterized by intense positive height anomalies over the Eurasian and east Pacific regions, roughly at the time and where blocking activity in those respective sectors is the strongest (Fig. 5.7). Therefore, the evolution of geopotential height anomalies will be taken as the base field to describe the evolution of those blocking events. In addition, anomalies in planetary waves 1 and 2, displayed in Figures 5.15 to 5.18 are used to qualitatively evaluate each contribution in the stratosphere-blocking variability.

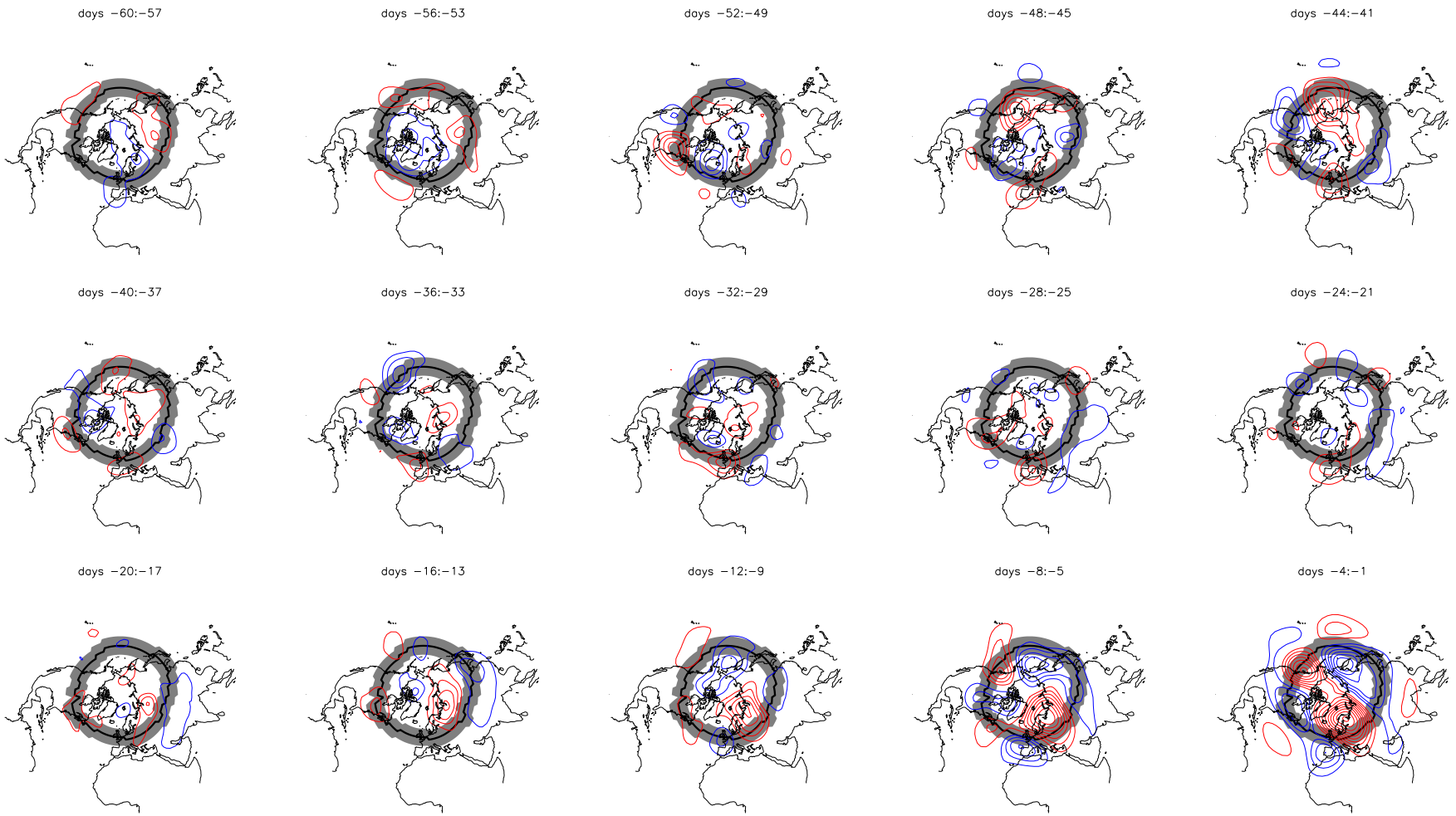

Figure 5.13: Figures 5.13 and 5.14: 4-day averaged daily geopotential height anomalies at 500 hPa spanning the 60-day PRE-SSW to the 60-day POST-SSW period. Positive height anomalies are displayed in red and negative anomalies in blue. Contours are drawn every 5 meters from -60 m to 60 m, but the zero contour is omitted. The solid black line is the central latitude of blocking, taken as the latitude of the maximum storm track intensity; the grey area represents $\pm 7.5^{\circ}$ around the storm track latitude allowed for blocking identification.

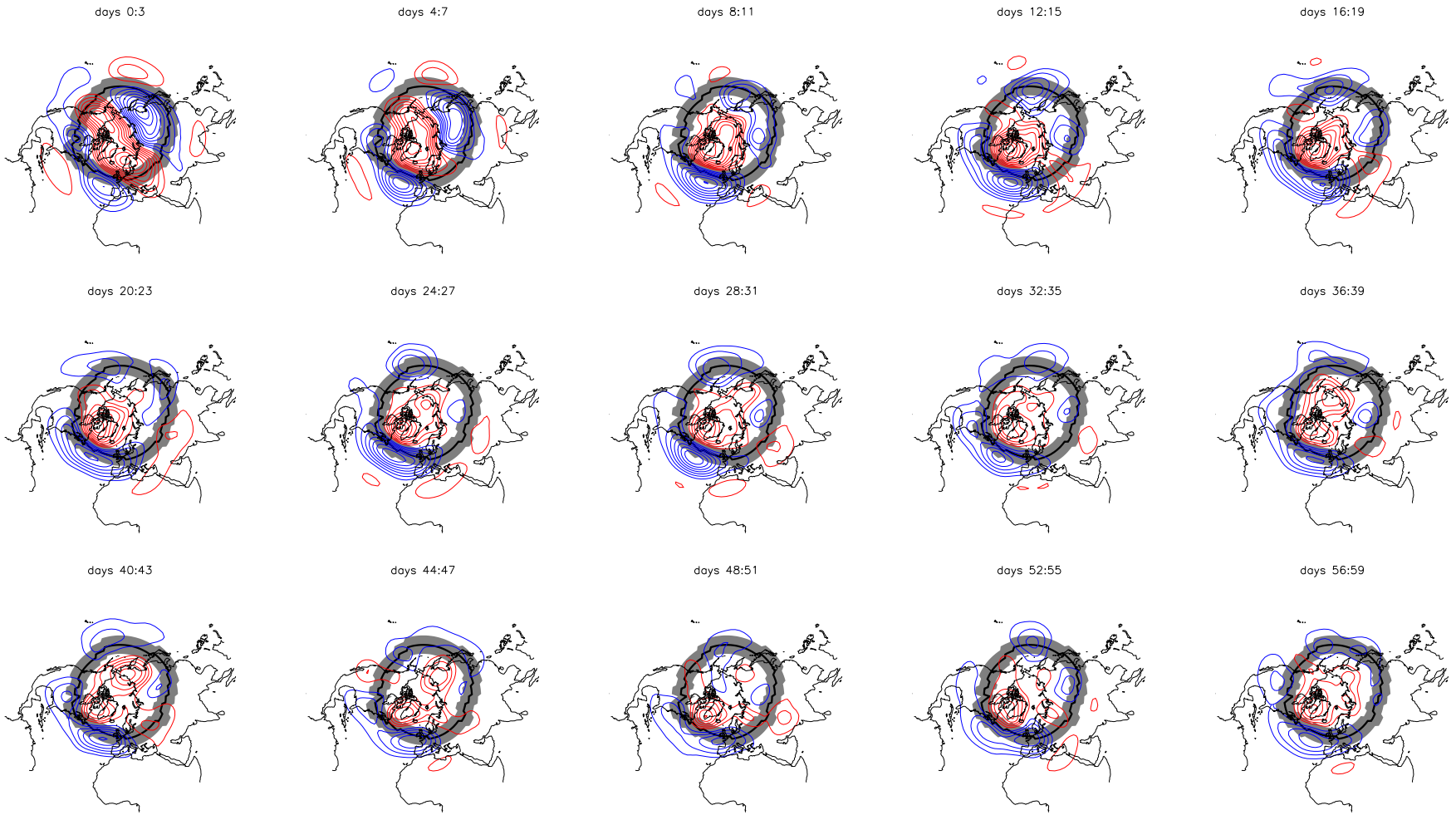

Figure 5.14: Figure 5.13 continued.

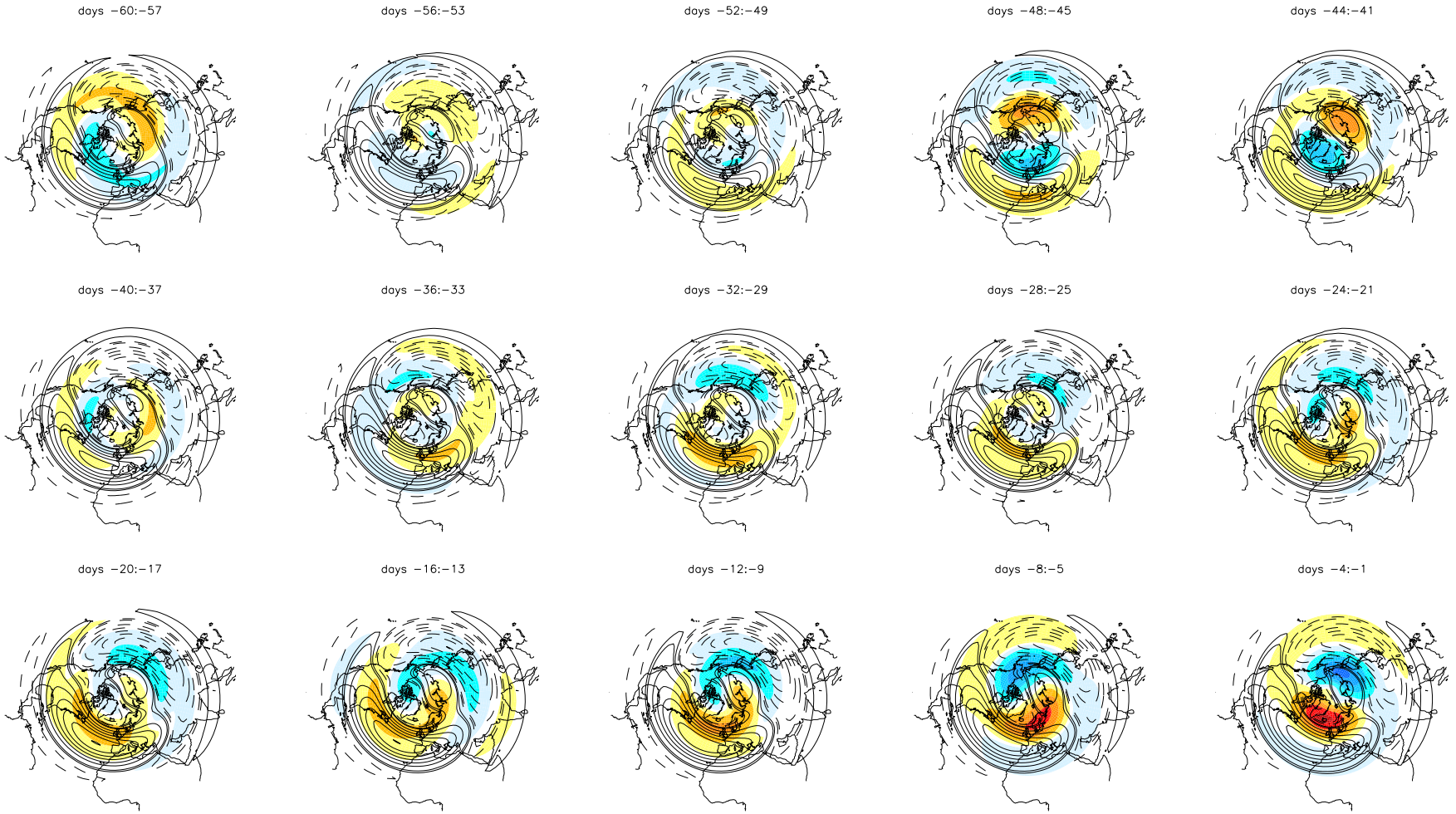

Figure 5.15: Figures 5.15 and 5.16:4-day averaged planetary height wavenumber 1 at 500 hPa, for the same period and time intervals as in Figure 5.13. Contours are the full field given each 14 meters between -130 m and 130 m. Positive (negative) values are given as the solid (dashed) lines. Shaded areas are anomalies from the annual cycle with contour intervals at [-30,-20,-15,-10,-5,-1,1,5,10,15,20,30] meters.

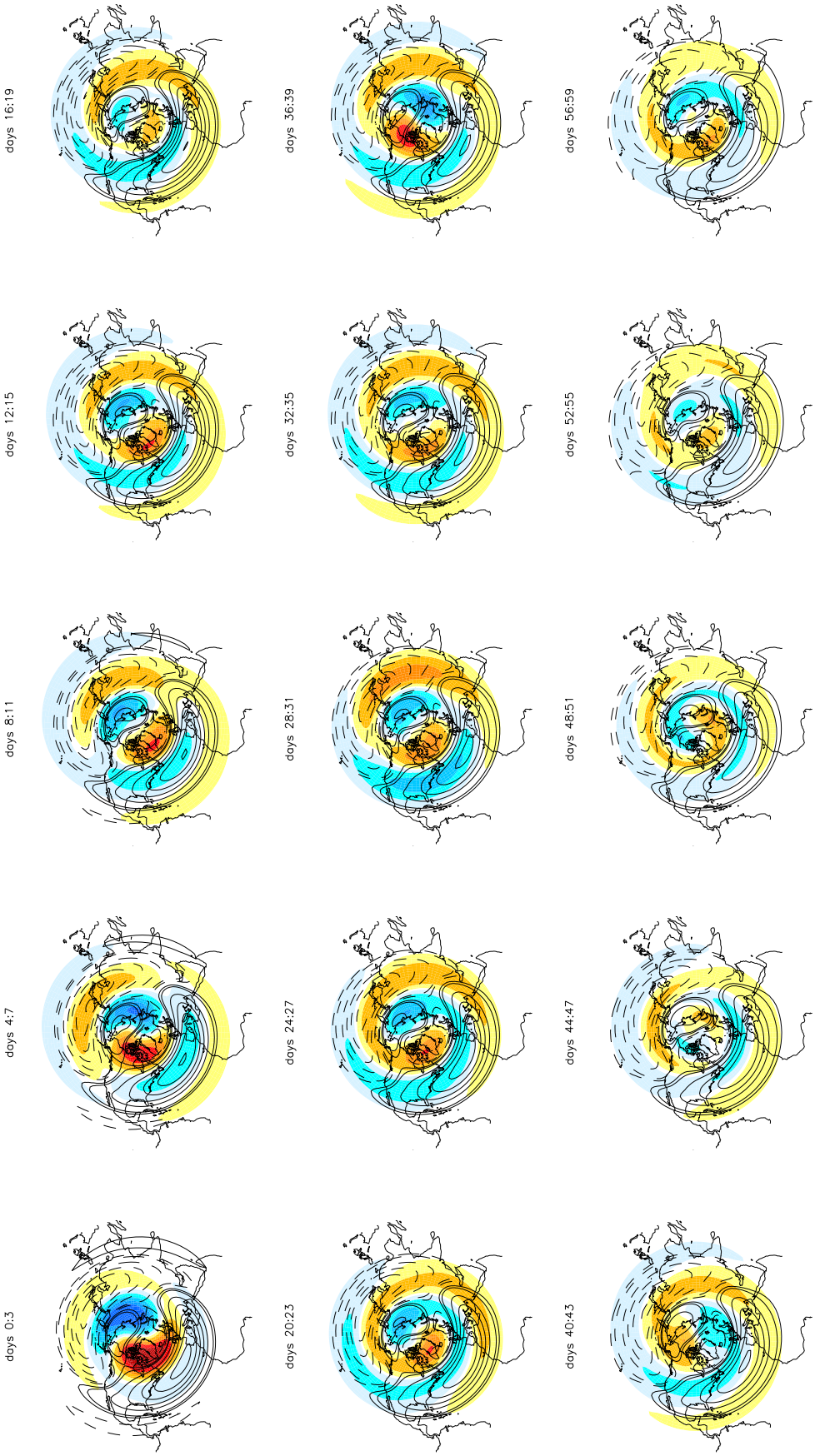

Figure 5.16: Figure 5.15 continued.

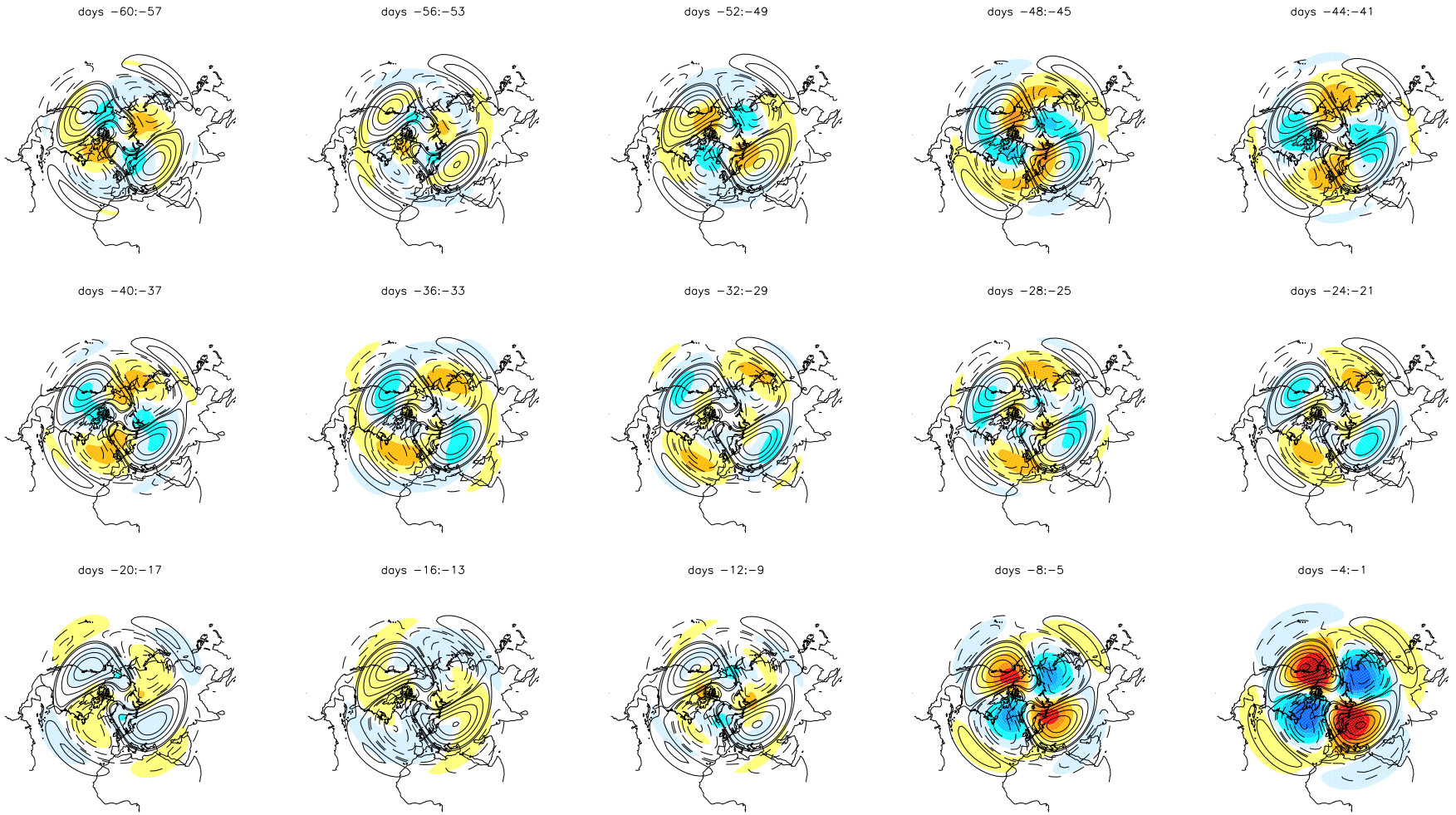

Figure 5.17: Same as Figure 5.15 but for wavenumber 2. Anomaly contours are the same; full field contours are given every 12 meters between -110 m and 110 m.

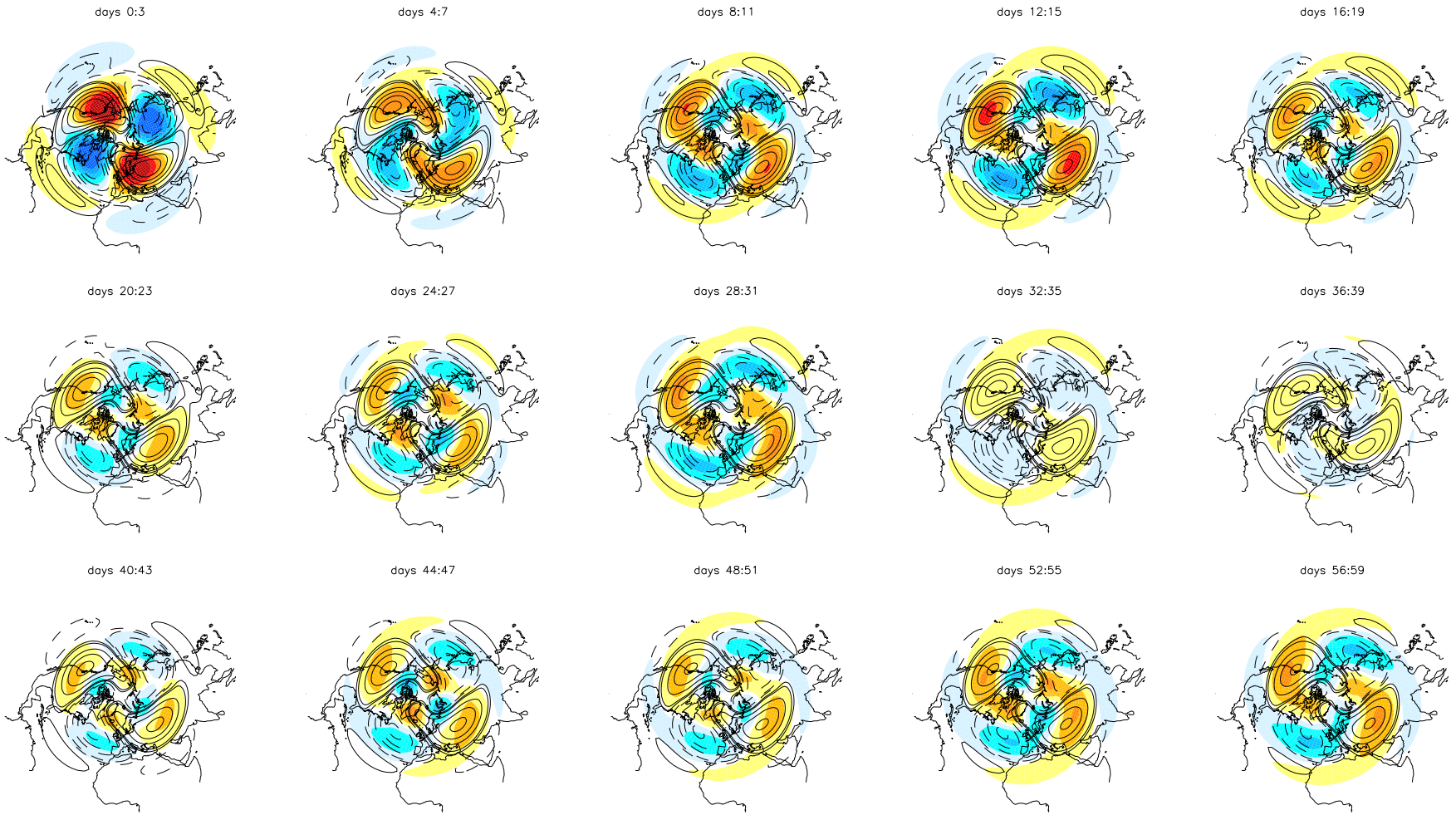

Figure 5.18: Figure 5.17 continued.

In the first panel (days -60:-57) of Figure 5.13, a middle latitude positive height anomaly located over the Eurasian sector moves westward and strengthens, accompanied by amplifying PW 1 and 2 also displacing westward, until they reach the east Pacific sector, with a strong anticyclonic anomaly at (days -44:-41). In the following period (days -40:-17), the geopotential height flow is mostly characterized by small-scale anomalies, and small anomalous amplitudes in PW 1 and 2. At days -16:-13, another positive anomaly forms over the northern part of the Eurasian sector, and this time this anomalous anticyclone is accompanied by an amplifying PW 1 further toward the pole. At this time, there is also a weak negative height anomaly located over Canada, associated with a reinforcement of the negative wavenumber 1 signal at high latitudes. In the next panel (days -12:-9), the positive height anomaly strengthens over the Eurasian sector, whereas the negative height anomaly moves south-westward, as it is pushed from southern latitudes by amplifying PWs 1 and 2. Within days -8:-5, a more prominent amplification of PWs 1 and 2 at high latitude is evident (Fig. 5.12, 5.15 and 5.17). Simultaneously, the anomalously high Eurasian anomaly substantially amplifies, where the positive wavenumber 1 and 2 signals increase, whereas the Pacific positive signal, mainly due to wavenumber 2, is associated with a developing anticyclonic anomaly over northwest Canada. From that period, the Pacific height anomaly increases and the PW 2 continuously amplifies, to both reach a maximum at days -4:3, and gradually decrease until the end of the period analysed. From the time when the Pacific anomaly is at a maximum, the anomaly decreases and also moves slowly westward over Alaska, with both PWs 1 and PW 2 being visibly associated with this displacement. The Eurasian height anomaly, although also dependent on the amplifying PW 2, seems to mainly evolve with PW 1, as they both increase until days 0:+3, when they start to slowly move westward over Scandinavia, and then more rapidly over the Atlantic basin, where they both decrease in amplitude. A strong anomalous geopotential height dipole over the Atlantic then persisted until days 36:39. After that period, the large-scale features of the flow slowly disappear, while smaller-scale disturbances start to re-appear. Note that the high geopotential height anomaly over Eurasia has been shown to be a precursor of weak stratospheric polar vortex events in other studies based on re-analysis or model simulation dataset (Martius *et al.*, 2009; Kolstad and Charlton-Perez, 2011).

A few days prior the onset of the SSWs (days -4:-1) the strong anomalous anticyclonic anomalies in both the Pacific and Eurasian regions connect up via the polar region, and during the warmings anomalously high (low) geopotential heights are located over polar (mid-latitude) regions. As the vortex recovers, the positive height anomalies are then slowly displaced off the pole. During the warmings, simultaneous high-latitude blocking events in the Euro-Atlantic and Pacific regions are therefore expected. This is supported by the study of Woollings *et al.* (2008), who found a significant link between the occurrence of high latitude blocking events in the Atlantic and Pacific sectors, with Atlantic blocking events leading Pacific blocks by 1-3 days. This quasi-simultaneous occurrence of blocks in the two sectors arise because of a large-scale distortion of the polar trough over Canada, initiated over southern Alaska and Greenland by developing anticyclonic anomalies, often in connection with a large-scale disturbance of the stratospheric polar vortex. The evolution of the simultaneous blocking events presented in Woollings *et al.* (2008) is very similar to the synoptic description in this present study.

The retrogression of the anomalously high geopotential heights (blocking) seems to be linked with the low-frequency westward travelling large-scale planetary wave anomalies, favouring anomalously high blocking occurrence in various regions as they move. This is further supported by Naujokat *et al.*

(2002), who studied three individual blocking events in the north Atlantic, and suggested the possibility that blocking may initiate and decay on a timescale similar to that of the travelling wave period. Michelangeli and Vautard (1998) argued that one precursor of the Euro-Atlantic blocks is a high-latitude retrograding wavenumber 1 a few days preceding the blocking onsets. The anomalous westward-moving of PW 1 is also evident in the latitudinal average composite (Fig. 5.6), and is reminiscent of the Branstator-Kushnir 20-25 day oscillation (Branstator, 1987; Kushnir, 1987). Mid- or high-latitude tropospheric disturbances related to such oscillation cycles are characterized by westward motion and a life cycle of growth and decay over a period of about three weeks. The roughly concurrent occurrence of enhanced eastern Pacific blocks and anomalous westward-moving PW 1 (compare Figures 5.6 and 5.7) is also supported by Kushnir (1987) with the observation that large-scale Pacific dipole blocking structures propagate westward and go through a life-cycle in phase with the 20-25 day oscillation.

This synoptic description provides further evidence that enhanced activity in both PW 1 and 2 are associated with an increased blocking activity at high latitudes over the Euro-Atlantic and northeast Pacific regions. The main changes in blocking activity (Fig. 5.7) and in the large-scale height field (Fig. 5.13 and 5.14) begin about 20 (10) days before SSW onset over the Euro-Atlantic (Pacific) region. Once the warmings initiate, amplitudes of PW 1 and 2 progressively decrease along with the anomalous anticyclonic conditions over the Pacific sector, while high geopotential height anomalies and stronger than normal blocking activity over the Euro-Atlantic region persist until the end of the period analysed.

The suggestion that the annual cycle of blocking activity over the Euro-Atlantic and Pacific basins could be strongly influenced by a low-frequency cycle of the stratospheric polar vortex, is supported by the synoptic evolution of anomalous height and PW fields being consistent with the blocking statistics seen in Figures 5.7 and 5.10. A large number of studies support the fact that some blocking events accompany amplifying PWs in the mid-troposphere (e.g., this is particularly well known for the amplification of the stationary waves, see Chapter 4), and that the preconditioning of the background flow could be more or less favourable for the development and maintenance of blocking (Naujokat *et al.*, 2002; Martius *et al.*, 2009).

5.6 Concluding remarks

The focus of this chapter has been to study the relationship between Northern Hemisphere tropospheric blocking and SSW events, in a long, multi-century climate simulation. In particular, the precursor role of blocking on SSWs and the influence of SSWs on blocking were explored over the main regions affected by blocking (i.e., the Euro-Atlantic and Pacific sectors). The discussion advanced through the investigation of composites for a selection of fields, in an attempt to unfold aspects of the underlying large-scale dynamics that precede and follow the onset of SSWs in relation with the annual cycle of blocking activity. The use of a long climate model simulation provides a very much larger sample of SSW events than is available in the recent instrumental/re-analysis period, greatly increasing the power of the statistical analyses to distinguish real effects from random effects. This is limited by the ability of the model to simulate the real climate system, but this study also provides a valuable validation of the model, since some of the results presented here are supported by a number of studies exploring the stratosphere-troposphere relationships in reanalysis datasets or for individual case studies.

The main conclusion drawn from this analysis is that the entire low-frequency cycle during the weakening and breakdown of stratospheric polar vortex is associated with mid-tropospheric wave disturbances and anomalous circulations, which modulate to some extent the annual cycle in blocking activity. The occurrence of SSWs enhances the wintertime blocking frequency in the Euro-Atlantic region and inhibits it in the west Pacific sector, while no significant relationship was found beyond the 40-day periods preceding and following the onset date of SSWs (i.e., in autumn and spring, respectively). These SSW-related changes in blocking frequency were associated with a significant shift in the distribution of blocking lifetime toward longer wintertime Eurasian blocks in PRE-IN and shorter wintertime west Pacific blocks in POST-IN. Nevertheless, the results further indicate that once the SSWs initiate, an enhanced frequency of short-lasting blocking events at the expense of long-lasting blocks is associated with a rapid weakening of large-scale planetary wave anomalies and an increased wave contribution from smaller-scale disturbances.

CHAPTER 6

Blocking-related extreme weather events: model validation and future changes

6.1 Introduction

6.1.1 Extreme weather events: a general introduction

A precise definition of an extreme weather event is difficult to formulate (Beniston, 2004). In general, an extreme event is characterized as a very rare and/or unexpected intense event with severe impacts on the economy (insurance costs), society (loss of life and human health) and the environment (destruction of natural habitats). However, the severity of an event is highly dependent on the vulnerability and adaptability of the society and/or ecosystem under consideration. In socioeconomic terms extreme weather events are most damaging in developed countries, while the deadliest events often occur in developing countries where people live in vulnerable and marginalised areas (Tompkins, 2002). Scientifically speaking, the severity of an extreme weather event is often characterized on the basis of (1) *how rare they are*, which involves notions of frequency of occurrence, (2) *how intense they are*, which involves notions of threshold exceedance and (3) *how persistent they are*, which involves notions of duration-based indices. Moreover, the characteristics of extreme weather events vary depending on the region and time of the year they occur, and also on their spatial and temporal scales as illustrated in Figure 6.1. Therefore, the definition of an extreme weather event should be specifically formulated according to where and when it occurs and according to its spatial and temporal scales, in order to gain understanding of their relationships with climate variability. Two important aspects of climate fluctuations could influence the incidence and dimensions of extreme weather events. First, the large-scale circulation patterns conducive to the build-up and anomalous transport of heat and moisture may influence the spatial and temporal variability of weather anomalies (e.g., Tomozeiu *et al.* (2005), Goubanova *et al.* (2010)) and of extreme events (e.g., Xoplaki *et al.* (2003), Haylock and Goodess (2004), Carril *et al.* (2008), Blenkinsop *et al.* (2009)). Second, climate change, especially the increase in global surface temperatures, can be expected to impact locally via changes in regional extreme events (Beniston *et al.*, 2007; Trenberth *et al.*, 2007; Planton *et al.*, 2008).

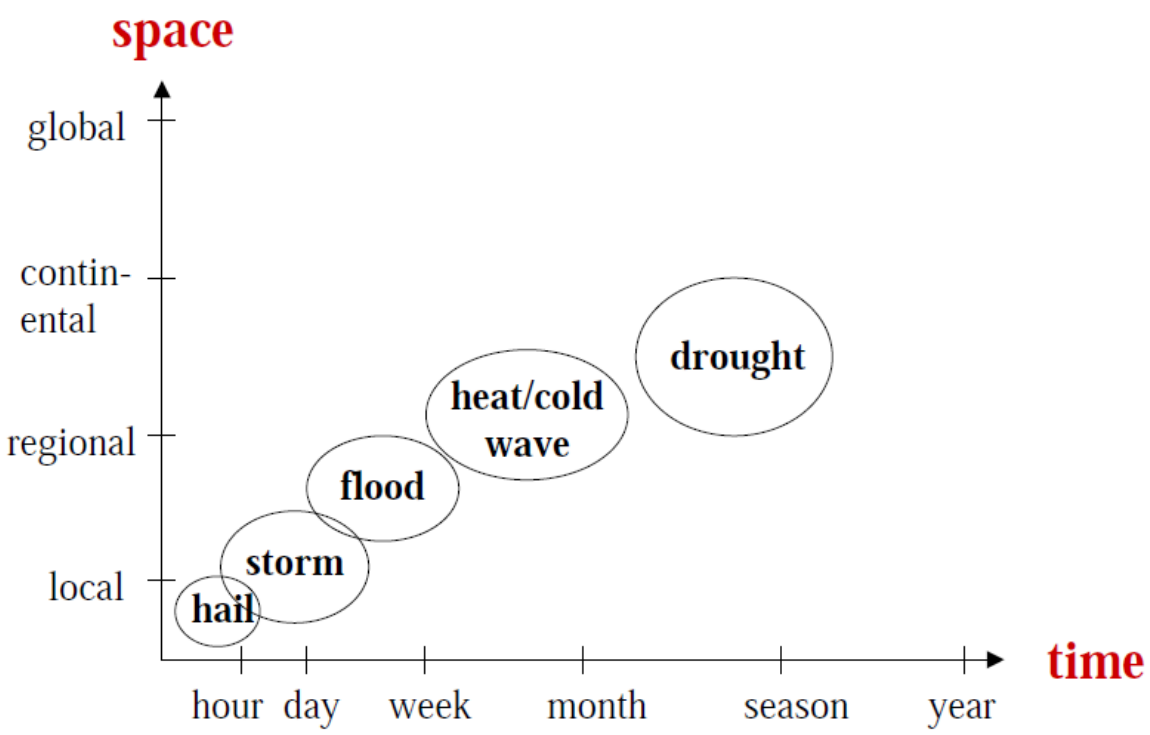

Figure 6.1: Schematic representation of the spatial and temporal scales of extreme climate events. Taken from Sillmann (2009).

6.1.2 Extreme weather events and their connection with atmospheric blocking

6.1.2.1 Observation- and model-based studies

Atmospheric blocking plays a key role in the regional climate variability and occurrence of extremes due to its quasi-stationary and persistent characteristics (Rex, 1950a,b; Sillmann and Croci-Maspoli, 2009). Under blocking conditions, the normal zonal flow is interrupted by strong and persistent meridional flow, leading to anomalous transport of heat and moisture (Black *et al.*, 2004; Carrera *et al.*, 2004). The normal progression of the synoptic-scale cyclones and anticyclones is disturbed, as the systems are often forced to the north or south of the blocking anticyclone, leading to anomalous storm tracks and precipitation patterns (Trigo *et al.*, 2004; Nakamura and Wallace, 1990; Carrera *et al.*, 2004).
Carrera *et al.* (2004) used the NCEP/NCAR reanalysis dataset to examine the statistical relationships between Alaskan blocking events and weather extremes (beyond the upper and lower terciles of the daily distributions) over north America during the winter seasons between 1979 and 2000. They found that southeast of the block there is a shift in the daily mean surface temperature distribution toward colder temperatures, associated with a reduced variance of surface temperatures and a shift in the tail of the distribution toward more extreme cold days. The opposite occurs over western Alaska (northeast of the block), with a shift in the daily mean surface temperature distribution toward warmer temperatures, and more extreme warm days. A similar analysis of extremes in daily precipitation revealed that the blocking events are associated with a southward shift of the Pacific storm track, leading to a higher frequency of heavy precipitation equatorward of the blocking anticyclone. The regional changes in temperature and precipitation during the Alaskan blocking conditions were attributed to anomalous transports of heat and moisture associated with changes in the circulation pattern and in the position of the storm track.

Similar conclusions were drawn over the Euro-Atlantic region, where Trigo *et al.* (2004) studied the impact of blocked and zonal flows on various climate indicators (850 hPa temperature field, minimum and maximum surface temperature, transient eddies, precipitation) using the NCEP/NCAR reanalysis dataset from 1958 to 1997 during the winter season. They showed that blocked and zonal flows induce (1) anomalous advection of heat, controlling the lower tropospheric temperature field, and (2) strong meridional shifts of the synoptic-scale cyclonic activity and consequently of the mean precipitation patterns.

Atmospheric blocking episodes are not only associated with anomalous storm tracks and anomalous advection of heat and moisture. Strong anticyclonic blocking patterns can induce subsiding movements that can further heat the surface through enhanced adiabatic warming (Green, 1977; Xoplaki *et al.*, 2003). Furthermore, the long clear-sky periods associated with the blocking anticyclone contribute to enhanced daytime solar radiative heating over the region under consideration (Black *et al.*, 2004). The extreme temperatures and lack of precipitation in Europe from May to August 2003 were related with a persistent blocking anticyclone over western Europe throughout the period (Black *et al.*, 2004; Beniston, 2004). Anomalous displacement of the storm track, and anomalously clear sky and downward net radiative fluxes were mostly responsible for the extremely warm and dry conditions. The land surface warmed and dried to such an extent that the lack of soil moisture strongly reduced latent cooling by evaporation and thereby amplified the surface temperature anomalies. The ground also played an important role in accumulating heat during the day up to a point that its gradual release during the night offset night-time cooling by upward long-wave radiation under a clear sky, slowing the decrease in air temperature before sunrise. The fact that the nocturnal stable boundary layer is usually shallow under anticyclonic conditions, leads to the formation of fog at higher latitudes (where the night-time temperatures are sufficiently cold, allowing the air to saturate near the ground), and amplify the offset action of night-time radiative cooling (Black *et al.*, 2004).

6.1.2.2 Atmospheric blocking and its impact on extremes under a warmer climate

The study of atmospheric blocking under future scenarios has not been well addressed yet. This is partly due to the lack of ability in climate models to provide a realistic representation of this phenomenon (D'Andrea *et al.*, 1998; Scaife *et al.*, 2010; Vial and Osborn, 2011; Matsueda and Palmer, 2011). Therefore, the largest interest has so far focused on the understanding of blocking-related systematic model biases and of the dynamical mechanisms underlying the blocking variability in order to improve its representation in forecast and climate models.

Matsueda *et al.* (2009) is one of the few studies addressing the impact of anthropogenic climate change on blocking frequency. The study was carried out using various horizontal resolution AGCMs (at 180 km, 120 km, 60 km and 20 km grid resolution) under the SRES A1B emission scenario over the whole Northern Hemisphere during the winter season from 2075 to 2099. The projected changes using a three-member initial-value ensemble simulation at 60-km resolution revealed a significant decrease in both frequencies of Euro-Atlantic and Pacific blocking in the western part of each blocking region (corresponding to the present-day blocking regions), where the westerly jet is projected to increase in strength, while no significant changes are estimated in the eastern part of each region. The number of Euro-Atlantic blocks is projected to decrease for almost all blocking spell durations, whereas the decrease in the number of Pacific blocking events is mainly evident for long-duration events. Matsueda *et al.* (2009)

argued that long-lived ($>$ 25 days) Euro-Atlantic and Pacific blocking episodes could even disappear in a future climate.

The projected changes are somewhat different according to model resolutions. The highest-resolution 20 km model, which provides the most accurate representation of Euro-Atlantic blocking in the present-day climate, shows similar changes in Euro-Atlantic blocking frequency and persistence, as also predicted with the 60 km ensemble simulation. However, the lowest-resolution model, which strongly underestimates the present-day frequency of Euro-Atlantic blocking, shows no apparent future changes in Euro-Atlantic blocking frequency and duration. In the Pacific sector, all the models predict a decrease in the frequency and persistence of blocking. The lowest-resolution model (which shows a good agreement with the reanalysis) provides the largest changes in blocking duration, while the highest-resolution model (which overestimates by the most the frequency of blocking) shows the least prominent changes in both the frequency and persistence of blocking. Finally, in both the Euro-Atlantic and Pacific regions, the 20-km resolution model is the only one predicting a reduction of blocking on the west side of each present-day blocking sectors, as also indicated in the ensemble simulation. At other model resolutions, the frequency of blocking decreases uniformly, regardless of the longitude in each blocking region. Although Matsueda *et al.* (2009)'s results tend to show an overall decrease in the frequency and persistence of blocking, they nevertheless highlight some degree of uncertainties regarding the accuracy of the predictions.

The decreased frequency of European blocking events is consistent with the work of Sillmann and Croci-Maspoli (2009), who examined the impact of blocking on present (1961-1990) and future (2160-2199) mean and extreme climate events over Europe, using the ECHAM5/MPI-OM AOGCM. It was found that in the A1B scenario, European blocking could experience a reduced frequency of occurrence (by 8% on average, the statistical significance not being specified), with less (more) blocks in the southwestern (northeastern) part of the domain. As a result, a larger part of Europe could be affected by anomalously cold and dry winter months, while the anomalously warm and wet conditions over Greenland could remain largely unchanged. These results are also reflected in the correlation analysis between blocking frequency and the seasonal extremes of minimum and maximum temperature and maximum 5-day precipitation; the correlations tend to be weakened (strengthened) where the number of blocks is reduced (enhanced).

Goubanova *et al.* (2010) examined the link between large-scale weather regimes (including European blocking) and European mean temperatures in a present (1970-1999) and future (2070-2099 - under the SRES A2 emission scenario) climates using the variable-grid LMDZ AGCM with a finer resolution zoom over Europe, where the effective resolution of the model was approximately 150 x 150 km^2. It was shown that changes in the temperature distributions over Europe were not explained by changes in the regimes's structures (i.e., their geopotential height patterns), nor by changes in their frequency of occurrence, but rather by changes in the mean temperature gradient over the continent, with a stronger (weaker) warming over the northeast (southwest) part of the domain. The consequences for anomalous advection of heat in different circulation regimes are then different in the future climate. In the case of European blocking, the mean winter temperature is predicted to decrease over the eastern part of the continent, which is consistent with the results of Sillmann and Croci-Maspoli (2009), previously described.

Despite the small number of studies addressing the impact of blocking on extremes under a future climate, there seems to be a consistency between the model simulations analysed so far, which show that

although an increase in global surface temperatures is predicted, the influence of blocking on the regional climate seems to remain robust. In particular, Euro-Atlantic blocking may undergo an eastward shift of the blocking pattern with a reduced frequency of blocking events, and a tendency toward a colder and drier climate under the blocking action (i.e., over central and eastern Europe) could still be expected in a future climate.

However, whether the changes in precipitation and temperatures are caused by changes in the blocking itself - explaining only 14% of the winter variability in the Euro-Atlantic region (Scherrer *et al.*, 2006), or by other large-scale weather regimes, or by changes in other climate variables (e.g., soil moisture, cloudiness), affecting the global average temperature and precipitation spatial distributions, still remains uncertain. Moreover, uncertainties in the accuracy of the predictions arise, as the simulated changes in precipitation and temperature extremes are dependent on climate models being able to simulate the large-scale circulation patterns, their relationships with the regional climate variability and subgrid scale processes.

6.1.3 Aim

The aim of this study is twofold. First, the observed relationship between climate averages and extremes over Europe and European atmospheric blocking (see Section 6.1.2) is revisited and compared with two simulations of the present-day and future climate. In addition, an attempt is made to quantify the contribution of changes in blocking to the total changes in climate extremes. The model used is the IPSL-LMDZ4 variable-grid AGCM with a finer resolution zoom over Europe, which in turn forces a higher-resolution regional model over France. Second, an assessment of the model is performed in order to (1) analyse the impact of using a variable-grid model on the representation of blocking and (2) discuss the implications of the dependence between model resolution and the simulation of extreme weather events.

6.2 Model configuration

6.2.1 Description

The model configuration used in this study consists of a dynamical downscalling approach in two steps[1]:

- **Two-way self-nesting between global and regional scales of motion**, using the version 4.0 of the variable-grid LMDZ AGCM (the atmospheric component of the IPSL-CM4 model, see Table 4.1) with a finer-resolution zoom over Europe (Hourdin *et al.*, 2006). The resolution of the model is 300 km outside and 100 km inside the zoomed region (i.e., Europe). Unlike the nesting approach that incorporates a regional model (forced by prescribed lateral boundary conditions) into a large-scale global model, the approach with a variable-grid AGCM is operating in a standalone manner, as illustrated in Figure 6.2, and the model is free to have its own behaviour inside the zoomed

[1]There are no references for these information describing the model configuration; they were provided by Laurent Li (Laboratoire de Météorologie Dynamique (LMD) in Paris) - see `www.cima.fcen.uba.ar/UMI/documents/2011/li_lmdz_user_201103.ppt`

domain without the need for a driving GCM to provide conditions at the regions boundaries (Fox-Rabinovitz *et al.*, 2006; Goubanova and Li, 2007). In other words, the model runs as a AGCM with the only difference that a variable resolution grid is used instead of a traditional uniform grid. This model configuration provides an attractive framework since it allows self-consistent interactions between global and regional scales of motion, and therefore provides a better treatment of scale interaction (e.g., between the large-scale circulations and synoptic eddies). In addition, the finer-resolution zoom in limited regions can be adjusted towards the research problem, without requiring a fine grid resolution throughout the entire model domain, which would substantially reduce computing capabilities.

- **One-way nesting from Europe to France:** the information (atmospheric temperature and circulation) resulting from the two-way nesting is then recorded every six hours, and used to force a higher 20-km resolution regional model over France (i.e., one-way nesting), to optimise the treatment of more local weather events (e.g., extremes).

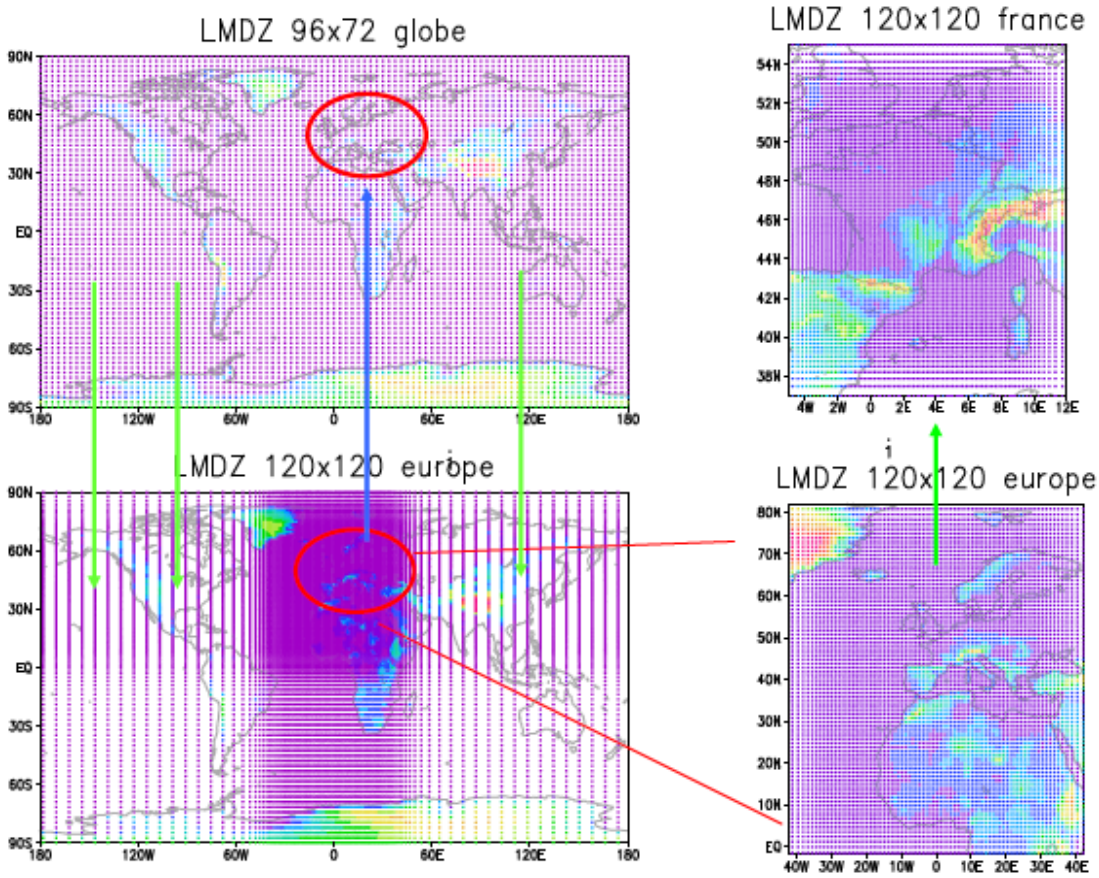

Figure 6.2: Schematic representation of the model configuration used in this study. The two-way nesting between the global model and regional model over Europe is displayed on the left panel. The one-way nesting between Europe and France is on the right. Figures provided by Laurent Li (Laboratoire de Météorologie Dynamique (LMD) in Paris).

For the control simulation the model employs, as lower boundary conditions and driving forcing, the Atmospheric Model Intercomparison Project (AMIP) II time-averaged climatological values (i.e., with a fixed annual cycle) of the sea-surface temperature (SST, originally at $1°x1°$ resolution, and then

interpolated to the atmospheric model grid) and sea-ice extent observed over the period 1961-1990[2]. For the future climate projection, the boundary conditions were constructed from the outputs of the coupled IPSL-CM4 model under the A1B emission scenario, whereby the differences of the forcing variables (SST and sea ice extension) between the future and present-day states of the coupled model were computed, and added to the observed values of the current climate (Goubanova and Li, 2007). The future period for this study is from 2020 to 2049.

For reference through this chapter, the different simulations are referred to with respect to their resolution (LR for global, MR for Europe and HR for France), and whether they simulate the control (CTRL) or future (A1B) scenario (e.g., MR-CTRL, HR-A1B). The grid schemes of the three versions of the model are illustrated in Figure 6.3.

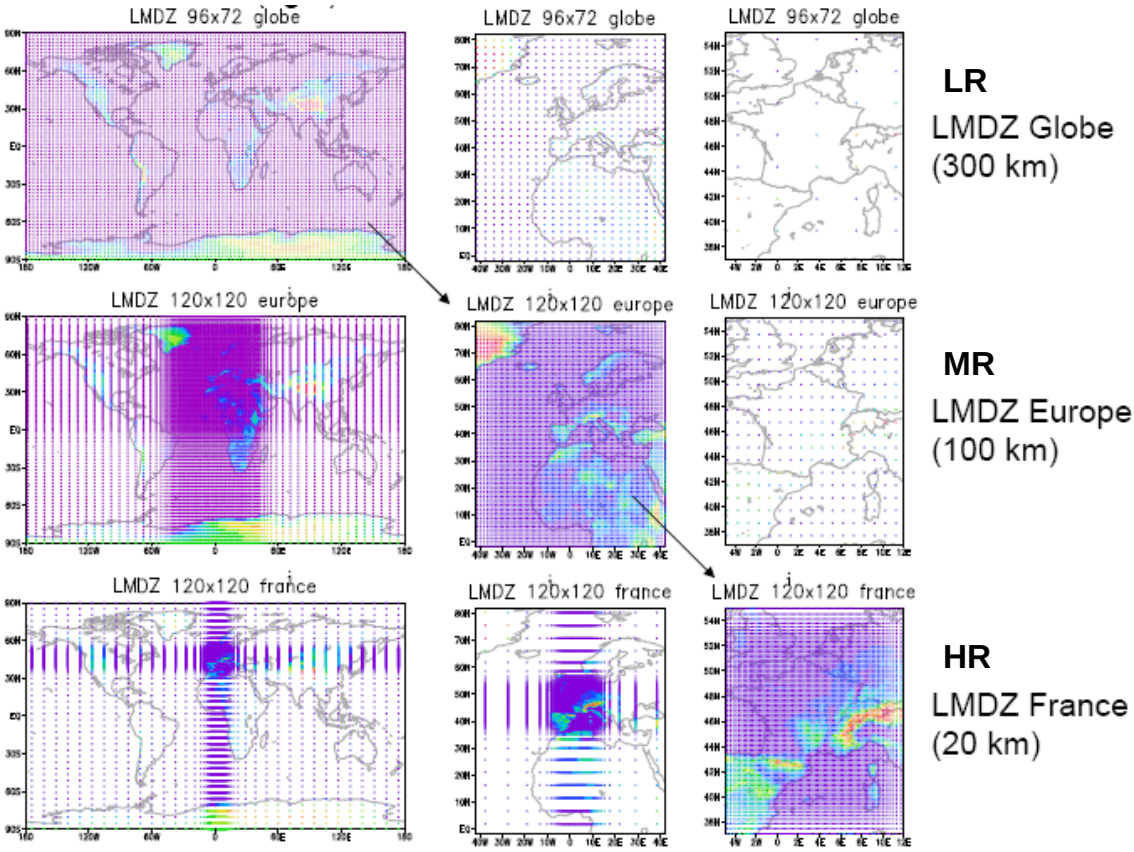

Figure 6.3: LMDZ grid schemes for the whole earth (left), for Europe (middle) and for France (right) in the three versions of the model (see description in the text). Figures provided by Laurent Li (Laboratoire de Météorologie Dynamique (LMD) in Paris).

[2]See `http://www-pcmdi.llnl.gov/projects/amip/AMIP2EXPDSN/BCS/amip2bcs.php` for more details

6.2.2 How well does the 2-way self-nested model simulate blocking compared to its AGCM and AOGCM homologue?

Figure 6.4 shows the frequency and duration of blocking within the European sector (refer to Section 6.3.1 for more details about blocking detection specific to this study) for three versions of the LMDZ4 climate model:

- IPCM4 is the uniform-resolution IPSL-CM4 atmosphere-ocean coupled model (used in Chapter 4), which simulates its own climatology.
- GLOBAL is the uniform-resolution atmospheric component of IPCM4, driven by observed SST/sea-ice extent.
- MASTER (also referred to as LR CTRL in this study) is the same as GLOBAL, except that it has the finer-resolution zoom over Europe (as described in Section 6.2.1)

IPCM4 is clearly the version of the model that underestimates the most the frequency of blocking days (Fig. 6.4a, blue line). This systematic bias (also observed in most atmosphere-ocean coupled models; see Chapter 4 and other studies e.g., D'Andrea *et al.* (1998) and Scaife *et al.* (2010)), is due to an insufficient number (or even total absence) of medium spells and long-lasting blocking episodes (above 9-day persistence; blue line in Figure 6.4b), and a shift in blocking lifetime distributions towards shorter blocks (i.e., the frequency of 5-day blocking events is overestimated in Figure 6.4b). When coupled models run in a standalone manner (i.e., without flux adjustments between the oceanic and atmospheric model), as it is the case for IPCM4 (and most current atmosphere-ocean coupled models), they tend to drift to their own climate, creating significant systematic errors in the simulation compared with observations (McGuffie and Henderson-Sellers, 2005, pp. 208). This is however not the case for atmosphere-only climate models (such as GLOBAL) as they are forced with observed SST and sea-ice extension (i.e., and hence prevented from drifting too far from the observed climatology).

GLOBAL is slightly improved relative to the coupled model, with an increase of nearly 23% in the number of blocked days (compare the blue and magenta lines in Fig. 6.4a). The maximum duration of blocking episodes in this version is the lowest, but the frequency of blocking episodes is improved for all spell durations between 5 and 11 days (Fig. 6.4b). Thus, the improvement in blocking statistics from IPCM4 to GLOBAL is attributed to the more realistic climatology due to fixed observed SST/sea-ice extent (the existence of a climate drift in IPCM4 was shown in Marti *et al.* (2006)). It is however worth pointing out that the use of a fixed SST (i.e., with an annual cycle but no interannual variability - e.g., ENSO) in GLOBAL is not perfect and could therefore have induced some errors in the simulation of blocking (Ferranti *et al.*, 1994b; Slingo *et al.*, 1996; D'Andrea *et al.*, 1998).

The major improvement in blocking simulation is however not from IPCM4 to GLOBAL, but from GLOBAL to MASTER. Although MASTER underestimates the frequency of blocking days (by about 21%) this version of the model shows a substantial improvement compared to the two other versions, with an increase in the number of blocked days of about 36% compared to GLOBAL (see legend in Figure 6.4a). In addition, MASTER is the only model simulating relatively long-lasting blocking episodes, and the model is now able to capture blocking events longer than 14 days (Fig. 6.4b). These results clearly demonstrate the importance of the high horizontal resolution in the Euro-Atlantic region (Matsueda *et al.*, 2009; Tibaldi *et al.*, 1997) and scale interaction between the large-scale circulation and

synoptic-scale eddies (Austin, 1980; Shutts, 1983; Illari, 1984) for a climate model to provide an improved representation of blocking.

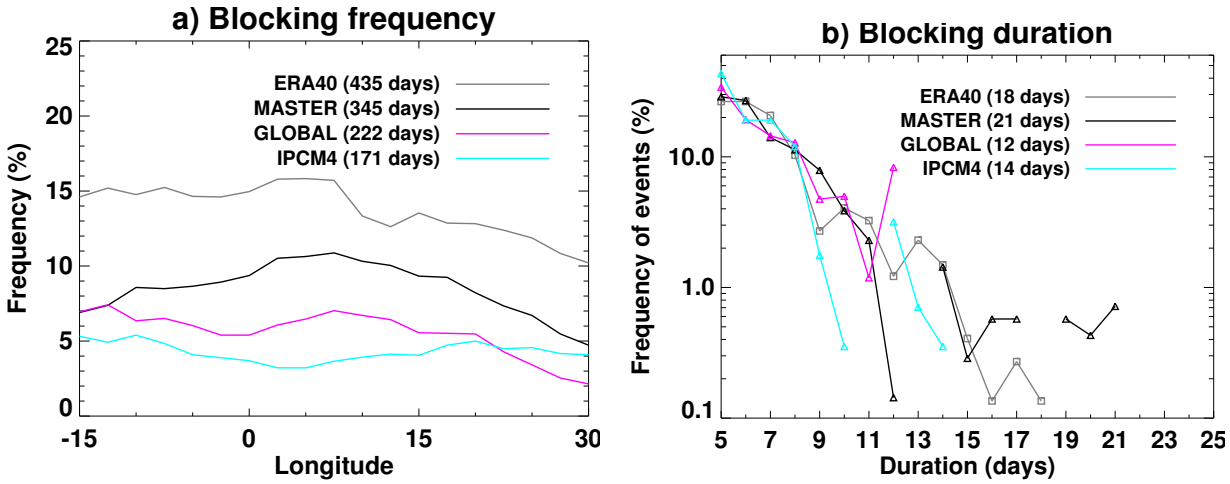

Figure 6.4: Blocking statistics for different versions of the LMDZ4 control simulation. ERA-40 (grey line), LR CTRL (also referred to as MASTER, black line), IPCM4 (blue line) is the coupled model, and the GLOBAL version (magenta line) is the atmospheric component of IPCM4. (a) Frequency of all days that are part of large-scale blocking episodes as a function of longitude. The total number of blocked days for each simulation is given in brackets in the legend. (b) Blocking duration defined as the average frequency of large-scale blocking episodes (at least 5 days duration) as a function of duration (days) for the European region. The maximum duration of blocking episodes is given in brackets in the legend.

6.3 Methodology and data

6.3.1 Blocking indicator

The blocking index BI has been calculated, following the methodology described in Chapter 3, on daily fields of 500 hPa geopotential height during the winter (DJF) season throughout each 30-year simulation. As blocking is a large-scale phenomenon, it is detected in the global version of the LMDZ model in the present-day and future simulations, respectively referred to as LR CTRL and LR A1B. ERA-40 reanalysis dataset is used for the verification of the CTRL climate model simulation. The model output have been regridded (using bilinear interpolation) at 2.5° resolution to match the resolution of the reanalysis, and the blocking index is calculated at each longitude and time step across the European domain (15°W - 30°E). Finally, a large-scale blocking episode is defined when a local and instantaneous blocking candidate spans at least 15° longitude and persists for at least 5 days within that sector.

For this study, the BI blocking index is preferred to the BI_{stlat} index, as the former captures more blocking episodes in the European sectors - without also capturing too many non-blocked episodes (in ERA-40, less than 8% of the European patterns identified by BI as blocking are actually considered not to be blocked on inspection; refer to Chapter 3). This index provides more blocked day occurrences, and therefore a larger sample size that is essential for the analysis of extremes during those blocking days.

6.3.2 Indices for extreme events

There are various methods to characterize extreme weather events, such as non-parametric approaches by defining percentile-, threshold- or duration-based indices (Frich *et al.*, 2002; Sillmann and Roeckner, 2008), or parametric approaches for example with the *extreme value theory* (Sillmann and Croci-Maspoli, 2009; Carey-Smith *et al.*, 2010) that is used to analyse the statistical behaviour of a climate variable in the tail of its probability distribution, and extrapolate the results towards extreme values with much larger return periods than those observed (Frei, 2003). Although this type of analysis provides valuable information for climate change impact assessment (i.e., extremely rare and damaging events with return periods of 20, 30, 50 or 100 years can be estimated and predicted), the uncertainty due to limited sample size can be substantial (Frei, 2003).

The focus of this study is on the non-parametric approach, with percentile-based indices characterising moderate and statistically robust extreme events with short return periods (90 days is the approximate return period[3] for a 1% quantile of 30-year wintertime daily values). The Expert Team on Climate Change Detection Monitoring and Indices (ETCCDMI) defined a core of 27 recommended indices for precipitation and temperature indicators, to be use for describing many aspects of extremes, including frequency, amplitude and persistence (Klein Tank *et al.*, 2009). This study only focuses on the frequency characteristic of extremes; a set of 16 frequency-based indices have been used for that purpose (described in Table 6.1), with 4 being selected from the ETCCDMI catalogue (i.e., tn10n, tn90n, tx10n, tx90n). Additional user-defined thresholds are used in order to consider different extreme amplitudes (i.e., more severe events: 5^{th}, 95^{th} percentiles and more moderate events: 25^{th}, 75^{th} percentiles). Percentile-based thresholds are also used for moderate and more severe extreme precipitation indicators. The reason for choosing percentile-based thresholds rather than fixed thresholds (e.g., count of days when daily rainfall exceed 20 mm, from the ETCCDMI catalogue) is that the number of days exceeding percentile thresholds provides a meaningful sample for every region and at all elevations. rdn is the only indicator using a fixed threshold, which can indicate regions vulnerable to droughts when daily rainfall is lower than 1 mm. This type of indices (ETCCDMI or user-defined indices) has been widely used in previous studies interested in analysing changes in climatic extremes from observed instrumental/re-analysis dataset (Frich *et al.*, 2002; Klein Tank and Können, 2003; Aguilar *et al.*, 2005; Carril *et al.*, 2008) or in climate change model projections (Kiktev *et al.*, 2003; Beniston *et al.*, 2007; Sillmann and Roeckner, 2008; Sillmann and Croci-Maspoli, 2009).

This analysis requires daily total precipitation (r), daily minimum 2-metre temperature (tn) and maximum 2-metre temperature (tx) fields for the same 30-year periods of integration as for the blocking analysis.

For the temperature fields, the percentile thresholds are computed for each calendar-day, in order to relate the occurrence of extremes with anomalies in circulation patterns (blocking/non-blocking flow). The use of calendar-day thresholds ensures that cold (warm) temperature extremes are not biased to occur in the climatological coldest (warmest) months. However, the sample size to compute calendar-day thresholds on a 30-year daily data sample is limited (e.g. with only 30 occurrences for the 15 December). Therefore, in order to account for the reduced sample size, the thresholds are computed from 5-day windows centered on each calendar-day. For example, the threshold for the 15 December is computed using the 13, 14, 15, 16 and 17 December, for each year within the control period (1961-1990). In that

[3] A return period is the average time between extreme events of the same or larger magnitude; the magnitude of a 1-year return period event is, on average, exceeded once in a year (Hennessy *et al.*, 1997).

Temperature indices		
tn25n	cold nights	Count of days where tn $< 25^{th}$ percentile
tn10n*	very cold nights	Count of days where tn $< 10^{th}$ percentile
tn5n	extremely cold nights	Count of days where tn $< 5^{th}$ percentile
tn75n	warm nights	Count of days where tn $> 75^{th}$ percentile
tn90n*	very warm nights	Count of days where tn $> 90^{th}$ percentile
tn95n	extremely warm nights	Count of days where tn $> 95^{th}$ percentile
tx25n	cold days	Count of days where tx $< 25^{th}$ percentile
tx10n*	very cold days	Count of days where tx $< 10^{th}$ percentile
tx5n	extremely cold days	Count of days where tx $< 5^{th}$ percentile
tx75n	warm days	Count of days where tx $> 75^{th}$ percentile
tx90n*	very warm days	Count of days where tx $> 90^{th}$ percentile
tx95n	extremely warm days	Count of days where tx $> 95^{th}$ percentile
Precipitation indices		
r75n	wet days	Count of days where r $> 75^{th}$ percentile on rainy days only (r < 1 mm)
r90n	very wet days	Count of days where r $> 90^{th}$ percentile on rainy days only (r < 1 mm)
r95n	extremely wet days	Count of days where r $> 95^{th}$ percentile on rainy days only (r < 1 mm)
rdn	dry days	Count of days where r < 1 mm

Table 6.1: Description of the 16 indices for temperature and precipitation extremes used in this study. tn, tx and r denote the daily minimum 2-metre temperature, the daily maximum 2-metre temperature and daily total precipitation, respectively. The 4 temperature indices marked with an asterisk are selected from the ETCCDMI catalogue (see online at `http://cccma.seos.uvic.ca/ETCCDI/list_27_indices.shtml`). The 12 other indices follow the same definition, but with a wider range of user-defined thresholds for extreme exceedances.

sense, each calendar-day threshold is computed using 5 days x 30 years = 150 values, and the 10^{th} and 90^{th} percentiles correspond to the 15^{th} and 135^{th} values of the sample.

There is not such an annual cycle in the precipitation distribution, as it is more dependent on anomalies in the circulation flow, travelling eddies and convective storms, than on the seasons as it is the case for temperature (i.e., length of daylight hours and intensity of incoming solar radiation) (Klein Tank *et al.*, 2009). Therefore, only one threshold is used for the computation of rainfall extremes using all wet days only (> 1 mm) in the base period. Finally, threshold exceedances in the present-day and future climates are counted with respect to present-day thresholds calculated within the base period (1961-1990), for both the temperature and precipitation indicators.

All model-based indices described in Table 6.1 are calculated from data generated with the two versions of the variable-grid LMDZ model over Europe ($\sim 1.5^\circ$ resolution, referred to as MR) and France ($\sim 0.33^\circ$ resolution, referred to as HR). The analysed model experiments represent the present-day (1961-1990) climate and a near future climate (2020-2049) under the A1B emission scenario during the DJF season. Extreme indices are also computed for the European land-only gridded dataset E-OBS (Haylock *et al.*, 2008) at 0.25° resolution, and are used for the verification of the present-day climate simulations (MR CTRL and HR CTRL), with the latter regridded (using bilinear interpolation) at 0.25° resolution to match the resolution of the observations.

6.3.3 Method of analysis of blocking-related climate anomalies and extremes

To study the connection between blocking and extreme weather events, it is assumed that blocking days identified in the global lower resolution datasets (i.e., ERA-40 and LR CTRL/A1B) can be correlated with and are reflected in the atmospheric/weather conditions on the same days in the finer resolution

datasets (i.e., E-OBS and MR-CTRL/A1B and HR-CTRL/A1B). In that sense, all blocking days identified in the global dataset are defined as blocking days in the finer resolution datasets, being the actual datasets with which blocking-related extreme weather events are analysed.

The diagnostics used to examine the impact of blocking on present and future mean and extreme weather events over Europe, are described in the rest of this section.

Blocking signature for precipitation and temperature averages

To depict the typical flow pattern as well as the temperature and precipitation fields associated with European blocking, blocking signature maps are computed for daily fields of 500 hPa geopotential height, precipitation and 2-metre minimum and maximum temperature, as described in Chapter 4 (i.e., by subtracting the average field of all non-blocked days from the average field of all blocked days within the European region). Additional fields are also analysed to gain a better understanding of the link between blocking and extremes, such as the diurnal temperature range (DTR = tx - tn) in E-OBS, and the net surface solar radiation (SSR) and net surface thermal radiation (STR) fluxes in the ERA-40 dataset. Results are described in Section 6.6.

Statistical significance for extremes

A Chi-square test of contingency table (Wilks, 1995) is performed in order to determine the degree of association between blocking and extreme day occurrence for each grid box within the European domain. The daily time series for blocking and extreme occurrence are binary (1/0) arrays, with 1 for occurrence, 0 for non-occurrence. We are interested in knowing whether a blocking day will also be an extreme weather day in a particular place. This leads to 2x2 possible combinations of blocking and extreme pairs (for each grid box) as laid out in the contingency table shown below (Table 6.2). The values of the table (n_{11}, n_{10}, n_{01}, n_{00}) are obtained by counting the number of times each of the four possible combinations occurred. For example, the total count of blocking days being also extreme days is given by n_{11}. The total count (n) is given by the sum of all the possibilities, and is equal to the sample size of each data series.

		Extreme		
		1	**0**	
Blocking	**1**	n_{11}	n_{10}	$n_{11} + n_{10}$
	0	n_{01}	n_{00}	$n_{01} + n_{00}$
		$n_{11} + n_{01}$	$n_{10} + n_{00}$	$n_{11} + n_{10} + n_{01} + n_{00} = n$

Table 6.2: 2x2 contingency table of observed counts n_{ij} (i,j = 1,2) for the binary time series of blocking and extreme day occurrence.

Since random association implies statistical independence between extreme and blocking days, we also use the Chi-square test to verify (at the 5% significance level) the null hypothesis (H_0): Blocking days and extremes are independent, against H_A: Blocking days and extreme days are associated. In the case of H_0 being rejected - this occurs when the Chi-square statistic is greater than a critical value, which depends on the degrees of freedom of the distributed data (i.e., the degree of freedom is 1 for a 2x2 contingency table) and the chosen significance level - we conclude that blocking days and extreme days are associated, otherwise no conclusion about their association can be inferred.

Frequency diagnostic for extremes

As for the extreme analysis, we are first interested to know whether the blocking flow patterns over the European region contribute more or less to extreme frequencies than might be expected on the basis of their frequency of occurrence alone. For that to be done, the relative contribution of blocking to extreme frequencies with respect to their average frequency of occurrence is examined with the ratio R:

$$R = \frac{P_{blk}}{P_{tot}} \tag{6.1}$$

Where, P_{blk} and P_{tot} are the *proportion of blocked days with extremes* and the *total proportion of days with extremes*, respectively.

If $R > 1$, then the contribution of blocking to extremes is greater than average, while for values of R lower than 1 the contribution of blocking to extremes is lower than for average conditions. This diagnostic is applied to all the indices presented in Table 6.1 and over Europe where the Chi-square test is significant. Results are described in Section 6.7.1.

Duration diagnostic for extremes

Another aspect of extreme events that is important to consider is their persistence. The severe consequences and high human mortality of the 2003 European heatwave were aggravated by the persistence of the anticyclonic conditions over the continent, as the long clear sky periods and the increasingly dry land surfaces resulted in an amplification of the exceptionally high temperatures and thermal heat stress (Black *et al.*, 2004). Therefore, this study is also interested in the duration characteristics of extreme weather events, and whether blocking contributes to more or less persistent extremes than any other atmospheric circulation conditions (hereafter, referred to as non-blocking flow).

The persistence of extreme weather events is analysed by comparing the spatial average frequency of extreme events as a function of their spell duration between blocking and non-blocking situations. This diagnostic is applied to all the indices presented in Table 6.1, averaging over France only, where the Chi-square test is significant. Results are described in Section 6.7.2.

Supplementary diagnostics

Additional figures are included in Appendix C, in order to provide a full record of the basis for the results. The following diagnostics are presented in Appendix C:

- The difference in percentile indices for extreme events between (1) the observations and the model and (2) the high-resolution and low-resolution model (Fig. C.1 to C.5)
- The total number of extreme days during blocking conditions (Fig. C.6 to C.11)
- The total number of extreme days during non-blocking conditions (Fig. C.12 to C.17)
- The difference in the number of extreme days between the high-resolution and low-resolution model during (1) blocking and (2) non-blocking conditions (Fig. C.18 to C.23)
- The difference in the frequency of extreme weather events between the observations and the model (Fig. C.24)

6.4 Blocking climatologies

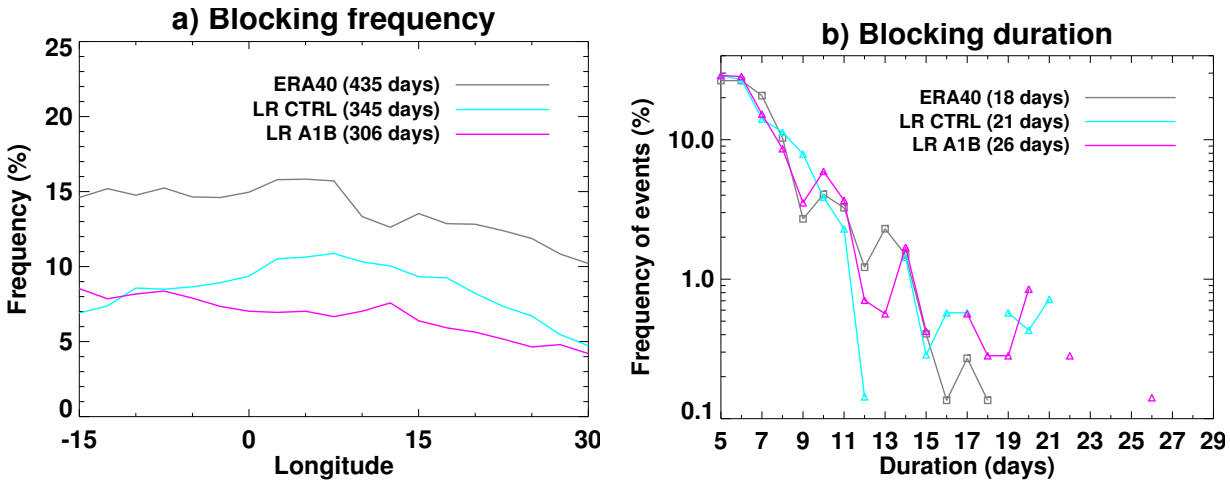

Figure 6.5: (a) Frequency of all days that are part of large-scale blocking episodes as a function of longitude, for ERA-40 (grey line), the control simulation (blue line) and the future simulation (magenta line). The total number of blocked days for each simulation is given in brackets in the legend. (b) Blocking duration defined as the average frequency of large-scale blocking episodes (at least 5 days duration) as a function of duration (days) for the European region. The maximum duration of blocking episodes is given in brackets in the legend.

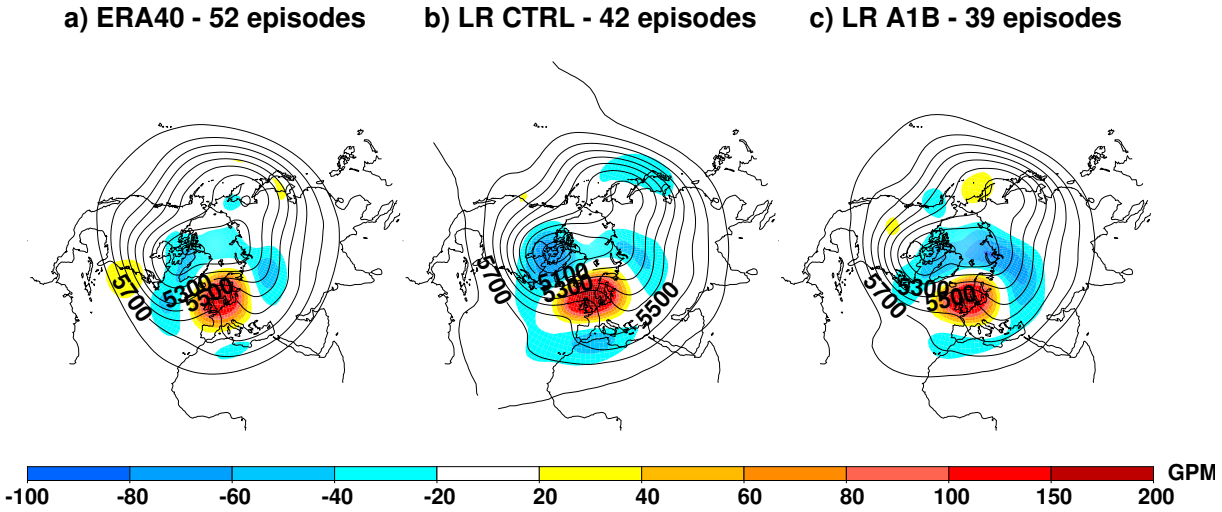

Figure 6.6: Composite analysis on the full (solid contours) and anomaly (color shading) 500 hPa geopotential height fields averaged for all blocking episodes belonging to the European sector for (a) ERA-40, (b) LR CTRL and (c) LR A1B. The composite on the anomaly field for each episode is first obtained by subtracting the field average of all winter days from the field average of all blocked days belonging to each episode. The number of blocking episodes for each simulation is given at the top of each panel.

The climatologies of blocking have first been analysed for ERA-40, LR CTRL and LR-A1B; the frequency, duration and average composite of blocking episodes are presented in Figures 6.5 and 6.6.

6.4.1 Model validation

Winter blocking days are about 21% less frequent in CTRL than in ERA-40, with a gradual increase in model error as we approach the Atlantic basin from about 10°E to 15°W (Fig. 6.5a). There is however a fairly good agreement concerning the location of the highest blocking activity, over the North Sea

between the British Isles and Scandinavia (0° - 15°E). Although the model suffers an overall lack of blocking days and episodes (the latter being underestimated by about 19%), the model is nevertheless able to simulate long-lasting blocks (Fig. 6.5b), with even a slight overestimation of the frequency of long-lasting blocking episodes (> 15 days) and of the maximum spell duration (21 days for CTRL, 18 days for ERA-40). The model shows also a tendency to overestimate the amplitude of the anomalous geopotential height field during blocking episodes (Fig. 6.6). In the reanalysis, the maximum anomaly of the blocking anticyclone reaches nearly 160 geopotential meters (GPM) over southern Scandinavia, whereas in CTRL the highest blocking anomaly is more zonally extended over Scandinavia and the British Isles, and its amplitude reaches 200 GPM, about 25% higher than in ERA-40. Furthermore, European blocking in LR CTRL shows a more pronounced dipole structure than in the reanalysis, with anomalous cyclonic conditions on the southern flank of the blocking anticyclone.

6.4.2 Projected changes

In A1B, the overall number of blocking days and episodes decrease by about 11% and 7% respectively relative to CTRL (Fig. 6.5a). There is little frequency change over the western and eastern parts of the European sector (15°W-5°W and 25°E-30°E), while the greatest change is found over the North Sea between the British Isles and Scandinavia (0°-15°E), where the blocking activity is the highest in CTRL (Fig. 6.5a). The result of the change is a westward shift of the maximum blocking activity over the eastern part of the Atlantic basin. The overall change in the number of European blocking events affects all spell durations greater than 7 days, with a slight tendency toward longer blocks (Fig. 6.5b). There is however a clear decrease in the amplitude of the anomalous blocking anticyclone, and the flow during blocking conditions appears more zonal relative to CTRL (compare Fig. 6.6b and c).

6.5 Climatology of European winter temperature and precipitation: daily mean and variability

In order to gain a better understanding of the relationship linking extreme weather events and blocking, as it is depicted from the observation/re-analysis dataset and as simulated by the model in the present-day and future climates (considered in Section 6.7), the mean and variability of wintertime temperature and precipitation over Europe are first being considered in this section.

6.5.1 Model validation

Daily mean

The spatial distribution of winter temperature and precipitation fields averaged over the 30-year present-day period (1961-1990) are generally well represented in the model (Figure 6.7). In particular, the northeast/southwest temperature gradient over Europe (i.e., cold temperatures over Scandinavia, and warmer conditions over southwestern Europe) is well captured and the model is able to simulate the highest rainfall amount on the windward side of mountainous regions (i.e., in Norway, Alps, Pyrenees) and over western coastal areas (e.g., in Ireland, Scotland).

However, maps of the 30-year averages of precipitation and temperature differences between the

model (MR CTRL and HR CTRL) and the observations reveal that over most of Europe, the model suffers a cold and wet bias, reaching -8°C and +3 mm over the plateaux, and -10°C and +10 mm in mountainous areas (Fig. 6.8). A number of factors could be responsible for these model errors, ranging from large-scale circulation biases, poor parametrization of large-scale precipitation processes, errors in clear-sky radiation and clouds, parametrization of land-surface schemes (Stone and Weaver, 2003; Moberg and Jones, 2004; Coindreau *et al.*, 2007). In addition, the differences between the model and the observations is partly attributed to inaccuracies and errors in the E-OBS dataset, which arise from inhomogeneities in the station measurements, the network density of the meteorological station and the interpolation from station to gridded data (Hofstra *et al.*, 2009).

A sensitivity experiment with the atmospheric GCM LMDZ4, carried out by Coindreau *et al.* (2007), suggests that the wet and cold bias could be attributed to an imperfect parametrization of the hydrological exchanges between the land surface and the atmosphere. They found that using the current land-surface scheme the evaporation rates are too high, which induce a cascade of positive feedbacks on rainfall, soil water content and surface evaporation, the latter being conducive of colder day-time surface temperature. However, these errors in evaporation rates would also be expected to cause night-time greenhouse effect warming, and this is not observed in the model. This indicates that errors in the parametrization of the land-surface scheme alone are not sufficient to explain the temperature biases during the night.

Circulation biases regarding the lack of blocking days (Fig. 6.5a), itself possibly related to a strengthened zonal flow from the Atlantic (as it was shown to be often the case in climate models in Chapter 4; see also Scaife *et al.* (2010)), would be expected to cause milder conditions over large parts of western Europe (Moberg and Jones, 2004). This is not observed either, but this type of systematic error in the large-scale circulation could at least be related to the reduced (enhanced) cold (wet) bias over western parts of Europe (Fig. 6.8a, d, g).

Night-time temperatures are influenced by clouds: by increasing the outgoing longwave radiation during the night (i.e., too few clouds as in Figure 6.11c), nights can be colder (Stone and Weaver, 2003; Moberg and Jones, 2004). Figure 6.11 suggests that this factor may have contributed to the temperature biases observed in Figure 6.8e, with an underestimation of low cloud cover particularly prominent over northeastern regions where the cold bias is the strongest, while middle and high clouds tend to have a relatively small impact on night-time temperatures (i.e., lower cloud bases increase night-time temperatures more efficiently through downward longwave radiation than higher cloud bases) (Dai *et al.*, 1999).

The wet and cold biases are greater in the high resolution simulation at high altitude and over coastal areas (Fig. 6.8c, f and i). Warmer and drier conditions however prevail on the lee side of mountainous ranges (e.g., on the eastern side of the Alps and northern side of the Pyrenees). This indicates that the dynamics of the model (i.e., large-scale circulation and model resolution) contribute nevertheless partly to the overall cold and wet biases of the model. Dynamical aspects could also explain the warm bias over coastal areas during the night in MR CTRL, which decreases (even disappears at places) in the HR CTRL simulation. This is consistent with a higher small-scale variability in the latter (Fig. 6.10c, f), whose role is particularly important where strong temperature contrasts exist (e.g., land/sea gradient is less sharp in low than high resolution models), and where the surface is not homogeneous (e.g., presence of mountains).

Daily variability

The daily standard deviation of temperature and precipitation in the observations and the model is shown in Figure 6.9. It is generally larger in northern and eastern parts of Europe and smaller in the south for temperature, while for precipitation the variability is higher over western Europe, and especially on the windward side of mountain ranges. These patterns can partly be explained by considering the synoptic variability off the Atlantic ocean (Fig. 6.12a and b), which bring mild and rapidly changing weather conditions over Europe, due to the high-frequency transition of cyclonic systems, troughs and ridges. In addition, in northern areas (e.g., Scandinavia), and particularly at night-time, the temperature variability is larger (compare for instance Figures 6.9a and d), possibly because it is less damped by the evaporative latent heat flux than further south and than during the day (i.e., northern areas and night-time periods are more frequently snow- or ice-covered, so there is less evaporative cooling that would compensate for the warm oceanic air masses advected over Europe) (Gregory and Mitchell, 1995). Note also that in some regions the proximity of the ocean reduces the variability of temperature (e.g. over the British Isles).

Figures 6.9 and 6.10 show an underestimation of the precipitation daily variability over most parts of western Europe and coastal areas of Norway in MR CTRL, while higher variability is simulated in mountainous areas (i.e., over the Alps, Massif Central and Spanish mountain ranges). In addition, MR CTRL underestimates the temperature variability over most parts of western Europe and Scandinavia, and overestimates it over eastern parts of Europe (Fig. 6.10a, d). Note also that the positive bias in temperature variability over eastern Europe extends to central Europe during night-time (Fig. 6.10d). The systematic errors in the Atlantic storm track, regarding its underestimated intensity and eastward extension (as shown by comparing Figures 6.12a and b), may contribute to the too small daily variability in temperature and precipitation over western Europe and Scandinavia (Cao *et al.*, 1992; Gregory and Mitchell, 1995). Besides, the positive bias of temperature variability over eastern Europe (and central Europe at night-time) could be associated with the cold temperature bias (being particularly prominent over central Europe at night-time; compare Figures 6.8a and d). According to the previous discussion (see also Gregory and Mitchell (1995)), this cold bias could be associated with more frequent snow-covered land surfaces in those regions, reducing the latent heat flux in the surface heat budget.

Finally, models usually have less variability when they are run at low resolution than when they are run at high resolution (Tustison *et al.*, 2001). This is also the case for HR CTRL, whose variability is enhanced over most parts of the domain (Fig. 6.10c, f, i). The model (HR CTRL) is now able to better represent the daily standard deviation of precipitation and temperature over most regions, except where the positive bias, seen in MR, increases in HR (e.g., eastern France for tn in Fig. 6.10f, over mountainous regions for rr in Fig. 6.10i).

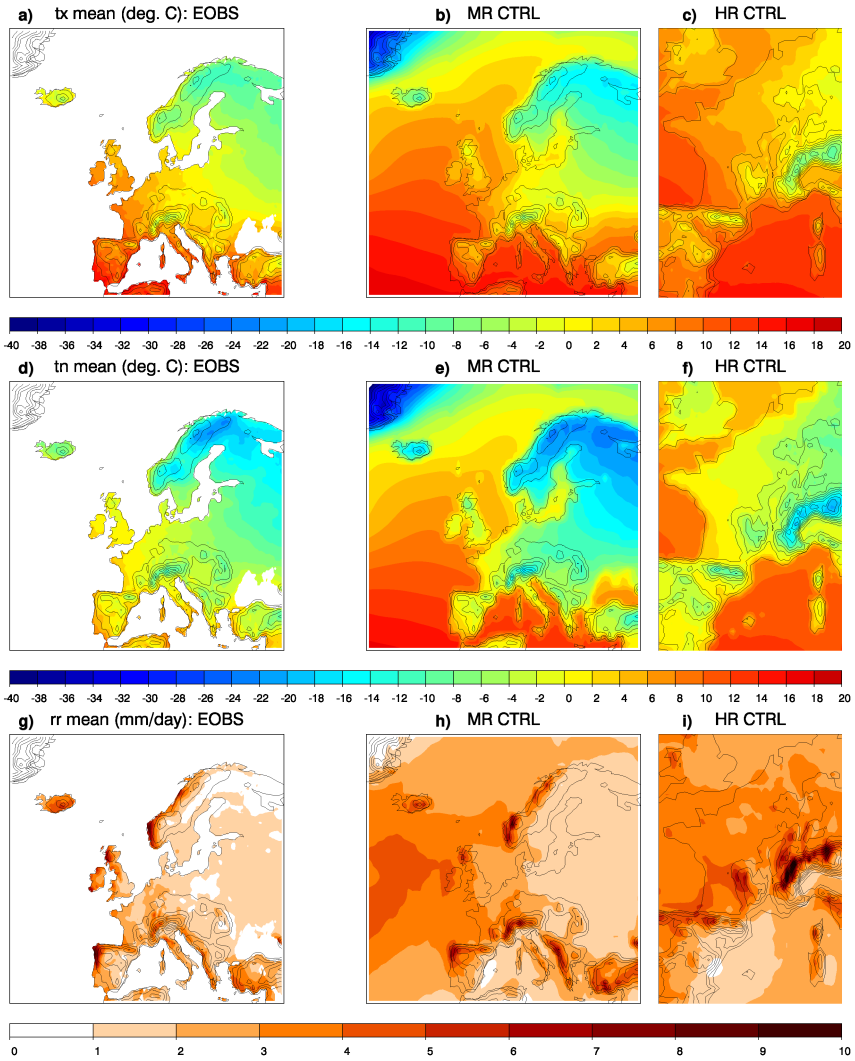

Figure 6.7: Time mean precipitation- and temperature-based fields for EOBS (left), MR CTRL (middle) and HR CTRL (right) for the present-day wintertime period (DJF, 1961-1900). The fields displayed from the top to bottom row are the daily maximum temperature (tx), the daily minimum temperature (tn), expressed in °C, and daily total precipitation (rr) in millimeters.

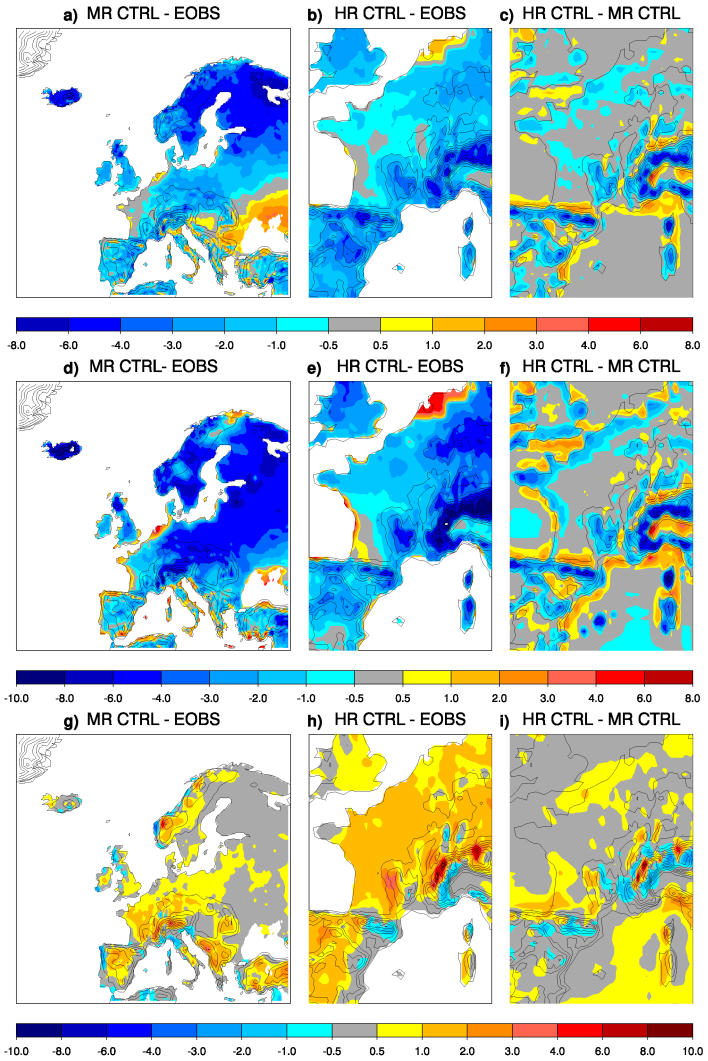

Figure 6.8: Differences of time mean precipitation- and temperature-based fields for MR CTRL - EOBS (left), HR CTRL - EOBS (middle) and HR CTRL - MR CTRL (right) for the present-day wintertime period (DJF, 1961-1900). The fields displayed from the top to bottom row are the daily maximum temperature (tx), the daily minimum temperature (tn), expressed in °C, and daily average precipitation (rr) in millimeters.

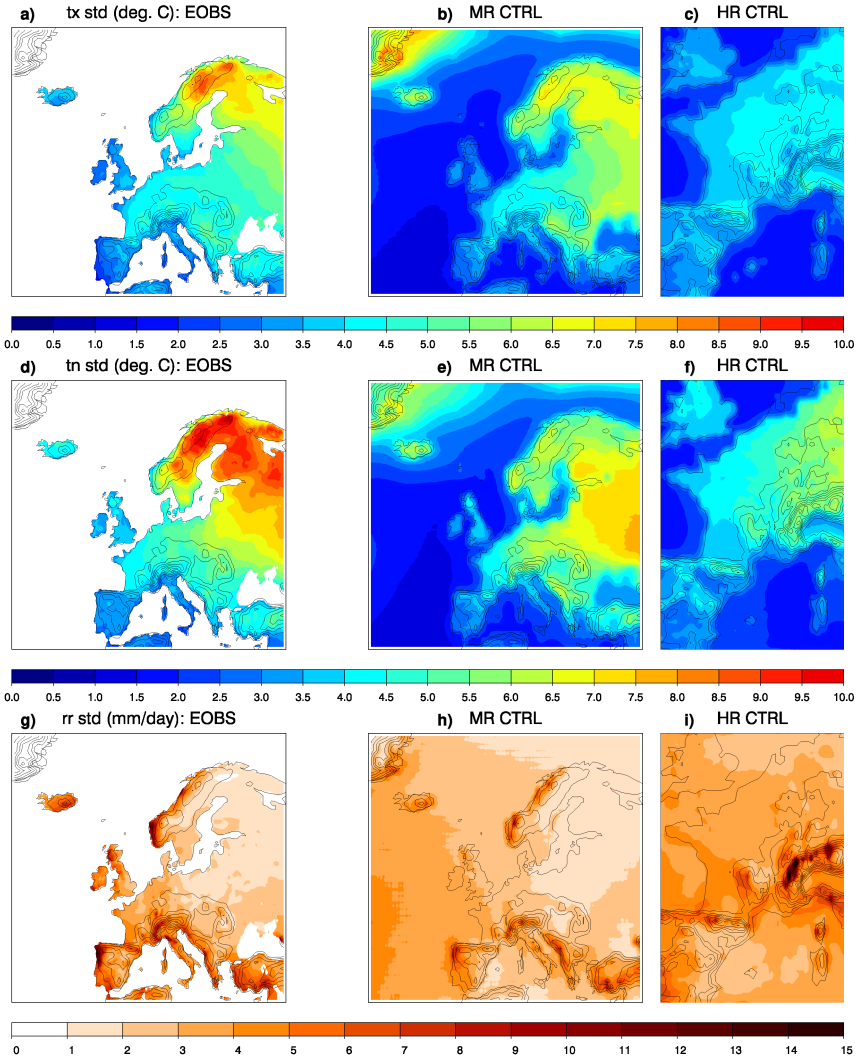

Figure 6.9: Same as Figure 6.7, but for the daily standard deviation.

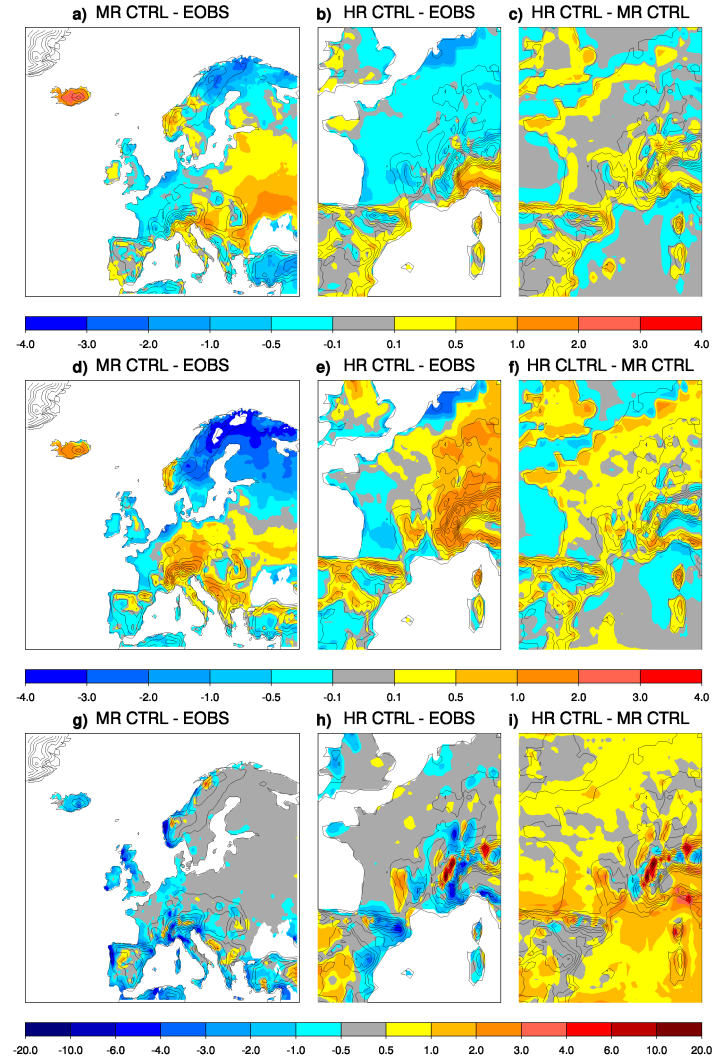

Figure 6.10: Same as Figure 6.8, but for the daily standard deviation.

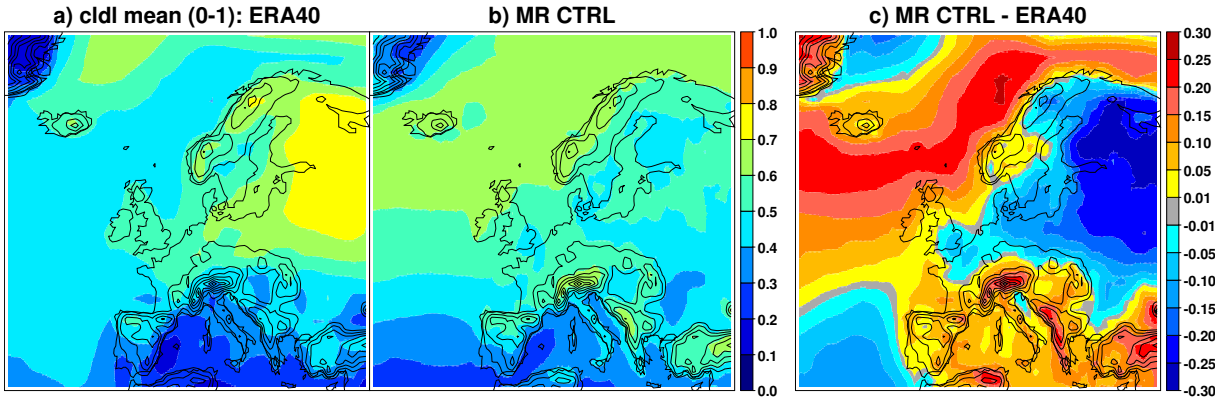

Figure 6.11: Time mean low cloud cover (cldl) for (a) ERA-40 and (b) MR CTRL (middle), expressed as a fractional areas (0-1), for any cloud with low cloud base (< 3.2 km above the ground), including clouds that may have high cloud tops above 3.2 km. The difference of time mean cloud cover (MR CTRL - ERA-40) is displayed in (c).

6.5.2 Projected changes

To analyse changes in the mean and variability for precipitation and temperature indicators in the projection of the 21^{st} century, the 30-year time intervals in the CTRL (1961-1990) and A1B (2021-2050) simulations are chosen, and the time mean and standard deviation for these periods are compared in Figures 6.13 to 6.16.

Temperature

The projected changes of daily minimum and maximum temperature fields show a general increase in the mean, with a southwest/northeast gradient of the change, where northeastern Europe experiences the largest increase, with an average warming ranging between +3°C and +5°C over eastern Europe and parts of Scandinavia (Fig. 6.14a, c). In Norway, parts of France and of the British Isles and the region of the Balkans, the model simulates a lesser mean temperature change between +2°C and +3°C, and the smallest warming reaches +2°C over parts of Spain, France and southern UK, as well as in Ireland. This southwest/northeast gradient of the change results in the reduction of the northeast/southwest temperature gradient observed over Europe; it is therefore expected to induce different advection of heat in a future climate.

The shift in the daily minimum and maximum temperature distribution toward warmer mean conditions and the reduced spatial temperature gradient over Europe is associated with a decreased variance, being more pronounced in northeast than southwest Europe (Fig. 6.16a, c). The effect of these projected changes on the incidence of extreme temperature events would be expected to be conducive of a decreased occurrence of given extreme cold weather events. In addition, the projected temperature changes in the mean and variability tend to be more important during the night than during the day (compare Fig. 6.16a (tx) and c (tn)), which is indicative of a reduced diurnal temperature range. Although changes in the large-scale atmospheric and/or oceanic circulation could be one plausible factor influencing this projected warming over Europe, the reduced diurnal temperature range suggests that changes in feedback processes (e.g., clouds, snow/ice albedo, soil moisture) might also play an important role in the overall temperature changes (Dai *et al.*, 1999). In addition, the more prominent warming at higher than lower latitudes could be indicative of a positive feedback by the surface snow/ice albedo. In that sense, warmer

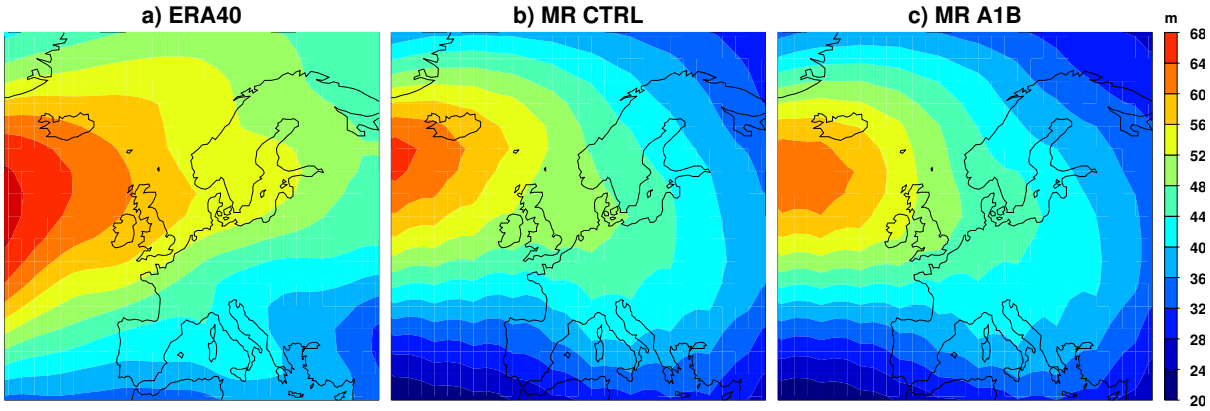

Figure 6.12: Storm track at 500 hPa, defined as the standard deviation of the band-pass filtered (2-8 days) 500 hPa geopotential height field, for (a) ERA-40, (b) MR CTRL and (c) MR A1B.

temperatures over Europe would be conducive of enhanced snow and ice melt in northern regions, reducing the surface albedo and consequently increasing the absorption of solar radiation (Charney *et al.*, 1979; Bony *et al.*, 2006).

Precipitation

The projected changes for precipitation reveal a wetter winter climate over most of Europe, except for southeast Spain and mountainous areas, which are indicated to be up to 20% drier (Fig. 6.14e). A southwest/northeast gradient of the change can also be observed for precipitation, with 5% to 15% increased rainfall amount for most of western Europe, and above 50% over parts of Scandinavia and eastern Europe. The model predicts similar changes for the precipitation variability (Fig. 6.16e), with an increase in rainfall ranging between 1% and 20% over most of Europe (above 50% over parts of Scandinavia), and a 1% to 15% decrease over Spain, mountainous regions and over coastal areas of Norway. Some of the changes in rainfall could be attributed to a reduction of cyclonic activity over western parts of Europe and Scandinavia, as it is illustrated in Figure 6.12c by a reduced extension of the storm track over those regions. Different moisture advection due to changing circulation regimes and/or to changes in the mean precipitation pattern (i.e., southwest/northeast gradient of the change), cloud cover and soil moisture are, among others, plausible factors that could influence the change in rainfall distributions over Europe (Trenberth *et al.*, 2003; Trigo *et al.*, 2004; Tomozeiu *et al.*, 2005).

Finally, note that the differences in the projected changes between MR and HR are particularly prominent for the precipitation field (mean and variability) in mountainous areas (compare Fig. 6.14e and f for the mean and Fig. 6.16e and f for the daily variability), suggesting that downscalling is probably a necessary step in modeling to enable a more precise analysis for precipitation. On the other hand, the similarity of the MR and HR temperature patterns indicate that perhaps downscalling is not crucial for that variable.

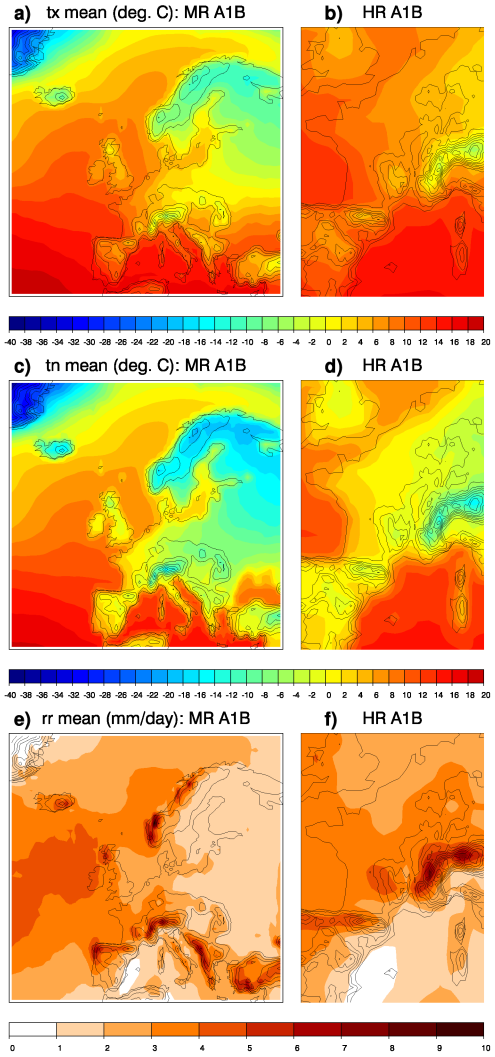

Figure 6.13: Same as Figures 6.7, but for projected changes under the A1B scenario. MR A1B (left) and HR A1B (right).

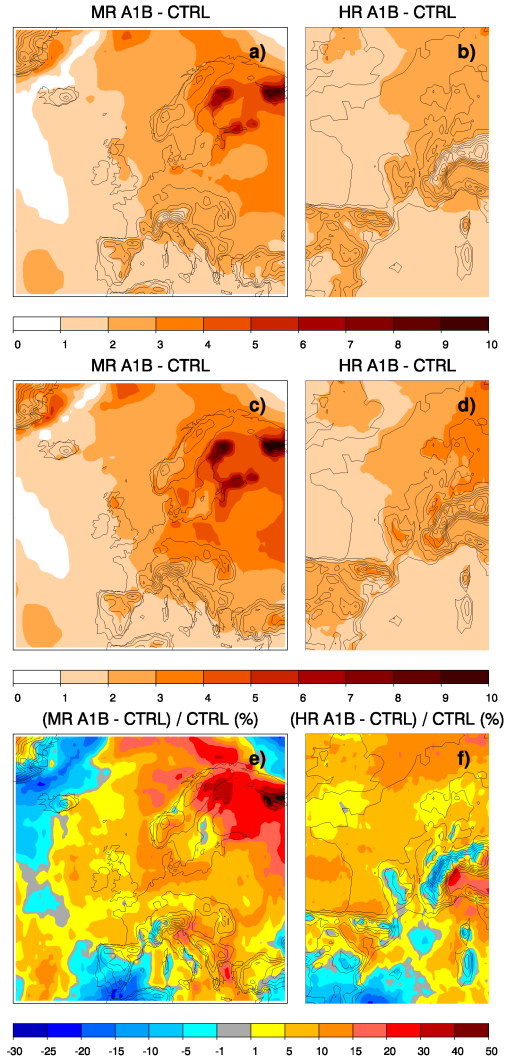

Figure 6.14: Projected changes under the A1B (2021-2050) scenario, relative to CTRL (1961-1990) for MR (left) and HR (right), given by the absolute difference for temperature fields, and the percentage difference for precipitation.

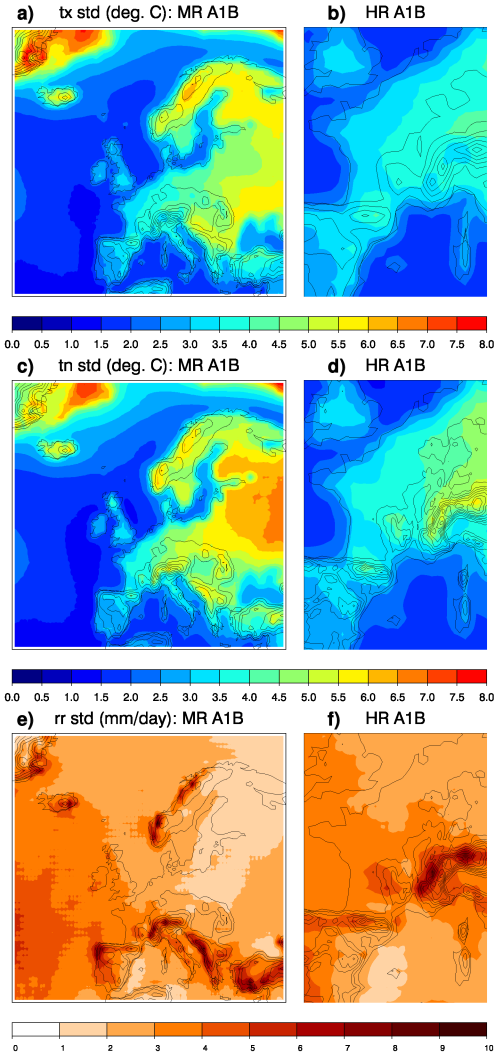

Figure 6.15: Same as Figure 6.13, but for the daily standard deviation.

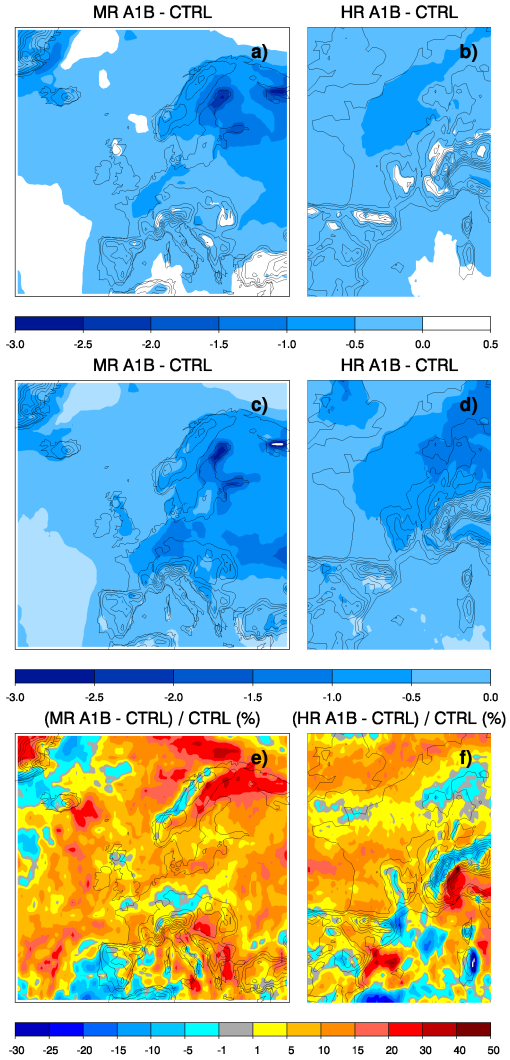

Figure 6.16: Same as Figure 6.14, but for the daily standard deviation.

6.6 Blocking signatures for precipitation and temperature averages

An analysis of the impact of European blocking on the regional climate is presented in Figure 6.17, as blocking signature maps (see Section 6.3.3) computed for daily fields of 500 hPa geopotential height, precipitation, 2-metre minimum and maximum temperatures, as well as the diurnal temperature range (DTR = tx - tn) for the present-day and future simulations.

6.6.1 Observations

The signature maps of daily maximum and minimum temperatures (Fig. 6.17a and f, respectively) show positive anomalies over Scandinavia, British Isles, Iceland and northeastern Europe, reaching a maximum of +9°C over north Scandinavia, and resulting from the northerly inflow of warm oceanic air masses. Cold anomalies, ranging between -0.1°C and -5°C are located over central and southern Europe, regions experiencing anomalous advection of cold and dry continental air during European blocks. The effect of anomalous advection can be recognised with isolated areas of warm anomalies on the lee side of mountainous areas (over the Alps, the Cordillera Cantánbrica and Sistema Central in Spain), caused by the Foehn winds[4] (Fig. 6.17a). However, as it can be seen in the signature maps of the diurnal temperature range (Fig. 6.17k), other important factors (e.g., clouds, soil moisture) could influence the surface temperature (Dai *et al.*, 1999). Here, blocking-related anomalies in the net radiative fluxes are considered in Figure 6.19. Over large parts of central and eastern Europe, the DTR increases during blocking conditions. This may be achieved by enhanced net surface solar radiation and net surface thermal radiation during long clear-sky periods associated with the anticyclonic conditions, as suggested from Figure 6.19a. Over parts of Scandinavia, British Isles and Iceland, the DTR decreases and is consistent with reduced net thermal radiation, while anomalies in the net solar radiation remain fairly small. The signature maps of daily average precipitation (Fig. 6.17p) show, over most of the continent, drier conditions, the exception being over the coastal areas of Norway on the windward side of the mountainous range, the east coast of Spain and some Mediterranean islands and over Iceland, regions which are exposed to strong anomalous advection of moist air masses.

It is worth mentioning that these patterns of blocking-related climate anomalies are highly dependent on the location of blocking. Figure 6.18 shows an alternative picture for blocking situated to a more northwest location of that presented in Figure 6.17, over the Atlantic basin between 45°W and 0°. In this case, cold anomalies (ranging between -0.1°C and -4°C) cover most of Europe (except northern parts of Scandinavia, Iceland and Greenland), as the anomalous anticyclonic circulation pulls colder air than normal, originating much further north near polar regions than during European blocking (compare the geopotential height anomaly contours between Figures 6.17 and 6.18). Northern parts of Scandinavia tend to experience slightly warmer conditions during Atlantic blocking (up to +2°C) as a result of the northerly inflow of warm oceanic air masses over land. On the other hand, anomalous advection of warm and humid air from southern parts of the Atlantic ocean brings warm anomalies over Greenland (up to +6°C) and Iceland (between +1°C and +4°C).

For the precipitation field (Fig. 6.18c), the pattern exhibits drier conditions under the action of the blocking high, over northwestern parts of Europe (e.g., France, British Isles, south Scandinavia, where anomalies reach -2 mm/day), and increased rainfall over regions that are influenced either by inflow

[4]Foehn winds are dry and hot winds, warmed adiabatically when descending along the lee side of mountains.

of oceanic air masses (up to +2 mm/day over coastal areas of Scandinavia and up to +4 mm/day over Greenland) or by enhanced cyclonic conditions (up to +2 mm/day over the Mediterranean basin and southeastern Europe).

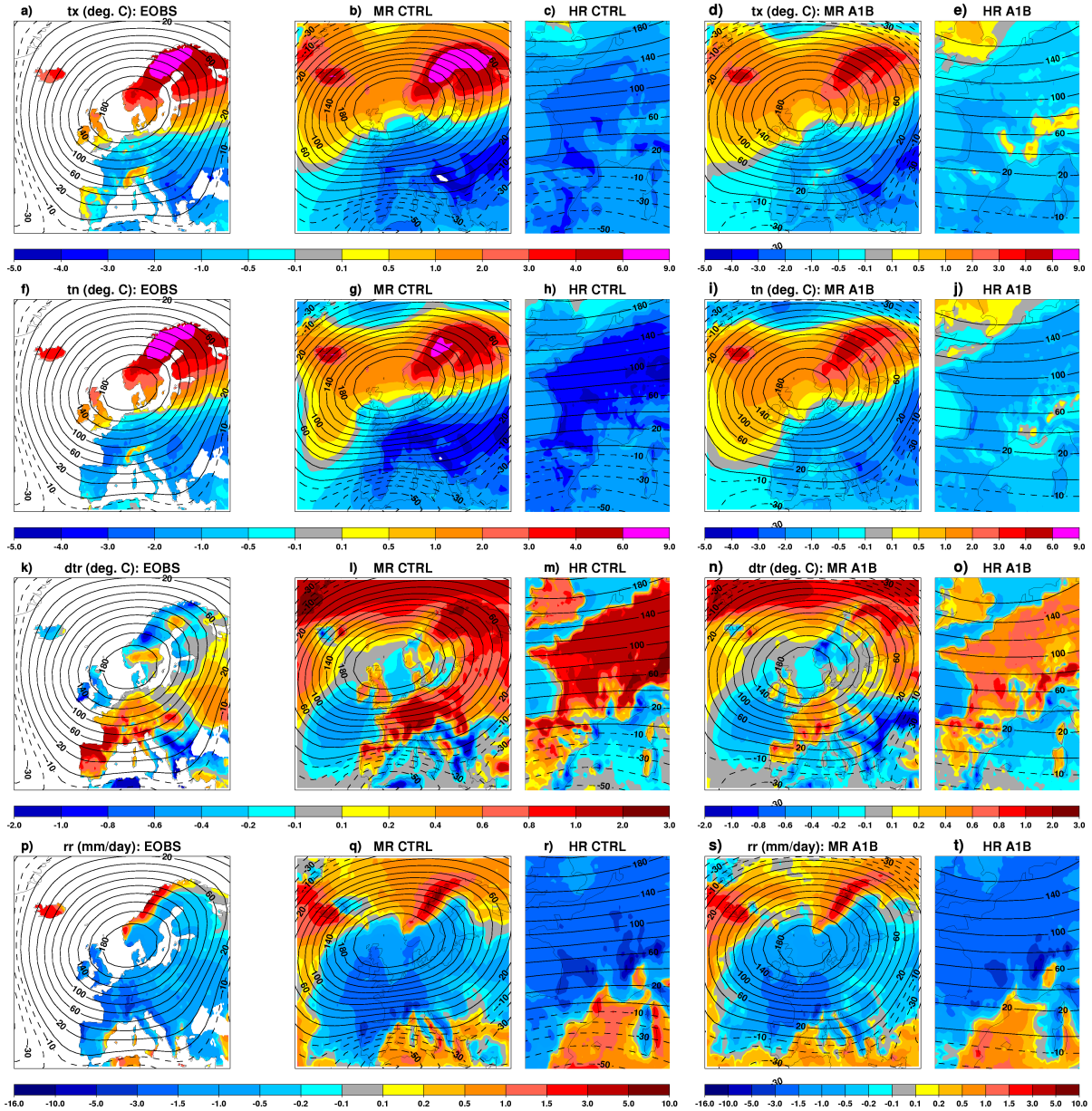

Figure 6.17: Blocking signature maps (computed by subtracting the average field of all non-blocked days from the average field of all blocked days within the European region) for precipitation- and temperature-based fields (color shading) and for the 500 hPa geopotential height (contours). Present-day simulations (EOBS, MR CTRL and HR CTRL) are displayed in the first three columns, future climate simulations (MR A1B and HR A1B) are in the last two columns. The fields displayed from the top to bottom row are the daily maximum temperature (tx), the daily minimum temperature (tn), the diurnal temperature range (dtr) and daily average precipitation (rr). Note that the robustness of those results depends partly on the number of blocked days in ERA-40 and the model simulations (see Figure 6.5).

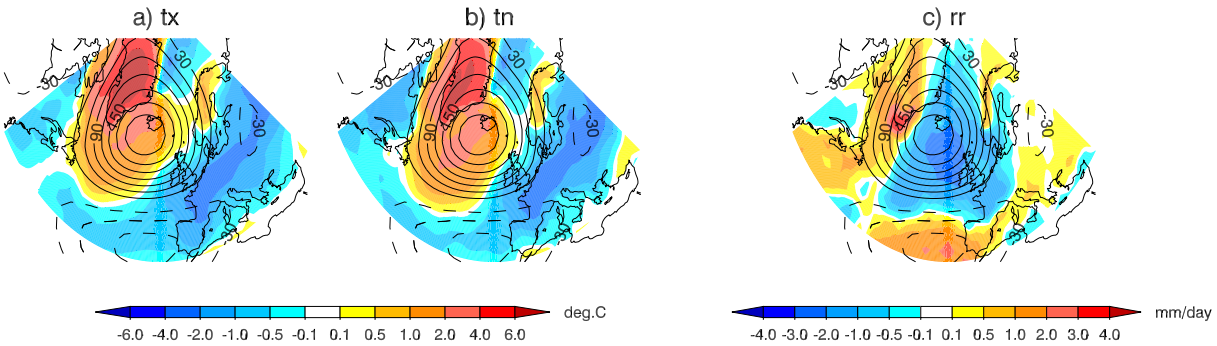

Figure 6.18: Same as Figure 6.17, but the blocking index is calculated at each longitude and time step across the Atlantic domain (40°W - 0°). The fields displayed from left to right are the daily maximum temperature (tx), the daily minimum temperature (tn) and daily average precipitation (rr) for the reanalysis ERA-40.

6.6.2 Model validation

The model simulates the impact of European blocking on the temperature and precipitation fields relatively well, although the temperature patterns are slightly displaced to the north due to the differences in blocking signature and anomalous advective winds, which tend to be more zonal over eastern and central Europe in the model. For instance in Figure 6.17b and g only the northern part of UK experiences positive temperature anomalies, while in ERA-40/E-OBS (Fig. 6.17a and f) the whole country is affected by warmer conditions, due to a more southerly direction of the anomalous flow. Another difference between the observed and simulated blocking impact concerns the amplitude of the signatures, being higher in the model than in the observations. Enhanced amplitudes in temperature and precipitation anomalies could be caused by more intense and persistent blocking episodes (refer to Section 6.4), generating more persistent and stronger advective winds. In addition, the average gradient between where the anomalous advection of air masses originates (e.g., northeastern Europe in Figure 6.7b) and the region experiencing the anomalous weather condition (e.g., France in Figure 6.7b) is overestimated. Therefore, even with similar strength in the advective winds, the advection of cold air masses over France ($V.\nabla\Psi$, where V is the advective wind and Ψ the advected quantity) would be greater in the model than in the observation.

The effect of blocking on DTR is overestimated and positive over most of Europe, and even opposite sign in the model compared to E-OBS over the British Isles and Scandinavia (compare Fig. 6.17k and i). On the other hand, the net solar radiation gained during the day is greater than the net thermal radiation lost during the night (Fig. 6.19b and e), and this alone compared with the radiative fluxes from ERA-40 (Fig. 6.19a and d), would not cause the model to overestimate the DTR. However, the diurnal temperature range is also influenced by soil moisture content (Dai *et al.*, 1999; Coindreau *et al.*, 2007). Drier conditions over central and eastern Europe (Fig. 6.17q), are likely to reduce the soil moisture content, which in turn would decrease both day-time surface evaporative cooling and night-time greenhouse effect warming. According to Figure 6.19b, the former is reduced by positive anomalies in the net solar radiation, while the latter is enhanced by the net thermal radiative fluxes (Fig. 6.19e). Anomalously dry conditions and absorbed net solar radiation being overestimated in the model, could contribute to increase the day-time temperature more in the model than observed (compare Fig. 6.17b and g with Fig. 6.17a and f), and explain the DTR overestimation over most of Europe (compare Fig. 6.17k and l).

The higher resolution model (HR CTRL) seems to improve some aspects of the simulation, such as the diurnal temperature range and precipitation in the Mediterranean basin (Fig. 6.17m and r), but a clear Foehn effect near the Alps (as seen in Fig. 6.17a or f) cannot be simulated, even in HR CTRL.

6.6.3 Projected changes

Projected changes in the blocking signature maps (Fig. 6.17, last two columns) show similar spatial patterns to the CTRL simulations, although the amplitude of the signatures decreases in the A1B scenario, especially for the temperature fields (Fig. 6.17d and i). This may be due to the changes in the blocking pattern, with less intense geopotential height anomalies and more zonal flow during blocking conditions in the A1B scenario (Section 6.4). In that sense, anomalous advective winds are weaker, and the net radiative fluxes are presumably reduced as well, as is suggested in Figure 6.19c and f. In addition, recall that the model predicts a southwest/northeast gradient of the changes in average precipitation and temperature, with greater (lower) warming and wetter conditions over northeastern (southwestern) Europe (Fig. 6.14). This acts to weaken the climatological spatial gradient and thus reduce the geographical contrasts across the continent. Therefore, the advection of cold and dry continental air masses over central Europe is expected to be weaker in the future scenario, as the advected term $\nabla\Psi$ is smaller. Similarly, the advection of warm and humid oceanic air masses over Scandinavia and eastern Europe is also expected to be weaker.

The DTR signature decreases as well under the A1B scenario (compare Fig. 6.17n and l). It seems to be associated with larger changes in day-time temperature over Scandinavia (compare Fig. 6.17d and b), and larger changes in night-time temperature over central Europe (compare Fig. 6.17i and g). These results are consistent with the changes in the net radiative fluxes, with the most prominent decrease in solar radiation over Scandinavia (Fig. 6.19c) and in thermal radiation over central Europe (Fig. 6.19f). The influence of blocking on net surface solar radiation is notably weakened in the future projection, which must be due to a smaller modification of albedo (i.e., clouds, snow).

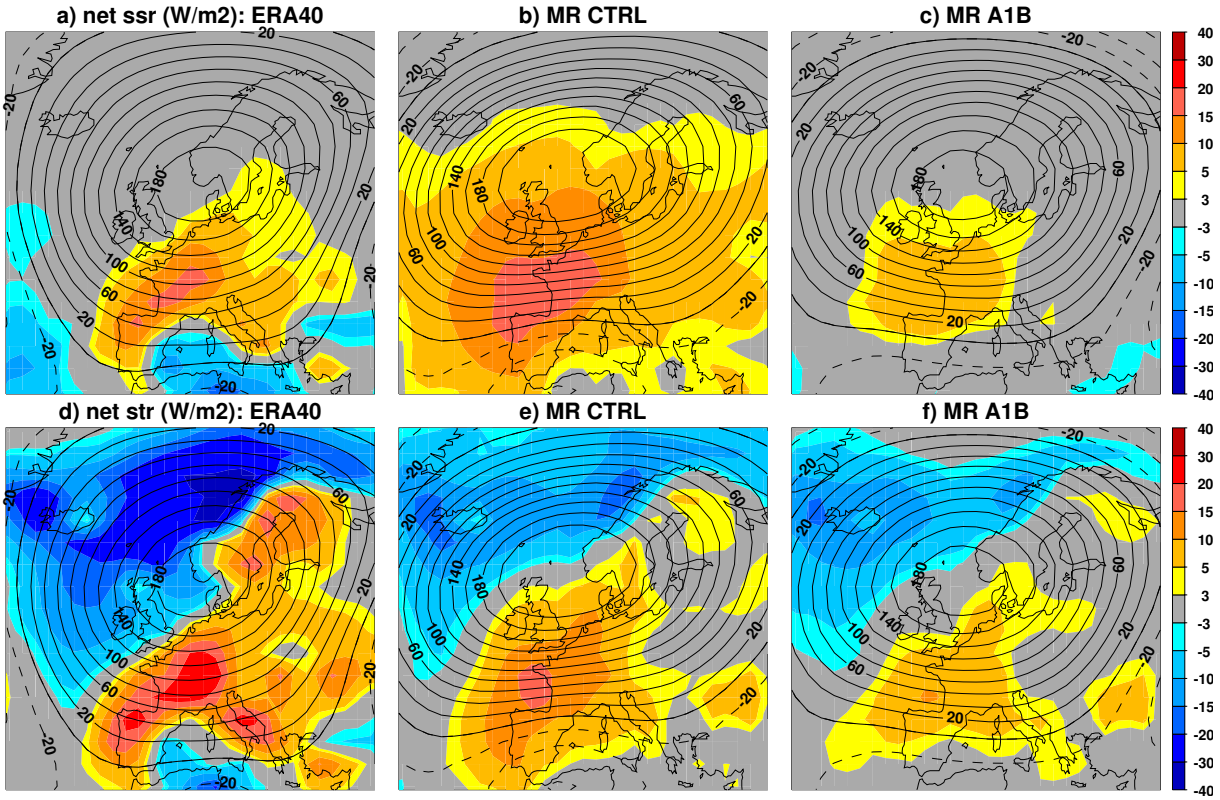

Figure 6.19: Same as Figure 6.17, but for the net surface solar radiation (SSR, top) and the net surface thermal radiation (STR, bottom) for ERA-40 (left), MR CTRL (middle) and MR A1B (right). SSR, defined as the absorbed solar radiation at the surface, is dependant on the albedo (SSR = incident solar flux - incident solar flux x albedo); Under clear-sky conditions, high (low) values of SSR are found for example over the Oceans (desertic areas). Net STR (under clear-sky conditions) depends on the temperature of the surface; high surface temperatures increase the STR, for instance over the Oceans. The presence of clouds can reduce both the SSR and STR, depending on the nature of the clouds (Dai *et al.*, 1999).

6.7 Blocking impact on extreme precipitation and temperature events

6.7.1 Contribution of blocking to extreme weather event frequencies

The relative contribution of blocking to extreme weather event frequencies with respect to average conditions (analysed with the ratio R in Eq. 6.1) in the present-day and future climates are shown in Figures 6.20 for cold day extremes, 6.21 for cold night extremes, 6.22 for warm day extremes, 6.23 for warm night extremes, 6.26 for rainfall extremes and 6.27 for dry extremes (refer to Table 6.1 for the listing of extremes). Results are displayed only for the regions where the association between blocking and extreme days is significant at the 5% significance level; white areas are therefore regions where significance is not reached, and could be the result of simultaneous occurrence of extreme and blocking days "by chance". The regions of non-significance tend to be located (1) where the precipitation and temperature mean anomalies are weak (e.g., northeastern Europe for cold anomalies - compare Fig. 6.17a, b with Fig. 6.20a, b), and (2) where the total number of extremes (in blocking and non-blocking days - Figures C.8 to C.13) is too small. The latter point is particularly relevant for the A1B simulations, as for instance over parts of Scandinavia for cold extremes in Figures C.8d, i, n and C.14d, i, n, where the number of extremes during both blocking and non-blocking days is very small. This test of significance also provides a good indication of the regions being the most or least severely affected by different types

of extreme weather events during blocking conditions. Over central Europe the significance of the results tends to be reduced as the severity of the extremes increases (i.e., as the percentile increases), while over Scandinavia results tend to be significant for moderate as well as for strong extremes (e.g., in Figure 6.22). This indicates that extreme weather events occurring over Scandinavia are highly influenced by blocking, compared with the central and western Europe region, which is less severely affected by blocking-related extremes.

Model validation

During European blocking, northern Europe experiences more warm and wet (less cold and dry) extreme weather conditions than on average, due to the anomalous advection of air masses from the southern North Atlantic ocean over Scandinavia. On the other hand, anomalously cold and dry continental air from northeastern countries is advected, and brings more cold and dry (less warm and wet) extremes over southern and central parts of Europe.

The likelihood of extremes during blocked situations tend to increase with extreme severity. For instance over Norway, the observed likelihood of extreme warm days is between 2 and 2.5 times higher during blocking for tx75n, between 2.5 and 3 times higher for tx90n and up to 4 times higher for tx95n (Fig. 6.22a, f, k). A similar tendency is observed for $R < 1$ (when extremes are less likely to occur during blocking than average conditions), where in Figure 6.23a, f, k over western parts of France for instance, $0.4 < R < 0.8$ for tn75n, $0.2 < R < 0.6$ for tn90n and $0 < R < 0.6$ for tn95n.

The model simulates similar patterns, but the statistical significance of the results is greater and the ratios (R) are overestimated. In other words, the degree of association between blocking and extreme day occurrence and the contribution of blocking to extremes with respect to average conditions (whether it is positive or not) are overestimated by the model (despite the fact that the frequency of blocking days is underestimated - see Figure 6.5). For instance, the observed contribution of blocking to the 5^{th} percentile of the daily minimum temperature distribution (tn5n) is between 1.5 and 2 times higher than average over western parts of France and northern parts of Spain (Figure 6.21k), where as the model simulates R values ranging between 2.5 and 4 (Figure 6.21l; up to twice the observed values). In addition, significant simulated ratios (greater than one) spread over all western and central Europe, while in the observations only parts of western Europe and the Balkans are significantly affected by the 5^{th} percentile cold night extreme events. Two possible reasons for an overestimated blocking impact, previously suggested in Section 6.6, are (1) blocking episodes are more intense (compare the blocking anticyclonic anomalies between Fig. 6.6a and b) and persistent (see legend in Fig. 6.5b) - i.e., advective winds are stronger and more persistent, and (2) the average gradient between where the anomalous advection of air originates and the region experiencing the anomalous weather condition is overestimated (compare for instance Fig. 6.7a and b, where the average temperature gradient between Scandinavia and western France is overestimated in the model).

The observed contribution of blocking to cold extremes tends to be greater during the night than during the day (Fig. 6.25a, f, k), while contribution to warm extremes is greater during the day than during the night (Fig. 6.24a, f, k). This difference of blocking impact between day- and night-time temperature extremes cannot be achieved by anomalous advection alone. It is however consistent with positive anomalies in incoming solar and outgoing thermal radiation fluxes over most of Europe (Fig. 6.19a, d). In that sense, the effect of anomalous radiative fluxes alone is expected to be conducive of colder nights

and warmer days over the entire continent, except maybe over the coastal regions of Scandinavia, where nights would experience less radiative cooling. As a result, cold nights and warm days are expected to be more frequent than warm nights and cold days, whether the contribution of blocking on cold and warm extremes is greater or lower than average.

The model simulates different features with that respect. According to Figure 6.19b, e, the simulated anomalies in incoming solar and outgoing thermal radiation fluxes are also positive, so a tendency for more frequent cold nights and warm days than warm nights and cold days is also expected in the model. This was observed for the blocking signature maps in Figure 6.17l (i.e., positive DTR), and it is also the tendency for moderate extremes (25^{th} and 75^{th} percentiles in Fig. 6.25b and 6.24b). However, for more severe extreme temperatures, the simulated contribution on cold extremes tends to be greater during the day than during the night over central regions such as eastern France, Germany, Austria and northern Italy. As for warm extremes, the difference of blocking impact between day- and night-time extremes decreases with the severity of the events, such that for high percentiles (e.g., tx95n), the contribution of blocking is similar during the day and the night. This presumably results from noise in the composites, due to small sample sizes of extreme blocking days above a certain percentile threshold (see Figures C.10l, m and C.11l, m).

Projected changes

For all extreme indices and everywhere over Europe (except for cold extremes over Scandinavia), the contribution of blocking to the occurrence of extreme weather events is projected to be lower in the future scenario, whether the contribution is positive or not. The contingency/Chi-square analysis suggests also that the relationship between blocking and extreme days is less robust in the future climate (i.e., the area covered by significant results is reduced in A1B relative to CTRL).

Blocking-related extreme cold events are barely existent in the A1B scenario, particularly for strong extremes (i.e., tx5n, tn10n and tn5n in Figures 6.20 and 6.21). Most of this change is more likely to be attributed to the average global warming over Europe (see Section 6.5.2), than to changes in blocking characteristics (i.e., reduced frequency and intensity - Fig. 6.5 and 6.6). Indeed, the projected changes in the mean climate, indicating a shift in the temperature distributions toward warmer mean conditions with a reduced variance (Section 6.5.2), are consistent with the decreased number of extreme cold events, seen in Figures C.8, C.9, C.14 and C.15, whether they occur in blocking or non-blocking days. Precautions have to be taken here when analysing the changes in blocking-related cold extreme events, as the overall changes in blocking and extreme frequencies strongly reduce sample sizes and the robustness of the results. Nevertheless, although the results regarding blocking-related cold extremes in A1B are not significant over most parts of the domain (see Fig. 6.20 and 6.21), Figures 6.28a to l show that the contribution of blocking to cold extreme frequency with respect to the average conditions of the future climate tends to be lower (higher) over central and western Europe (Scandinavia) in the A1B scenario (i.e., $R_{A1B} - R_{CTRL} < 0$ over the whole domain, with $R_{CTRL} > 1$ over central and western Europe and $R_{CTRL} < 1$ over Scandinavia in Figures 6.20 and 6.21).

The number of warm extremes over Europe increases in the A1B scenario in both blocking and non-blocking conditions (Fig. C.10, C.11, C.16 and C.17), so the results regarding the projected changes in blocking-related warm extremes can be analysed with more confidence, as the sample sizes are increased compared to the CTRL scenario. Although this change in warm extreme frequency is likely to be attributed to the average global warming over Europe, blocking events also contribute to an increased

frequency of warm extremes over central and western Europe (i.e., $R_{A1B} - R_{CTRL} > 0$ over central and western Europe in Figures 6.28m to x, where $R_{CTRL} < 1$ in Figures 6.22 and 6.23). However, over Scandinavia, blocking contributes to a decreased warm extreme frequency in the A1B scenario (i.e., $R_{A1B} - R_{CTRL} < 0$ over Scandinavia in Figures 6.28m to x, where $R_{CTRL} > 1$ in Figures 6.22 and 6.23).

In the future climate, blocking episodes will bring "milder" weather conditions over Scandinavia (i.e., less frequent warm and cold extremes during blocking relative to average conditions in A1B than in CTRL), and over central Europe blocking-related events are likely to be shifted toward warmer extremes (i.e., less (more) frequent cold (warm) extremes during blocking relative to average conditions in A1B than in CTRL), although it is important to keep in mind that the results regarding cold extremes are mostly non-significant over the whole European domain.

As it is discussed in Section 6.6.3, the southwest/northeast gradient of the average warming over Europe (Fig. 6.14a and c) is conducive of weaker anomalous advection of cold (warm) air masses over central Europe (Scandinavia) during blocking situations, and therefore triggering less cold (warm) extremes over those respective regions, in addition of more warm (less cold) extremes over the entire continent due to the average global warming.

The relative contribution of blocking to extreme precipitation indicators also have a tendency to be lower in the future climate (i.e., $R_{A1B} - R_{CTRL} < 0$ ($R_{A1B} - R_{CTRL} > 0$) in Figure 6.29, where $R_{CTRL} > 1$ ($R_{CTRL} < 1$) in Figures 6.26 and 6.27), with more (less) frequent blocking-related extreme precipitation (dry) events over central and western Europe, whereas Scandinavia will experience less (more) frequent blocking-related extreme precipitation (dry) events in the future than in the present-day climate.

Recall from Section 6.5.2 that the mean precipitation increases over the entire continent, with a larger (smaller) increase over northeast (southwest) Europe. As a result, anomalous advection of humid (dry) air masses over Scandinavia (central and western Europe) is expected to be lower, explaining the lower contribution of blocking to high rainfall and dry day extremes over all Europe.

In addition to the changes in the mean climate, anomalous advective winds are expected to be weaker due to less intense blocking episodes (compare the blocking anticyclonic anomalies between Fig. 6.6b and c), therefore reducing even more the contribution of blocking to extreme frequencies with respect to average conditions.

Generally speaking, although the contribution of blocking to extreme weather events tend to be reduced in the future climate (except maybe for cold extremes over Scandinavia), the spatial distribution of extremes within the blocking regime remains mostly unchanged, with blocking events still being conducive of more warm and wet (less cold and dry) extreme weather conditions than on average over northern Europe, whereas more cold and dry (less warm and wet) extremes than on average occur over southern and central parts of Europe.

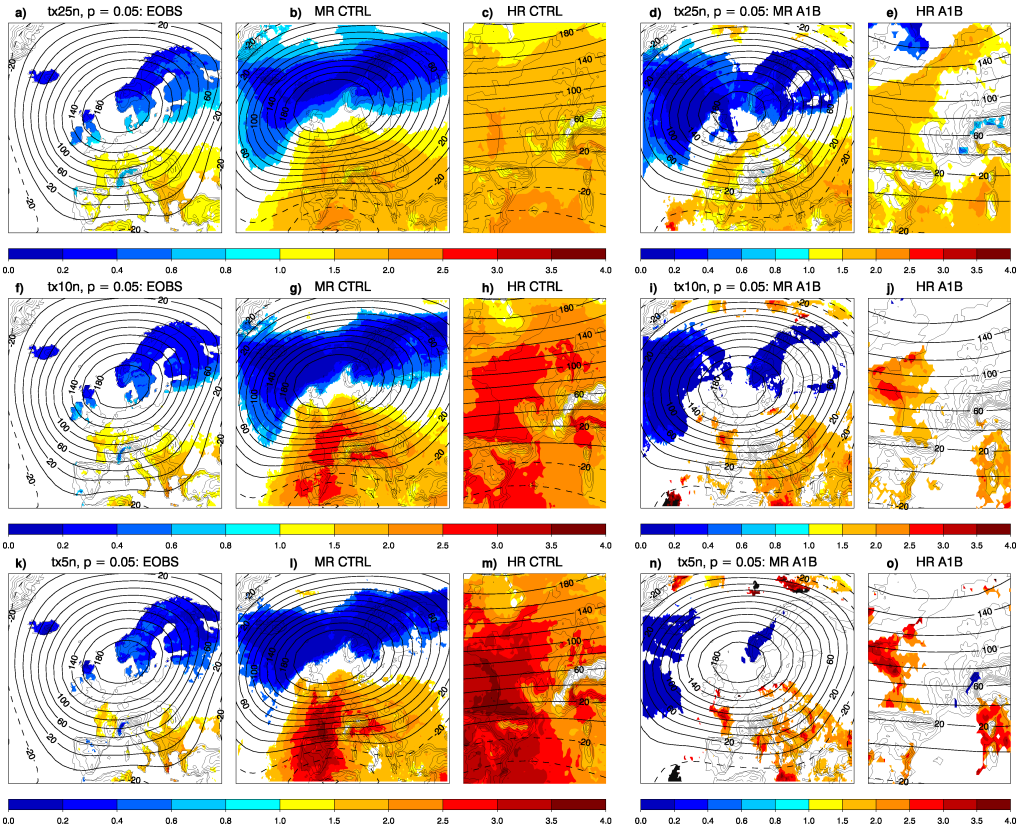

Figure 6.20: Relative contribution of blocking to **cold day extreme** frequencies with respect to average conditions. For values above (below) 1 the contribution of blocking to extremes is greater (lower) than average conditions. White areas correspond to regions where the Chi-square test is not significant. Solid (dashed) black contours represent positive (negative) values of the blocking geopotential height signature. The fields displayed from the top row to the bottom row are the 25^{th}, 10^{th}, 5^{th} percentile of the daily maximum temperature distribution (tx25n, tx10n, tx5n). From left to right: EOBS, MR CTRL, HR CTRL, MR A1B and HR A1B.

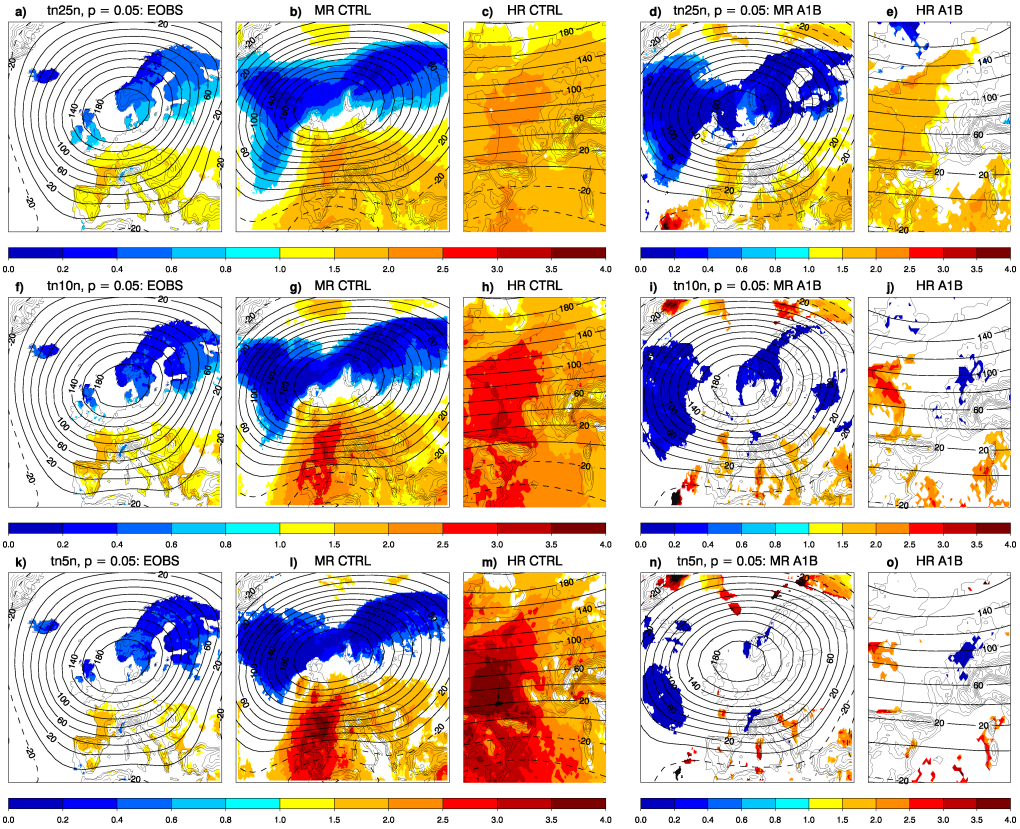

Figure 6.21: Same as Figure 6.20, but for **cold night extremes**, with the 25^{th}, 10^{th}, 5^{th} percentile of the daily minimum temperature distribution (from top to bottom: tn25n, tn10n, tn5n)

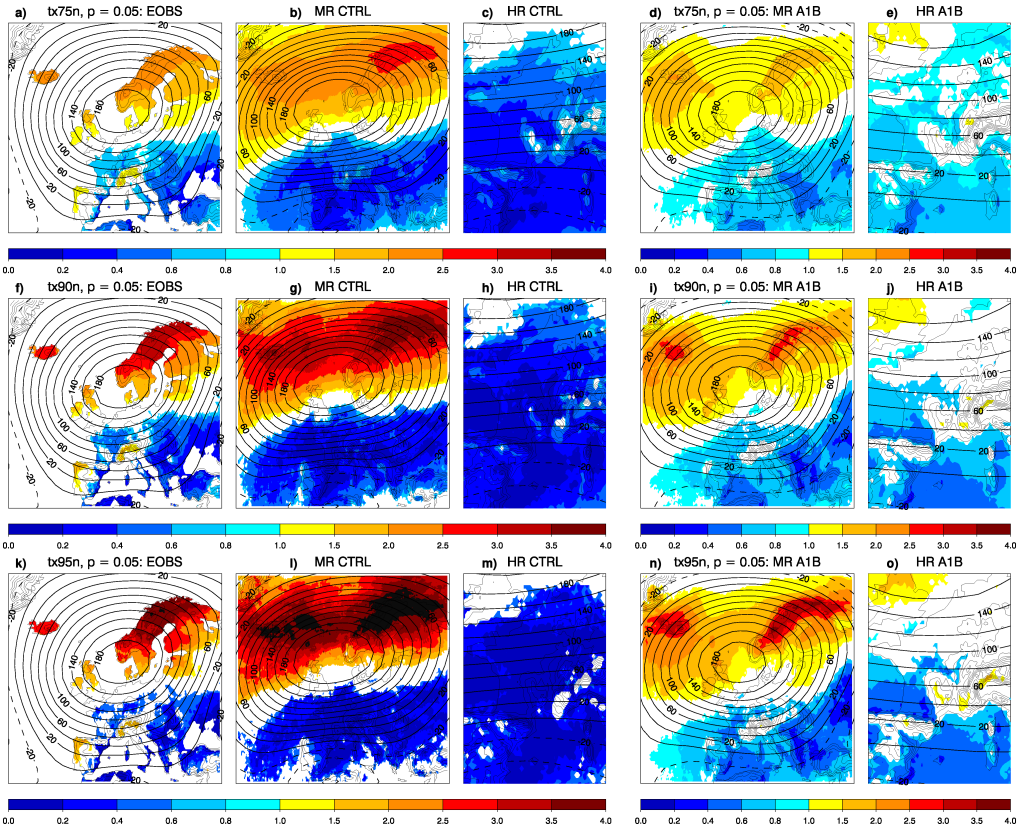

Figure 6.22: Same as Figure 6.20, but for **warm day extremes**. From top to bottom: 75^{th}, 90^{th}, 95^{th} percentile of the daily maximum temperature distribution (tx75n, tx90n, tx95n).

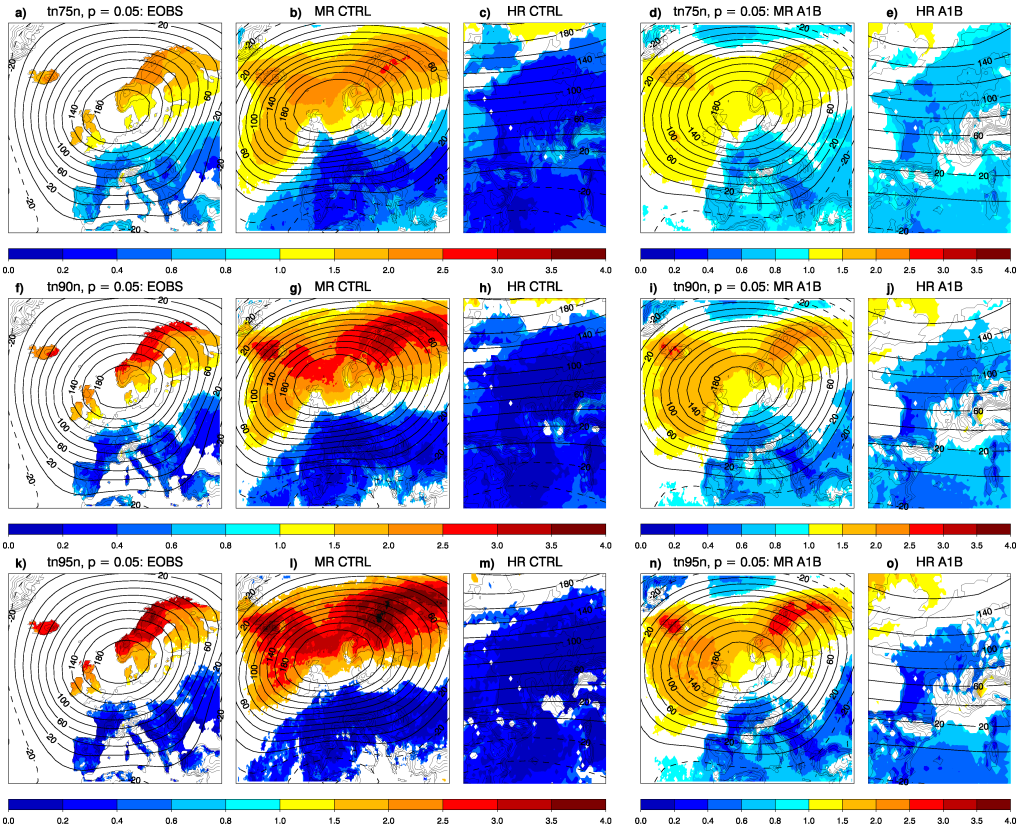

Figure 6.23: Same as Figure 6.21, but for **warm night extremes**. From top to bottom: 75^{th}, 90^{th}, 95^{th} percentile of the daily minimum temperature distribution (tn75n, tn90n, tn95n).

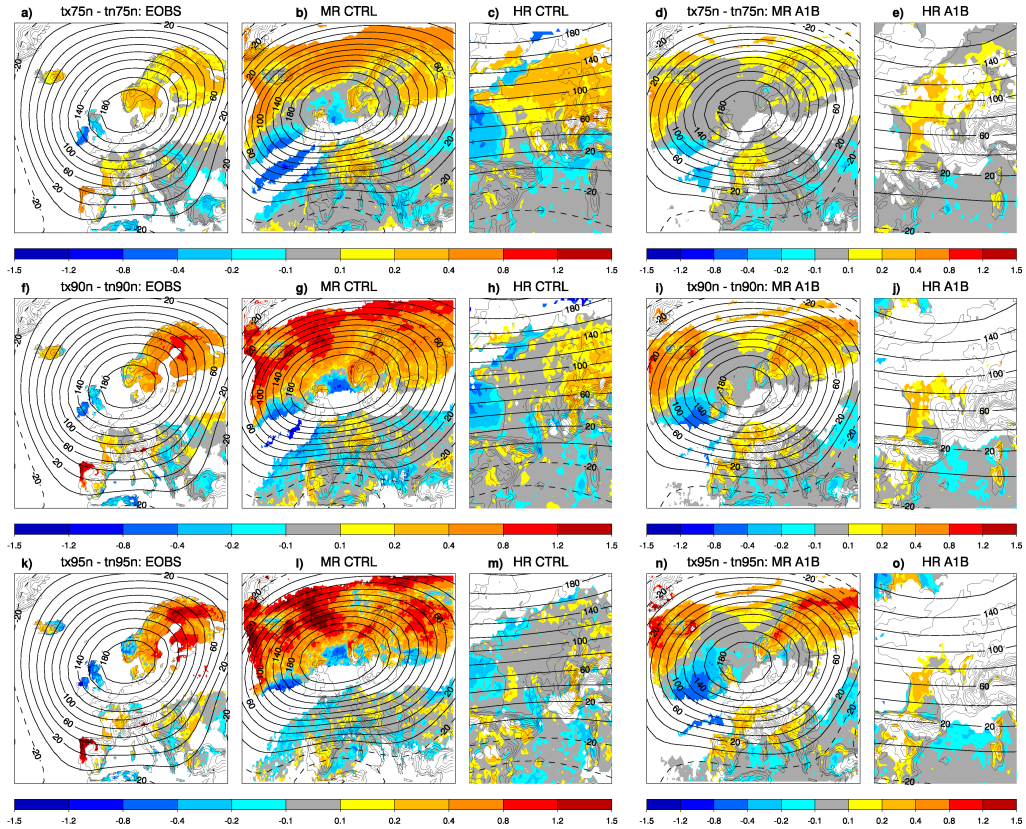

Figure 6.24: Differences in the relative contribution of blocking to **warm extreme** frequencies with respect to average conditions, between the day-time and night-time temperature extremes (e.g., tx75n - tn75n in panel a) for **warm extremes**. From top to bottom are displayed the 75^{th}, 90^{th}, 95^{th} percentile of the daily maximum and minimum temperature distribution.

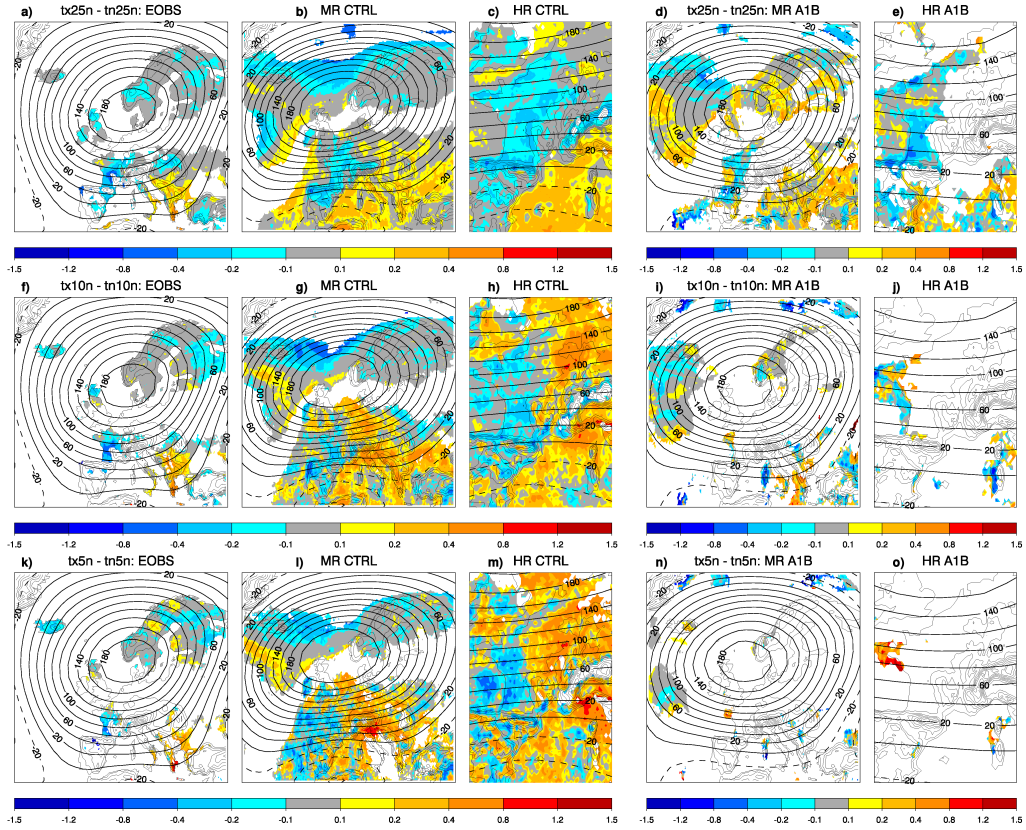

Figure 6.25: Same as Figure 6.24, but for **cold extremes**. From top to bottom: 25^{th}, 10^{th}, 5^{th} percentile of the daily maximum and minimum temperature distribution.

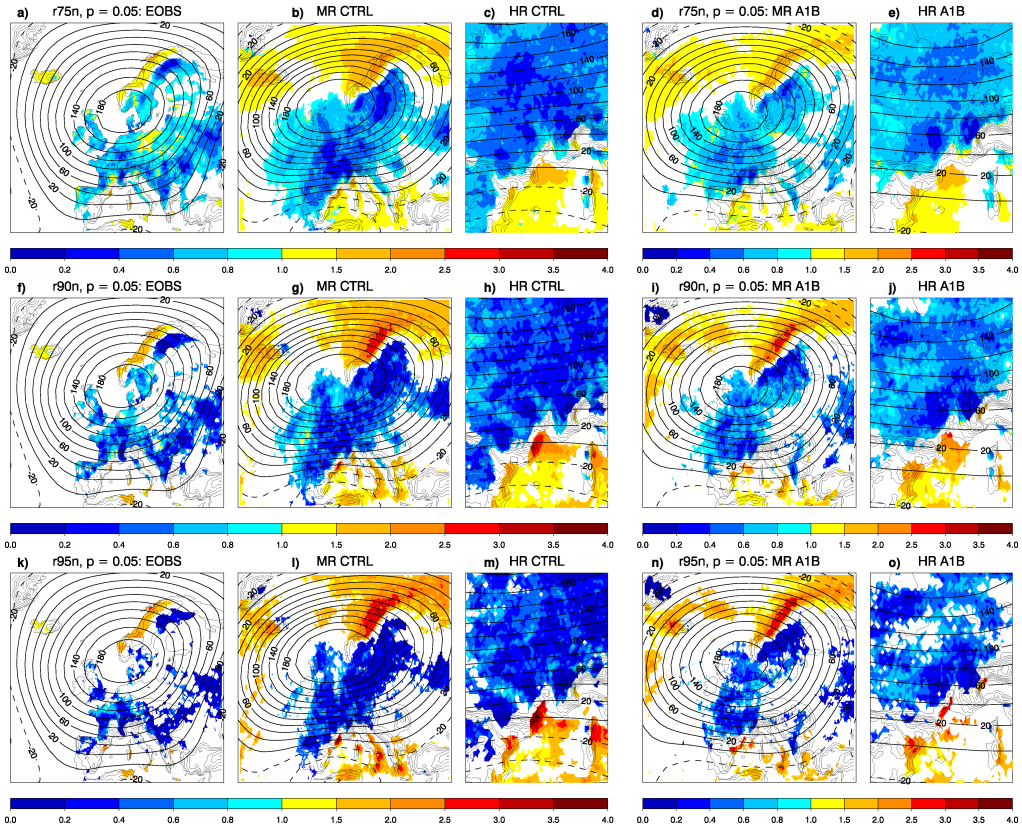

Figure 6.26: Same as Figure 6.23, but for **precipitation extremes**. From top to bottom: 75^{th}, 90^{th}, 95^{th} percentile of the daily average precipitation distribution, on rainy days only (r75n, r90n, r95n).

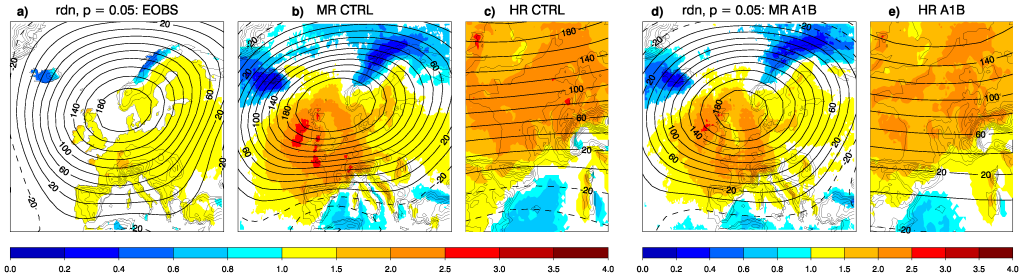

Figure 6.27: Same as Figure 6.26, but for **dry days**, where r $<$ 1 mm.

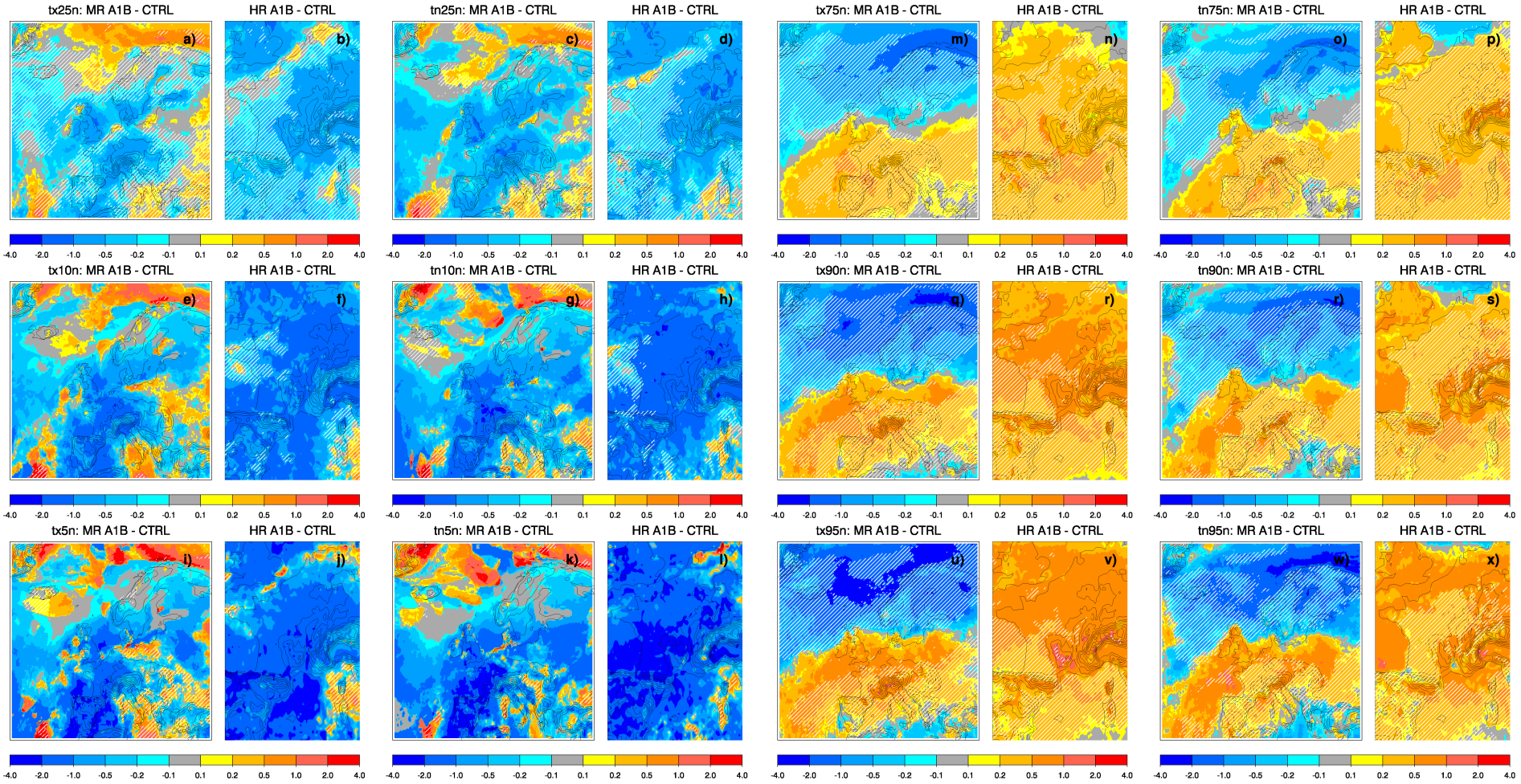

Figure 6.28: Projected changes of the relative contribution of blocking to extreme temperature event frequencies with respect to average conditions (i.e., defined by $R_{A1B} - R_{CTRL}$, where R_{CTRL} and R_{A1B} represent the ratio values for the CTRL and A1B scenarios, respectively, shown in Figures 6.20 to 6.23.) Positive (negative) values where $R_{CTRL} > 1$ ($R_{CTRL} < 1$) indicate that the contribution of blocking to extremes increases in the A1B scenario (e.g., over Scandinavia for cold extremes). Conversely, the contribution of blocking to extremes decreases in the A1B scenario if $R_{A1B} - R_{CTRL} > 0$ where $R_{CTRL} < 1$ or if $R_{A1B} - R_{CTRL} < 0$ where $R_{CTRL} > 1$, as it is the case over the whole domain for warm extremes. White hatched areas indicate regions where the Chi-square test is significant at the 5% level in both the CTRL and A1B scenarios.

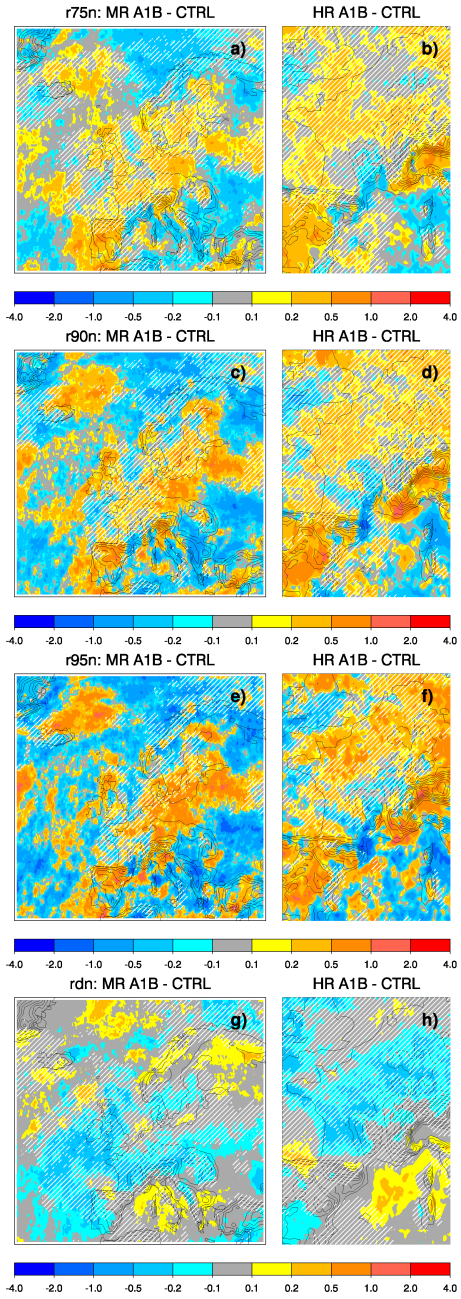

Figure 6.29: Same as Figure 6.28, but for extreme precipitation and dry events.

6.7.2 Persistence of extreme events for blocking and non-blocking flows

The spatial average frequency of extreme weather events over France as a function of their spell duration is now analysed, and results are presented in Figures 6.30 to 6.35 for blocked and non-blocked conditions. The frequency of events is considered instead of the count, in order to compare the results between blocking and non-blocking flows as well as between the model and the observations, regardless of the sample sizes being substantially different between blocking and non-blocking days and among the datasets. Note, however, that this diagnostic is limited by the persistence of blocking episodes, and therefore durations of extreme events occurring during non-blocking periods that are greater than the longest blocking episode are not meaningful for assessing the influence of blocking on the persistence of long runs of extreme weather (e.g., tn75d for EOBS above 21 days, Fig. 6.33a). Recall the maximum duration of blocking episodes: 18 days for ERA-40, 21 days for CTRL and 26 days for A1B (see legend in Figure 6.5b). The other precaution to take when interpreting these results is with respect to their statistical significance. As the severity of extremes increases, the number of events decreases (see Table 6.3), and therefore the robustness of the results as well. In addition, during blocking episodes, France experiences more (less) cold and dry (warm and wet) weather events, and therefore the results for blocking-related warm and wet extremes are less significant than for blocking-related cold and dry extremes. Finally, the number of cold (warm) extremes is predicted to decrease (increase) under the A1B scenario, therefore results are more robust for warm than cold extremes in the A1B simulations. The average number of extreme events over France for blocking and non-blocking conditions (where the Chi-square test is significant) is indicated in Table 6.3.

Extreme Indices	EOBS		MR CTRL		HR CTRL		MR A1B		HR A1B	
	blocking	non-blocking	blocking	non-blocking	blocking	non-blocking	blocking	non-blocking	blocking	non-blocking
tx25	47	164	43	172	43	173	21	89	22	91
tx10	23	80	30	80	30	82	10	32	9	33
tx5	14	48	20	46	20	46	4	12	4	14
tn25	49	169	46	162	45	164	21	80	22	81
tn10	26	83	28	75	28	77	5	22	5	23
tn5	16	45	18	41	18	43	1	10	2	11
tx75	38	197	18	206	20	206	42	268	42	268
tx90	15	105	6	118	7	117	26	230	26	225
tx95	7	57	2	70	2	69	19	185	20	172
tn75	35	210	17	208	17	207	39	254	39	257
tn90	13	115	5	123	5	119	22	202	23	199
tn95	5	65	2	70	2	69	12	153	14	147
r75	13	167	14	261	14	255	18	287	18	287
r90	4	80	5	129	5	124	7	148	7	144
r95	2	43	2	71	2	67	4	86	4	83
rd	88	359	70	291	72	319	65	301	67	325

Table 6.3: Average number of extreme weather events over France (where the Chi-square test is significant) for each simulation under blocking and non-blocking conditions.

Model validation

Observed extreme weather events tend to be more persistent during non-blocking than blocking episodes (being meaningful for extreme events lasting less than 18 days only, as it is the maximum duration of blocking episodes - Fig. 6.5b). However, when extremes occur during non-blocking periods, their persistence decreases as their intensity increases. This feature is less prominent during blocking conditions, which suggests that the persistence of blocking-related extreme events is related to the nature of the blocking episode (duration/strength), while during non-blocking flow the persistence of extreme events is more dependent on their severity (see for instance, Fig. 6.30a, d, g). As a result, when the most severe extremes are considered (i.e., the 5^{th} and 95^{th} percentiles), the blocking and non-blocking

profiles of extremes events persistence are almost identical (i.e., the contribution of blocking to extreme events relative to non-blocking periods increases with extreme intensity). This relationship is observed for cold-day, cold-night and warm-day extremes only. For the precipitation and warm-night indicators, both blocking and non-blocking related extreme events are less persistent as their intensity increases. These observed relationships could be explained as follows. Under non-blocking flow, the weather conditions over France tend to be mild and rapidly changing due to the high-frequency transition of cyclonic systems, troughs and ridges, so the persistence of extreme events, when they occur, is expected to be relatively short-lasting. On the other hand, blocking flow provides settled weather conditions, which persist longer than during non-blocked conditions (according to the definition of blocking episodes), until the large-scale circulation returns to zonal. However, as the blocking anticyclone (e.g., over France) is associated with clear-sky conditions (Fig. 6.19), the likelihood of extreme rainfall and warm-night events is expected to be very small.

The observed relationships are captured by the model for cold-day extreme events only (Fig. 6.30b, e, h). For cold-night extremes, while the simulated maximum duration of the blocking-related events is nearly constant as their intensity increases (i.e., it captures well the observed relationship under blocking conditions), the model is also able to simulate long-lasting cold-night events ($>$ 21 days) for moderate and strong percentiles when they occur during zonal conditions (Fig. 6.31b, e, h). This feature could possibly be linked with the average cold bias and/or a model deficiency related to the night-time radiative cooling processes (e.g., less clouds due to underestimated storm activity enhances night-time radiative cooling) (see Section 6.5.1). For warm extremes however (in Fig. 6.32 and 6.33b, e, h), the likelihood of extremes decreases substantially as their persistence and intensity increase under both blocking and non-blocking flows (i.e., the model captures the observed relationship under non-blocking conditions only). This can also be linked with the model cold bias, and possibly to the stronger and/or more persistent nature of the simulated blocking events (Fig. 6.5b and 6.6), leaving no chance for warm extremes to persist (due to stronger and/or more persistent cold advection).

The difference (CTRL - EOBS) in the average frequency of extreme events as a function of their duration is analysed in Figure C.24. The model tends to overestimate (underestimate) the frequencies of blocking-related cold and rainfall (warm and dry) extremes; the same biases as in the average climate, being colder and wetter in the model simulations than in the observations (refer to Section 6.5.1).

Under non-blocking conditions:

- the precipitation biases are the same as during blocking
- frequencies of cold extreme events are underestimated, except for short-lasting cold-night events ($<$ 3 days)
- frequencies of warm extremes tend to be overestimated for moderate intensity and long-lasting events and underestimated for strong and short-lasting events.

Overall, the amplitude of model errors is larger during blocking than non-blocking conditions.

The fact that the sign of the biases is the same during blocked flow as average, and that the amplitude of model errors are larger under blocking than non-blocking conditions, suggests that the model systematic errors are more related to a model deficiency in processes taking place during blocking than in any other atmospheric situation.

Projected changes

The projected changes in extreme events persistence (over France only) are represented in Figures 6.30 to 6.35 by the red lines for blocking (solid) and non-blocking (dashed) situations. As in the CTRL scenario, extreme weather events tend to be more persistent during non-blocking than blocking episodes.

For cold events (Fig. 6.30 and 6.31), the frequency of blocking-related extremes is lower in the A1B for all spell durations. However for non-blocking situations, although the number of cold extreme events is predicted to be lower in A1B (see Table 6.3), their proportion (with respect to the total number of cold extreme events) is higher and increases with extreme severity. The relationship observed in the CTRL simulation (i.e., the contribution of blocking to extreme cold-day events relative to non-blocking periods increases with extreme intensity) tends to be reversed in the A1B scenario: as the intensity of extremes increases, the proportion of blocking-related cold events decreases, while the proportion of non-blocking extreme events increases. Extremely cold spells during winter, for which blocking episodes contribute substantially in this present-day climate simulation (see Figures 6.20 and 6.21), are predicted to occur less often, particularly during blocking flow. Note however that although this change in the relationship between blocking/non-blocking flow and cold extremes might be true, the statistical confidence in those results is limited by the very low number of cold events considered in the A1B scenario (i.e., 2 blocking-related events on average for tn5n, 5 for tn10n - see Table 6.3).

The number of extreme warm events increases in A1B, and both the persistence and proportion of warm extremes increases in both blocking and non-blocking situations (Fig. 6.32 and 6.33). In addition, the more intense the events are, the greater the changes are. For instance, extreme events greater than the 90^{th} percentile are predicted to occur as often (and even more) in A1B during blocking episodes than in CTRL during non-blocking periods.

For the rainfall indicators (Fig. 6.34), the proportion of moderate extremes tend to be higher during blocking episodes and unchanged (or even lower) during non-blocking periods (e.g., for HR in Figure 6.34c), while the tendency is reversed as the intensity of rainfall events increases (i.e., more (less) frequent 95^{th} percentile rainfall extremes during non-blocking (blocking) flow - Fig. 6.34h and i).

For dry extremes (Fig. 6.35) the frequency of events decreases during both blocking and non-blocking flows, without affecting the relative likelihood of occurrence between blocking and non-blocking periods (i.e., the proportion of short (long) dry spells being higher within blocking (non-blocking) periods in both the CTRL and A1B simulations.

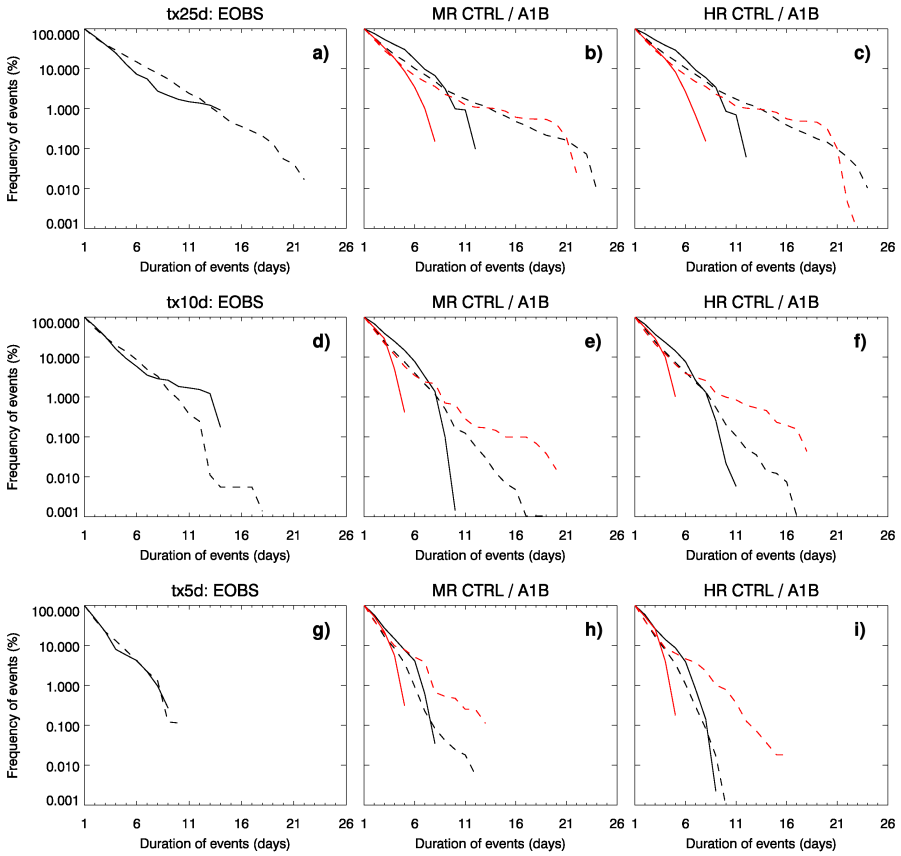

Figure 6.30: Average frequency of **cold-day extreme events** as a function of spell duration over France, blocked (solid lines), non-blocked (dashed lines) situations, for (from left to right) EOBS, MR and HR. MR and HR A1B projected changes are shown by the red lines. Extreme indices are displayed at the top of each panel.

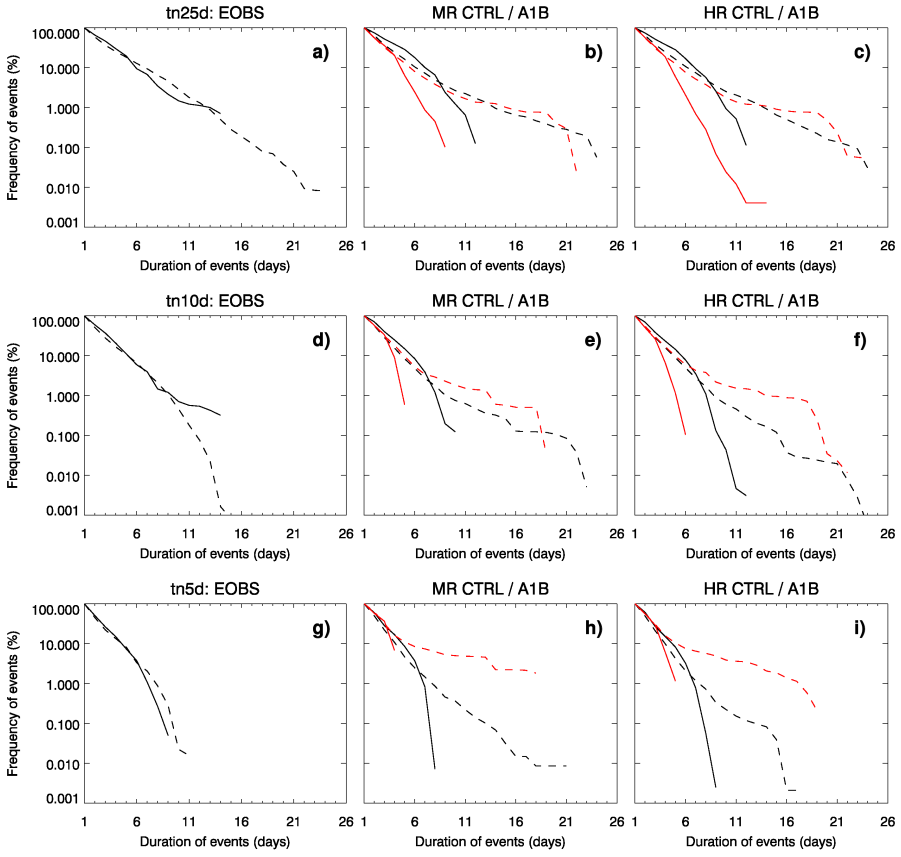

Figure 6.31: Same as Figure 6.30, but for **cold-night extreme events**.

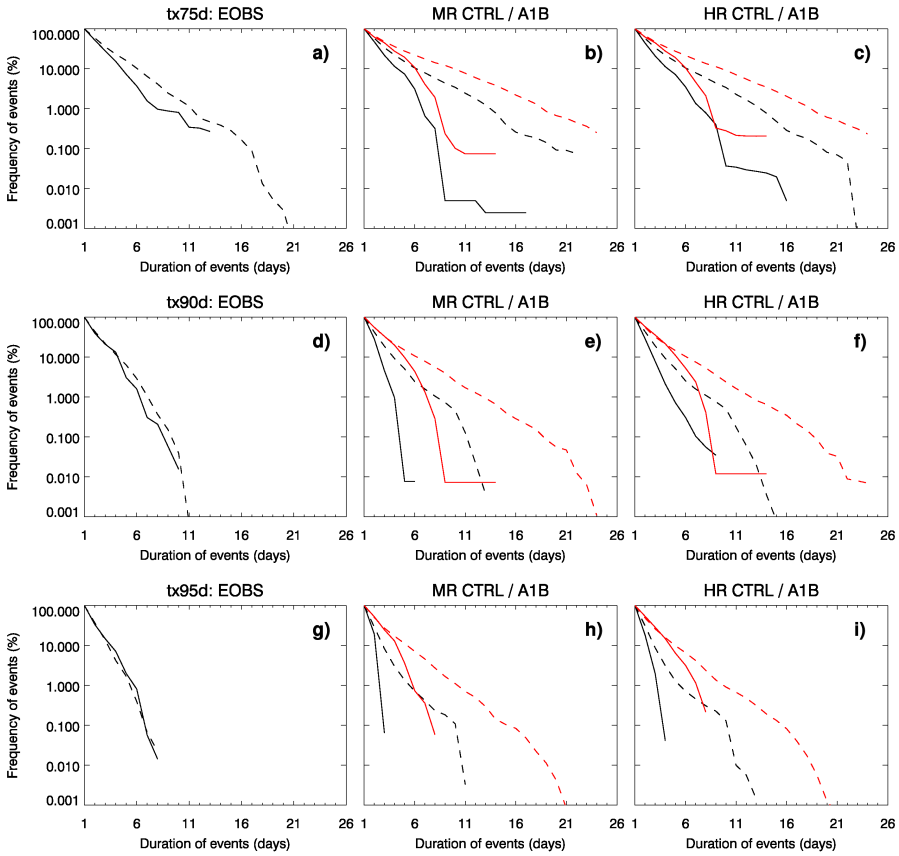

Figure 6.32: Same as Figure 6.30, but for **warm-day extreme events**.

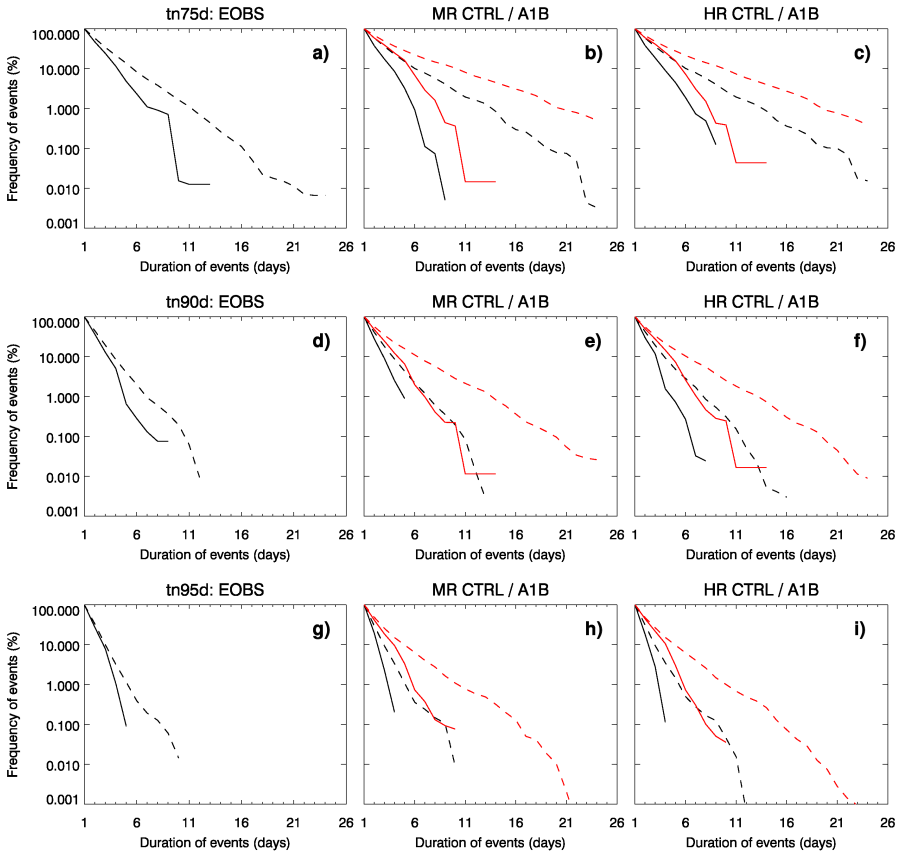

Figure 6.33: Same as Figure 6.32, but for **warm-night extreme events**.

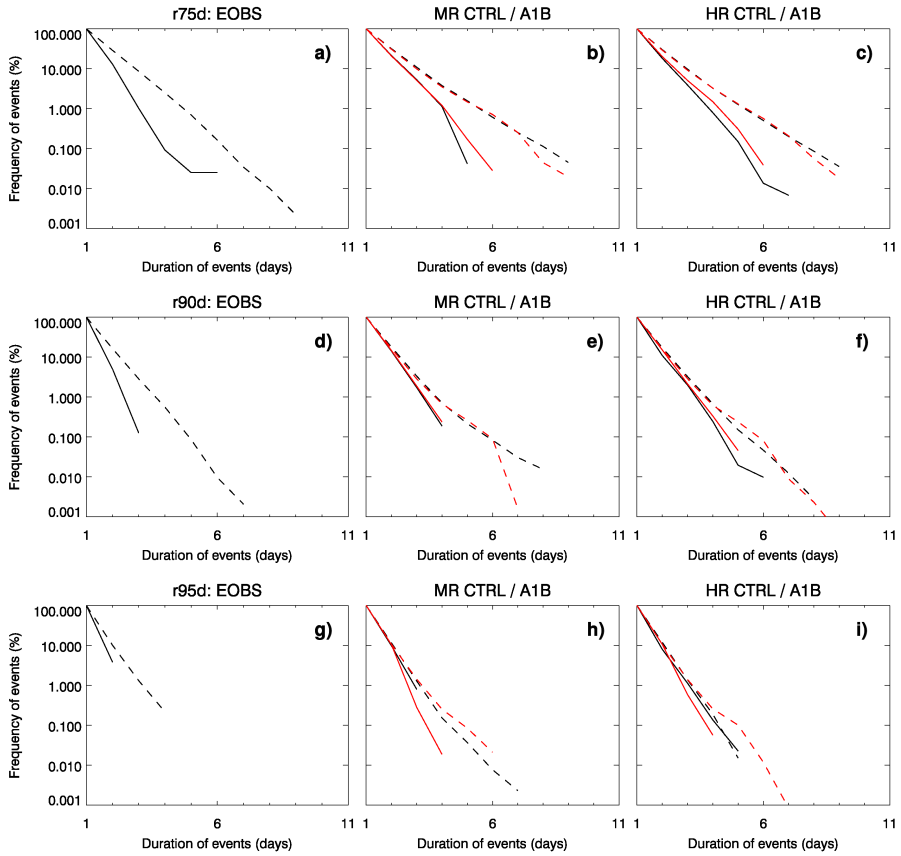

Figure 6.34: Same as Figure 6.30, but for **rainfall extreme events**.

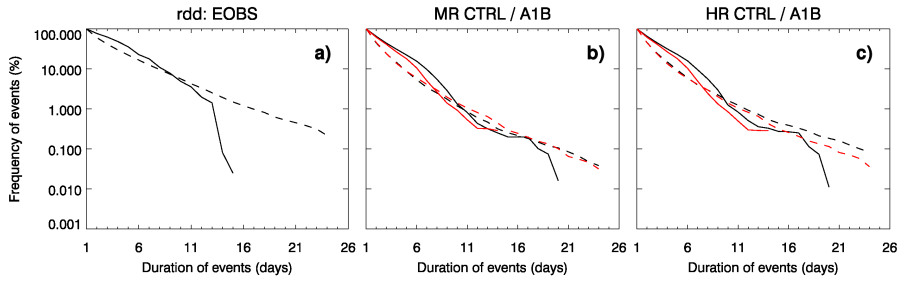

Figure 6.35: Same as Figure 6.34, but for **dry-day events**.

6.7.3 Sensitivity of blocking-related extremes to model resolution

The final focus of this study is to analyse the effect of increased horizontal resolution over the zoomed area of the model (i.e., from 120 km to 20 km over France) on extreme weather events.

One direct effect of increasing the horizontal resolution of the model might be an increased magnitude of temperature and precipitation extremes. This would not necessarily be linked with an improved model performance, but could simply be due to the increased resolution. A climate variable represented by areally-averaging processes over a grid box (as it is the case here for the LMDZ model and, to some extent that depends on the density of observations, E-OBS), tend to have lower variability and extreme values (Giorgi and Marinucci, 1996; Tustison *et al.*, 2001; Frei, 2003; Haylock *et al.*, 2008; Chen and Knutson, 2008; Kanamitsu and DeHaan, 2011), especially where the topography is complex (e.g., the Alps) and at land-sea boundaries. Increasing the horizontal resolution (i.e., reducing the size of the grid

box) is therefore expected to increase the magnitude of extremes. This is supported in this present study by (1) the spatial patterns of the time-mean systematic errors in Figure 6.8, and (2) the spatial patterns of the extreme percentiles in Figures C.2 to C.1, with colder and wetter conditions (i.e., for the mean climate and for the magnitude of extreme values) in HR than in MR, particularly at high elevation and over coastal areas.

Percentiles for extreme weather events are climatology-dependent, so in order to take into account the model biases seen in Section 6.5.1, the percentiles are computed for each model simulation, therefore masking the large differences in the absolute intensity of extremes seen between the high and low resolution simulations (e.g., at high altitude and at the warm ocean/cold land boundaries - Fig. C.2 to C.1). As a result of using these "bias correction" percentile thresholds, both simulations (MR and HR) provide very similar results in terms of blocking contribution to extreme frequencies, with almost identical spatial patterns and the same order of magnitude of the ratios R (see Section 6.7.1). This implies that the mechanisms responsible for the occurrence of extremes under the action of blocking are robust to changes in horizontal model resolution. Note that France is localised in the blocking area where the wind is the weakest (compare height contours in Fig.C.18a and e for instance), so the dynamics of the model (advection, horizontal resolution) might be less important in that region. This further implies that the evolution of surface weather conditions in the zoomed area (i.e., France) is more influenced by physical parameterizations of the model. The fact that similar results are obtained in the lower and higher resolution simulation therefore suggests that the parameters and assumptions used to represent subgrid-scale processes (e.g., for the representation of clouds, precipitation, gravity-wave drag) are reasonably insensitive to the horizontal resolution of the model, for resolutions from 20 km to 120 km.

The main difference however (when it exists) is in the spatial patterns of the statistical significance of results, which tends to be more homogeneous in MR than HR (compare for instance Fig. 6.23l and m), and particularly where the topography is sharper (e.g., over the Alps). This indicates that the simulated relationship between blocking and extreme days is slightly stronger at lower than higher resolution in both the CTRL and A1B simulations. Although it seems to be of minor importance relative to the differences arising between EOBS and CTRL, this feature can possibly be explained by a higher spatial and temporal small-scale variability in the higher-resolution simulation. In a low-resolution model, temperature and precipitation variability depend especially on the large-scale circulation. However, as the resolution increases, other factors may contribute to the climate variability at a more local scale.

Despite considerable model biases, the low-resolution simulation (MR) reproduces fairly well prominent patterns of mean and extreme precipitation and temperature (Fig. 6.7 and 6.20 to 6.27), which provides confidence that the higher-resolution simulation (HR) might be capable of improving these patterns at a more local scale, since smaller-scale disturbances arising from physical forcing (i.e., surface heterogeneities, sharper and complex topographic features, coastlines) are better resolved (Giorgi and Marinucci, 1996). If it is the case, a better resolved flow could possibly inhibit the buildup and/or persistence of climate extremes, or lead to the formation of isolated extremes such as in the lee of mountains.

This is illustrated in Figures C.18 to C.23, which display the difference (HR - MR) in the number of extreme days during blocking and non-blocking situations over France for the CTRL and A1B scenarios. Under the present-day non-blocking periods France is exposed to a westerly flow, advecting warm and humid air masses over that region (in absolute, not in anomaly terms), while during blocking

episodes relatively cold and dry air masses are advected by a northerly flow. If the model has limited surface roughness, topography and turbulent fluxes to redistribute the advected air masses, extreme weather events of the same nature as the advected air will form homogeneously over the land-surface: warm and wet extremes during non-blocking, and cold and dry extremes during blocking episodes. However, when small-scale variability is more strongly represented (in higher resolution models - HR), the occurrence of extreme weather is more heterogeneous over the land, and extremes do not necessarily have the same nature as the advected flow, especially where the topography is sharp and complex. This could explain why we can see for instance less cold extremes overall in HR than in MR during blocking episodes, except on the windward side of the Alps (Fig. C.18).

Despite the differences found between HR and MR (i.e., in the magnitude of extremes, mean climate, blocking contribution at a local scale), whether or not increasing the horizontal resolution of the model improves the realism of the results is a difficult question to answer from this study.

Evaluating the "true" added value of high-resolution against coarser-resolution models can be a difficult task. Tustison *et al.* (2001) and Kanamitsu and DeHaan (2011) addressed the problem of using traditional metrics as a measure for added value (e.g., root mean squared error, temporal correlation, bias error - the latter being used in this present study), which incorporate a combination of different types of errors, making it difficult to evaluate the "true" added value of the model skills. Of particular relevance for this discussion, it might be difficult to identify whether the exact cause of the added value is from the 'representativeness error of model grid value' (i.e. the error in representing data at another scale than the model's inherent scale), or from the error associated with observations, or from the model error itself (i.e., being representative of the true skill of the model). The problem when trying to assess model performances at different model resolutions is that the representativeness error is dependent on the scale of the model; the higher the resolution of the model, the smaller the representativeness error (Tustison *et al.*, 2001). This is an important issue from a modeler's point of view. When the total bias is reduced in HR compared to MR, as it is the case for instance in Figure 6.10 (compare panels g and h), one cannot literally conclude that HR performs better than MR, as a part of this improved fit to observations is due to a smaller representativeness error in HR than in MR. However, the interpretation of this total model bias might be different from a user point of view, interested in the final model product only.

6.8 Concluding remarks

This study focuses on the relationship between European blocking and extreme temperature and precipitation events in the variable-grid LMDZ4 AGCM simulations of the present-day and future climate.

Using a two-way nesting model configuration between global and regional model simulations it is first demonstrated that the representation of atmospheric blocking in the Euro-Atlantic region is substantially improved with respect to frequency and duration, compared with its AGCM and even AOGCM homologues.

Observed blocking impact on climate averages and extremes

Blocking signature maps of 500 hPa geopotential height, surface temperature and precipitation fields reveal a dipole structure with cold temperatures over central and western Europe and warm temperatures

over northern Europe, above 55°N. Furthermore, southwestward flow anomalies to the east of the blocking core region and northeastward flow anomalies to the west lead to drier conditions over central and western Europe and wetter conditions over coastal areas of Scandinavia. These results are largely consistent with the findings relating blocking frequency and selected indices of extreme events. In particular, the relative contribution of blocking to extreme weather event frequencies with respect to average conditions suggest that more cold and dry (less warm and wet) extreme weather conditions affect central and western Europe, below 55°N. This is primarily caused by the anomalous northeasterly flow but also by enhanced night-time radiative cooling due to reduced humidity and cloudiness in the presence of blocking. On the other hand, more warm and wet (less cold and dry) extremes over northern Europe (above 55°N) are observed, with a stronger impact during the day due to enhanced day-time solar warming. Finally, the likelihood of extremes during blocked (non-blocked) situations increases (decreases) with extreme intensity.

Simulated blocking impact on climate averages and extremes

In spite of large model systematic errors in blocking (with less frequent but more persistent and intense episodes) and in the amplitude of the mean, variability and extreme precipitation and temperature fields, the model is able to reproduce reasonably well the relative contribution of blocking to climate anomalies and extreme frequencies with respect to non-blocking and average conditions, respectively. The most prominent model deficiency is an overestimation of the blocking impact increasing with extreme intensity, which is probably caused by (1) more intense and persistent blocking episodes, being conducive of stronger and more persistent advective wind anomalies, and (2) errors in the north/south mean temperature and precipitation gradients over Europe, being conducive of overestimated advected air mass anomalies. Finally, note that the differences between the medium and high resolution models are particularly prominent at a local scale over mountainous and coastal areas. This can be understood by the fact that the increased horizontal resolution of the model over France certainly improves the representation of complex topographical features (e.g., the Alps), coastlines and surface roughness, which can in turn improve the regional climate where large-scale flows, forced by topography and surface contrasts, are important (Mass *et al.*, 2002). Having said that, increasing the horizontal resolution of the model does not necessarily result in an improved model performance (Giorgi and Marinucci, 1996; Kanamitsu and DeHaan, 2011).

Projected changes

In the A1B scenario, the frequency of winter blocking days in the European region is slightly diminished (by 11% on average, with respect to the present-day blocking frequency). Similar changes in blocking frequency were found by Sillmann and Croci-Maspoli (2009), with fewer blocks over the central and eastern parts of the domain, and a tendency for more blocks over the western sector. In addition, blocking episodes are projected to be less intense but persist longer. These changes in blocking climatology, but more especially the warmer and wetter conditions associated with a decrease in the southwest/northeast mean temperature and precipitation gradients over Europe, are conducive of a similar pattern but reduced amplitude of blocking impact in climate anomalies and frequencies with respect to the average conditions of the future climate. Overall, in the future climate, blocking episodes will bring milder weather events over Scandinavia with less extreme conditions, and over central Europe events are predicted to be shifted toward warmer and wetter extremes with less cold and dry and more

warm and wet extremes during blocking episodes relative to average conditions.

The results presented in this chapter, which currently imply mild conditions over northern Europe during European blocking, tend to go against a large number of studies (e.g., Hurrell (1995); Trigo *et al.* (2002)) which demonstrate that the negative phase of the NAO (being often associated with the North Atlantic blocking) leads to cold and dry winter conditions across northern Europe and above-average temperatures and precipitation in Greenland, and across southern and eastern Europe. These somewhat contradictory results are, however, clearly explained by the sensitivity of blocking-related climate anomalies over Europe to the location of blocking. Indeed, this study reveals that blocking in a more northwest location of the European block (over the Atlantic, between 45°W and 0°) leads to similar conditions as during the negative phase of the NAO (i.e., cold and dry conditions across northern Europe and warm and wet conditions over Greenland, and across southern and eastern Europe).

CHAPTER 7

Summary and outlook

The aim of this thesis was to advance our understanding of wintertime Northern Hemisphere atmospheric blocking through different aspects, including its representation in climate models, dynamical processes linked with blocking life-time and variability, and its influence on regional weather events in the present-day and future climate. These areas of research were addressed throughout the thesis, and will be summarised here with insights and suggestions for further work that could build on the results from this study.

7.1 The representation of blocking in climate models

An assessment of six AOGCMs was undertaken in order to evaluate their ability in simulating winter atmospheric blocking highs in the Northern Hemisphere. The poor representation of atmospheric blocking in climate models is a long-standing problem (e.g. D'Andrea et al, 1998), and despite considerable effort in model development, there is only a moderate improvement in blocking simulation. The two preferred regions of blocking development, in the Euro-Atlantic and North Pacific, are relatively well captured by most of the models. However, the prominent error in blocking simulations consists of an underestimation of the total frequency of blocking episodes over both regions. A more detailed analysis revealed that this error is associated with an insufficient number of medium spells and long-lasting episodes, and a shift in blocking lifetime distributions towards shorter blocks in the Euro-Atlantic sector. In the Pacific, results are more diverse; the models are equally likely to overestimate or underestimate the frequency at different spell lengths. Blocking spatial signatures are relatively well simulated in the Euro-Atlantic sector, while errors in the intensity and geographical location of the blocks emerge in the Pacific.

Analysis of multiple simulations and periods demonstrated that these errors are real and not the result of internal variability or changes in the external forcing. However, it was found that model performances in blocking simulations can be affected by the choice of the blocking detection method and of the diagnostic.

The impact of models' systematic errors on blocking simulation has also been analysed. The time-mean atmospheric circulation biases affect the frequency of blocking episodes, and the maximum event duration in the Euro-Atlantic region, while they sometimes cause geographical mislocations in the Pacific sector. The analysis of the systematic error in temporal variance has revealed a negative relationship between the amplitude of the high-frequency variability in the areas affected by blocking and blocking frequency. The blocking responses to errors in the low-frequency variability are different according to

the region considered; the amplitude of the low-frequency variability is positively related to the blocking frequency and persistence in the Euro-Atlantic sector, while no such consistency is observed in the Pacific.

One common problem of the AOGCMs used in this study, and many other climate and forecast models is to simulate too strong westerlies (Fig. 4.14) and to underestimate the frequency of blocking (Fig. 4.5). Those two facts might in fact be linked together, and one possible explanation has been given by Palmer (2001) using the concept of non-linearity of the climate system, and specifically the way governing equations are approximated at sub-grid scale by deterministic bulk formulae - conventional parameterization schemes neglect the variability of atmospheric components that are energetically weak.

Suppose the atmospheric circulation in the extratropics has a bimodal distribution with a dominant and more stable regime (zonal flow), and a sub-dominant regime (blocked flow). Neglecting even a small percentage of the variability can have an important impact on the resolved flow because of the influence of non-linearity of unresolved scales, and might in particular underestimate the synoptic-scale variability that triggers the transition between the zonal and blocked flow. As a result, the dominant and more stable regime is overpopulated and characterized by a westerly bias, and the frequency of the sub-dominant regime (atmospheric blocking) will inevitably be underestimated.

This line of thought is supported by the results presented in this study. According to the bimodal regime of the atmospheric circulation and non-linearity described by Palmer (2001), the underestimated amplitude of the high-frequency variability itself is consistent (to some extent) with a downstream westerly bias (within the blocking area - compare for instance Figures 4.24f and 4.14d in this present study). In addition, the bias correction exercise (presented in Section 4.8) revealed a coherent and substantial improvement in blocking simulations after removal of the time-mean bias.

Some studies are currently addressing this problem (Palmer, 2001; Berner *et al.*, 2008), which can be alleviated by representing sub-grid scale processes by simple non-linear stochastic-dynamic systems coupled to the resolved flow, so that kinetic energy of the unresolved flow can be *backscattered* to the large-scale components of the flow. Berner *et al.* (2008) found a significant reduction of systematic error, and an increase in the frequency of Pacific blocking. This approach is an appealing alternative to the current widely used conventional parameterization schemes to reduce the systematic bias that most climate models have in the middle latitudes, and deserves much further investigation.

7.2 Aspects of the relationship between blocking dynamics and stratospheric sudden warmings

It is widely believed that there is a link between the occurrence of stratospheric sudden warming (SSW) and tropospheric blocking events. However, the rarity of SSWs and the ubiquity of blocking events gave rise to controversies in the literature on the statistically significant and physically meaningful connection between both phenomena. Here, the relationship between Northern Hemisphere tropospheric blocking and SSW events was examined in the IPSL-CM5A multi-century climate simulation. This study therefore provides for the first time a robust climatology of blocking-related SSWs, being limited however by the ability of the model to simulate the real climate system. Nevertheless, some results presented here are supported by other studies exploring the stratosphere-troposphere relationships in reanalysis datasets or for individual case studies (e.g., the warming events in December 1987, 1988

and 2001 analysed by Naujokat *et al.*, 2002).

Overall, the results show a robust connection between the occurrence of SSWs and blocking in both the Euro-Atlantic and Pacific regions. The 40-day periods preceding and following the onset date of SSWs are marked by an enhanced frequency of blocking days in the Euro-Atlantic region and a reduced frequency in the west Pacific, with a significant shift in the distribution of blocking lifetime toward longer Eurasian blocks before the warmings and shorter west Pacific blocks after the onset of SSWs. During the weakening and breakdown of the stratospheric polar vortex, blocking events initiate, grow and displace in connection with large-scale disturbances of planetary waves 1 and 2. Finally, the results further indicate that once the SSWs initiate, an enhanced frequency of short-lasting blocking events at the expense of long-lasting blocks is associated with a rapid weakening of large-scale planetary wave anomalies and an increased wave contribution from smaller-scale disturbances.

I have shown in this study the existence of robust precursors to SSWs (i.e., amplified, vertically propagating large-scale planetary waves and tropospheric blocking). One path for a continuation of this work would be to identify the wave forcing that preceded the weakening of the stratospheric polar vortex.

Particular attention is currently being turned to diabatic processes due to anomalous surface conditions. A number of studies have suggested that the interannual variability in October Eurasian snow cover influences the wave activity flux entering the stratosphere in winter, in turn affecting the strength of the polar vortex (Saito and Entekhabi, 2001; Cohen *et al.*, 2007; Kolstad and Charlton-Perez, 2011). In that sense, higher than normal autumn snow cover leads to a chain of events, including an anomalously strong Siberian high and colder surface temperatures across northern parts of Eurasia in fall, increasing the wave activity flux entering the stratosphere in late fall and early winter through snow-forced diabatic cooling and topographic forcing (Cohen *et al.*, 2007), finally leading to the weakening and breakdown of the stratospheric polar vortex.

Diabatic heating also affects wave activity and blocking variability. Croci-Maspoli and Davies (2009) showed that the anomalously cold temperatures over Europe in winter 2005/06 were linked with a series a blocking events (in December and January) arising from a reduction of potential vorticity at upper tropospheric levels, which were initially influenced by latent heating (through condensation of water vapour associated with extratropical cyclones), due to the warmer than normal surface conditions over the Atlantic. It happened that these blocking episodes were also accompanied by a strong stratospheric sudden warming event in January 2006 (Scaife and Knight, 2008).

These case studies indicate that cross-isentropic diabatic mass transport, due to anomalous surface conditions, could play an important role in the incipient stage of blocking and in the vertical wave activity flux. The question could also be addressed as to whether this type of diabatic process is a necessary (and eventually sufficient) condition to the wave forcing that precedes SSWs. These ideas have not been studied extensively yet, and would require further research. It would be useful to examine, using this or other multi-century climate simulations, anomalies in other fields (e.g., sea level pressure, SST, precipitating snow) and wave activity flux diagnostics (to localise in a 3-dimensional space the source of the upward-propagating planetary waves) during periods preceding the onset date of SSWs, in order to identify the nature (i.e., diabatic heating/cooling) of the source region, as well as its location. Experimental set-ups would then be required to test the hypothesis that cross-isentropic diabatic advection triggers the combined occurrence of blocking and SSW events. For instance, by performing further case studies in

a similar manner as Scaife and Knight (2008), who performed numerical experiments using prescribed SST and sea-ice forcings, in order to investigate the importance of each influence in reproducing the 2005/06 European winter.

There are important implications of studies of this kind for operational forecasting and longer climate trends. Of particular relevance for the climate change perspective, if snow cover or SST anomalies can force a blocking and SSW response (through the combination of cross-isentropic and planetary wave generation mechanisms described above), then changes in snow cover distribution and surface temperatures (associated with the increase in global surface temperatures due to climate change) can be expected to impact on the long-term blocking and SSW variability, and therefore on surface weather conditions and regional extreme climatic events.

7.3 Regional impacts of blocking and its potential for change

The relationships between atmospheric blocking and extreme weather events over Europe were investigated in observation/re-analysis dataset and climate model simulations of the present-day and a future projection (under the SRES A1B emission scenario) of wintertime climate, and the sensitivity of the results to the model horizontal resolution was assessed. The model used was the IPSL-LMDZ4 variable-grid atmosphere-only GCM with a finner resolution zoom over Europe, where the effective resolution of the model is approximately 120 x 120 km^2 (referred to as MR). The information resulting from the MR simulation was then used to force a higher 20-km resolution regional model over France (hereafter, HR). The results presented in this study are based on a series of statistical diagnostic tools (for blocking, climate averages and extremes, as described in Section 6.3), and on a selection of user-defined percentile-based indices (calculated within the base period 1961-1990) characterising moderate and more severe extreme temperature and precipitation events.

In spite of large systematic errors in blocking and in the amplitude of the mean, variability and extreme precipitation and temperature fields, the model is able to reproduce reasonably well the relative contribution of blocking to climate anomalies and extreme frequencies with respect to non-blocking and average conditions, respectively. During European blocking, northern Europe experiences more warm and wet (less cold and dry) extreme weather conditions, due to the anomalous advection of air from southern Atlantic ocean over Scandinavia, whereas anomalously cold and dry continental air from northern countries is advected, and brings more cold and dry (less warm and wet) extremes over southern parts of Europe. The likelihood of extremes during blocked situations tends to increase with extreme intensity and persistence. Observed and simulated blocking-related extreme weather events seem to be primarily caused by anomalous advection but also by enhanced night-time radiative cooling due to reduced humidity and cloudiness in the presence of blocking. The most prominent model deficiency is an overestimation of the blocking impact increasing with extreme intensity, which is presumably caused by (1) more intense and persistent blocking episodes and (2) errors in the north/south mean temperature and precipitation gradients over Europe.

Statistical results presented in this thesis and in other studies (e.g., Sillmann and Croci-Maspoli, 2009), indicate that the frequency of winter blocking days in the European region decreases (by 11% on average in this study) under A1B anthropogenic scenario for climate change. Blocking events are projected to be less intense but more persistent, with fewer (more) blocks over the central and eastern parts (western part) of the domain.

The changes in blocking climatology, and the warmer and wetter mean conditions associated with a decrease in the southwest/northeast mean temperature and precipitation gradients over Europe, are conducive of a similar pattern but reduced amplitude of blocking impact in climate anomalies and frequencies with respect to the average conditions of the future climate. Overall, in the future climate, blocking episodes bring milder weather events over Scandinavia with less extreme conditions, and over central Europe events are predicted to be shifted toward warmer and wetter extremes with less cold and dry and more warm and wet extremes during blocking episodes relative to average conditions.

Finally, it should also be emphasized that blocking-related climate anomalies are highly dependent on the blocking location, and that blocking in a more northwest location of the European block (over the Atlantic, between 45°W and 0°) leads to NAO-like anomalies in its negative phase (i.e., cold and dry winter conditions across northern Europe and above-average temperatures and precipitation in Greenland, and across southern and eastern Europe).

One result that should attract further research involves the robustness of the relationships between atmospheric blocking and extreme weather events in the zoomed area (i.e., France) to changes in horizontal model resolution. This result was hypothetically attributed to the fact that France is localised in the blocking area where the wind is the weakest, implying that blocking-related extremes would be more influenced by physical than dynamical processes in that region.

Further analysis is required however to test this hypothesis. If, for instance, large differences arise between the medium and high resolution models when the latter is forced over a region where the dynamics play a major role during blocking (e.g., over Scandinavia where the winds are stronger), then the hypothesis (that blocking-related extremes evolve mostly with the influence of physical processes) can be validated. The model configuration used in this study (i.e., with HR forced over France) could then be used to further understand the physical processes governing the existence of blocking-related extremes (e.g. cloud radiative forcing, heat and moisture fluxes, soil moisture) in the core of the blocking region.

Perhaps the largest limitation of this study is the use of only a 30-year dataset. It has been shown that results are relatively robust over most of the European domain for moderate extremes, but 30 years is certainly too short a period to examine the influence of blocking on more intense extremes, and especially on cold extremes in the future climate simulation. A study of this kind could be undertaken in a century time-scale climate simulation to widen the spatial distribution of statistically significant results. The variable-grid version of the new IPSL/LMDZ model (IPSL-CM5), which participates to the phase five of the Coupled Model Intercomparison Project (CMIP5), could soon be used for that purpose given the imminent availability of a 500-year simulation with a finner resolution zoom over Europe (where the effective resolution of the model is approximately 50 x 50 km^2).

This study could also be complemented by an extreme value analysis in order to evaluate the intensity and frequency of extremely rare and damaging events (i.e., lying farther in the tails of probability distribution of weather variables) that occur for instance once every 20 years. However, the uncertainty due to limited sample size would then be even more critical with an analysis of this kind, and would definitely require the examination of longer time series.

Appendix A

Supplementary material for Chapter 3

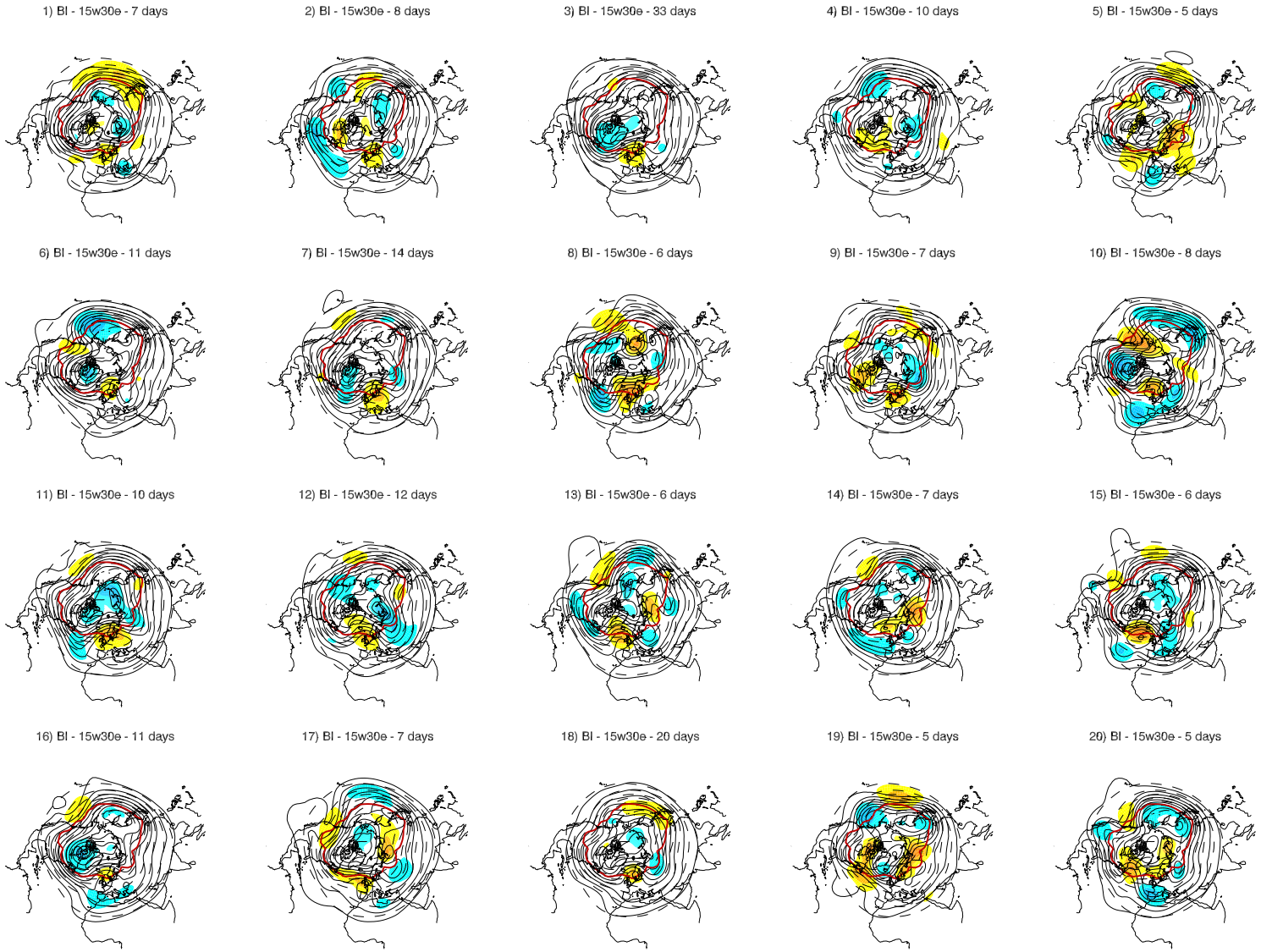

Figure A.1: Full (black dashed line) and anomaly (color shading) 500 hPa geopotential height fields averaged for the life-cycle of large-scale blocking episodes in Europe (EUR, 15°W-30°E), identified with the *BI* index. The solid black line is the 500 hPa climatological mean state in winter. The solid red line is the central latitude of blocking, taken as the latitude of the maximum storm track intensity.

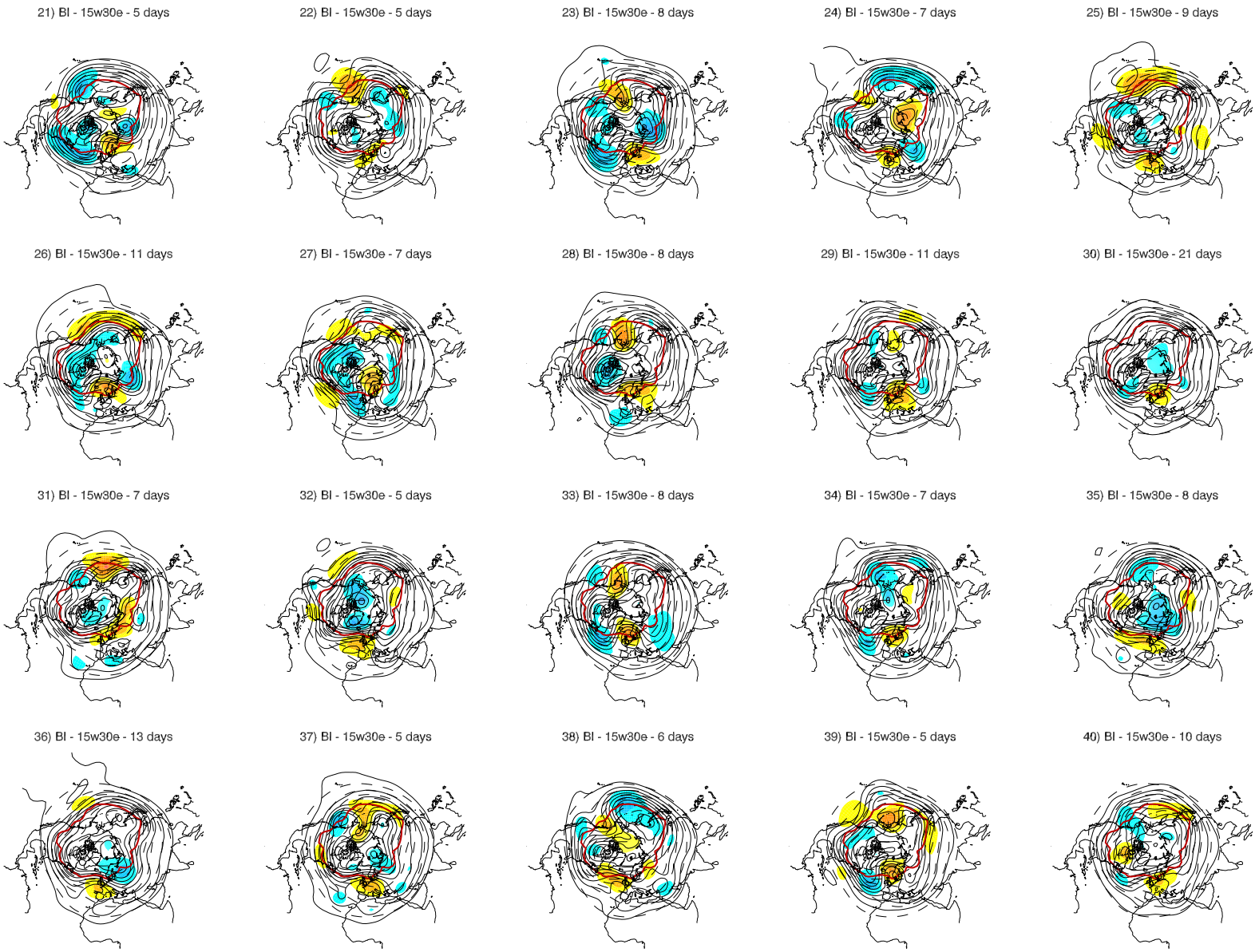

Figure A.1: Continued from previous page.

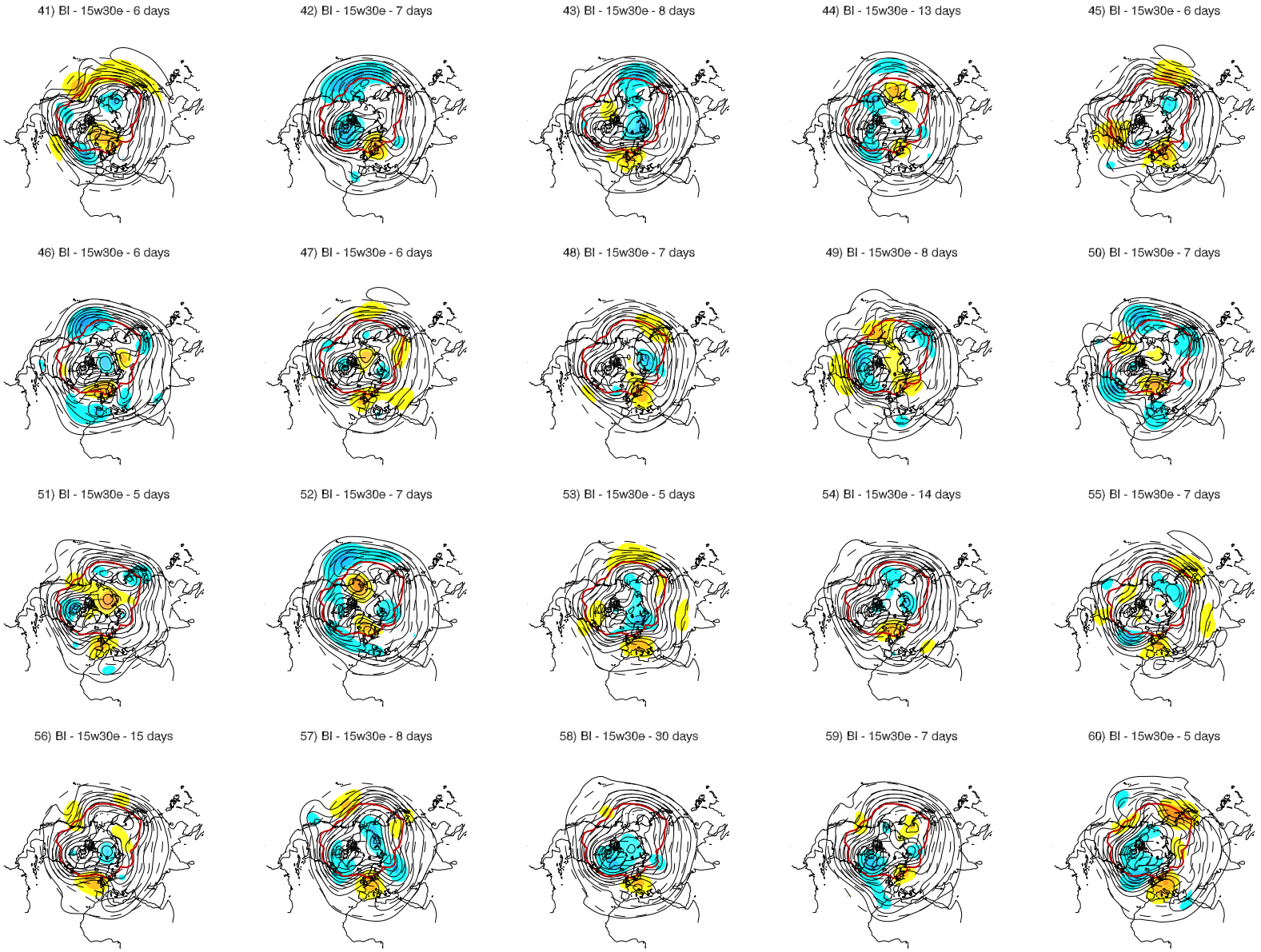

Figure A.1: Continued from previous page.

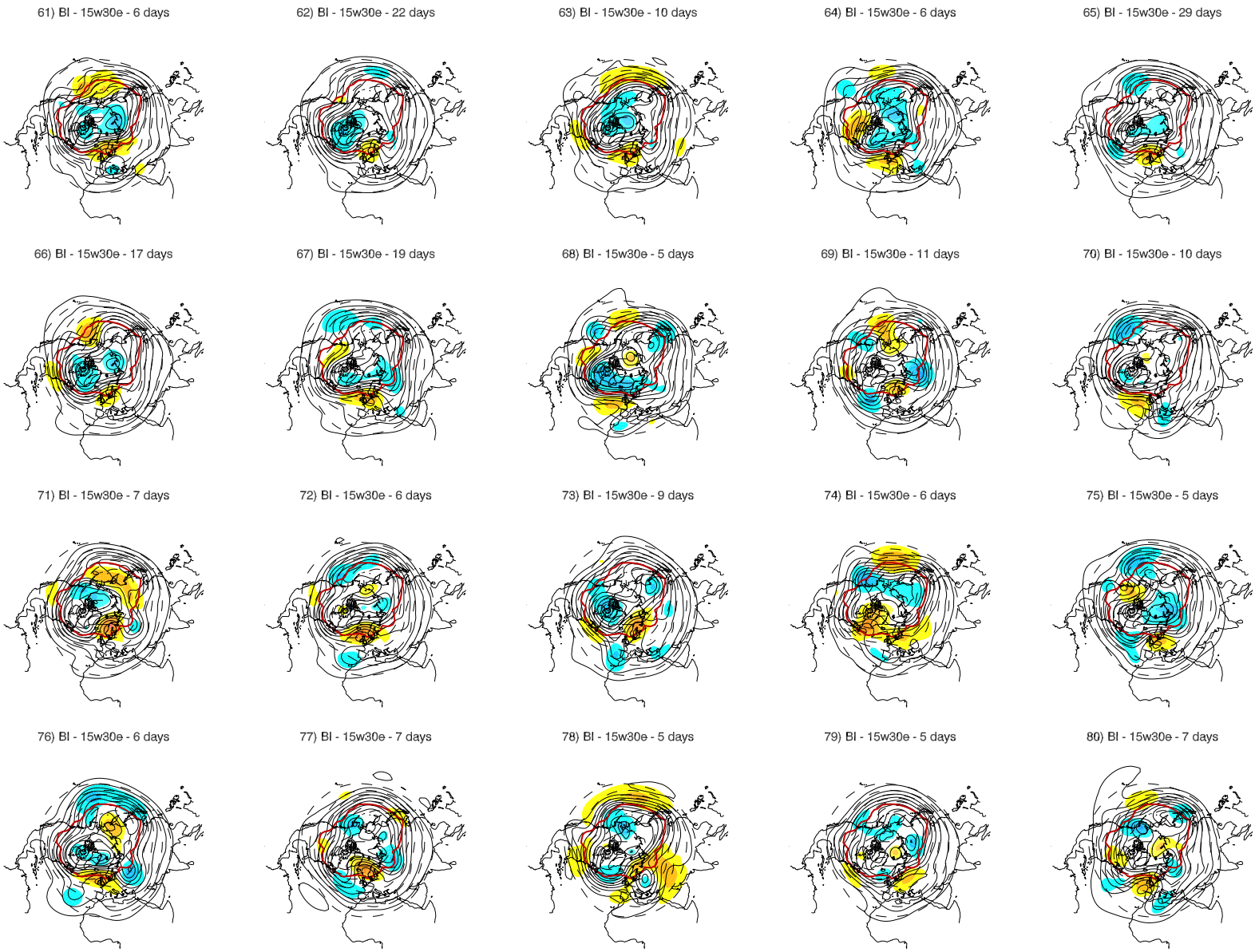

Figure A.1: Continued from previous page.

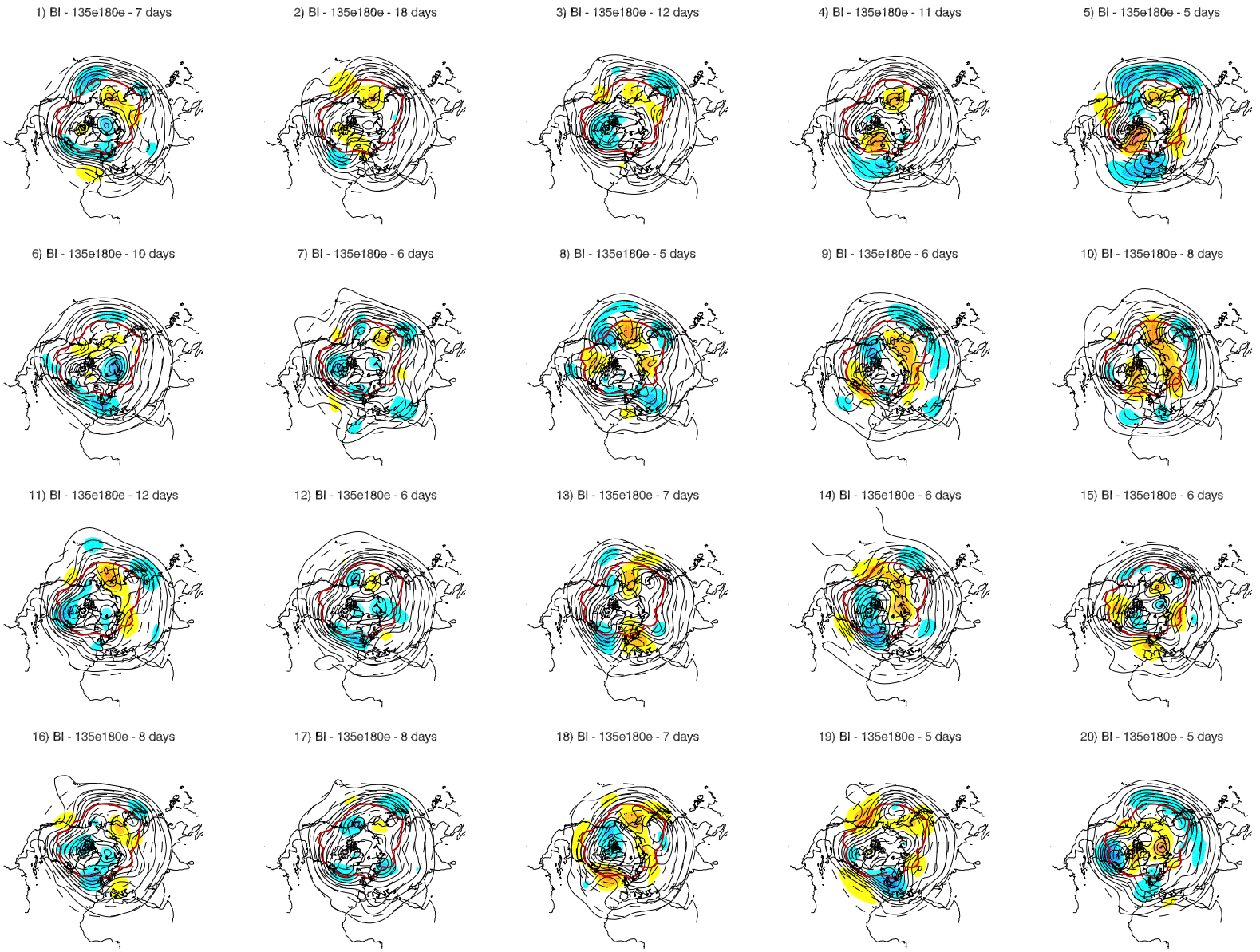

Figure A.2: Same as Figure A.1, but for blocking episodes occurring in western Pacific (WPAC, 135°E-180°E).

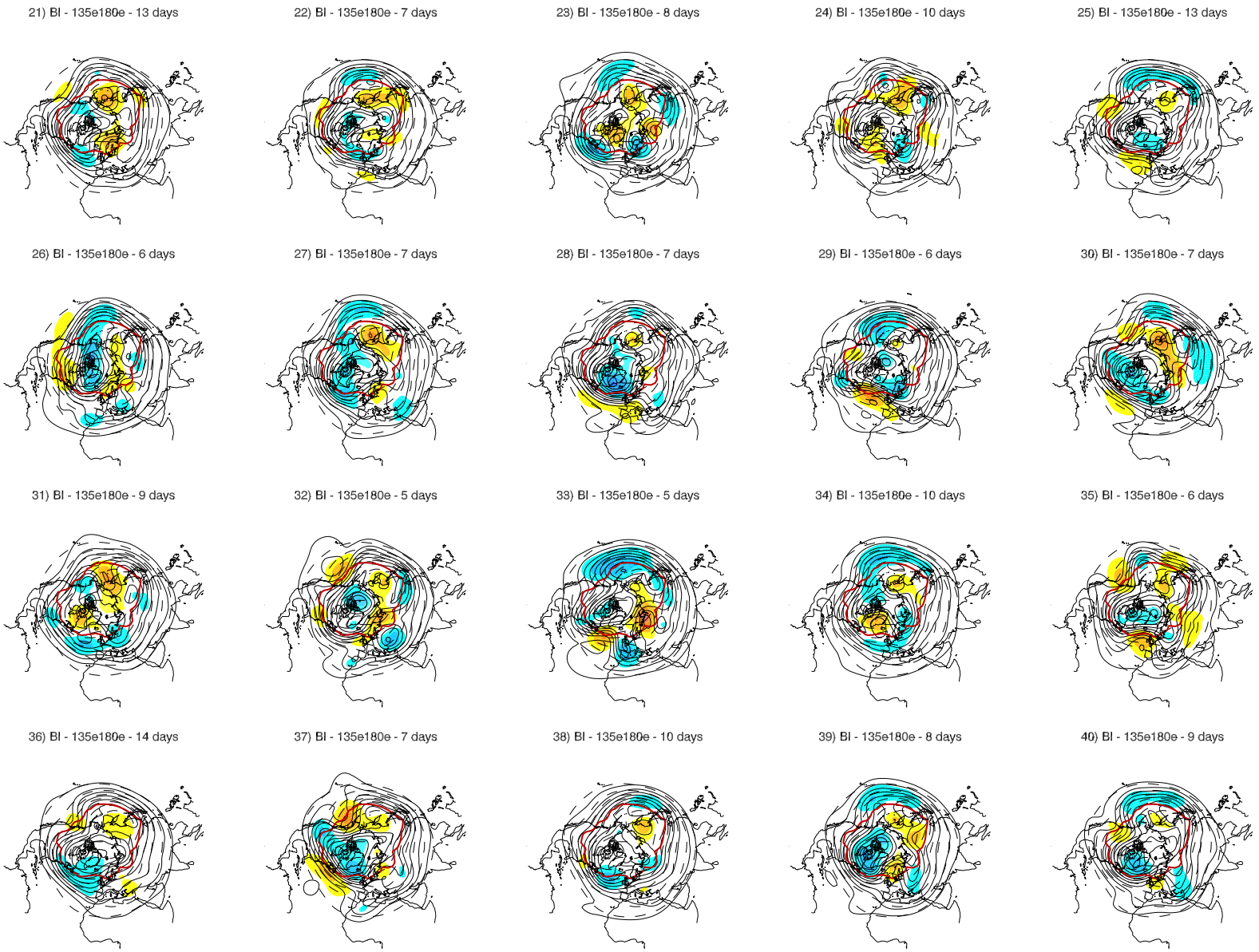

Figure A.2: Continued from previous page.

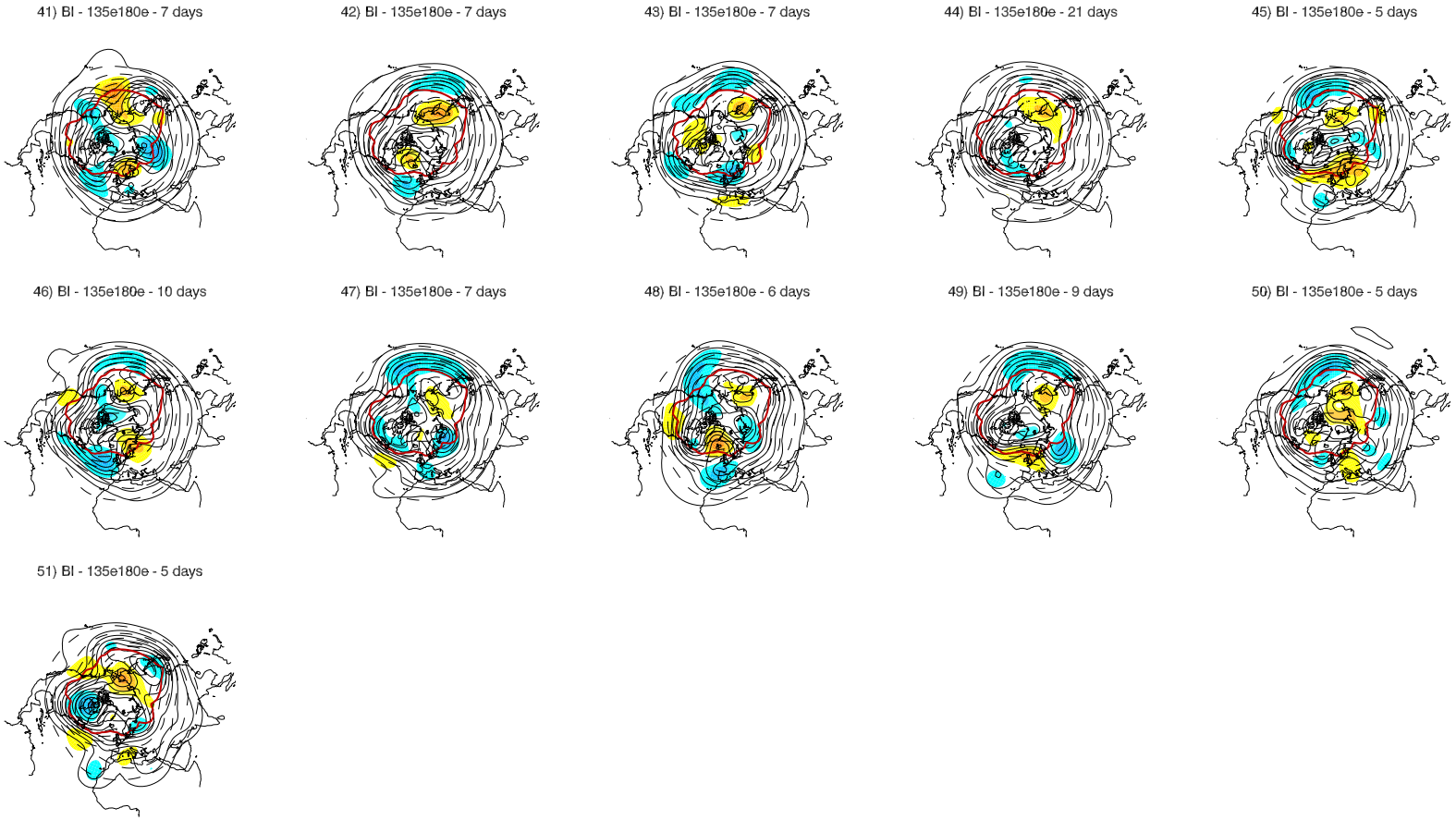

Figure A.2: Continued from previous page.

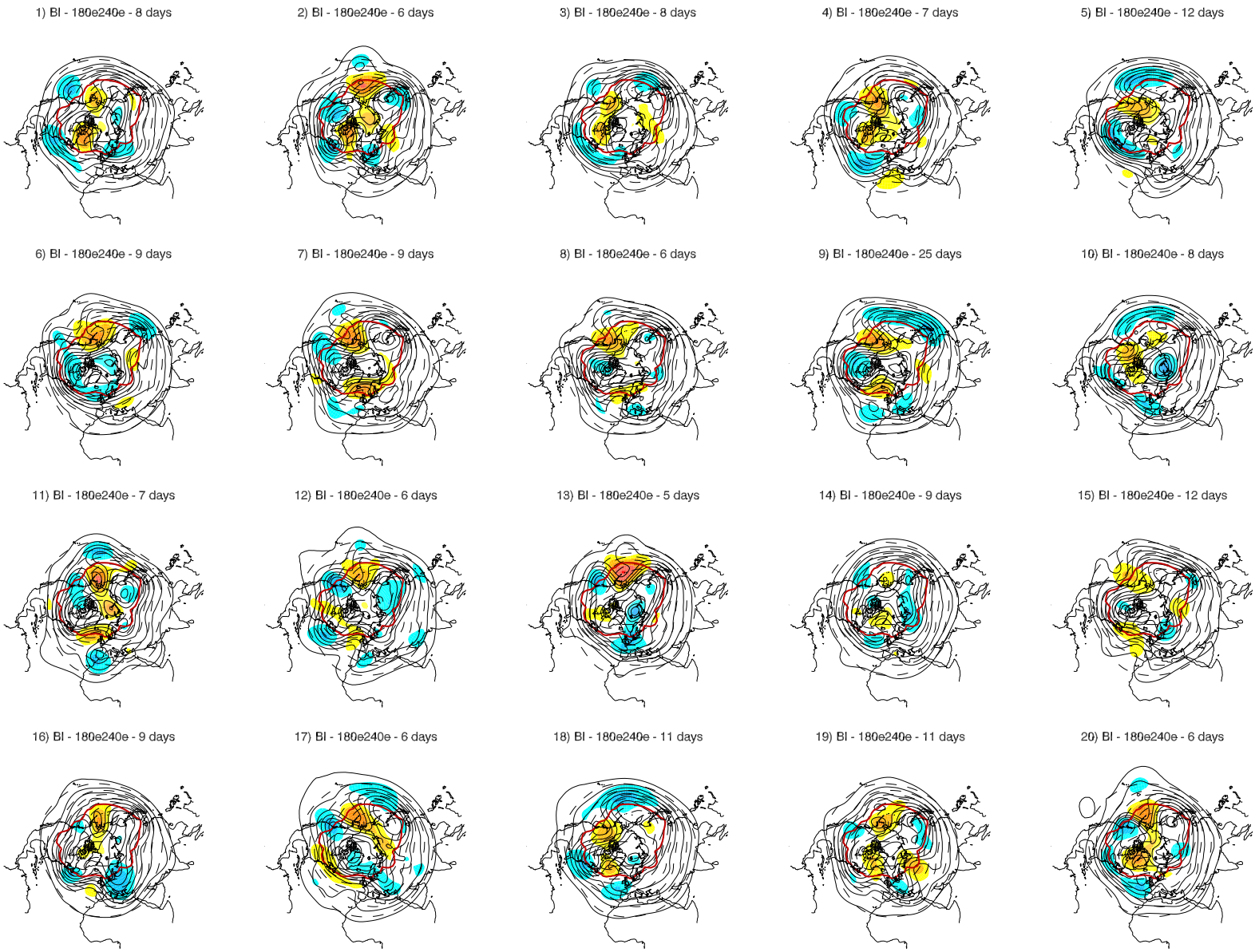

Figure A.3: Same as Figure A.2, but for blocking episodes occurring in eastern Pacific (EPAC, 180°E-240°E).

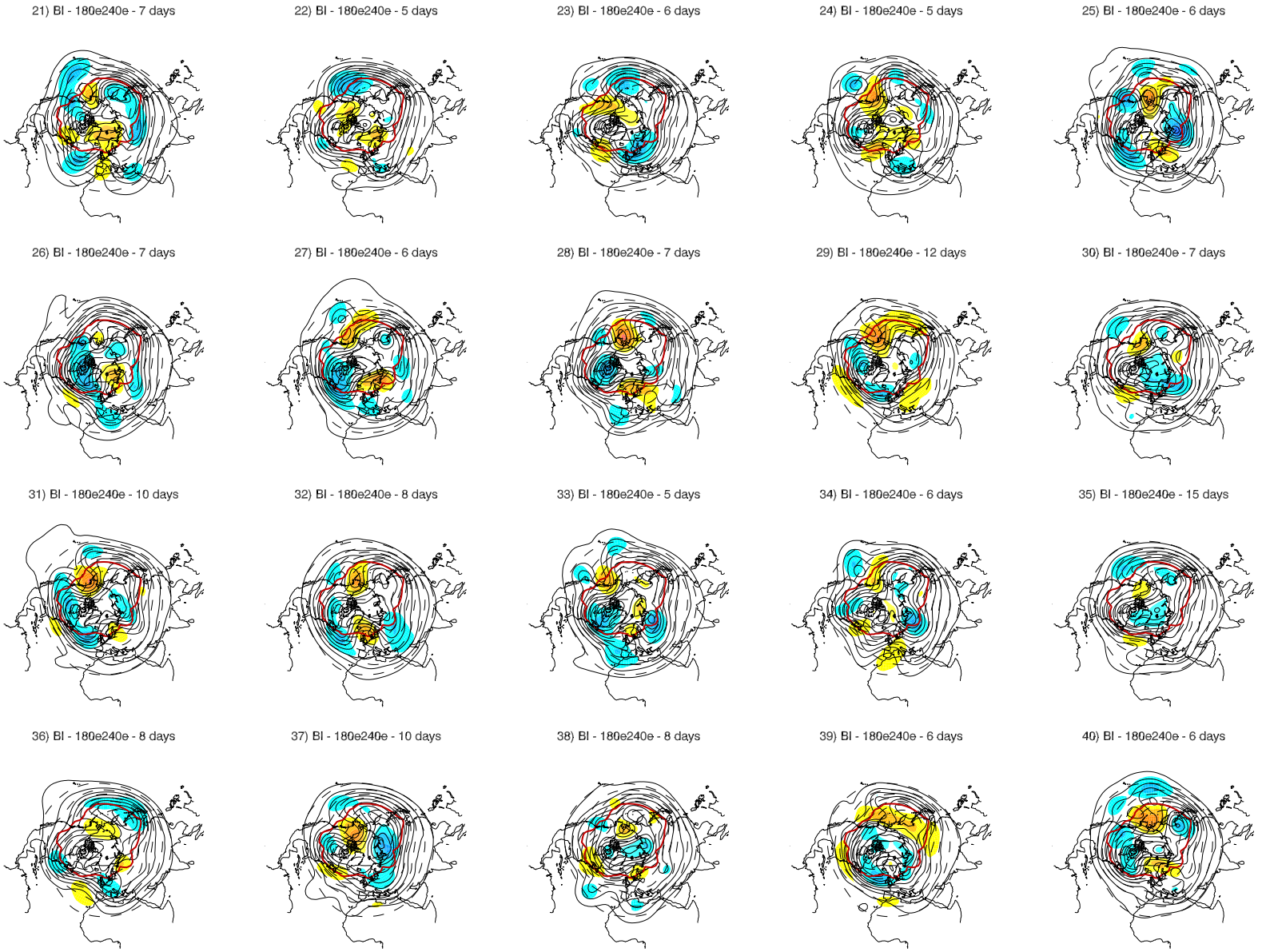

Figure A.3: Continued from previous page.

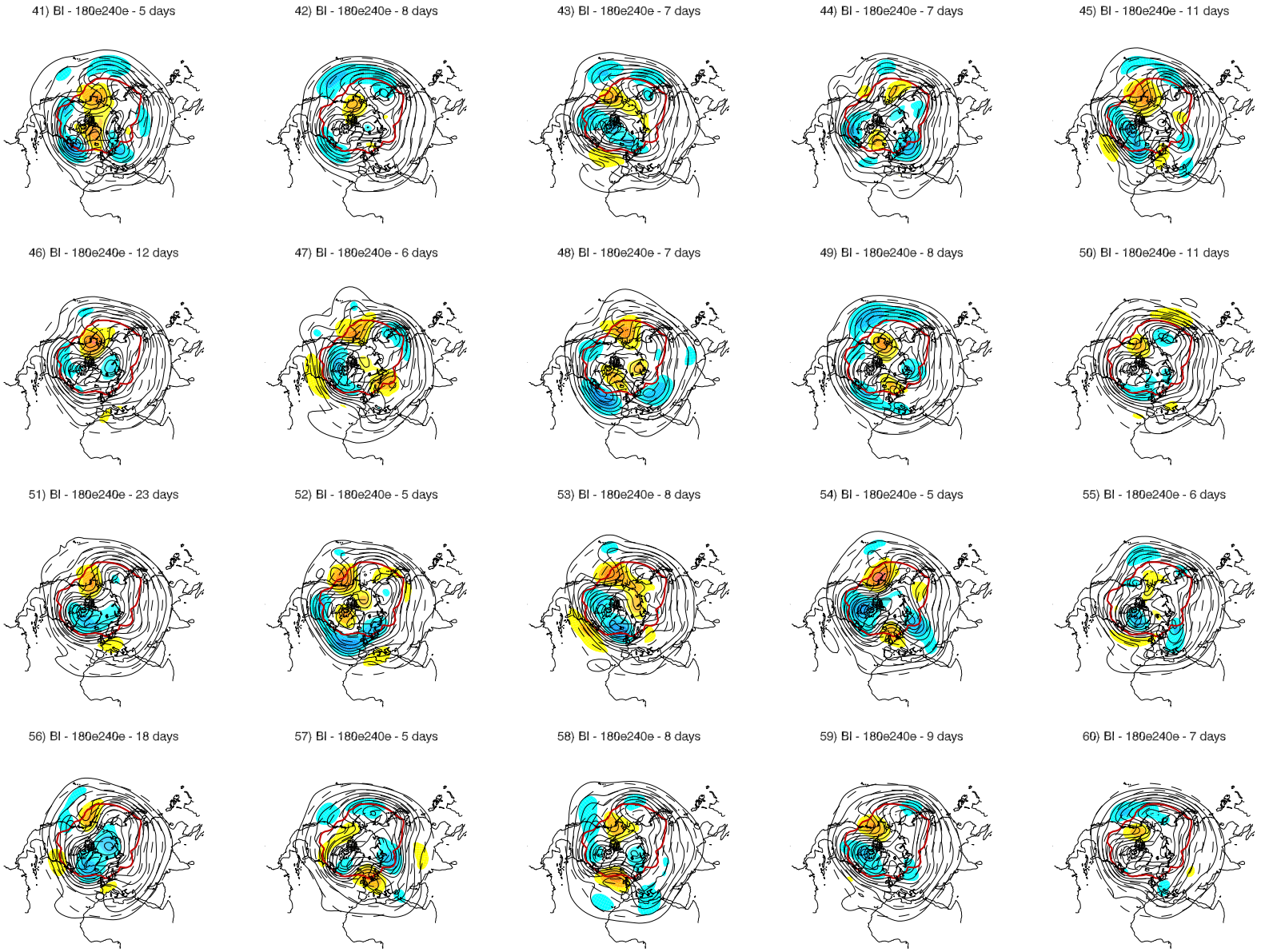

Figure A.3: Continued from previous page.

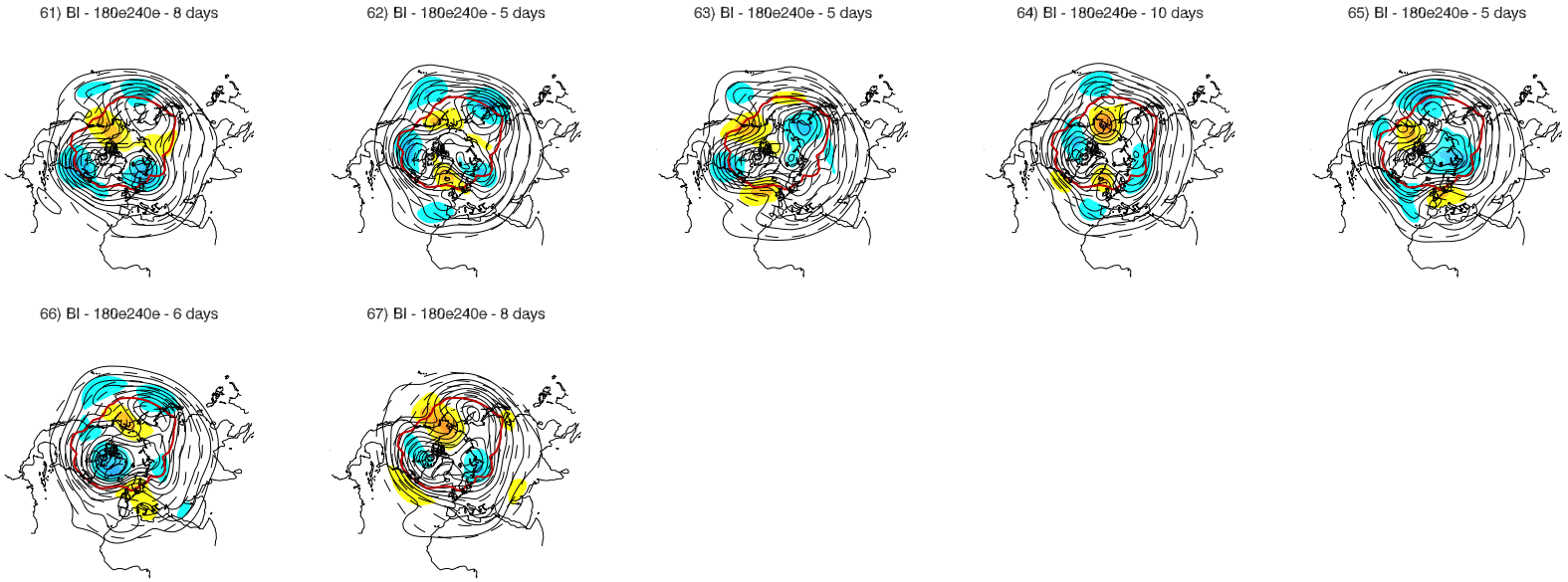

Figure A.3: Continued from previous page.

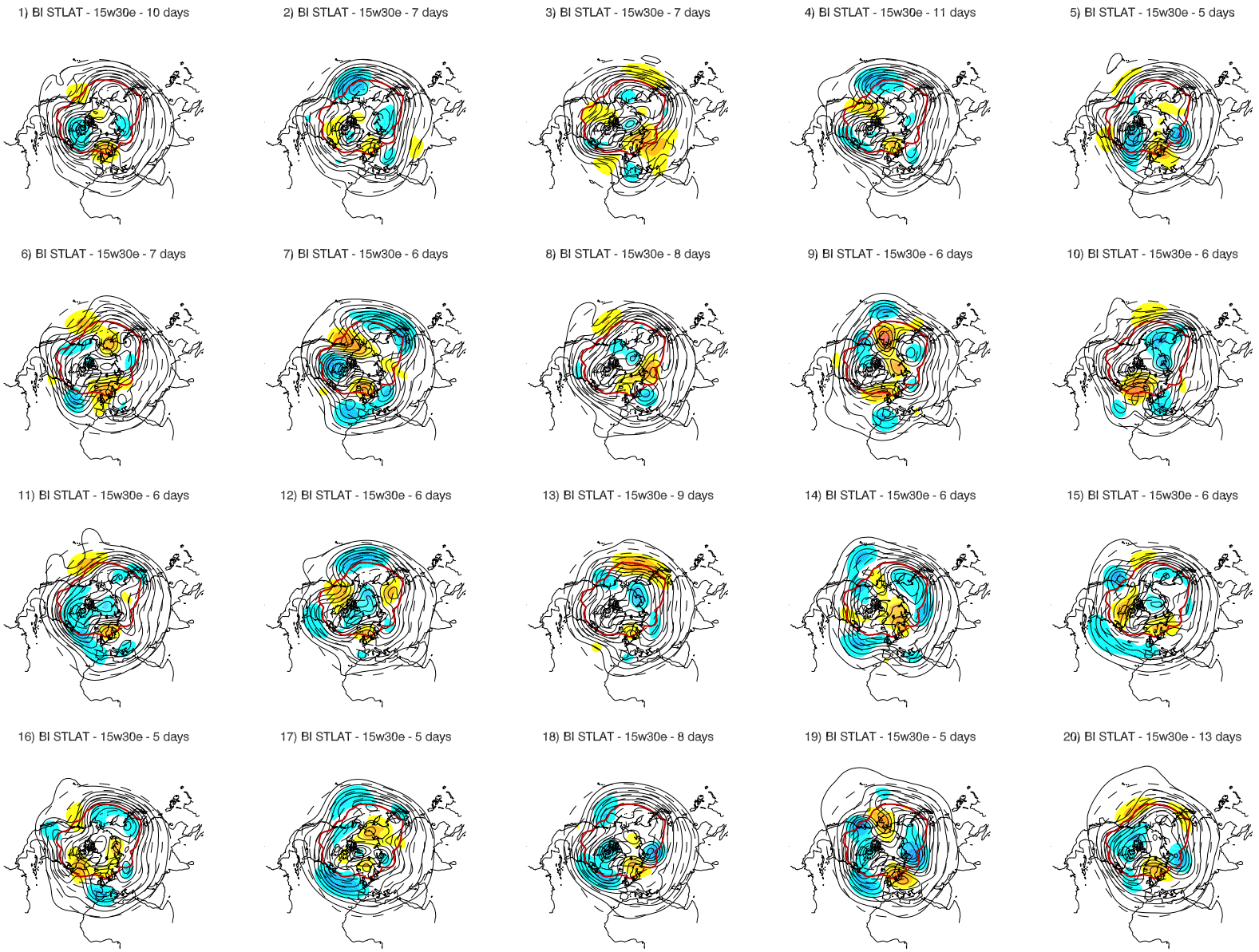

Figure A.4: Full (black dashed line) and anomaly (color shading) 500 hPa geopotential height fields averaged for the life-cycle of large-scale blocking episodes in Europe (EUR, 15°W-30°E), identified with the *BI* index. The solid black line is the 500 hPa climatological mean state in winter. The solid red line is the central latitude of blocking, taken as the latitude of the maximum storm track intensity.

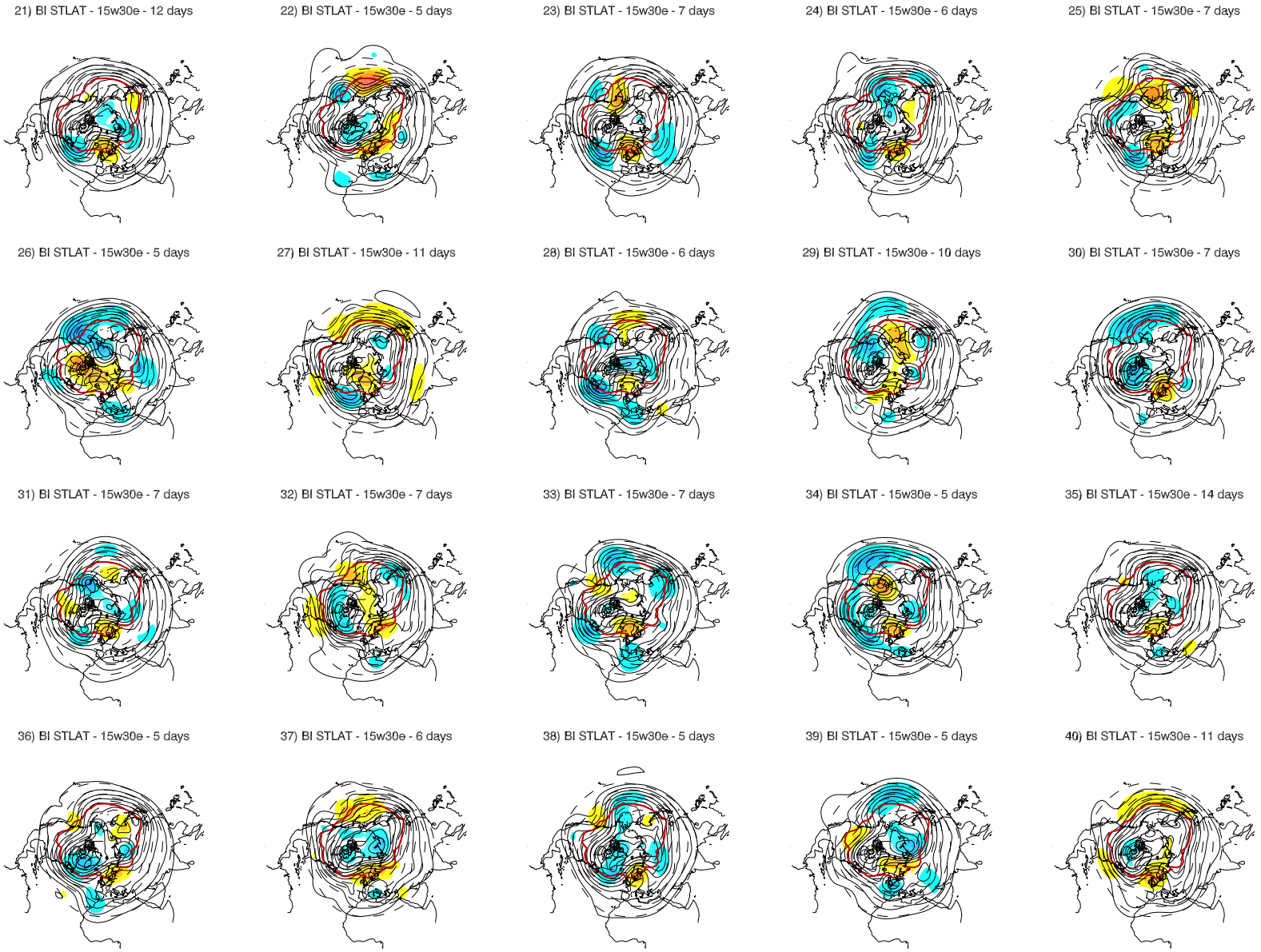

Figure A.4: Continued from previous page.

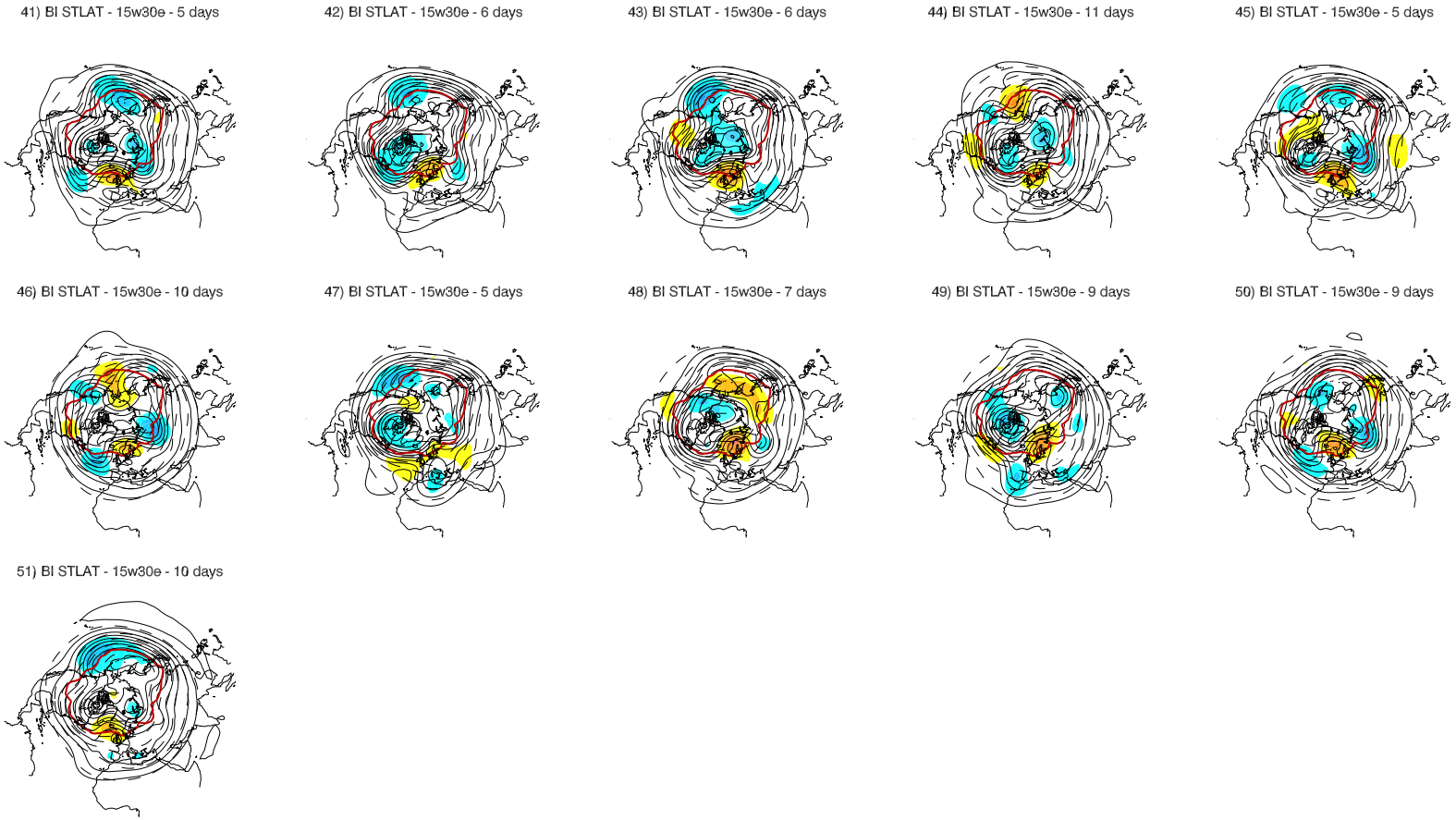

Figure A.4: Continued from previous page.

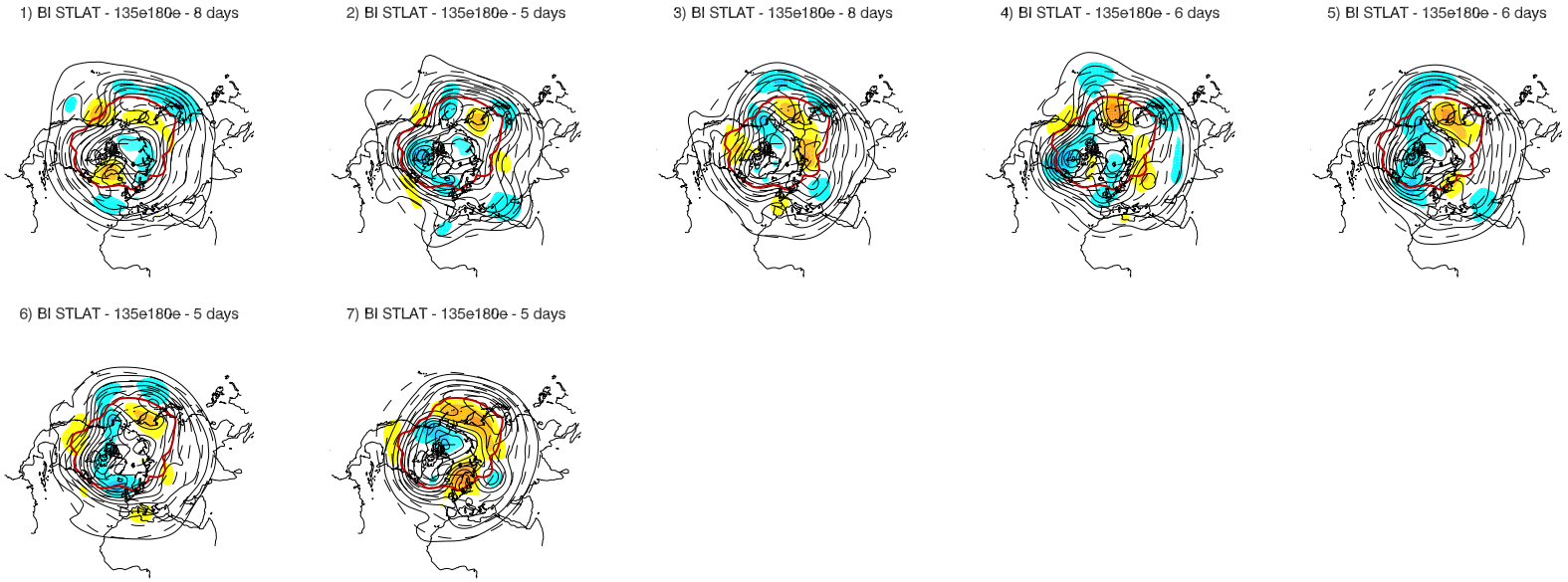

Figure A.5: Same as Figure A.1, but for blocking episodes occurring in western Pacific (WPAC, 135°E-180°E).

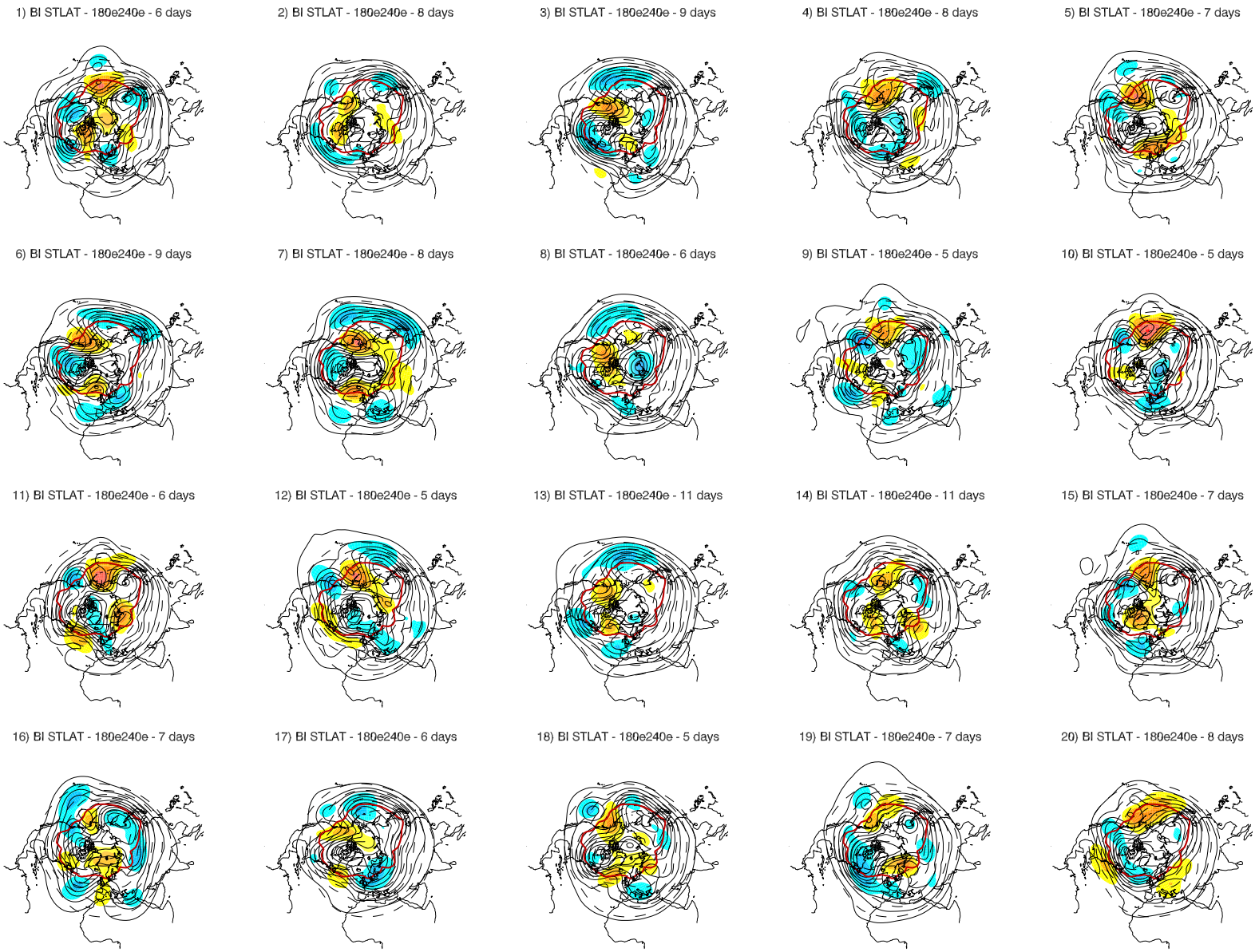

Figure A.6: Same as Figure A.2, but for blocking episodes occurring in eastern Pacific (EPAC, 180°E-240°E).

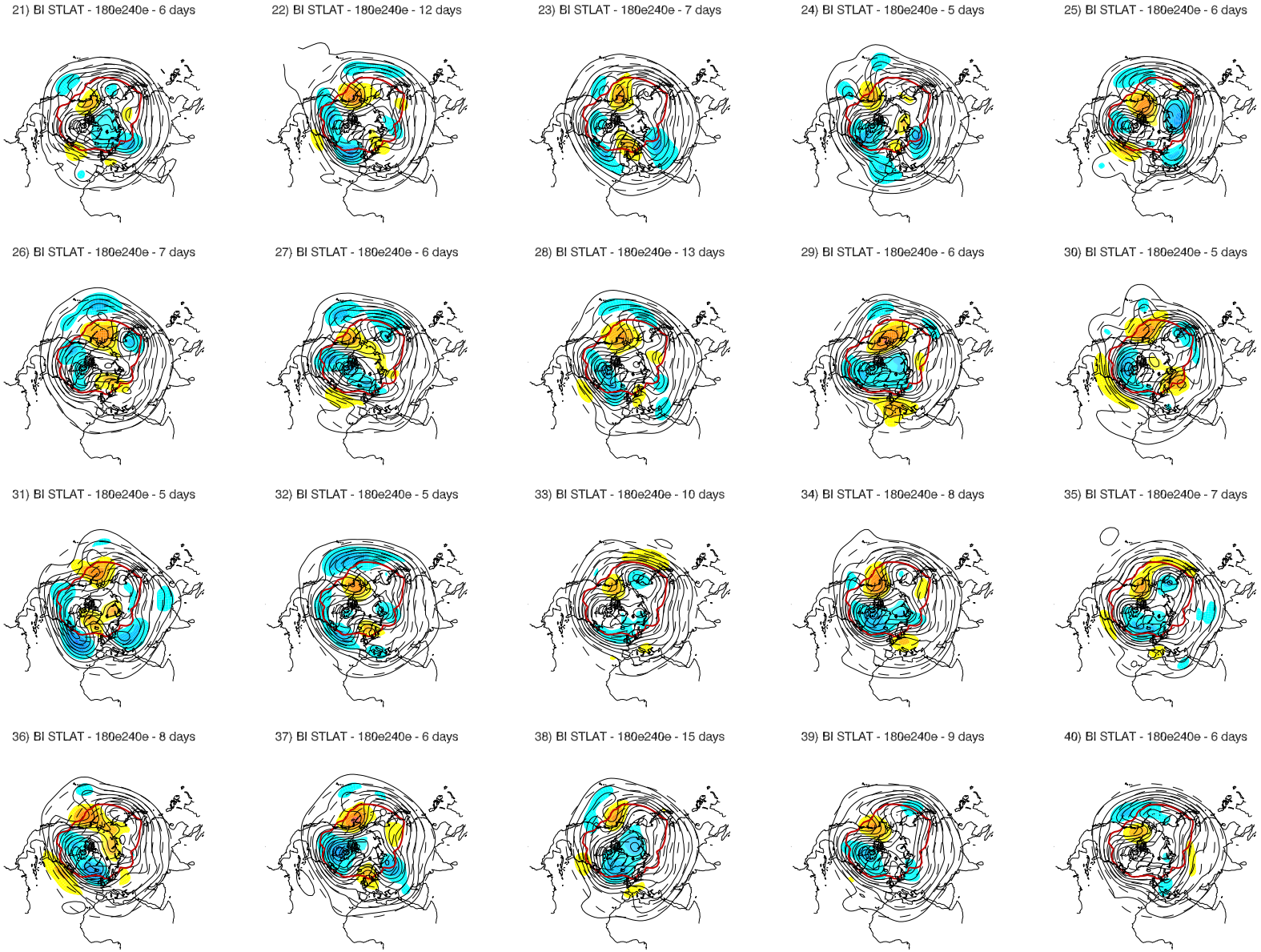

Figure A.6: Continued from previous page.

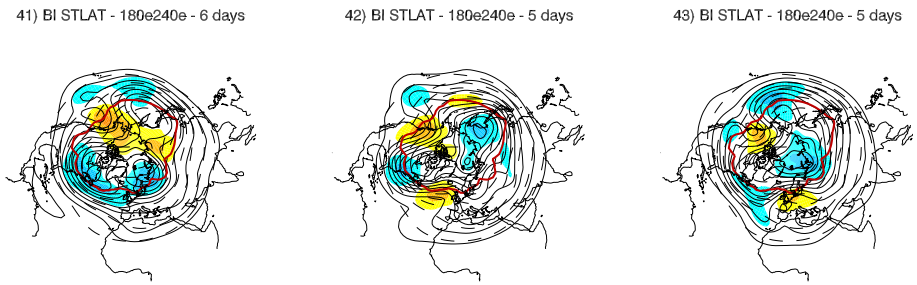

Figure A.6: Continued from previous page.

Appendix B

Supplementary material for Chapter 4

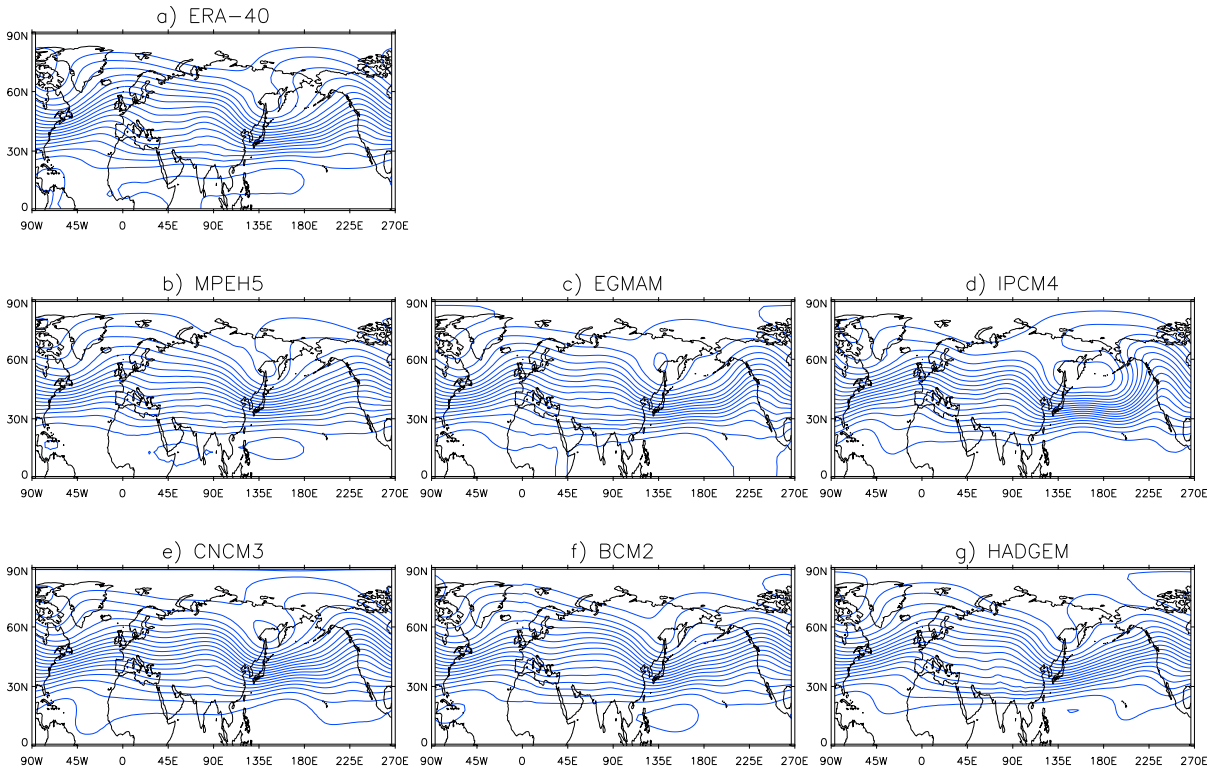

Figure B.1: Time-average 500 hPa geopotential field for the 6 AOGCMs used in Chapter 4.

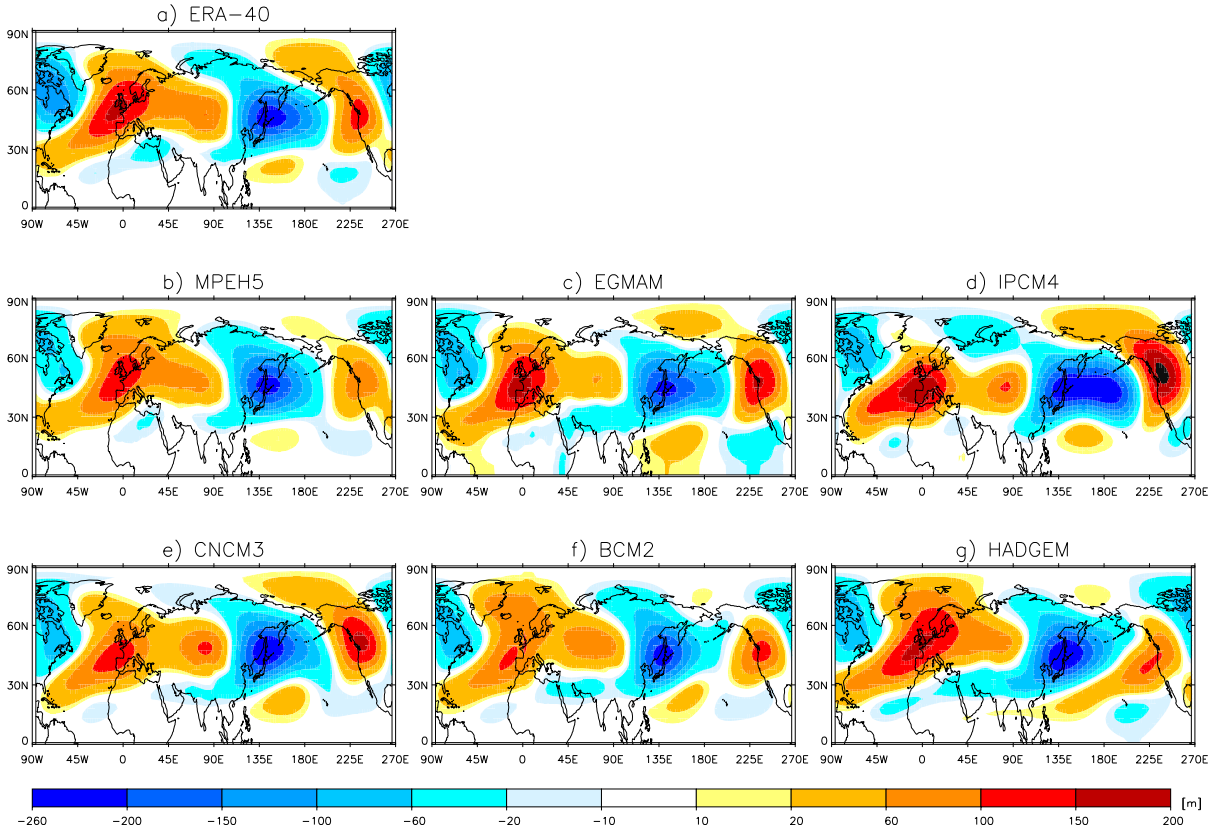

Figure B.2: Stationary wave at 500 hPa for the 6 AOGCMs used in Chapter 4.

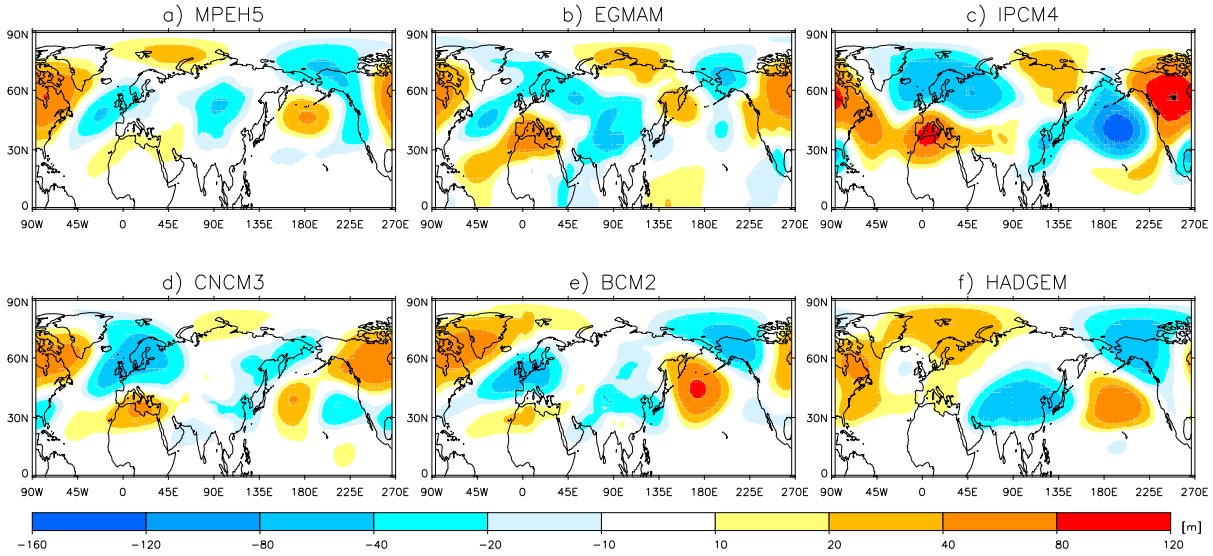

Figure B.3: Systematic error of the stationary wave for the 6 AOGCMs used in Chapter 4.

Appendix C

Supplementary material for Chapter 6

Comparison of model and observation-based percentile indices for extreme events

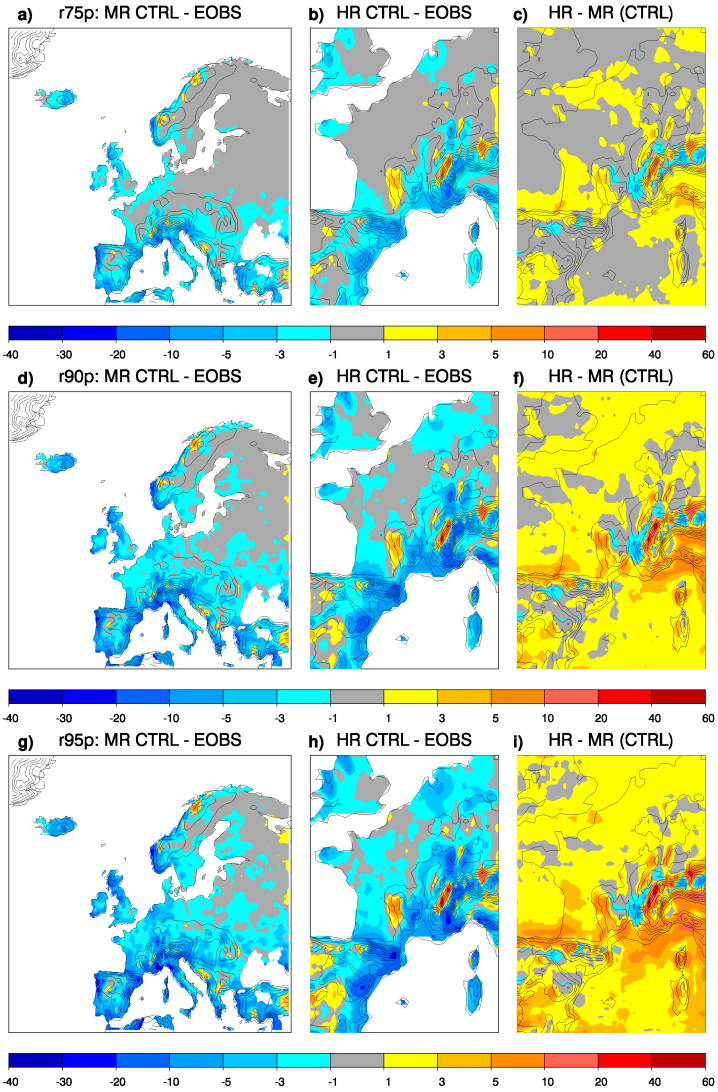

Figure C.1: Differences of **precipitation extreme percentiles** for MR CTRL - EOBS (left), HR CTRL - EOBS (middle) and HR CTRL - MR CTRL (right). Units are in mm/day.

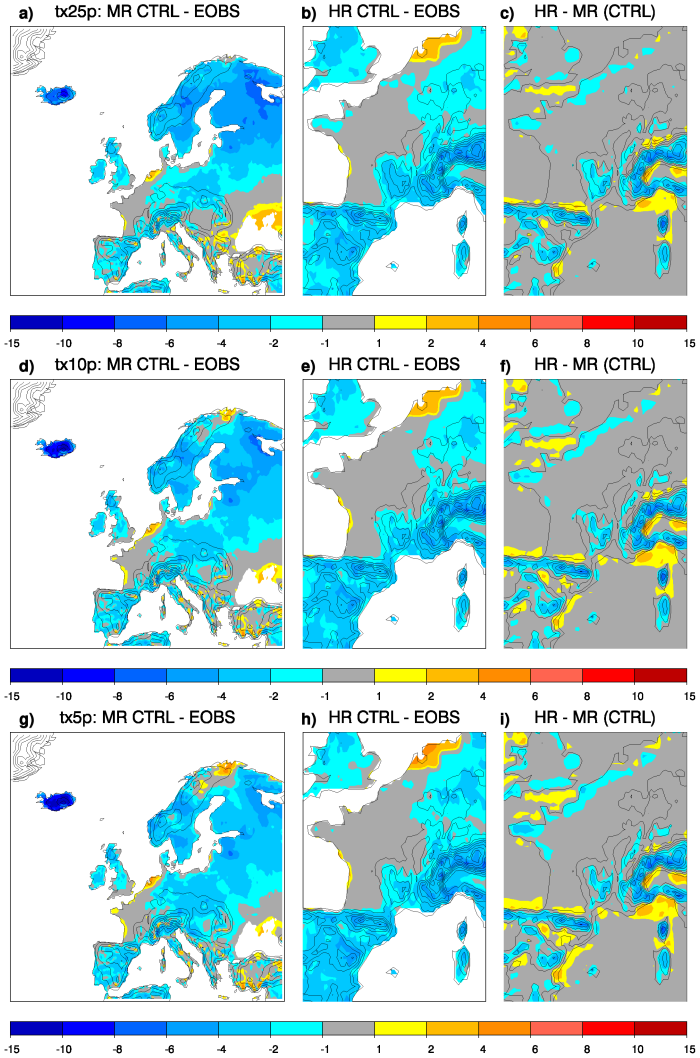

Figure C.2: Same as Figure C.1, but for **cold-day extremes**. Units are in °C

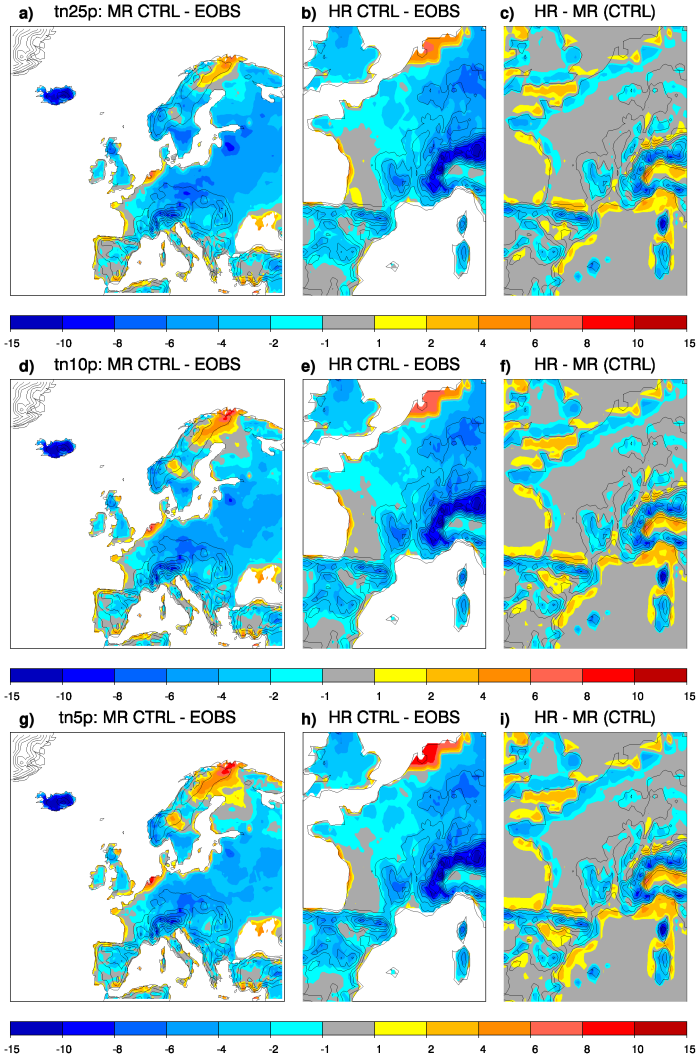

Figure C.3: Same as Figure C.1, but for **cold-night extremes**.

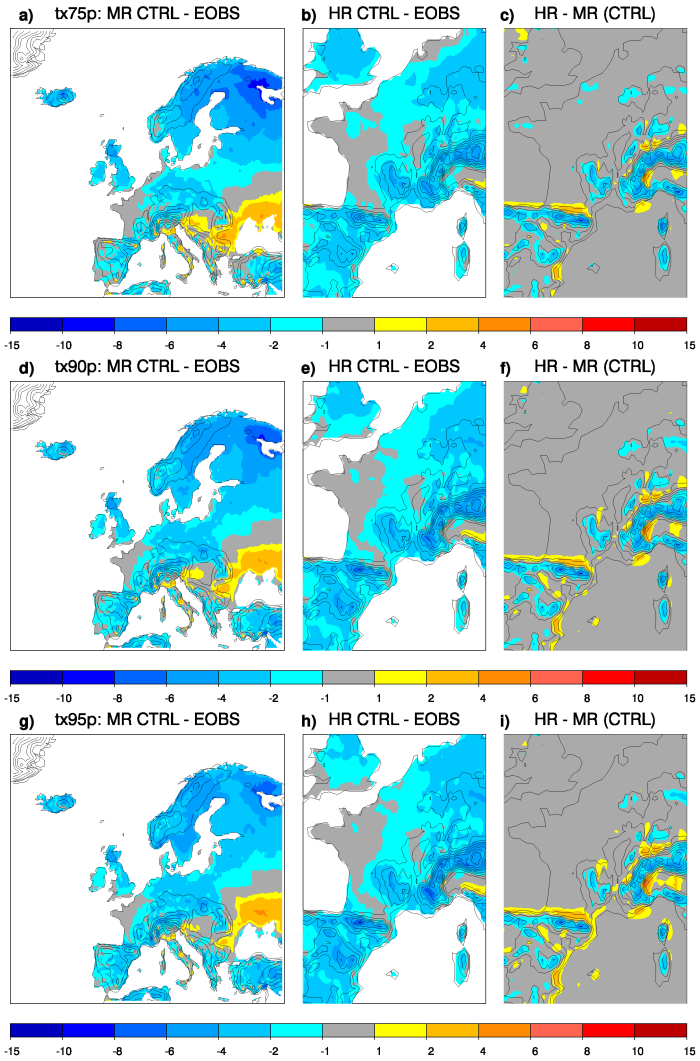

Figure C.4: Same as Figure C.1, but for **warm-day extremes**

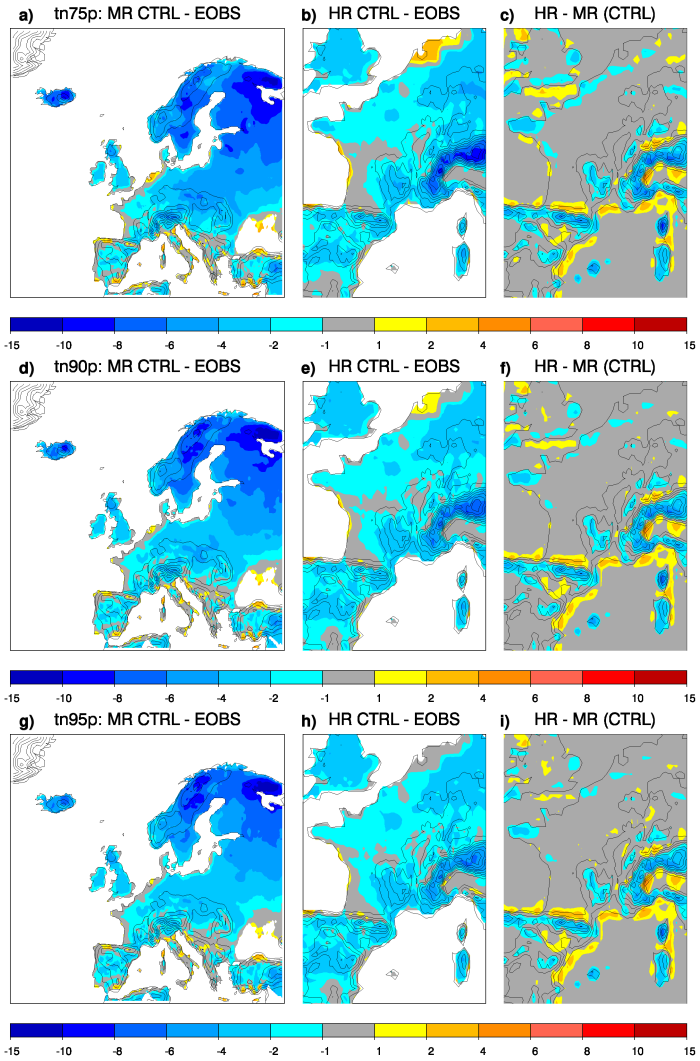

Figure C.5: Same as Figure C.1, but for **warm-night extremes**.

Total number of extreme days during blocking conditions

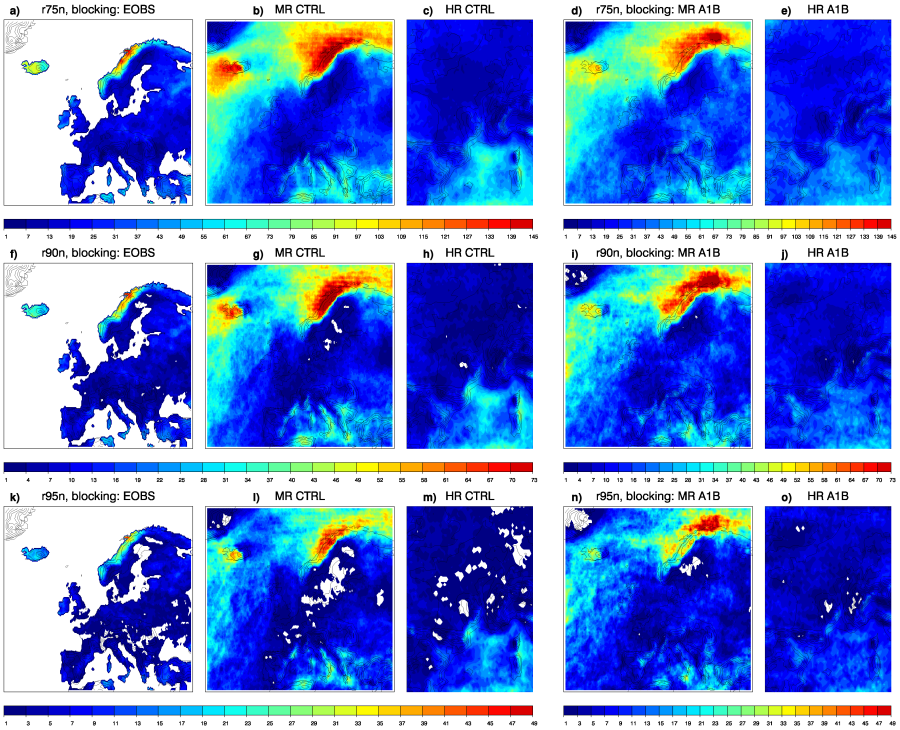

Figure C.6: Total number of **precipitation extremes** within **blocking conditions**. The fields displayed from the top row to the bottom row are the 75^{th}, 90^{th}, 95^{th} percentile of the daily average precipitation distribution, on rainy days only (r75n, r90n, r95n). From left to right: EOBS, MR CTRL, HR CTRL, MR A1B and HR A1B.

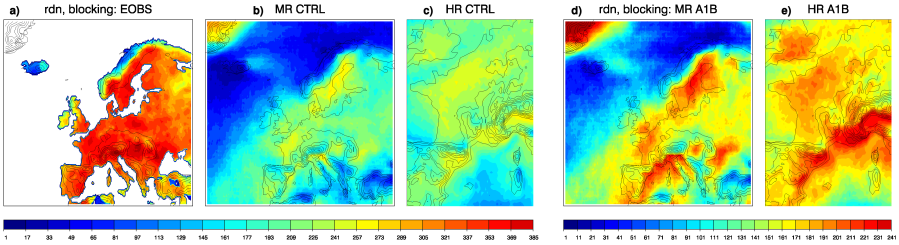

Figure C.7: Same as Figure C.6, but for **dry days**, where r $<$ 1 mm.

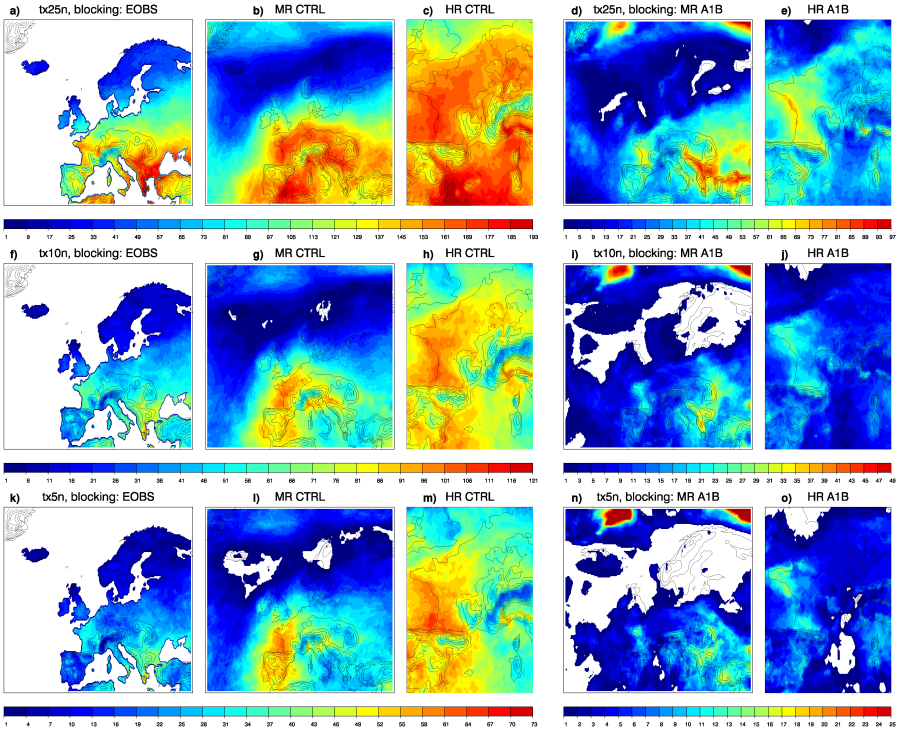

Figure C.8: Same as Figure C.6, but for **cold day extremes**. From top to bottom: 25^{th}, 10^{th}, 5^{th} percentile of the daily maximum temperature distribution (tx25n, tx10n, tx5n).

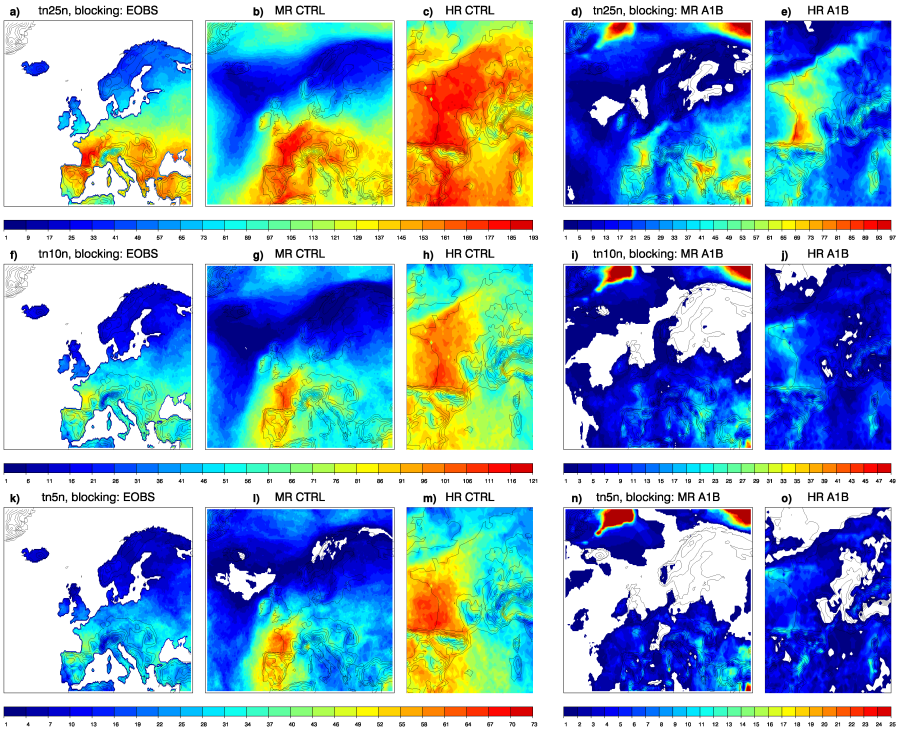

Figure C.9: Same as Figure C.8, but for **cold night extremes**, with the 25^{th}, 10^{th}, 5^{th} percentile of the daily minimum temperature distribution (from top to bottom: tn25n, tn10n, tn5n).

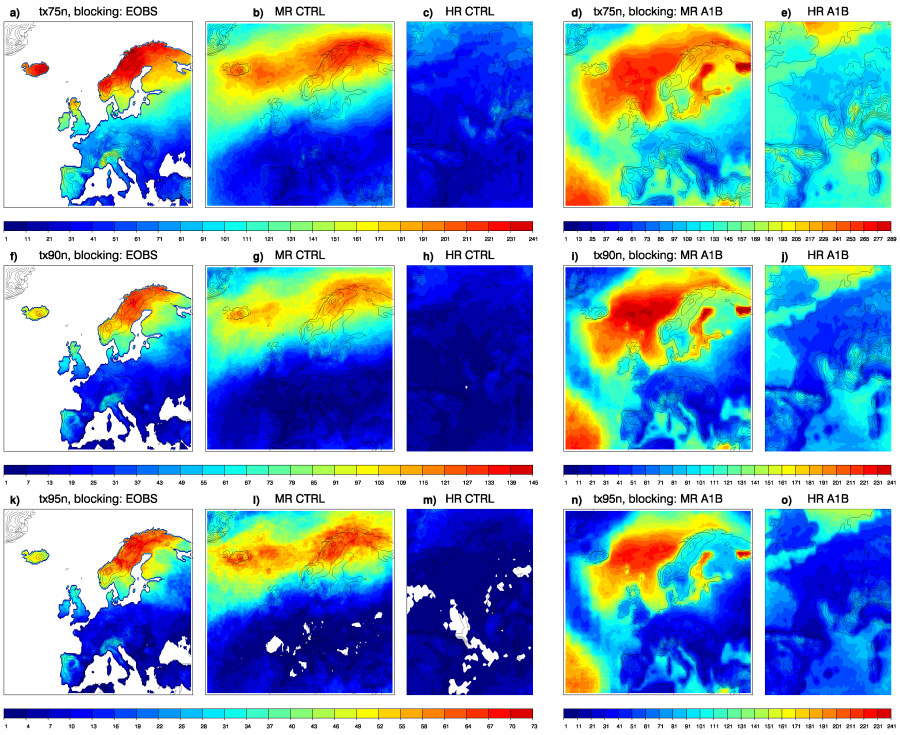

Figure C.10: Same as Figure C.8, but for **warm day extremes**. From top to bottom: 75^{th}, 90^{th}, 95^{th} percentile of the daily maximum temperature distribution (tx75n, tx90n, tx95n).

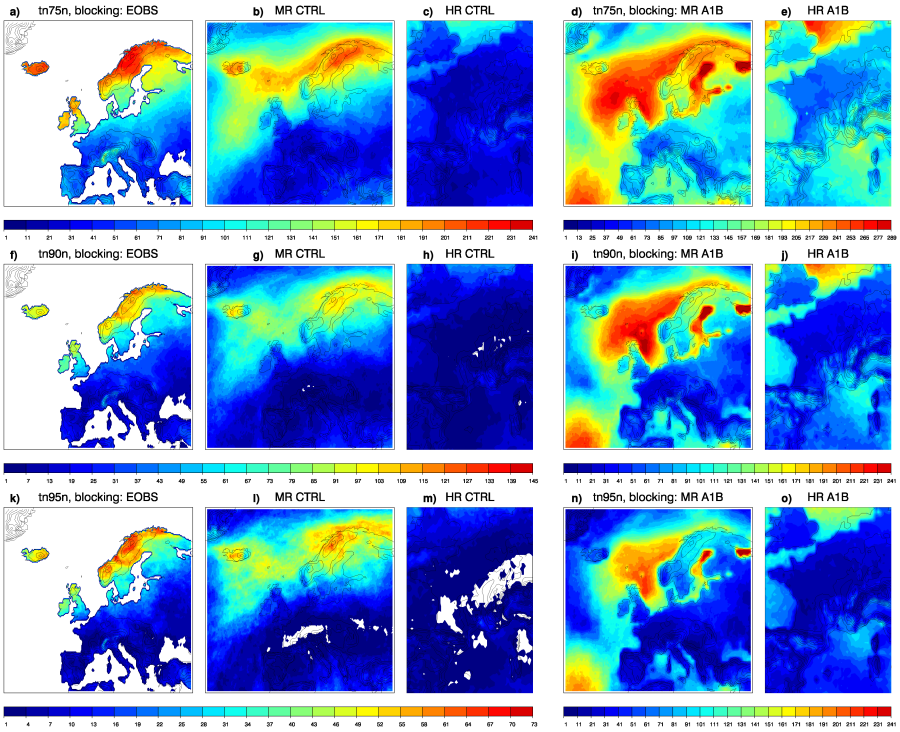

Figure C.11: Same as Figure C.9, but for **warm night extremes**. From top to bottom: 75^{th}, 90^{th}, 95^{th} percentile of the daily minimum temperature distribution (tn75n, tn90n, tn95n).

Total number of extreme days during non-blocking conditions

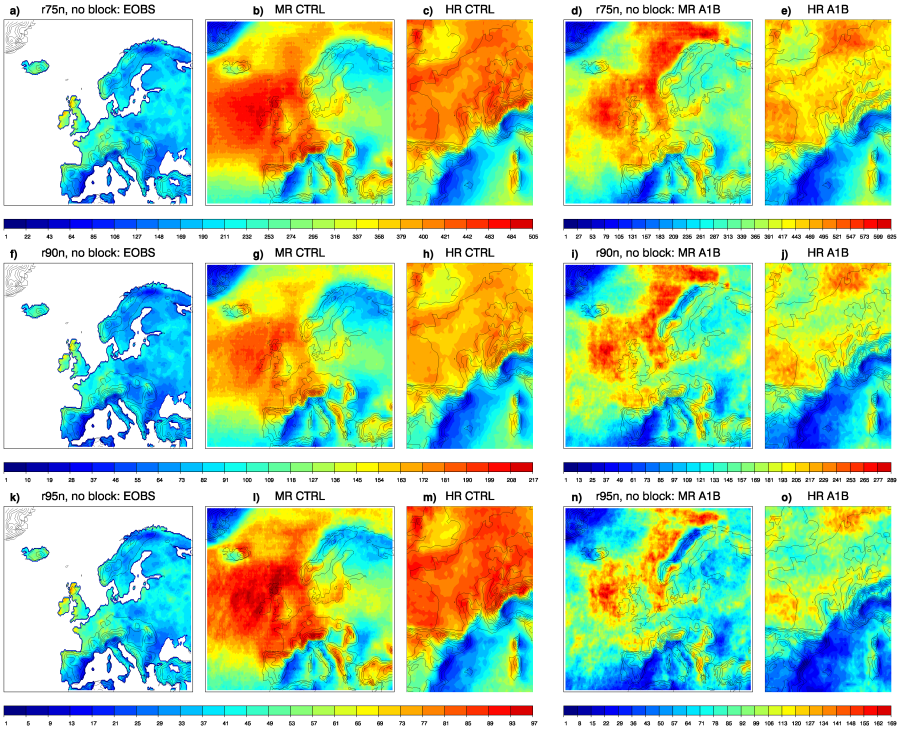

Figure C.12: Same as Figure C.6, but for **precipitation extremes** within **non-blocking conditions**.

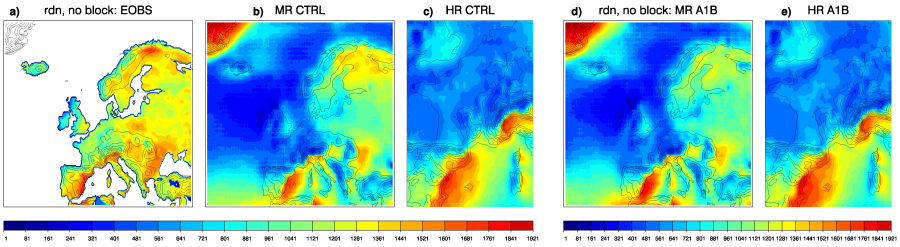

Figure C.13: Same as Figure C.12, but for **dry days**, where r $<$ 1 mm.

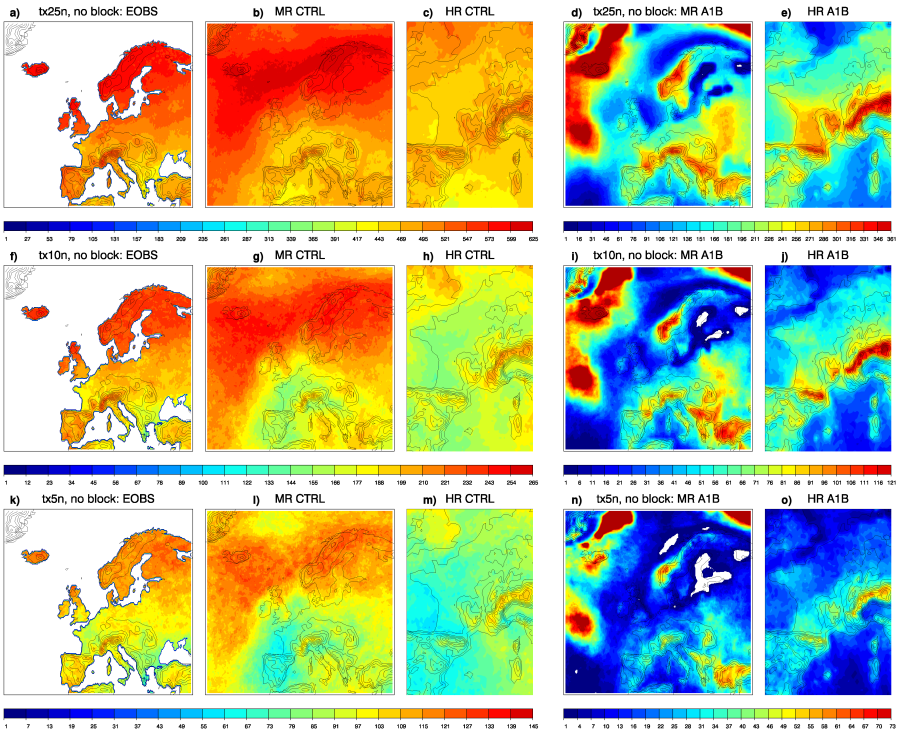

Figure C.14: Same as Figure C.6, but for **cold day extremes**. From top to bottom: 25^{th}, 10^{th}, 5^{th} percentile of the daily maximum temperature distribution (tx25n, tx10n, tx5n).

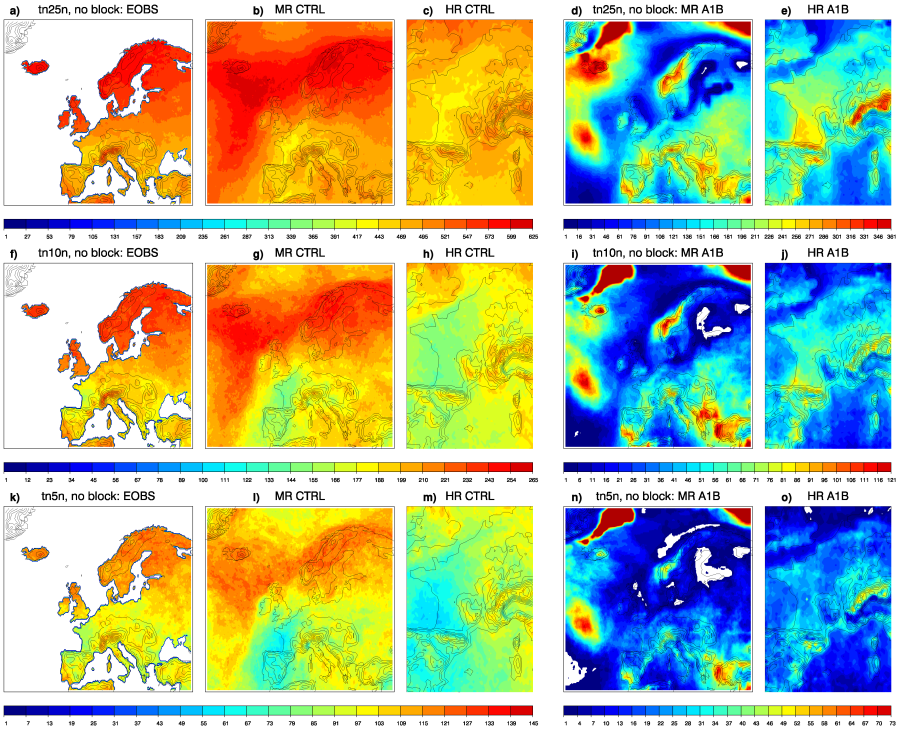

Figure C.15: Same as Figure C.14, but for **cold night extremes**. From top to bottom: 25^{th}, 10^{th}, 5^{th} percentile of the daily minimum temperature distribution (tn25n, tn10n, tn5n).

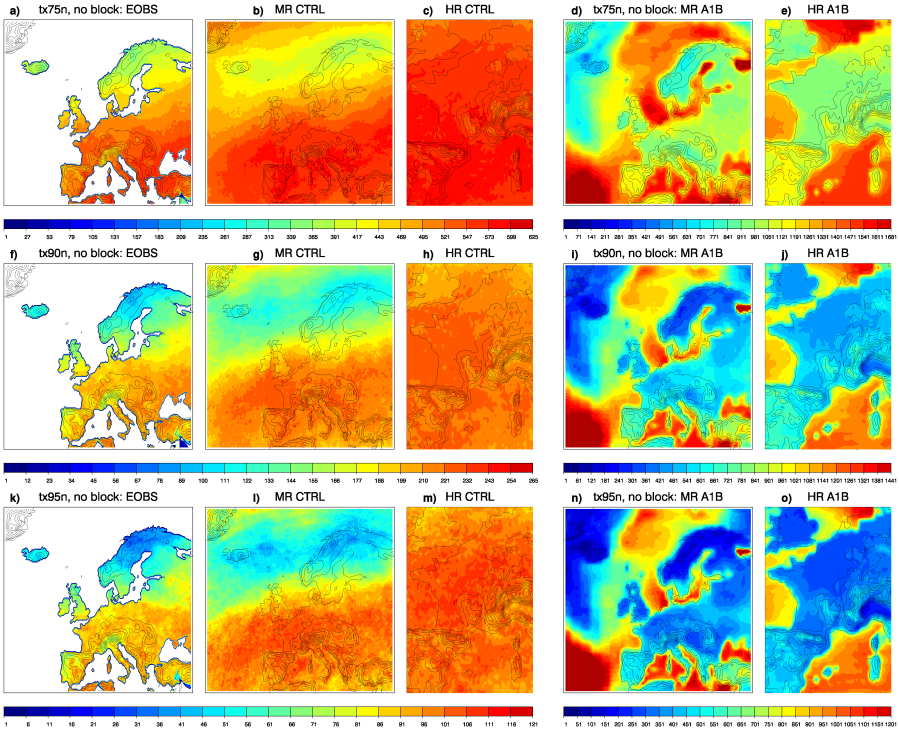

Figure C.16: Same as Figure C.14, but for **warm day extremes**. From top to bottom: 75^{th}, 90^{th}, 95^{th} percentile of the daily maximum temperature distribution (tx75n, tx90n, tx95n).

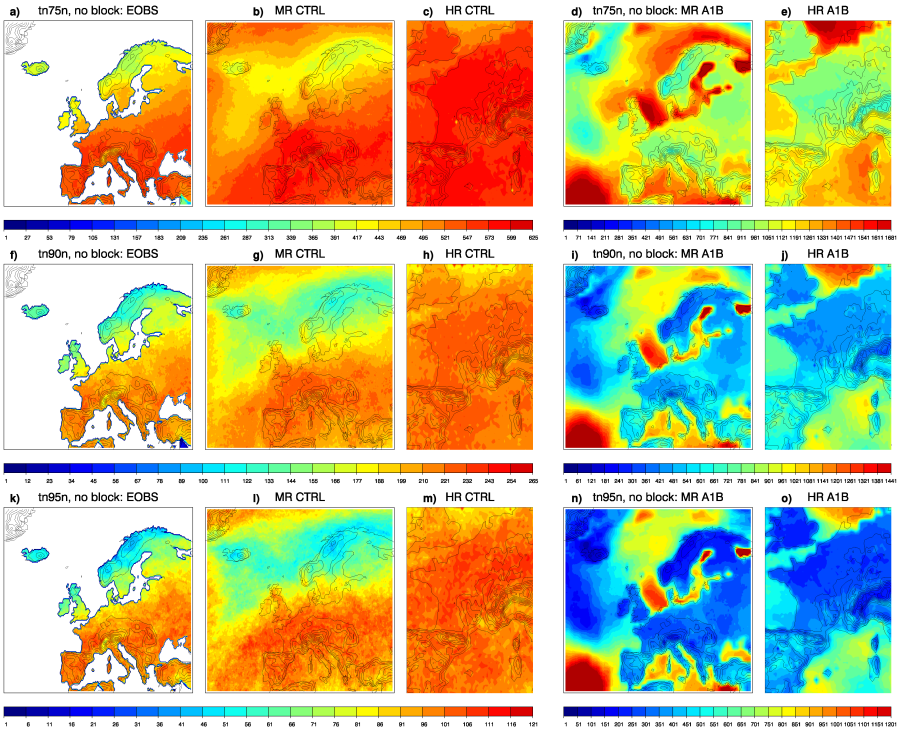

Figure C.17: Same as Figure C.15, but for **warm night extremes**. From top to bottom: 75^{th}, 90^{th}, 95^{th} percentile of the daily minimum temperature distribution (tn75n, tn90n, tn95n).

Difference in the number of extreme days between HR and MR

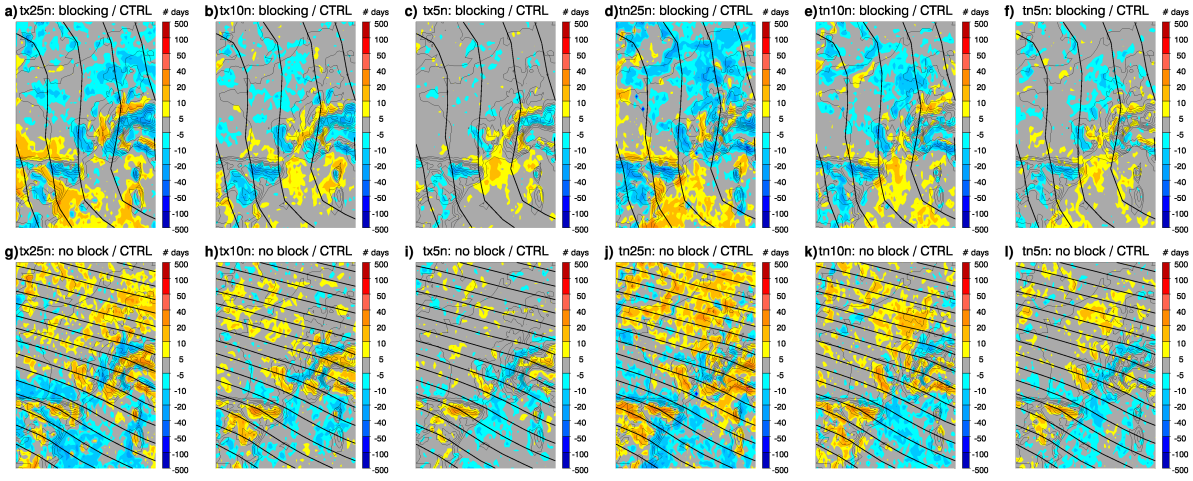

Figure C.18: Differences (HR - MR) in the number of **cold extreme** days for the CTRL simulations. Black contours represent the geopotential height field during blocking (top panels) and non-blocking (bottom panels) periods.

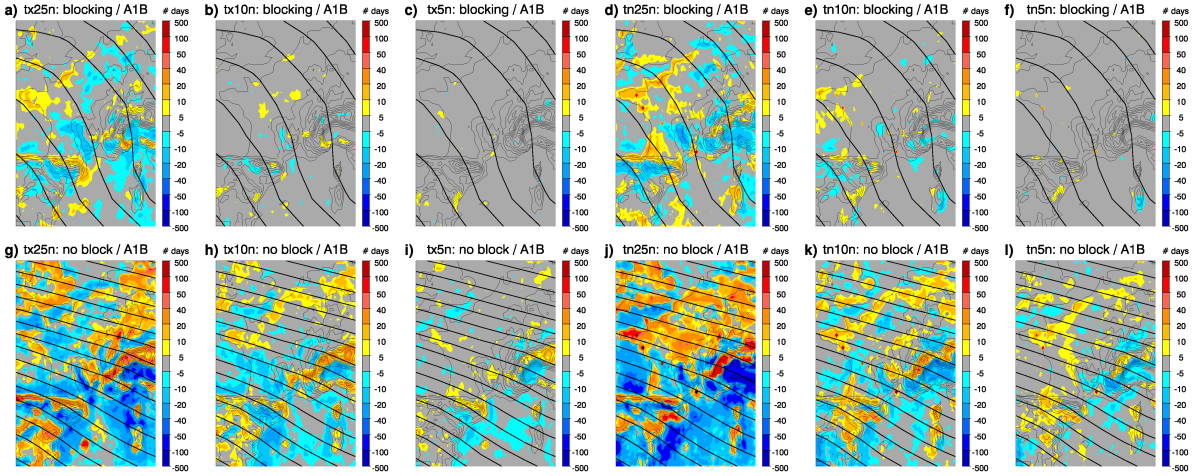

Figure C.19: Same as Figure C.18, but for the A1B scenario.

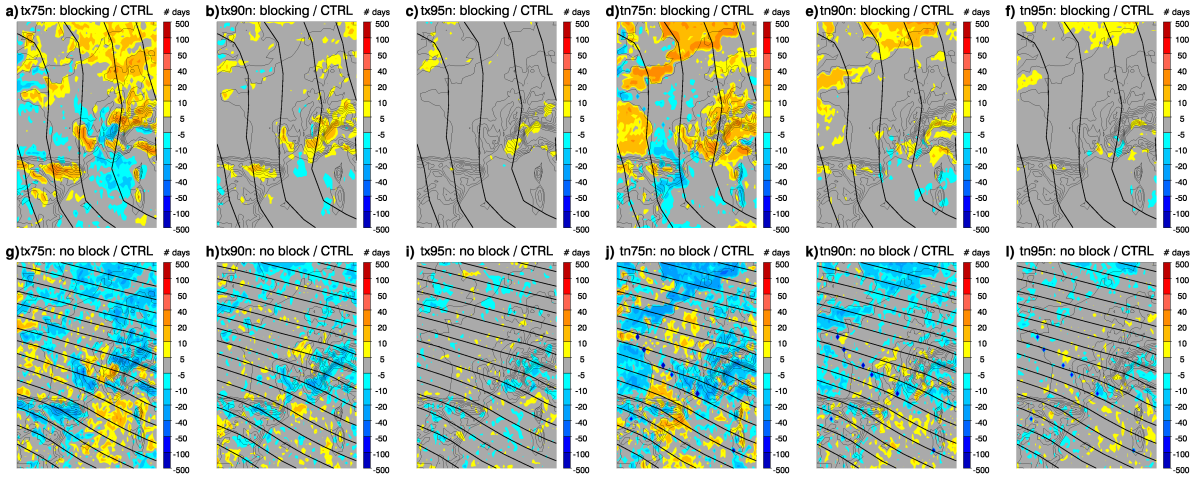

Figure C.20: Differences in the number of **warm extreme** days for MR - HR for the CTRL simulations.

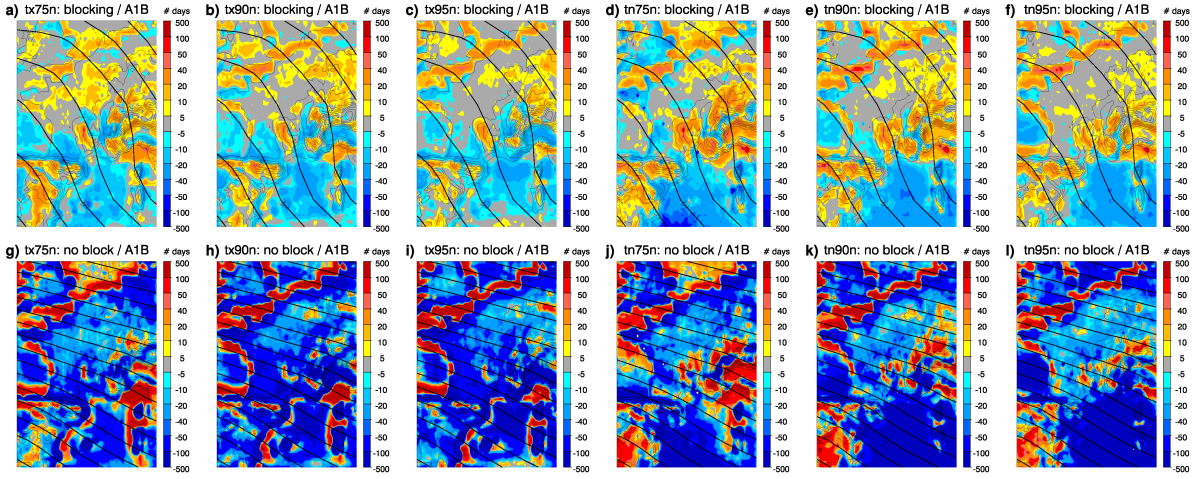

Figure C.21: Same as Figure C.20, but for the A1B scenario.

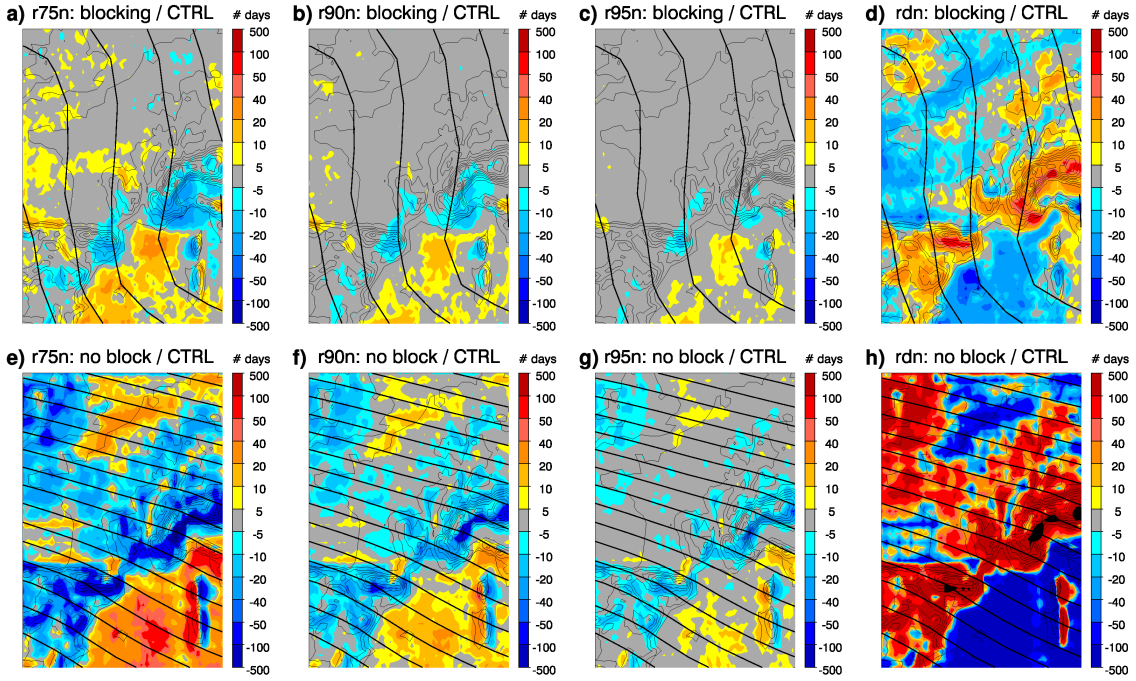

Figure C.22: Differences in the number of **rainfall and dry extreme** days for MR - HR for the CTRL simulations.

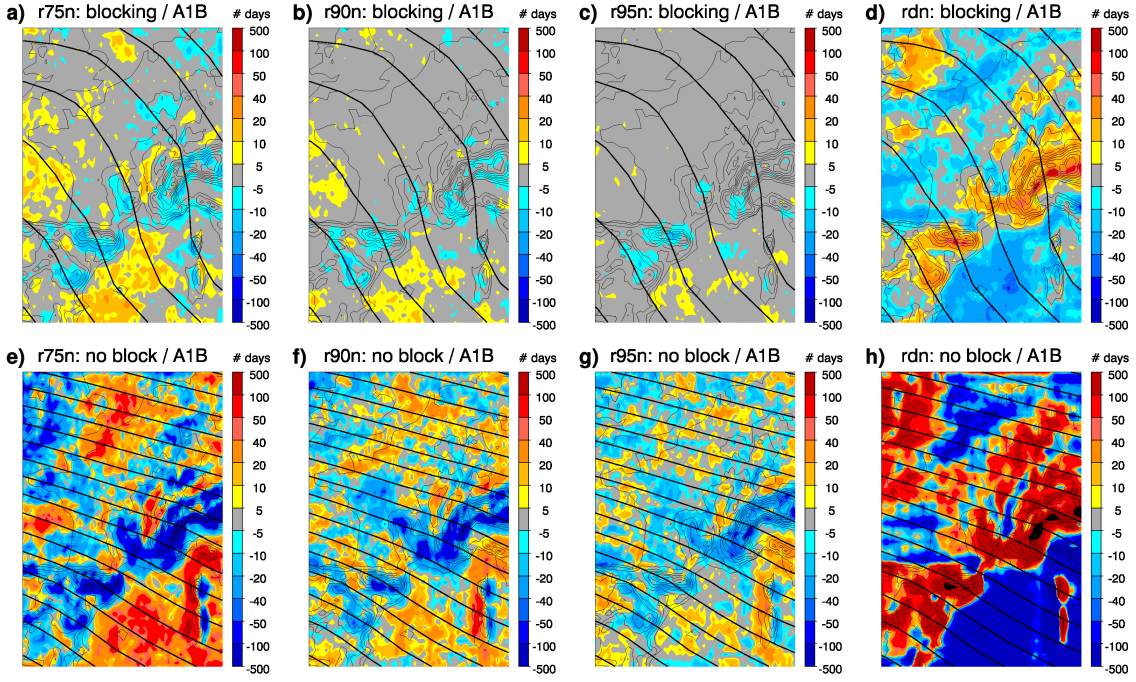

Figure C.23: Same as Figure C.22, but for the A1B scenario.

Difference in the frequency of extreme weather events between E-OBS and the model

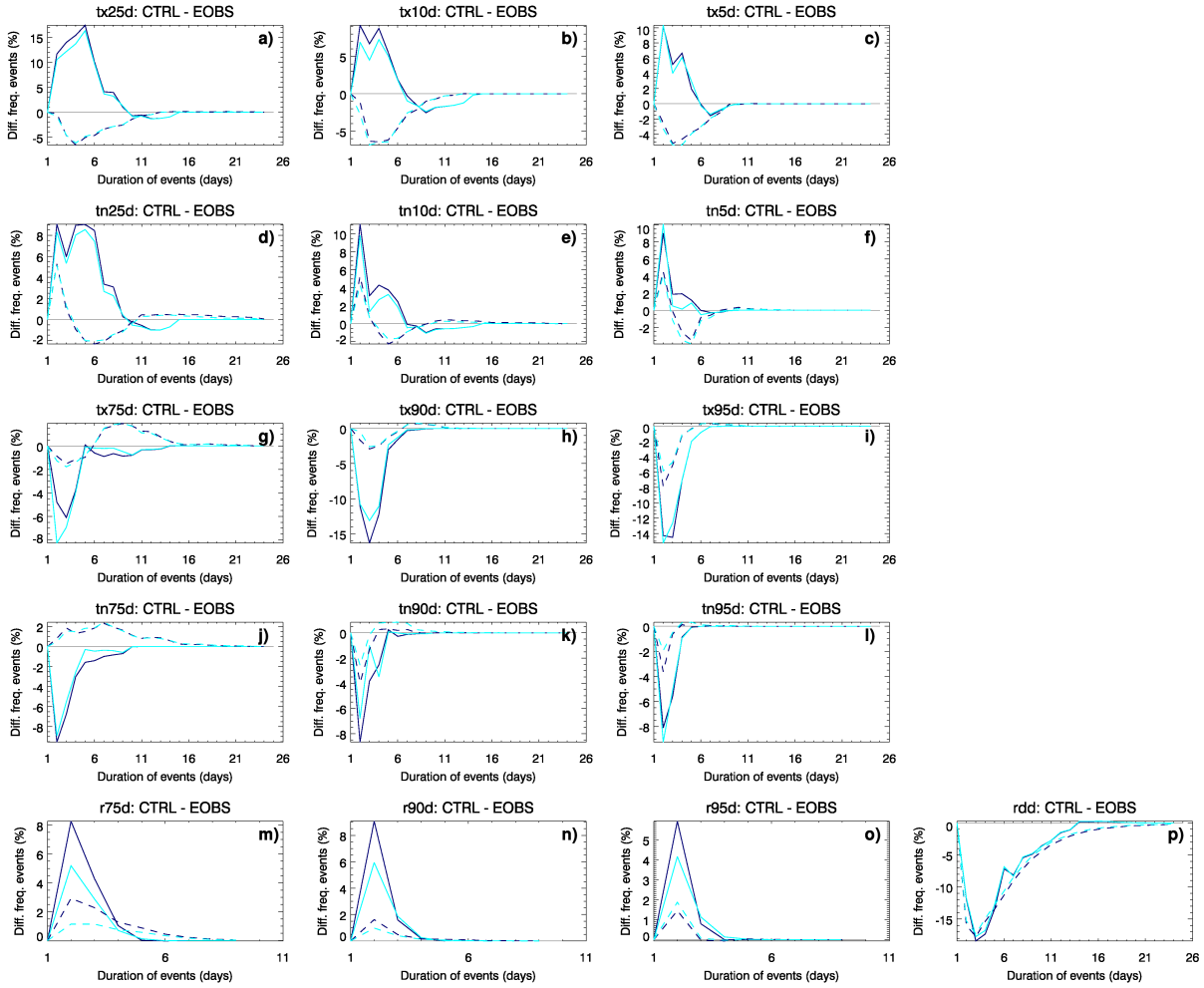

Figure C.24: Differences in the average frequency (in %) of extreme weather events as a function of spell duration over France, blocked (solid lines), non-blocked (dashed lines) situations, for EOBS - CTRL (MR, navy and HR, cyan).

References

Aguilar, E., T. C. Peterson, P. R. Obando, R. Frutos, J. A. Retana, M. Solera, J. Soley, I. G. Garcia, R. M. Araujo, A. R. Santos, V. E. Valle, M. Brunet, L. Aguilar, L. Alvarez, M. Bautista, C. Castanon, L. Herrera, E. Ruano, J. J. Sinay, E. Sanchez, G. I. H. Oviedo, F. Obed, J. E. Salgado, J. L. Vazquez, M. Baca, M. Gutierrez, C. Centella, J. Espinosa, D. Martinez, B. Olmedo, C. E. O. Espinoza, R. Nunez, M. Haylock, H. Benavides, and R. Mayorga (2005), Changes in precipitation and temperature extremes in Central America and northern South America, 1961-2003, *Journal of Geophysical Research-Atmospheres*, *110*, 15.

Anderson, J. L. (1993), The climatology of blocking in a numerical forecast model, *Journal of Climate*, *6*, 1041–1056.

Andrews, D. G., J. R. Holton, and B. L. Conway (1987), *Middle atmosphere dynamics*, vol. 40, Academic Press.

Arai, M., and H. Mukougawa (2002), On the effectiveness of the eddy straining mechanism for the maintenance of blocking flows, *International Symposium on Stratospheric Variations and Climate*, pp. 1089–1102.

Austin, J. (1980), The blocking of middle latitude westerly winds by planetary waves, *The Quarterly Journal of the Royal Meteorological Society*, *106*, 327–350.

Baldwin, M. P., and T. J. Dunkerton (1989), The stratospheric major warming of early December 1987, *Journal of the Atmospheric Sciences*, *46*, 2863–2884.

Barriopedro, D., R. Garcia-Herrera, A. R. Lupo, and E. Hernandez (2006), A climatology of Northern Hemisphere blocking, *Journal of Climate*.

Barriopedro, D., R. Garcia-Herrera, and R. M. Trigo (2010), Application of blocking diagnosis methods to General Circulation Models. Part I: a novel detection scheme, *Climate Dynamics*, *19*, 1042–1063.

Beniston, M. (2004), The 2003 heat wave in Europe: A shape of things to come? An analysis based on Swiss climatological data and model simulations, *Geophysical Research Letters*, *31*.

Beniston, M., D. B. Stephenson, O. B. Christensen, C. A. T. Ferro, C. Frei, S. Goyette, K. Halsnaes, T. Holt, K. Jylha, B. Koffi, J. Palutikof, R. Scholl, T. Semmler, and K. Woth (2007), Future extreme events in European climate: an exploration of regional climate model projections, *Climatic Change*, *81*, 71–95.

Berggen, R., B. Bolin, and C.-G. Rossby (1949), An Aerological Study of Zonal Motion, its Perturbations and Break-down, *Tellus*, *1*(2), 14–37.

Berner, J., F. J. Doblas-Reyes, P. T. N., G. J. Shutts, and A. Weisheimer (2008), *Impact of a quasi-stochastic cellular automaton backscatter scheme on the systematic error and seasonal prediction skill of a global climate model*, Tech. Rep. D1.13, ECMWF.

Berrisford, P., B. J. Hoskins, and E. Tyrlis (2007), Blocking and Rossby wave breaking on the dynamical tropaupose in the Southern Hemisphere, *Journal of the Atmospheric Sciences*, *64*, 2881–2898.

Black, E., M. Blackburn, G. Harrison, B. J. Hoskins, and J. Methven (2004), Factors contributing to the summer 2003 European heatwave, *Weather*, *59*, 217–223.

Blenkinsop, S., P. D. Jones, S. R. Dorling, and T. Osborn (2009), Observed and modelled influence of atmospheric circulation on central England temperature extremes, *International Journal of Climatology*, *29*, 1642–1660.

Boer, G. P., K. Arpe, M. Blackburn, M. Déqué, W. L. Gates, T. L. Hart, H. Le Treut, E. Rockner, D. A. Sheinin, I. Simmonds, R. N. B. Smith, T. Tokioka, R. T. Wetherald, and D. L. Williamson (1992), An intercomparison of the climates simulated by 14 atmospheric general circulation models, *Journal of Geophysical Research*, *97*, 12,771–12,786.

Bony, S., *et al.* (2006), How well do we understand and evaluate climate change feedback processes?, *Journal of Climate*, *19*, 3445–3482.

Brankovic, C., and F. Molteni (1997), Sensitivity of the ECMWF model northern winter climate to model formulation, *Climate Dynamics*, *13*, 75–101.

Branstator, G. (1987), A striking example of the atmosphere's leading travelling pattern, *Journal of the Atmospheric Sciences*, *44*, 2310–2321.

Brayshaw, D. J., B. J. Hoskins, and M. Blackburn (2008), The storm-track response to idealized SST perturbations in an aquaplanet GCM, *Journal of the Atmospheric Sciences*, *65*, 2842–2860.

Cao, H. X., J. F. B. Mitchell, and J. R. Lavery (1992), Simulated diurnal range and variability of surface temperature in a global climate model for present and doubled CO2 climates, *Journal of Climate*, *5*, 920–943.

Carey-Smith, T. K., S. M. Dean, J. Vial, and C. Thompson (2010), Changes in precipitation extremes for New Zealand: climate model predictions, *Weather and Climate*, *30*, 20–45.

Carlson, T. N. (1991), *Mid-latitude weather systems*, Harper Collins Academic.

Carrera, M. L., R. W. Higgins, and V. E. Kousky (2004), Downstream weather impacts associated with atmospheric blocking over the Northeast Pacific, *Journal of Climate*, *17*, 4823–4839.

Carril, A. F., S. Gualdi, A. Cherchi, and A. Navarra (2008), Heatwaves in Europe: areas of homogeneous variability and links with the regional to large-scale atmospheric and SSTs anomalies, *Climate Dynamics*, *30*, 77–98.

Cash, B. A., and S. Lee (2000), Dynamical processes of block evolution., *Journal of Atmospheric Sciences*, *57*, 3202–3218.

Cehelsky, P., and K. K. Tung (1987), Theories of multiple equilibria and weather regimes - a critical reexamination. Part II: baroclinic 2-layer models, *Journal of the Atmospheric Sciences*, *44*(21), 3282–3303.

Charlton, A. J., and L. M. Polvani (2007), A new look at stratospheric sudden warmings. Part I: Climatology and modeling benchmarks, *Journal of Climate*, *20*, 449–469.

Charney, J. G., and J. . G. DeVore (1979), Multiple-flow equilibria in the atmosphere and blocking, *Journal of Atmospheric Sciences*, *36*, 1205–1216.

Charney, J. G., and A. Eliassen (1949), A Numerical Method for Predicting the Perturbations of the Middle Latitude Westerlies, *Tellus*, *1*, 38–54.

Charney, J. G., J. Shukla, and K. C. Mo (1981), Comparison of a barotropic blocking theory with observation, *Journal of the Atmospheric Sciences*, *38*, 762–779.

Charney, J. G., and D. Straus (1980), Form-Drag Instability, Multiple Equilibria and Propagating Planetary Waves in Baroclinic, Orographically Forced, Planetary Wave Systems, *Journal of Atmospheric Sciences*, *37*, 1157–1176.

Charney, J. G., *et al.* (1979), *Carbon dioxide and climate: a scientific assessment : report of an Ad Hoc Study Group on Carbon Dioxide and Climate, Woods Hole, Massachusetts, July 23-27, 1979 to the Climate Research Board, Assembly of Mathematical and Physical Sciences, National Research Council*, National Academy of Sciences : available from Climate Research Board.

Chen, C.-T., and T. Knutson (2008), On the verification and comparison of extreme rainfall indices from climate models, *Journal of Climate*, *21*, 1605–1621.

Chen, W. Y., and H. M. Van Den Dool (1997), Asymmetric Impact of Tropical SST Anomalies on Atmospheric Internal Variability over the North Pacific, *Journal of the Atmospheric Sciences*, *54*, 725–740.

Cohen, J., M. Barlow, P. J. Kushner, and K. Saito (2007), Stratosphere-troposphere coupling and links with Eurasian land surface variability, *Journal of Climate*, *20*, 5335–5343.

Coindreau, O., F. Hourdin, M. Haeffelin, A. Mathieu, and C. Rio (2007), Assessment of physical parameterizations using a global climate model with stretchable grid and nudging, *Monthly Weather Review*, *135*, 1474–1489.

Colucci, S. J. (1985), Explosive cyclogenesis and large-scale circulation changes: Implications for atmospheric blocking, *Journal of the Atmospheric Sciences*, *42*(24), 2701–2717.

Colucci, S. J. (1987), Comparative diagnosis of blocking versu nonblocking planetary-scale circulation changes during synoptic-scale cyclogenesis, *Journal of the Atmospheric Sciences*, *44*(1), 124–139.

Colucci, S. J. (2001), Planetary-Scale Preconditioning for the Onset of Blocking, *Journal of the Atmospheric Sciences*, *58*, 933–942.

Colucci, S. J., and T. L. Alberta (1996), Planetary-scale climatology of cyclogenesis and blocking, *Monthly Weather Review*, *124*, 2509–2520.

Croci-Maspoli, M., and H. C. Davies (2009), Key dynamical features of the 2005/06 European winter, *Monthly Weather Review*, *137*, 664–678.

Croci-Maspoli, M., C. Schwierz, and H. C. Davies (2007a), Atmospheric blocking: space-time links to the NAO and PNA, *Climate Dynamics*, *29*, 713–725.

Croci-Maspoli, M., C. Schwierz, and H. C. Davies (2007b), A multifaceted climatology of atmospheric blocking and its recent linear trend, *Journal of Climate*, *20*, 633–649.

Dai, A., K. E. Trenberth, and T. R. Karl (1999), Effects of clouds, soil moisture, precipitation, and water vapor on diurnal temperature range, *Journal of Climate*, *12*, 2451–2473.

D'Andrea, F., S. Tibaldi, M. Blackburn, G. Boer, M. Déqué, M. Dix, B. Dugas, L. Ferranti, T. Iwasaki, A. Kitoh, V. Pope, D. Randall, E. Roeckner, D. Straus, W. Stern, H. V. Den Dool, and D. Williamson (1998), Northern Hemisphere atmospheric blocking as simulated by 15 atmospheric general circulation models in the period 1979-1988, *Climate Dynamics*, *4*, 385–407.

Diao, Y., J. Li, and D. Luo (2006), A New Blocking Index and Its Application: Blocking Action in the Northern Hemisphere, *Journal of Climate*, *19*, 4819–4839.

Doblas-Reyes, F. J., M. J. Casado, and M. A. Pastor (2002), Sensitivity of the Northern Hemisphere blocking frequency to the detection index, *Journal of Geophysical Research*, *107*.

Doblas-Reyes, F. J., M. Déqué, F. Valero, and D. B. Stephenson (1998), North Atlantic wintertime intraseasonal variability and its sensitivity to GCM horizontal resolution, *Tellus*, *50A*, 573–595.

Dole, R. M., and N. D. Gordon (1983), Persistent Anomalies of the Extratropical Northern Hemisphere Wintertime Circulation: Geographical Distribution and Regional Persistence Characteristics, *Monthly Weather Review*, *111*, 1567–1586.

Egger, J. (1978), Dynamics of blocking highs, *Journal of Atmospheric Sciences*, *35*, 1788–1801.

Elliot, R., and T. Smith (1949), A study of the effects of a large blocking highs on the general circulation in the Northern-Hemisphere westerlies, *Journal of Meteorology*, *6*, 67–85.

Feldstein, S. B. (2002), Fundamental mechanisms of the growth and decay of the PNA teleconnection pattern, *Quarterly Journal of the Royal Meteorological Society*, *128*, 775–796.

Feldstein, S. B. (2003), The dynamics of NAO teleconnection pattern growth and decays, *Quarterly Journal of the Royal Meteorological Society*, *129*, 901–924.

Ferranti, L., F. Molteni, C. Brankovic, and T. N. Palmer (1994a), Diagnosis of extra-tropical variabilit in seasonal integrations of the ECMWF model, *Journal of Climate*, *7*, 849–868.

Ferranti, L., F. Molteni, and T. N. Palmer (1994b), Impact of localized tropical SST anomalies in ensembles of seasonal GCM integrations., *Quarterly Journal of the Royal Meteorological Society*, *120*, 1613–1645.

Fox-Rabinovitz, M., J. Coté, B. Dugas, M. Déqué, and J. L. McGregor (2006), Variable resolution general circulation models: Stretched-grid model intercomparison project (SGMIP), *Journal of Geophysical Research*, *111*(D16104).

Franzke, C., S. B. Feldstein, and S. Lee (2011), Synoptic analysis of the Pacific-North American teleconnection pattern, *Quarterly Journal of the Royal Meteorological Society*, *137*, 329–346.

Franzke, C., S. Lee, and S. B. Feldstein (2004), Is the North Atlantic Oscillation a breaking wave?, *Journal of the Atmospheric Sciences*, *61*, 145–160.

Frederiksen, J. S. (1982), A unified three-dimensional instability theory of the onset of blocking and cyclogenesis, *Journal of the Atmospheric Sciences*, *39*, 969–982.

Frederiksen, J. S. (1983), A unified three-dimensional instability theory of the onset of blocking and cyclogenesis. II: Teleconnection patterns, *Journal of Atmospheric Sciences*, *40*, 2593–2609.

Frederiksen, J. S. (1989), The role of instability during the onset of blocking and cyclogenesis in Northern Hemisphere synoptic flows, *Journal of the Atmospheric Sciences*, *46*, 1076–1092.

Frederiksen, J. S., and R. C. Bell (1990), North Atlantic blocking during January 1979: Linear theory, *Quarterly Journal of the Royal Meteorological Society*, *116*, 1289–1313.

Frei, C. (2003), Statistical limitations for diagnosing changes in extremes from climate model simulations, *AMS annual meeting*, *14*, 1–6, 14th Symposium on Global Change and Climate Variations.

Frich, P., L. V. Alexander, P. Della-Marta, B. Gleason, M. Haylock, A. M. G. Klein Tank, and T. Peterson (2002), Observed coherent changes in climatic extremes during the second half of the twentieth century, *Climate Research*, *19*, 193–212.

Giorgi, F., and M. R. Marinucci (1996), An investigation of the sensitivity of simulated precipitation to model resolution and its implications for climate studies, *Monthly Weather Review*, *124*, 148–166.

Goubanova, K., and L. Li (2007), Extremes in temperature and precipitation around the Mediterranean basin in an ensemble of future climate scenario simulations, *Global and Planetary Change*, *57*, 27–42.

Goubanova, K., L. Li, P. Yiou, and F. Codron (2010), Relation between large-scale circulation and European winter temperature: Does it hold under warmer climate?, *Journal of Climate*, *23*, 3752–3760.

Green, J. (1977), The weather during July 1976: Some dynamical considerations of the drought, *Weather*, *32*, 120–126.

Gregory, J. M., and J. F. B. Mitchell (1995), Simulation of daily variability of surface temperature and precipitation over europe in the current and 2 CO2 climates using the UKMO climate model, *Quarterly Journal of the Royal Meteorological Society*, *121*, 1451–1476.

Grose, W. L., and B. J. Hoskins (1979), On the Influence of Orography on Large-Scale Atmospheric Flow, *Journal of the Atmospheric Sciences*, *36*, 223–234.

Haines, K. (1989), Barotropic modons as prototypes for atmospheric blocking, *Journal of the Atmospheric Sciences*, *46*(20), 3202–3218.

Haines, K., and A. Hannachi (1995), Weather regimes in the Pacific from a GCM, *Journal of the Atmospheric Sciences*, *52*, 2444–2462.

Haines, K., and J. Marshall (1987), Eddy-forced coherent structures as a prototype of atmospheric blocking, *Quarterly Journal of the Royal Meteorological Society*, *113*(476), 681–704.

Hannachi, A. (1997), Low-frequency variability in a GCM: three-dimensional flow regimes and their dynamics, *Journal of Climate*, *10*, 1357–1379.

Hannachi, A., and A. O'Neill (2001), Atmospheric multiple equilibria and non-Gaussian behaviour in model simulations, *Quarterly Journal of the Royal Meteorological Society*, *127*, 939–958.

Hansen, A. R., and T.-C. Chen (1982), A spectral energetics analysis of atmospheric blocking, *Monthly Weather Review*, *110*, 1146–1165.

Hartmann, D. L., and S. J. Ghan (1980), A statistical study of the dynamics of blocking, *Monthly Weather Review*, *108*, 1144–1159.

Haylock, M., and C. Goodess (2004), Interannual variability of European extreme winter rainfall and links with mean large-scale circulation, *International Journal of Climatology*, *24*, 759–776.

Haylock, M., N. Hofstra, A. M. G. Klein Tank, E. J. Klok, P. D. Jones, and M. New (2008), A European daily high-resolution gridded data set of surface temperature and precipitation for 1950-2006, *Journal of Geophysical Research*, *113*.

Hennessy, K. J., J. M. Gregory, and J. F. B. Mitchell (1997), Changes in daily precipitation under enhanced greenhouse conditions, *Climate Dynamics*, *13*, 667–680.

Higgins, R. W., and S. D. Schubert (1994), Simulated Life Cycles of Persistent Anticyclonic Anomalies over the North Pacific: Role of Synoptic-Scale Eddies, *Journal of the Atmospheric Sciences*, *51*, 3238–3260.

Hinton, T. J., B. J. Hoskins, and G. M. Martin (2009), The influence of tropical sea surface temperatures and precipitation on north Pacific atmospheric blocking, *Climate Dynamics*, *33*, 549–563.

Hofstra, N., M. Haylock, M. New, and P. D. Jones (2009), Testing E-OBS European high-resolution gridded data set of daily precipitation and surface temperature, *Journal of Geophysical Research*, *114*(D21101).

Holton, J. (2004), *An introduction to dynamic meteorology*, no. v. 1 in International geophysics series, Elsevier Academic Press.

Holton, J. R., and C. Mass (1976), Statospheric vascillation cycles, *Journal of the Atmospheric Sciences*, *33*, 2218–2225.

Hoskins, B. J. (1987), Theories of blocking, *ECMWF Seminar Proceedings: The nature and prediction of extra-tropical cyclones*, *2*, 1–10.

Hoskins, B. J., I. N. James, and G. H. White (1983), The Shape, Propagation and Mean-Flow Interaction of Large-Scale Weather Systems, *Journal of the Atmospheric Sciences*, *40*, 1595–1612.

Hoskins, B. J., and D. J. Karoly (1981), The Steady Linear Response of a Spherical Atmosphere to Thermal and Orographic Forcing, *Journal of the Atmospheric Sciences*, *38*, 1179–1196.

Hoskins, B. J., M. McIntyre, and A. Roberston (1985), On the use and significance of isentropic potential vorticity maps, *Quarterly Journal of the Royal Meteorological Society*, *111*, 877–946.

Hoskins, B. J., and P. D. Sardeshmukh (1987), A diagnostic study of the dynamics of the northern hemisphere winter of 1985-86, *Quarterly Journal of Royal Meteorological Society*, *113*, 759–778.

Hourdin, F., I. Musat, S. Bony, P. Braconnot, F. Codron, J.-L. Dufresne, L. Fairhead, M.-A. Filiberti, P. Friedlingstein, J.-Y. Grandpeix, G. Krinner, P. LeVan, Z.-X. Li, F. Lott, *et al.* (2006), The LMDZ4 general circulation model: climate performance and sensitivity to parametrized physics with emphasis on tropical convection, *Climate Dynamics*, *27*, 787–813.

Hurrell, J. W. (1995), Decadal trends in the North Atlantic Oscillation: regional temperatures and precipitation, *Science*, *269*, 676–679.

Illari, L. (1984), A Diagnostic Study of the Potential Vorticity in a Warm Blocking Anticyclone, *Journal of the Atmospheric Sciences*, *41*, 3518–3526.

Jung, T. (2005), Systematic errors of the atmospheric circulation in the ECMWF forecasting system, *Quarterly Journal of Royal Meteorological Society*, *131*, 1045–1073.

Kaas, E., and G. Branstator (1993), The Relationship between a zonal Index and blocking activity, *Journal of Atmospheric Sciences*, *50*, 3061–3077.

Kallen, E. (1981), The nonlinear effects of orographic and momentum forcing in a low-order, barotropic model, *Journal of the Atmospheric Sciences*, *38*, 2150–2163.

Kalnay, E., M. Kanamitsu, R. Kistler, W. Collins, D. Deaven, L. Gandin, M. Iredell, S. Saha, G. White, J. Wollen, Y. Zhu, M. Chelliah, W. Ebisuzaki, W. Higgins, J. Janowiak, K. C. Mo, C. Ropelewski, J. Wang, A. Leetmaa, R. Reynolds, R. Jenne, and D. Joseph (1996), The NCEP/NCAR 40-year reanalysis project, *Bulletin of American Meteorological Society*, *77*, 437–471.

Kanamitsu, M., and L. DeHaan (2011), The added value index: a new metric to quantify the added value of regional models, *Journal of Geophysical Research*, *116*, D11,106.

Kiktev, D., D. M. H. Sexton, L. Alexander, and C. K. Folland (2003), Comparison of modeled and observed trends in indices of daily climate extremes, *Journal of Climate*, *16*, 3560–3571.

Klein Tank, A. M. G., and G. P. Können (2003), Trends in indices of daily temperature and precipitation extremes in Europe 1946-99, *Journal of Climate*, *16*, 3665–3680.

Klein Tank, A. M. G., F. W. Zwiers, and X. Zhang (2009), *Guidelines on Analysis of extremes in a changing climate in support of informed decisions for adaptation*, Tech. Rep. WCDMP-No. 72, WMO-TD No. 1500, World Meteorological Organization.

Kolstad, E., and A. Charlton-Perez (2011), Observed and simulated precursors of stratospheric polar vortex anomalies in the Northern Hemisphere, *Climate Dynamics*, *37*, 1443–1456.

Korteweg, D. J., and G. D. Vries (1895), On the change of form of long waves advancing in a rectangular channel, and on a new type of long stationary waves, *Philosophical Magazine*, *39*, 442–443.

Kuroda, Y., and K. Kodera (2001), Variability of the polar night jet in the Northern and Southern Hemispheres, *Journal of Geophysical Research*, *106*, 20,703–20,713.

Kushnir, Y. (1987), Retrograding wintertime low-frequency disturbances over the North Pacific Ocean, *Journal of the Atmospheric Sciences*, *44*, 2727–2741.

Labitzke, K. (1965), On the mutual relation between stratosphere and troposphere during periods of stratospheric warmings in winter, *Journal of Applied Meteorology*, *4*, 91–99.

Legras, B., and M. Ghil (1985), Persistant anomalies, blocking and variations in atmospheric predictability, *Journal of the Atmospheric Sciences*, *42*, 433–471.

Lejenäs, H., and H. Økland (1983), Characteristics of Northern Hemisphere blocking as determined from a long time series of observational data, *Tellus A*, *35*, 350–362.

Limpasuvan, V., D. W. J. Thompson, and D. L. Hartmann (2004), The life cycle of the northern hemisphere sudden stratospheric warmings, *Journal of Climate*, *17*.

Liu, Q. (1994), On the definition and persistence of blocking, *Tellus*, *46 A*, 286–298.

Lockwood, J. G. (2005), *Atmospheric circulation, global*, pp. 126–134, Encyclopedia of Earth Sciences Series, Springer.

Lott, F., L. Fairhead, F. Hourdin, and P. Levan (2005), The stratospheric version of LMDz: dynamical climatologies, arctic oscillation, and impact on the surface climate, *Climate Dynamics*.

Lupo, A. R., and P. J. Smith (1995a), Climatological features of blocking anticyclones in the northern hemisphere, *Tellus Series a-Dynamic Meteorology and Oceanography*, *47*, 439–456.

Lupo, A. R., and P. J. Smith (1995b), Planetary and synoptic-scale interactions during the life cycle of a mid-latitude blocking anticyclone over the North Atlantic, *Tellus*, *47A*, 575–596.

Malanotte-Rizzoli, P., and P. J. Hancock (1987), Coherent structures in a baroclinic atmosphere. Part IV: A comparison between theory and data, *Journal of the Atmospheric Sciences*, *44*(17), 2506–2529.

Malanotte-Rizzoli, P., and P. Malguzzi (1987), Coherent structures in a baroclinic atmosphere. Part III: Block formation and eddy forcing, *Journal of the Atmospheric Sciences*, *44*, 2493–2505.

Malguzzi, P., and P. Malanotte-Rizzoli (1984), Nonlinear stationary rossby waves on nonuniform zonal winds and atmospheric blocking. Part I: the analytical theory, *Journal of the Atmospheric Sciences*, *41*(17), 2620–2628.

Malguzzi, P., and P. Malanotte-Rizzoli (1985), Coherent structures in a baroclinic atmosphere. Part II: A truncated model approach, *Journal of the Atmospheric Sciences*, *42*, 2463–2477.

Malguzzi, P., and A. Speranza (1981), Local multiple equilibria and regional atmospheric blocking, *Journal of the Atmospheric Sciences*, *38*, 1939–1948.

Marin, F. (2009), Solitons: Historical and Physical Introduction, in: *Encyclopedia of Complexity and Systems Science* (Meyers, R. A., ed.), pp. 8464–8479, Springer New York.

Marques, R., and V. B. Rao (1999), A diagnosis of a long-lasting blocking event over the Southeast Pacific ocean, *Monthly Weather Review*, *127*, 1761–1776.

Marti, O., *et al.* (2006), *The new IPSL climate system model: IPSL-CM4*, Tech. rep., Institut Pierre Simon Laplace des Sciences de lEnvironnement Global IPSL Global Climate Modeling Group.

Martius, O., M. L. Polvani, and H. C. Davies (2009), Blocking precursors to stratospheric sudden warming events, *Geophysical Research Letters*, *36*.

Martius, O., C. Schwierz, and H. C. Davies (2007), Breaking waves at the tropopause in the wintertime Northern Hemisphere: Climatological analyses of the orientation and the theoretical LC1/2 classification, *Journal of the Atmospheric Sciences*, *64*.

Mass, C. F., D. Ovens, K. Westrick, and B. A. Colle (2002), Does increasing horizontal resolution produce more skillful forecasts?, *Bulletin of American Meteorological Society*, pp. 407–430.

Matsueda, M., R. Mizuta, and S. Kusunoki (2009), Future change in Northern Hemisphere wintertime atmospheric blocking simulated by a 20-km mesh atmospheric global circulation model, *Journal of Geophysical Research*, *114*(D12114).

Matsueda, M., and T. N. Palmer (2011), Accuracy of climate change predictions using high resolution simulations as surrogates of truth, *Geophysical Research Letters*, *38*.

Matsuno, T. (1971), A dynamical model of the stratospheric sudden warming, *Journal of the Atmospheric Sciences*, *28*, 1479–1494.

McGuffie, K., and A. Henderson-Sellers (2005), *A climate modelling primer*, vol. 1, John Wiley.

McIntyre, M. (1982), How well do we understand the dynamics of stratospheric warmings?, *Journal of the Meteorological Society of Japan*, *60*, 37–64.

McWilliams, J. C. (1980), An application of equivalent modons to atmospheric blocking, *Dynamics of Atmospheres and Oceans*, *5*, 43–66.

McWilliams, J. C., G. R. Flierl, V. D. Larichev, and G. M. Reznik (1981), Numerical studies of barotropic modons, *Dynimics of Atmospheres and Oceans*, *5*(4), 219–238.

Michelangeli, P.-A., and R. Vautard (1998), The dynamics of Euro-Atlantic blocking onsets, *Quarterly Journal of the Royal Meteorological Society*, *124*, 1045–1070.

Michelangeli, P.-A., R. Vautard, and B. Legra (1995), Weather regimes: recurrence and quasi-stationarity, *Journal of Atmospheric Sciences*, *52*, 1237–1256.

Moberg, A., and P. D. Jones (2004), Regional climate model simulations of daily maximum and minimum near-surface temperatures across Europe compared with observed station data 1961-1990, *Climate Dynamics*, *23*, 695–715.

Molteni, F. (1996), On the Dynamics of Planetary Flow Regimes. Part II: Results from a Hierarchy of Orographically Forced Models, *Journal of the Atmospheric Sciences*, *53*(14), 1972–1992.

Mullen, S. L. (1986), The local balances of vorticity and heat for blocking anticyclones in a spectral general circulation model, *Journal of the Atmospheric Sciences*, *43*(13), 1406–1441.

Mullen, S. L. (1989), Model Experiments on the Impact of Pacific Sea Surface Temperature Anomalies on Blocking Frequency, *Journal of Climate*, *2*, 997–1013.

Nakamura, H., M. Nakamura, and J. L. Anderson (1997), The role of high- and low-frequency dynamics in blocking formation, *Monthly Weather Review*, *125*, 2074–2093.

Nakamura, H., and J. M. Wallace (1990), Observed changes in baroclinic wave activity during the life cycles of low-frequency circulation anomalies, *Journal of Atmospheric Sciences*, *47*, 1100–1116.

Namias, J. (1964), Seasonal persistance and recurrance of European blocking during 1958-1960, *Tellus*, *16*, 394–407.

Naujokat, B., K. Kruger, K. Matthes, J. Hoffmann, M. Kunze, and K. Labitzke (2002), The early major warming in December 2001 - exceptional?, *Geophysical Research Letters*, *29*(21).

Nitsche, G., J. M. Wallace, and C. Kooperberg (1994), Is there evidence of multiple equilibria in planetary wave amplitude statistics?, *Journal of the Atmospheric Sciences*, *51*(2), 314–322.

Palmer, T. N. (2001), A nonlinear dynamical perspective on model error: A proposal for non-local stochastic-dynamic parametrization in weather and climate prediction models, *Quarterly Journal of the Royal Meteorological Society*, *127*, 279–303.

Pelly, J., and B. J. Hoskins (2003), A new perspective on blocking, *Journal of Atmospheric Sciences*, *60*, 743–755.

Planton, S., M. Déqué, F. Chauvin, and L. Terray (2008), Expected impacts of climate change on extreme climate events., *Geoscience*, *340*, 564–574.

Polvani, L. M., and D. W. Waugh (2004), Upward wave activity flux as a precursor to extreme stratospheric events and subsequent anomalous surface weather regimes, *Journal of Climate*, *17*, 3514–3554.

Pozo-Vazquez, D., M. J. Esteban-Parra, F. S. Rodrigo, and Y. Castro-Diez (2001), The association between ENSO and winter atmospheric circulation and temperature in the north Atlantic region, *Journal of Climate*, *14*, 3408–3420.

Press, W. H., S. A. Teukolsky, W. T. Vetterling, and B. P. Flannery (1992), *Numerical recipes in Fortran: The Art of Scientific Computing (Second Edition)*, Cambrdge University Press.

Quiroz, R. S. (1986), The association of stratospheric warmings with tropospheric blocking, *Journal of Geophysical Research*, *91*, 5277–5285.

Reinhold, B. B. (1989), Comments on "Theories of multiple equilibria and weather regimes: A critical reexamination of baroclinic two-layer models", *Journal of the Atmospheric Sciences*, *46*, 1861–1864.

Reinhold, B. B., and R. T. Pierrehumbert (1985), Corrections to "Dynamics of weather regimes: quasi-stationary waves and blocking", *Monthly Weather Review*, *113*, 2055–2056.

Renwick, J. A., and M. J. Revell (1999), Blocking over the South Pacific and Rossby wave propagation, *Monthly Weather Review*, *127*, 2233–2247.

Renwick, J. A., and J. M. Wallace (1996), Relationships between North Pacific Wintertime Blocking, El Nino, and the PNA Pattern, *Monthly Weather Review*, *124*, 2071–2076.

Rex, D. (1950a), Blocking action in the middle troposphere and its effect upon regional climate. Part 1: An aerological study of blocking action, *Tellus*, *42*, 196–211.

Rex, D. (1950b), Blocking action in the middle troposphere and its effect upon regional climate. Part 2: The climatology of blocking action, *Tellus*, *2*, 275–301.

Ringer, M. A., G. M. Martin, C. Z. Greeves, T. J. Hinton, P. M. James, V. D. Pope, A. A. Scaife, and R. A. Stratton (2006), The physical properties of the atmosphere in the new Hadley Centre global environmental model (HadGEM1). Part II: Aspects of variability and regional climate, *Journal of Climate*, *19*, 1302–1326.

Saito, K., and J. Entekhabi (2001), Evolution of atmospheric response to early-season Eurasian snow cover anomalies, *Monthly Weather Review*, *129*, 2746–2760.

Sausen, R., W. Konig, and W. F. Sielman (1995), Analysis of blocking events from observations and ECHAM model simulations, *Tellus A*, *47*, 421–438.

Scaife, A. A., and J. R. Knight (2008), Ensemble simulations of the cold European winter of 2005-2006, *Quarterly Journal of the Royal Meteorological Society*, *134*, 1647–1659.

Scaife, A. A., T. J. Woollings, J. R. Knight, G. M. Martin, and T. J. Hinton (2010), Atmospheric blocking and mean biases in climate models, *Journal of Climate*, *23*, 6143–6152.

Scherrer, S., M. Croci-Maspoli, C. Schwierz, and C. Appenzeller (2006), Two-dimensional indices of atmospheric blocking and their statistical relationship with winter climate patterns in the Euro-Atlantic region, *International Journal of Climatology*, *26*, 233–249.

Schwierz, C., M. Croci-Maspoli, and H. Davies (2004), Perspicacious indicators of atmospheric blocking, *Geophysical Research Letters*, *31*, L06,125.

Scinocca, J. F., and K. Haines (1998), Dynamical Forcing of Stratospheric Planetary Waves by Tropospheric Baroclinic Eddies, *Journal of the Atmospheric Sciences*, *55*, 2361–2392.

Shabbar, A., J. Huang, and K. Higuchi (2001), The relationship between the wintertime North Atlantic Oscillation and blocking episodes in the north Atlantic, *International Journal of Climatology*, *21*, 355–369.

Shakina, N. P., and A. R. Ivanova (2010), The blocking anticyclones: the state of studies and forecasting, *Russian Meteorology and Hydrology*, *35*, 721–729.

Shutts, G. J. (1983), The propagation of eddies in diffluent jetstreams: Eddy vorticity forcing of "blocking" flow fields, *Quarterly Journal of the Royal Meteorological Society*, *109*(462), 737–761.

Shutts, G. J. (1986), A case study of eddy forcing during an Atlantic blocking episode, *Advances in Geophysics*, *29*, 135–162.

Sillmann, J. (2009), *Extreme climate events and Euro-Atlantic atmospheric blocking in present and future climate model simulations*, Tech. rep., Max Planck Institute for Meteorology.

Sillmann, J., and M. Croci-Maspoli (2009), Present and future atmospheric blocking and its impact on European mean and extreme climate, *Geophysical Research Letters*, *36*.

Sillmann, J., and E. Roeckner (2008), Indices for extreme events in projections of anthropogenic climate change, *Climatic Change*, *86*, 83–104.

Slingo, J. M., K. R. Sperber, J. S. Boyle, J.-P. Ceron, M. Dix, B. Dugas, W. Ebisuzaki, J. Fyfe, D. Gregory, J.-F. Gueremy, J. Hack, A. Harzallah, P. Inness, A. Kitoh, W.-M. Lau, B. McAvaney, R. Madden, A. Matthews, T. N. Palmer, C.-K. Park, D. Randall, and N. Renno (1996), Intraseasonal oscillations in 15 atmospheric general circulation models: results from an AMIP diagnostic subproject, *Climate Dynamics*, *12*, 325–357.

Stein, O. (2000), The variability of Atlantic-European blocking as derived from long SLP time series, *Tellus*, *52A*, 225–236.

Stone, D. A., and A. J. Weaver (2003), Factors contributing to diurnal temperature range trends in twentieth and twenty-first century simulations of the CCCma coupled model, *Climate Dynamics*, *20*, 435–445.

Straus, D. M. (2010), Synoptic-eddy feedbacks and circulation regime analysis, *Monthly Weather Review*, *138*(11), 4026–4034.

Taguchi, M. (2008), Is there a statistical connection between stratospheric sudden warming and tropospheric blocking events?, *Journal of the Atmospheric Sciences*, *65*, 1442–1454.

Taylor, K. E., R. J. Stouffer, and G. A. Meehl (2009), A summary of the CMIP5 experiment design.

Thompson, D. W. J., M. P. Baldwin, and J. M. Wallace (2002), Stratospheric connection to Northern Hemisphere wintertime weather: implications for prediction, *Journal of Climate*, *15*, 1421–1428.

Thompson, D. W. J., and J. M. Wallace (2001), Regional climate impacts of the Northern Hemisphere Annular Mode, *Science*, *293*, 85–89.

Tibaldi, S., F. D'Andrea, E. Tosi, and E. Roeckner (1997), Climatology of northern hemisphere blocking in the ECHAM model, *Climate Dynamics*, *13*, 649–666.

Tibaldi, S., and F. Molteni (1990), On the operational predictability of blocking, *Tellus A*, *42*, 343–365.

Tibaldi, S., A. Navarra, and L. Pedulli (1994), Northern and Southern hemisphere seasonal variability of blocking frequency and predictability, *Monthly Weather Review*, *122*, 1971–2003.

Tomozeiu, R., S. Stefan, and A. Busuioc (2005), Winter precipitation variability and large-scale circulation patterns in Romania, *Theoretical and Applied Climatology*, *81*, 193–201.

Tompkins, H. (2002), Climate change and extreme weather events: Is there a connection?, *Cicerone 3*, *3*, 1–5.

Treidl, R., E. Birch, and P. Sajecki (1981), Blocking action in the Northern Hemisphere: a climatological study, *Atmosphere-Ocean*, *19*, 1–23.

Trenberth, K. E., A. Dai, R. M. Rasmussen, and D. B. Pearson (2003), The changing character of precipitation, *Bulletin of American Meteorological Society*, pp. 1205–1217.

Trenberth, K. E., P. D. Jones, P. Ambenje, R. Bojariu, D. Easterling, A. Klein Tank, D. Parker, F. Rahimzadeh, J. A. Renwick, M. Rusticucci, B. Soden, and P. Zhai (2007), *Observations: Surface and Atmospheric Climate Change. In: Climate Change 2007: The Physical Science Basis. Contribution of Working Group I to the Fourth Assessment Report of the Intergovernmental Panel on Climate Change*, Cambridge University Press, Cambridge, United Kingdom and New York, NY, USA.

Trigo, R., R. Garcia-Herrera, J. Diaz, I. F. Trigo, and M. A. Valente (2005), How exceptional was the early August 2003 heatwave in France?, *Geophysical Research Letters*, *32*, L10,701.

Trigo, R., T. J. Osborn, and J. M. Corte-Real (2002), The North Atlantic Oscillation influence on Europe: climate impacts and associated physical mechanisms, *Climate Research*, *20*, 9–17.

Trigo, R., I. Trigo, C. DaCamara, and T. J. Osborn (2004), Climate impact of the European winter blocking episodes from the NCEP/NCAR reanalyses, *Climate Dynamics*, *23*, 17–28.

Tung, K. K., and R. S. Lindzen (1979), A Theory of Stationary Long Waves. Part I: A Simple Theory of Blocking, *Monthly Weather Review*, *107*, 714–734.

Tung, K. K., and A. J. Rosenthal (1985), Theories of multiple equilibria - a critical reexamination. Part I: barotropic models, *Journal of the Atmospheric Sciences*, *42*(24), 2804–2819.

Tustison, B., D. Harris, and E. Foufoula-Georgiou (2001), Scale issues in verification of precipitation forecasts, *Journal of Geophysical Research*, *106*, 11,775–11,784.

Tyrlis, E., and B. J. Hoskins (2008), The morphology of Northern Hemisphere blocking, *Journal of Atmospheric Sciences*, *65*, 1653–1665.

Uppala, S., P. Kallberg, A. Simmons, U. Andrae, V. D. C. Bechtold, M. Fiorino, J. Gibson, J. Haseler, A. Hernandez, G. Kelly, X. Li, K. Onogi, S. Saarinen, N. Sokka, R. Allan, E. Andersson, K. Arpe, M. Balmaseda, A. Beljaars, L. V. D. Berg, J. Bidlot, N. Bormann, S. Caires, F. Chevallier, A. Dethof, M. Dragosavac, M. Fisher, M. Fuentes, S. Hagemann, E. Holm, B. J. Hoskins, L. Isaksen, P. Janssen, R. Jenne, A. Mcnally, J.-F. Mahfouf, J.-J. Morcrette, N. Rayner, R. Saunders, P. Simon, A. Sterl, K. Trenberth, A. Untch, D. Vasiljevic, P. Viterbo, and J. Woolen (2005), The ERA-40 re-analysis, *Quarterly Journal of the Royal Meteorological Society*, *131*, 2961–3012.

Vautard, R. (1990), Multiple weather regimes over the north Atlantic: analysis of precursors and successors, *Monthly Weather Review*, *118*, 2056–2081.

Verdecchia, M., G. Visconti, F. D'Andrea, and S. Tibaldi (1996), A neural network approach for blocking recognition, *Geophysical Research Letters*, *23*(16), 2081–2084.

Verkley, W. T. M. (1984), The construction of barotropic modons on a sphere, *Journal of the Atmospheric Sciences*, *41*(16), 2492–2504.

Vial, J., and T. Osborn (2011), Assessment of Atmosphere-Ocean General Circulation Model Simulations of Winter Northern Hemisphere Atmospheric Blocking, *Climate Dynamics*.

Wallace, J. M., and D. S. Gutzler (1981), Teleconnections in the geopotential height field during the northern hemisphere winter, *Monthly Weather Review*, *109*, 784–812.

Wiedenmann, J., and A. Lupo (2002), The climatology of blocking Anticyclones for the Northern and Southern Hemispheres: block intensity as a diagnostic, *Journal of Climate*, *15*, 3459–3473.

Wiin-Nielsen, A. (1979), Steady states and stability properties of a low-order barotropic system with forcing and dissipation, *Tellus*, *31*, 375–386.

Wilks, D. S. (1995), *Statistical methods in the atmospheric sciences*, Academic Press.

Williamson, D. L., and J. G. Olson (1998), A comparison of semi-Lagrangian and Eulerian polar climate simulations, *Monthly Weather Review*, *126*, 991–1000.

Williamson, D. L., J. G. Olson, and B. A. Boville (1998), A comparison of semi-Lagrangian and Eulerian tropical climate simulations, *Monthly Weather Review*, *126*, 1001–1012.

Woollings, T. J., A. Charlton-Perez, S. Ineson, A. G. Marshall, and G. Masato (2010), Associations between stratospheric variability and tropospheric blocking, *Journal of Geophysical Research*, *115*.

Woollings, T. J., B. Hoskins, M. Blackburn, and P. Berrisford (2008), A new Rossby wave-breaking interpretation of the North Atlantic Oscillation, *Journal of the Atmospheric Sciences*, *65*.

Xoplaki, E., J. F. Gonzalez-Rouco, J. Luterbacher, and H. Wanner (2003), Mediterranean summer air temperature variability and its connection to the large-scale atmospheric circulation and SSTs, *Climate Dynamics*, *20*, 723–739.

Yamazaki, A., and H. Itoh (2009), Selective absorption mechanism for the maintenance of blocking, *Geophysical Research Letters*, *36*, 4.